

Discrete Element Modelling of Wire Meshes for Secured Drapery Applications

Antonio Pol

▶ **To cite this version:**

Antonio Pol. Discrete Element Modelling of Wire Meshes for Secured Drapery Applications. Engineering Sciences [physics]. Università degli Studi di Padova, 2021. English. ⟨NNT : ⟩. ⟨tel-04586625⟩

HAL Id: tel-04586625

https://hal.science/tel-04586625v1

Submitted on 24 May 2024

HAL is a multi-disciplinary open access archive for the deposit and dissemination of scientific research documents, whether they are published or not. The documents may come from teaching and research institutions in France or abroad, or from public or private research centers.

L'archive ouverte pluridisciplinaire **HAL**, est destinée au dépôt et à la diffusion de documents scientifiques de niveau recherche, publiés ou non, émanant des établissements d'enseignement et de recherche français ou étrangers, des laboratoires publics ou privés.



HAL Authorization



UNIVERSITÀ
DEGLI STUDI
DI PADOVA

Head Office: Università degli Studi di Padova

Department: Civil, Environmental and Architectural Engineering (ICEA)

Ph.D. COURSE IN: Science of Civil, Environmental and Architectural Engineering
CURRICULUM: Risk, Vulnerability, Environment, Health and Territory
SERIES: 33rd cycle

DISCRETE ELEMENT MODELLING OF WIRE MESHES FOR SECURED DRAPERY APPLICATIONS

Coordinator: Prof. Carmelo Maiorana
Supervisor: Prof. Fabio Gabrieli

Ph.D. student : Antonio Pol



Università degli Studi di Padova
PhD course in Science of Civil, Environmental and Architectural Engineering

Discrete element modelling of wire meshes for secured drapery applications

Candidate
Antonio Pol

Supervisor
Prof. Fabio Gabrieli

PhD Coordinator
Prof. Carmelo Maiorana

ciclo XXXIII, 2017-2020

Università degli Studi di Padova, Civil, Environmental and Architectural Engineering (ICEA).

Thesis submitted in partial fulfillment of the requirements for the degree of Doctor of Philosophy in Science of Civil, Environmental and Architectural Engineering. Copyright © 2020 by Antonio Pol.

A mia madre,
a mio padre

Acknowledgments

At the beginning of a long journey such as a doctoral thesis, one can barely imagine the amount of issues that one will encounter as well as the great satisfactions one will have the chance to experience. Now that I am at the end of this three-year journey, I feel a strong need to thank the people that helped me to face the former and that have made possible the latter.

At first, I would like to express my sincere gratitude to my supervisor Fabio Gabrieli. His attentive guidance and the trust that he has always granted me were fundamental to my doctoral experience. Since I was a bachelor student, Fabio has been a reference point for me, and these years working together have spurred on my personal and scientific growth.

I am thankful to my friends and colleagues, Veronica Girardi and Francesco Zarattini. I feel lucky to have had the pleasure[1] to share the office with them during my doctoral years. Their huge support was fundamental to overcome some rough patches. I am equally grateful to Francesca Ceccato e Lorenzo Brezzi for the uncountable advice that allowed me to face at best all the new experiences encountered during my first steps in the academic world.

I am grateful to Marion Bost and Andrea Galli for their careful reading of my thesis work and their many insightful comments and suggestions.

I would like to thank Maccaferri Innovation Center that has funded two years of my doctoral period and has provided the experimental data necessary for the development of this work. I am particularly grateful to Dr. Nicola Mazzon for the fruitful discussions and for making this collaboration as easy as possible.

I would also like to thank Dr. Klaus Thoeni for his invaluable help with the numerical aspects at a time when this was completely new to me.

Writing this section was probably the hardest task of my thesis, and that because my memory is short and the list of people that deserve to be thanked is extremely long. Therefore, I will try to by-pass this technical is-

[1] I cannot assure that they feel the same way

sue by thanking all the people that contributed to this thesis work, hopefully no one will feel excluded[2].

My special gratitude goes to Salomé for her unconditional support and huge patience all over these years, without which this thesis would probably not be completed.

Special thanks to my mother Alessandra and my father Paolo. Their humility and daily example have always guided me and have been fundamental to overcome the moments of doubt and discouragement. Even if it may sound a bit banal, I sincerely believe that without them nothing of this would have been possible.

[2]For any complaint, please contact me at ant.pol91@gmail.com

Abstract

Secured drapery systems are extensively used to mitigate the risk connected with shallow instabilities and rockfall in both soil and rock slopes. Despite the wide application of these systems, various features of their mechanical behaviour in field conditions remain unknown. This lack of knowledge is related to the fact that the standard laboratory configurations adopted for the mesh mechanical characterisation are poorly representative of the field conditions.

In this thesis, the Discrete Element Method is used in order to analyse the mechanical behaviour of wire meshes in secured drapery applications. Experimental results, obtained from several test configurations, are used to validate the mesh model. This has permitted the effectiveness of the adopted numerical approach in simulating the mechanical response of a wire mesh, from simple laboratory conditions to complex configurations in which the mesh interacts with multiple external bodies, to be proved.

The mesh model is adopted to address the problem of the punching behaviour of an anchored mesh. This represents a condition likely in secured drapery installations aimed to retain potentially unstable blocks along rock slopes. A parametric study is conducted, leading to the definition of simple analytical relations that can enable practitioners to account for the effect of the problem's variables on the mechanical response of the mesh system. A simple procedure allowing extension of the standard laboratory mechanical characterisation (i.e. standard UNI punch test) to a general field condition is also provided.

A large-scale model of a secured drapery system in soil retaining applications is implemented. The obtained results have permitted the force transmission mechanism inside the mesh system to be characterised, thus highlighting the role of the different system components. A parametric analysis is performed to investigate the role of several variables on the mechanical response of the mesh system. Particular attention is devoted to the evolution of the unstable process in the retained material. This has permitted the identification of a failure mechanism, in the retained material, that can be considered as typical of such kind of applications.

Keywords: Discrete Element Method, Flexible Facing, Rockfall Protection, Secured Drapery Systems, Slope Stability, Wire Meshes.

Contents

Contents **ix**

Introduction **1**

1 Drapery mesh systems: a state of the art **5**
1.1 Introduction 5
1.2 Simple drapery systems 10
1.2.1 Design methodology 12
1.3 Secured drapery systems 16
1.3.1 Laboratory tests 20
1.3.2 Field tests 21
1.3.3 Design methodologies 22
1.4 Conclusive remarks 31

2 Experimental tests for model calibration **33**
2.1 Standard UNI punch test on DT mesh type 34
2.2 Standard UNI punch test on MT1 and MT2 mesh types . . 38
2.3 Tensile test on MT1 and MT2 mesh types 44
2.4 Anchor punch test on the DT mesh type 49
2.5 Punch test against soil 52

3 Numerical methodology **57**
3.1 Discrete element method 57
3.1.1 DEM cycle 58
3.1.2 Contact law 59
3.1.3 Time step 60
3.1.4 Non-viscous damping 62
3.1.5 YADE DEM code 62

3.2 Discrete element modelling of wire meshes 63
3.2.1 Contact wire model 64
3.2.2 Node-Wire Based modelling approach 66
3.2.3 Cylinder-Wire Based modelling approach 67
3.3 Validation of the mesh numerical model 71
3.3.1 Punch test on DT mesh 71
3.3.2 Anchor punch test on DT mesh 74
3.3.3 Tensile test on MT1 and MT2 meshes 75
3.3.4 Punch test on MT1 and MT2 meshes 79
3.4 Comparison of the NWB and CWB modelling approaches . . 83
3.4.1 Tensile Test 83
3.4.2 Drop Test 85
3.4.3 Retaining test 88
3.4.4 Punch test 90
3.5 Conclusive remarks 92

4 Punching behaviour of a secured drapery system 95
4.1 Laboratory standard UNI punch test 96
4.1.1 Sensitivity analysis of the mesh-punch contact parameters 98
4.1.2 Internal mechanical behaviour of the mesh panel . . . 102
4.1.3 Parametric analysis 108
4.2 Punch test on an anchored panel: an idealisation of the in-situ conditions 119
4.2.1 Internal mechanical behaviour of the mesh panel . . . 123
4.2.2 Parametric analysis 127
4.3 Comparison of the mechanical behaviour of different mesh typologies 145
4.3.1 Laboratory standard UNI punch test conditions . . . 146
4.3.2 Idealised “in-situ” punch test conditions 151
4.4 Conclusive remarks 152

5 Punching behaviour at the mesh anchor plate connection: punch test against soil 157
5.1 Numerical modelling of the experimental test 158
5.1.1 Calibration phase of the numerical model 161
5.2 Investigation of the mechanical behaviour of the system . . . 163

5.2.1 Evaluation of the mesh-soil interaction 163
5.2.2 Evaluation of the force transmission mechanism . . . 166
5.2.3 Evaluation of the soil displacement field 172
5.3 Punch test against soil: towards an in-situ condition 173
5.3.1 Investigation of the mechanical behaviour of the system 173
5.3.2 Comparison with laboratory testing conditions 175
5.4 Parametric analysis 177
5.4.1 Mesh mechanical properties 177
5.4.2 Soil mechanical properties 179
5.4.3 Anchor plate dimension 181
5.5 Conclusive remarks 185

6 Secured drapery systems for slope stabilisation 189
6.1 Numerical model 190
6.1.1 Mesh numerical modelling 190
6.1.2 Soil numerical modelling 191
6.1.3 Mesh-soil problem numerical model 193
6.2 Numerical results 199
6.2.1 Investigation of the mechanical behaviour of the system 201
6.2.2 Soil displacement field 216
6.2.3 Mesh displacement field 222
6.3 Parametric analysis 225
6.3.1 Soil stiffness 228
6.3.2 Soil macroscopic friction angle 229
6.3.3 Soil-mesh contact friction angle 233
6.3.4 Slope angle 236
6.3.5 Thickness of the unstable soil layer 242
6.3.6 Mesh mechanical properties 248
6.3.7 Anchor plate dimension 252
6.3.8 Anchors' pattern 255
6.4 Conclusive remarks 262

Conlcusions and Perspectives 267

Annex A 275

Bibliography 281

Introduction

In the last decades, the urbanisation in mountainous regions has experienced a large growth. The number of civil structures and people that are potentially exposed to phenomena such as slope instabilities and rockfalls, at the present time, is therefore significantly higher than in the past. Moreover, the possible damage to infrastructures connecting the local communities and their industries to the piedmont areas may have an extremely negative impact on the local economy. The need of reducing the risk connected with the occurrence of these phenomena has led to the installation of numerous protective structures together with an increasing interest, from both the practical/industrial and academic fields, in the development of more efficient protective solutions. In particular, wire mesh structures have shown a great effectiveness in rockfall protection and slope face stabilisation, and nowadays they represent a widely adopted solution in practice.

Wire mesh structures are flexible structures composed of steel wire and/or high resistance steel cables that are connected between them following ordered geometric patterns. These structures can be used to face different problems, and according to their aim they can be divided in two macro-categories: rockfall fences and drapery systems. Former are aimed to intercept highly dynamic phenomena, as for instance falling rock blocks and boulders or debris flows, and to stop these phenomena by means of a high energy dissipation capacity. Several works, both from an experimental [33, 34, 50, 53, 77, 82, 89] and a numerical [2, 11, 23, 26, 27, 38, 39, 48, 54, 55, 60, 78, 79, 102] perspective, have been conducted in the recent past, permitting a significant improvement of the performances of rockfall fences. The drapery mesh systems are instead applied in order to control the falling trajectory (i.e. simple drapery) or to control and/or to retain (i.e. secured drapery) local unstable blocks. Furthermore, secured drapery systems are applied in order to contrast shallow

instabilities along soil or highly weathered/fractured rock slopes. Secured draperies are nowadays worldwide applied representing a very cost-effective solution, being characterised by a high rapidity and versatility of installation together with a good retaining capacity and a well adaptability to the slope morphology. Moreover, they have a low visual and environmental impact, if compared with alternative interventions based on rigid concrete or massive structures. Despite their broad utilisation, the comprehension of their mechanical behaviour, is still limited with possible negative consequences on the adequacy of the performance in field interventions. The main unknowns are related to the lack of data on field performances and to the low representativeness of the field conditions in the standard experimental mechanical characterisation.

This thesis work aimes to improve the knowledge of the mechanical behaviour of wire meshes in secured drapery applications in field conditions. Due to the difficulty, from both technical and economic reasons, to perform large scale experimental tests, it has been chosen to address the problem from a numerical perspective. The Discrete Element Method (DEM) is adopted in this thesis work.

The present thesis is structured in six main chapters.

In Chapter 1 a general introduction on drapery systems is presented. Then the main design methodologies that are reported in the literature are briefly presented and discussed.

In Chapter 2 the experimental tests that will be used for the validation of the mesh discrete element model are reported and discussed.

In Chapter 3 a brief introduction of the DEM is reported presenting the fundamental concepts of the method. A literature review regarding the application of this methodology to wire mesh structures is reported and the different approaches are discussed in detail. Moreover, an exhaustive description of the two approaches adopted in this thesis, namely the Node-Wire-Based (NWB) and the Cylinder-Wire-Based (CWB) approach, is reported. In the second part of Chapter 3, the validation of the mesh models that will be used in Chapter 4, Chapter 5 and Chapter 6 is presented, comparing the

numerical predictions with experimental the data obtained from the different test configurations described in Chapter 2. Finally, a comparison between the NWB and the CWB modelling approaches is reported.

In Chapter 4 the punching behaviour of a mesh panel is addressed. In the first part of Chapter 4, a detailed analysis of the mechanical behaviour of a mesh panel in the standard UNI punch test conditions is presented. The load transfer mechanism inside the mesh as well as the mechanical conditions of the wire elements are discussed. Then, the main variables of the problem are varied permitting their effect on the mesh mechanical behaviour to be understood, and highlighting the role of scale and geometrical effects. In the second part of Chapter 4, a modified version of the standard UNI punch test is presented considering a periodic anchored mesh panel. This test configuration aimes to represent an idealisation of the field conditions of an anchored mesh panel when loaded by an unstable rock block. A parametric analysis is finally performed permitting the role of the main variables of the problem to be analysed. From the numerical results, simple analytical relationships accounting for the effect of the problem's variables on the mechanical response of the mesh are defined. Finally, the punching behaviour of three different mesh types is briefly compared and discussed.

In Chapter 5 the local punching mechanism between the mesh anchor plate connection and a granular soil is addressed. In the first part of Chapter 5, experimental results are used to calibrate the numerical model, then the latter is used to provide an insight into the force transmission mechanism that characterises the mesh-plate-soil interaction. In the second part of Chapter 5, the boundary conditions of the problem are relaxed to move towards a more realistic schematisation of the field conditions. A parametric analysis is performed quantifying the influence of the problem's variables on the mechanical behaviour and the ultimate bearing capacity of the mesh-plate-soil system.

In Chapter 6 the mechanical behaviour of a secured drapery system in soil/debris retaining applications is addressed. In this perspective, an idealised large-scale "in-situ" model is considered. The mechanical behaviour of the mesh system and its components (i.e. anchors, mesh panels) is analysed from small deformations to failure conditions, providing specific force-

displacement curves that characterise the mesh system response to the soil movements. Furthermore, force and stress distributions on the mesh elements are analysed permitting the critical zones of the mesh system to be identified. Finally, the failure mechanism that occurs in the soil is identified. In the second part of Chapter 6, a parametric analysis is performed quantifying the influence of the problem's variables on the mechanical performance of the mesh system and on the soil movements. Moreover, non-trivial effects related to the geometry of the unstable soil layer are discussed.

The conclusions of the thesis work are provided and discussed and possible improvements and future perspectives are finally presented.

Chapter 1

Drapery mesh systems: a state of the art

In this chapter a general introduction on drapery mesh systems is presented. Firstly, an overview on the different applications of these system, as well as a description of the different system components and of the common practice are provided. Secondly, the design methodologies that are commonly adopted in practice are presented and briefly commented. Finally, some critical aspects of drapery systems are discussed.

1.1 Introduction

Drapery mesh systems are flexible structures composed of wire mesh strips or panels, which are draped over the slope face and anchored to the slope by means of special connection devices. Since the 1950s mesh draperies have started to be systematically applied along North American infrastructures [76], and nowadays they indisputably represent, together with rockfall fences, the most adopted solution for rockfall protection [107]. The drapery systems, differently from rockfall fences, are placed in adherence or in proximity to the slope face covering the latter. They are used to control the trajectories of falling rock blocks of moderate size (i.e. block size $\lesssim$ 1-1.5m [40, 76]) and in order to avoid the detachment of potentially unstable blocks from the slope face. More recently, they have been applied for improving the stability of the shallow portion of soil or highly weathered rock slopes, thus acting as flexible retaining facing. Examples of drapery mesh applications are shown

in Fig. 1.1. According to their purpose, the drapery mesh systems can be divided in two categories: simple (or unsecured) mesh drapery systems and secured mesh drapery systems. A detailed description of these two types of intervention will be presented in Sec. 1.2 and Sec. 1.3.

The broad utilisation of drapery mesh systems is mainly related to the following factors [40, 67, 103]:

- they represent a very effective way to control rockfall hazard also in interventions of large extension
- they represent a relatively economic solution
- they can be applied in hardly accessible areas
- the installation of the system is rapid
- they have a low visual and environmental impact
- they allow the growth of vegetation after the intervention
- they allow the free discharge of groundwater

Moreover, drapery systems represent a very versatile solution: they are commonly installed on slopes ranging from as flat as 35° to overhanging, and on very uniform to highly irregular slope faces. The vertical extension is also extremely wide: drapery systems have been successfully applied on slope heights of 150m, however, more commonly, the vertical extension ranges from 15 to 45m [76]. The core components of a drapery system are: the wire mesh, the connection/anchoring devices and the external support ropes (or cables).

The wire mesh is the system component that permits the interaction with the unstable volumes. It therefore ensures the trajectory control of the falling blocks, it allows the containment of debris, and, in secured drapery application, it permits a stabilising action on the unstable volume to be applied (after the activation of the mesh). Several mesh typologies are adopted in the practice (common mesh types are reported in Fig. 1.2) and they differ for the type of mesh fabric (e.g. chain link mesh, woven mesh), the geometry of the mesh cells (e.g. rhomboidal, hexagonal, rectangular, circular), the mechanical properties of the mesh elements (e.g. high resistance steel), type of elements (e.g. wires, twisted wires, ropes, spiral ropes). The choice of a specific mesh is mainly related to the required mesh resistance (i.e. tensile/puncturing and dynamic resistance) and to the slope morphology (the mesh deformability permits one to control the adherence of the latter to the slope face in the installation phase). In some cases, in order to improve the effectiveness of the intervention, two mesh typologies can be combined:



Figure 1.1: Examples of drapery mesh systems (courtesy of Dr. Giorgio Giacchetti).



(a) (b)

(c) (d)

Figure 1.2: Examples of mesh types: (a) chain link TECCO® mesh (Geobrugg), (b) hexagonal double twisted wire mesh (Maccaferri), (c) HR Steelgrid® wire mesh (Maccaferri), (d) HEA double knot mesh (Maccaferri).



(a) (b) (c)

Figure 1.3: Examples of connection of adjacent mesh sheets: (a) horizontal connection, (b) vertical connection with clips, (c) vertical connection with lacing wires (courtesy of Dr. Giorgio Giacchetti).

a mesh characterised by a high mechanical performances, as for instance the HEA mesh, to provide a high resistance and low deformability to the drapery system and a standard steel wire mesh, as for instance the double twisted mesh, used as a filter for the finer debris (as shown in Fig. 1.2d). Wire meshes are produced in panels that are generally characterised by a width $\leq$ 3m; thus in order to ensure the spatial continuity of the mesh along the slope face, the different panels have to be jointed between them. The mesh panels can be connected by using specific fastening devices (e.g. clips, clamps, hog rings, spiral joints), or they are seamed together with lacing wires as shown in Fig. 1.3. The anchoring system is generally composed of steel bars (or more recently also rope tendons [76]) and steel plates (other devices can be used). The bar elements are connected to a stable layer of the slope and the anchor plates permit the connection between the mesh and the anchoring system. The role of the latter is to allow the load transfer from the mesh to the stable part of the slope. It is therefore evident that the available resistance at the mesh-anchor connection controls the retaining capacity of the system. This aspect is particularly important in secured drapery application and will be discussed in the following of this thesis. Some examples



(a) (b) (c)

Figure 1.4: Examples of connection between the mesh and the anchor plate (courtesy of Dr. Giorgio Giacchetti).

of the connection between the mesh and the anchoring system are shown in Fig. 1.4. Finally, external ropes can be used to improve the mesh resistance and the may be installed at the time of the mesh system installation, or in a second phase, if the system need to be reinforced because of local failures of the mesh, or due to severe loads deriving from local (large) unstable volumes. Moreover, the adoption of external ropes permits a better adherence between the mesh and the slope face, due to the possibility of put in tension the external ropes during the installation phase [40]. This also permits a reduction of the deformability of the mesh system. Examples of the application of external ropes are shown in Fig. 1.5.

1.2 Simple drapery systems

Simple drapery systems consist a of a wire mesh draped over the slope face and anchored just at the top slope crest, or both at the top and bottom of the slope [5, 8]. They simply cover the slope surface susceptible of rockfall, however block detachments can occur and fall in-between the mesh and the slope face [96]. The purpose of a simple drapery system is to control the velocities and the trajectories of falling rock blocks, guiding these latter to the slope toe, thus avoiding the impact onto infrastructures or working areas below.

A common cause of failure is the debris accumulation at the toe of the mesh system [76]. Debris accumulation between the mesh and slope may

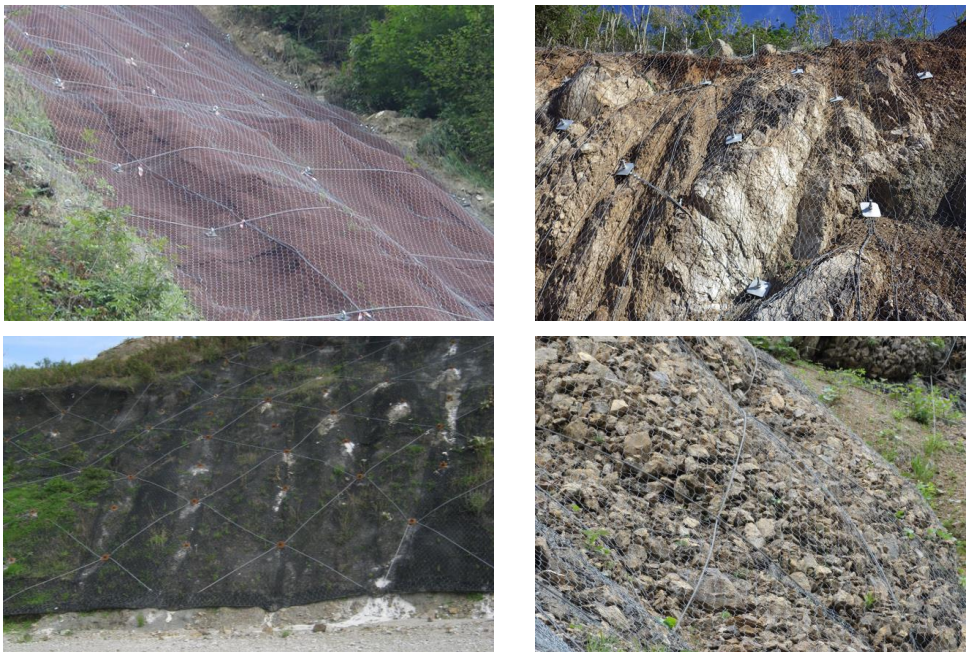
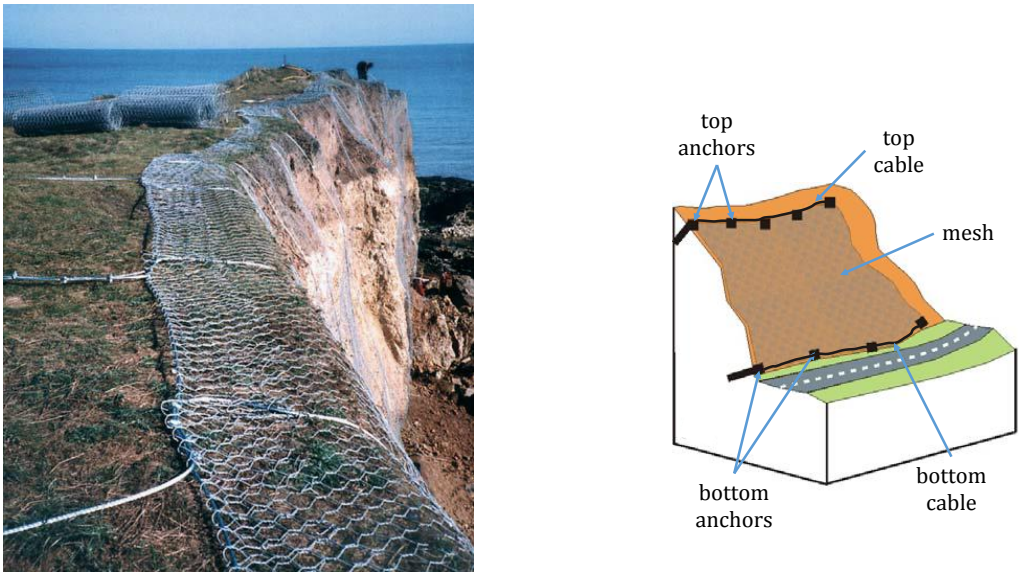


Figure 1.5: Examples of application of external ropes in secured drapery applications (courtesy of Dr. Giorgio Giacchetti).

occurred, especially when the system is fixed at the toe of the slope, or when the bottom of the mesh is buried by the snow. The periodic maintenance operations consisting in the removal of the accumulated debris ("cleaning operations") are therefore fundamental for ensuring the full efficiency of the mesh system. Failure related to excessive impact loading are instead less common.

Simple drapery systems (examples are shown in Fig. 1.1 and Fig. 1.6) are commonly applied along infrastructures and walking paths as well as in open pits and in coal and metalliferous mines to protect the portals for underground access [52]. Following the indication presented in [40], two different installation modalities are commonly adopted in practice:

- **simple drapery installed in adherence to the slope face:** this type of installation is possible in moderately steep to gentle slopes and permits a low retaining action improving the stability of small rock volumes. The mesh is fixed at the top of the slope and the mesh panels are unrolled on the slope face by climbing operators. For intervention along slopes characterised by a complex morphology, auxiliary anchors



(a) (b)

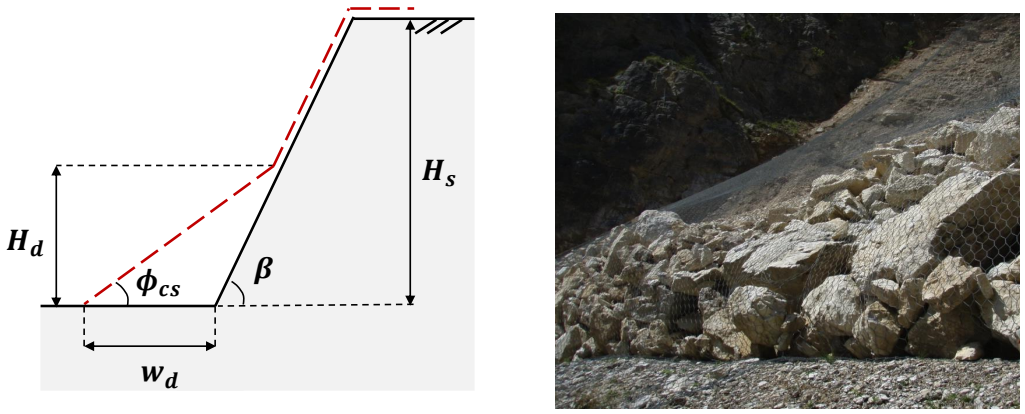
Figure 1.6: (a) Simple drapery intervention (courtesy of Officine Maccaferri SpA). (b) Scheme of a simple drapery application (modified from [40]).

and ropes can be used; the role of these reinforcing elements is particularly important to face the loads induced by the formation of snow and/or ice accumulation.

- **simple drapery installed not in adherence to the slope face:** this type of installation is applied in very steep to overhanging slopes. The mesh is simply fixed at the slope crest and unrolled over the slope face by its self-weight. In this case, the unstable blocks are relatively free to fall in the space between the mesh and the slope face.

1.2.1 Design methodology

Referring to the design of simple drapery interventions, only one methodology was found in the technical literature [76]. This methodology is based on the limit equilibrium method and considers that the mesh failure is related to an excessive load deriving from the debris accumulation at the toe of the mesh system. In the definition of the model a regular slope of height H_s inclined by an angle β with respect to the horizontal ground is considered. The loads considered in the stability analysis are the self-weight of the mesh and the weight of the debris accumulation, the latter being described as a



(a) (b)

Figure 1.7: (a) Geometrical scheme used in the design methodology proposed in [76] for the debris load. (b) Example of debris accumulation at the toe of a simple drapery (courtesy of Dr. Giorgio Giacchetti)

triangular deposit characterised by the geometrical parameters H_d, w_d and ϕ_{cs}. The geometrical scheme considered in the stability analysis is the one shown in Fig. 1.7. The factor of safety (at the limiting state of equilibrium) is defined as given by:

$$FS = \frac{f_a + f_w + f_d}{f_{dm} + f_{wm}} \tag{1.1}$$

where f_a represents the anchor resistance, f_w the contribution deriving from the friction at the interface between the mesh and the slope face, f_d the contribution of the accumulated debris to the available shear resistance, f_{dm} and f_{wm} are the mobilised forces due to the debris and mesh weight respectively. The different contributions are defined in the following.
The contribution f_a is given by:

$$f_a = n_a P \tag{1.2}$$

where n_a is the number of anchors and P is the capacity of an anchor (the weakest of anchor tensile strength, shear strength and ultimate pullout resistance of an anchor).
The contribution f_w is given by:

$$f_w = \gamma_w \frac{H_S}{\sin(\beta)} cos(\beta) tan(\delta) \tag{1.3}$$

where δ is the friction coefficient at the mesh-slope interface and γ_w is the mesh weight per unit area. Different values of the interface friction angle δ as a function of the slope morphology and surface roughness were proposed by Muhunthan et al. [76]: rough slope surface $\delta \geq 60°$, undulating slope surface $36° \leq \delta \leq 59°$, planar slope surface $25° \leq \delta \leq 35°$.
The contribution f_d is given by:

$$f_d = 0.5 H_d^2 \gamma_d \cos(\beta)[\cot(\phi_{cs}) - \cot(\beta)] \tan(\delta) \tag{1.4}$$

where γ_d is the unit weight of the debris.
The contribution f_{dm} is given by:

$$f_{dm} = 0.5 H_d^2 \gamma_d \sin(\beta)[(\cot(\phi_{cs}) - \cot(\beta)] \tag{1.5}$$

The contribution f_{wm} is given by:

$$f_{wm} = \gamma_w \frac{H_S}{\sin(\beta)} \tag{1.6}$$

The number of anchors required to satisfy the equilibrium of the system can be calculated by substituting Eqs. 1.2,1.3,1.4,1.5,1.6 into Eq. 1.1 and imposing FS equal to the unity.

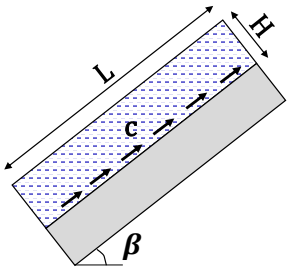
In cases in which the mesh system may be subjected to snow accumulation, a procedure to account for the snow load is defined in [76, 92]. The methodology is based on the limit equilibrium method and consider a regular slope, inclined by an angle β, and a uniform snowpack of thickness h_s as shown in the scheme reported in Fig. 1.8. Two different situations are considered, namely site temperature below and above the freezing temperature.

For temperatures below freezing, the snowpack, the mesh and the slope surface are considered frozen together, and thus it can be assumed that they behave as a continuous body. In this condition, the snowpack strength is schematised with a cohesive term c (based on experimental analysis [90]) and the force that the snowpack exerts on the mesh system is given by:

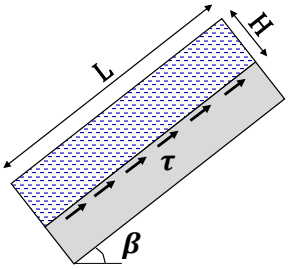
$$F_s = \gamma_{snow} H L \sin(\beta) - cL \tag{1.7}$$

where γ_{snow} represents the unit weight of the snowpack. The magnitude of c depends on the density (c is close to zero for loose snow) and on the temperature of the snowpack [90, 92].

For temperatures above freezing, the snowpack may be uncoupled from the slope surface, and the snow weight is directly transmitted to the mesh



(a)



(b)



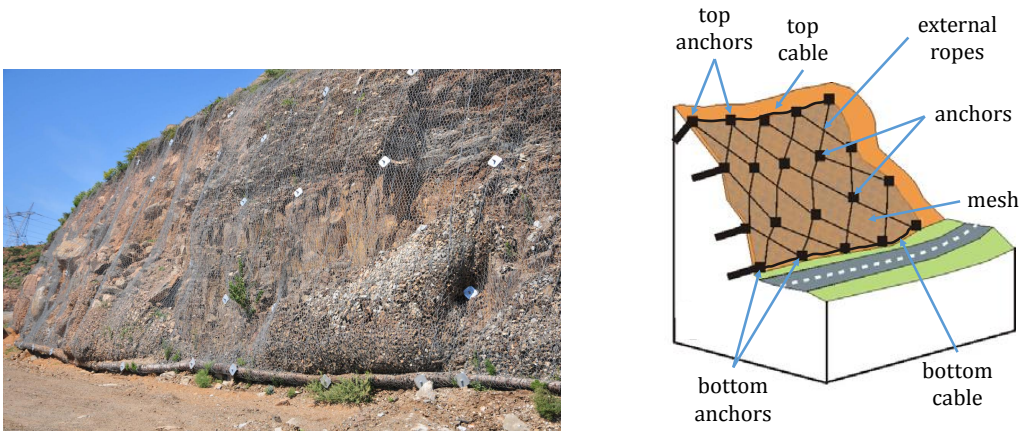
(c)

Figure 1.8: Geometrical scheme used in the design methodology proposed in [76] for the snow load: (a) temperature below freezing, (b) temperature above freezing. (c) Example of simple drapery subjected to snow load (courtesy of Dr. Giorgio Giacchetti).

system (this was confirmed by field measurements [76]). In this condition, the force that the snowpack exerts on the mesh system is given by:

$$F_s = \gamma_{snow} HL \sin(\beta) - \gamma_{snow} HL \cos(\beta) \tan(\delta) \tag{1.8}$$

A conservative value of F_s is obtained neglecting the stabilising frictional force between the mesh and the ground (i.e. assuming $\delta = 0$). However, the formation of a snow accumulation implies that the slope cannot be extremely steep, therefore the mesh would have a certain contact with the slope face, and thus the interface frictional interaction should be considered. For a sake of completeness, it should be mentioned that the company Officine Maccaferri SpA proposes a dimensioning method (MacRO 2 [51, 58]) which is based on the one above described.



(a) (b)

Figure 1.9: (a) Secured drapery intervention (courtesy of Dr. Giorgio Giacchetti), (b) scheme of a secured drapery application (modified from [40]).

1.3 Secured drapery systems

Secured drapery systems are flexible retaining structures composed of wire mesh panels, which are fixed to the slope by using a regular pattern of rock bolts and anchor plates. This permits the contact between the mesh and the slope surface to be improved (with respect to simple draperies); moreover the presence of the anchors allows the mesh reaction to the movement of the unstable volumes behind it. Secured drapery systems are largely applied along roads and railways in Central Europe and Japan [107] (simple drapery application are still preferred in North America [76]), as well as in urban areas as protective measures against rockfall. These systems are also worldwide applied in undergrounds working [76]. More recently, their use has been extended to soil retaining applications, coupling the wire mesh with geotextiles, having the latter only a filtering role for the finer material. Examples of secured drapery applications are shown in Fig. 1.1, Fig. 1.5 and Fig. 1.9.

These interventions have two main aims: (i) to control the detachment of rock blocks from the slope face and to limit the movement of the ones that may become detached, (ii) to improve the stability of the shallow portion of the slope [8, 40]. A fundamental aspect of secured drapery systems is related to the progressive activation of the retaining capacity with the system deformations. Before being able to exert a retaining force, the mesh system has

to undergo some deformations in order to exhaust the mesh fabric deformability and to develop a sufficient curvature for mobilising the membrane-like resistance of the mesh. From this moment, the retaining action of the mesh system progressively increases with the system deformation. Hence, in field application, the mesh applies a stabilising action on the unstable volume only once the latter has already started to slide. In this perspective the secured drapery systems should be classified as passive structures [13, 85]. In order to limit the initial deformability of the mesh in serviceability conditions, the density of the anchors can be augmented (number of anchor per unit mesh area), or stiffer mesh typologies can be adopted (out-of-plane stiffness). Alternatively, some manufactures declare to apply a pre-tensioning phase during the system installation, and that may lead to an "active" behaviour of the system. However, the possible effect of a pre-tensionig phase is largely debated both from researchers and practitioners [8, 12, 13, 40].

The failure of a secured drapery is generally related to two causes: (i) an excessive puncturing load due to a large volume pushing onto the mesh (see Fig. 1.10a), (ii) an excessive pressure deriving from a significant debris accumulation or large movements of the material behind the mesh system (see Fig. 1.10b). The former is commonly observed in applications along poorly to moderately fractured rock slope, while the latter is more likely when a mesh system is installed along highly weathered rock slope or in soil slopes.

The installation of a secured drapery system is generally divided in the following phases [40]:

- the mesh is fixed at the top of the slope (similarly to a simple drapery);
- the mesh is unrolled on the slope face (this operations is generally done by climbing operators);
- the rock bolts (or anchor nails) are installed (the drilling operations are generally manually conducted);
- the mesh is connected with the anchoring system by means of anchor plates or special devices. In this phase, some manufactures tension the mesh system in order to limit the deformation in serviceability conditions; this operation is done applying a pre-tension at the level of the anchor plate and/or installing and tensioning external ropes (the effectiveness of this "pre-tensioning" phase is largely debated [8, 12, 13]).

Secured drapery adopted for soil/debris retaining applications are limited to



(a) (b)

Figure 1.10: Examples of failure of secured drapery applications: (a) mesh puncturing due to an excessively large unstable volume (the presence of the external ropes permits avoidance of the free-fall of the rock block), (b) tear of the mesh due to an excessive debris accumulation at the toe of the system (courtesy of Dr. Giorgio Giacchetti).

unstable processes that interests a layer of thickness $\leq$ 3m. This is related to both technical and economic limitations. In fact, being the drilling operations for the bolts installation manually performed, the maximum depth is limited to 3-4m [40]; deeper holes are possible, but they require the adoption of heavier drilling machines and this strongly reduces the efficiency of the installation phase [40] (in terms of holes/hours).

In common practice, the anchor bolts are installed adopting two geometrical patterns, a diamond pattern and a square pattern. The choice of a specific pattern should be made considering:

- **the conditions of the unstable layer:** in interventions characterised by a significant slope height and a highly fractured superficial layer a diamond pattern should be preferred in order to limit the length of the free-fall corridors between the mesh and the slope face [40]. However, some volumes may remain trapped in the upper parts of the system leading to more costly cleaning operations;
- **the mesh typology:** the mechanical properties and geometrical orientation of the mesh elements significantly influences the force transmission mechanism inside the mesh. Accounting for the latter in the choice of the anchor pattern may permit the mechanical response of the mesh system to be optimised.

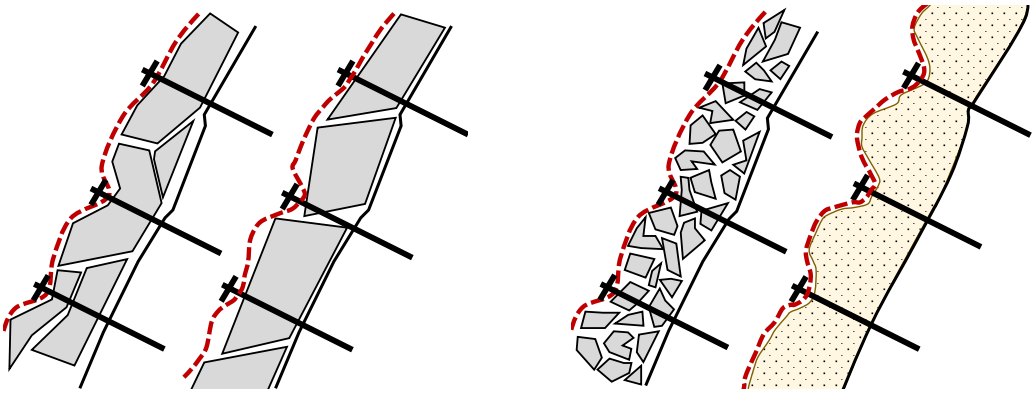


Figure 1.11: Conceptual scheme of the unstable layer characteristics: (a) poorly to moderate fractured layer, (b) highly fractured or soil-like layer.

In a secured drapery system both the anchor bolts and the mesh have a stabilising effect on the unstable material, however the importance of their role depends on the characteristics of the unstable volume to be retained [40]. In the case of an intervention aimed to stabilise moderately large rock blocks, or the superficial layer of a rock mass characterised by a large spacing between the fractures (in relation to the rock bolts length), the anchor bolts plays a major role, while the mesh has mostly the function of retaining small rock debris (see Fig. 1.11a). Conversely, if the superficial layer of the rock mass is highly fractured or the secured drapery is installed along a soil slope, the retaining action is mainly ensured by the mesh, while the anchors permit the load to be transferred from the mesh to the stable part of the slope (see Fig. 1.11b). Nevertheless, the interaction between the retained material and the anchor bolts and plates may determine the occurrence of some beneficial effects (e.g. a stabilising arching effect in the soil layer) that provide a further improvement of the effectiveness of the intervention.

In the performance of a secured drapery system, the available resistance at the connection between the mesh and the anchor plate has a fundamental importance. The mesh-plate connection allows the load transfer from the mesh to the anchor bolts (and so to a stable layer of the slope), thus permitting the system reaction to the movement of the unstable volumes behind it. This zone is therefore characterised by high stress levels and, most commonly, the failure of the mesh system originates from the failure



(a)



(b)

Figure 1.12: View of (a) the tensile test and (b) the punch test (courtesy of Officine Maccaferri SpA).

of some wire elements at the mesh-plate connection [40]. The resistance of the mesh-plate connection is controlled by the number and typology of the mesh element (i.e. wires and/or ropes) intercepted by the anchor plate (this aspect will be analysed in the following of this thesis work). Therefore particular attention should be given to the positioning of the anchor plates at the installation phase when adopting wire meshes composed of elements of different mechanical properties.

1.3.1 Laboratory tests

The mechanical characterisation of a wire mesh is commonly performed through two laboratory tests: the tensile test (see Fig. 1.12a) and the punch test (see Fig. 1.12b). In the tensile test, a mesh sheet is fixed to the testing rig at two opposite sides and a traction is applied to the mesh panel imposing a constant rate of displacement to one of the panel's sides. The outputs of the test are the tensile strength and the in-plane stiffness of the mesh. In the punch test, the mesh is fixed to a rigid frame and a loading condition perpendicular to the mesh plane is applied by moving a standardised punching device (the detail of this test will be discussed in Chapter 2). The outputs of the test are the out-of-plane resistance of the mesh panel and the force-displacement relationship. Differences between the various testing procedures, especially for the punch test configuration, exist and are related both to the differences in the test standards [4, 37, 99] and to different choices between manufactures (e.g. shape and dimension of the punching device). Therefore, the punching resistance (and force-displacement rela-

tionships when provided) declared in the technical sheets cannot be used for a direct comparison of the different mesh types.

Considering non-standardised laboratory procedures, a simple but instructive experimental work was conducted by Gratchev et al. [56] in order to study the role of the interface interaction at the rock-mesh contact. They performed a series of tilt tests and tests with increasing loads on a mesh sample and used small irregularly shaped concrete block to simulate different types of rock-mesh contact. They recommended an interface friction angle in the range 25°-30° combined with an estimation of the interlocking effect based on the slope surface characteristics.

1.3.2 Field tests

The laboratory test configurations are poorly representative of the real field conditions, thus they cannot provide a precise characterisation of the mechanical behaviour of a wire mesh in real applications. The main difference concerns the boundary conditions of the mesh panel. In field applications the mesh is locally fixed by the anchor plates, while in laboratory conditions the mesh is generally fixed along its outer boundary. As pointed out by different authors [8,44,105], this strong difference may lead to an erroneous quantification of the in-field response of the mesh both in terms of panel deformability and of panel ultimate strength. Moreover, especially in soil or debris retaining applications, the local loading condition represented by the punching device may be not the most adequate. The systematic adoption of large-scale and field test procedures for rockfall fences [11, 33, 34, 50, 53, 77, 82, 89] has permitted a characterisation of the in-field behaviour, consequently leading to a great improvement of the effectiveness of these systems. Moreover, the field results have been used for the development of refined numerical models [2, 23, 26, 27, 38, 39, 48, 54, 55, 60, 78, 79, 102], which have permitted the knowledge of the mechanical behaviour of the system and its components to be improved. Furthermore, the numerical studies have provided fundamental data to better understand the force transmission between the system elements. At the light of these results, the development of field and/or large-scale test procedures for secured drapery applications seems a promising strategy. Nevertheless, at the present time only two works dealing with field tests were found in the technical literature. Bertolo et al. [8] performed several in-field punch tests on a secured drapery system installed on a verti-



(a) (b)

Figure 1.13: (a) In-field punch test (after [8]), (b) large-scale retaining test (after [7]).

cal rock slope in Northern Italy (see Fig. 1.13a). They used different mesh typologies (i.e. hexagonal double twisted and HEA® mesh types) and they provided a set of force-displacement relationships characterising the system mechanical response. In the second work [6, 7, 18, 104], a large-scale inclinable steel frame filled by a granular material was used to investigate the behaviour of various flexible facings (see Fig. 1.13b). Wire meshes characterised by different resistance (i.e. TECCO® mesh type with different wire diameters) and different anchor spacing were adopted. In all the tests, the mesh systems reached the failure conditions, and the failure inclination as well as the system deformation (measured by a laser scanner) at different level of inclination were provided.

In addition to these two large-scale tests, monitoring data were reported in [76,92]. Furthermore, from a field measurement campaign on three secured drapery interventions in Northern Spain [12], it was reported that these mesh systems were barely prestressed and the effect of the pre-tensionsing phase is almost negligible.

1.3.3 Design methodologies

Despite the wide utilisation of secured drapery systems no official guidelines exist to help practitioners in the design of these systems [8], with the

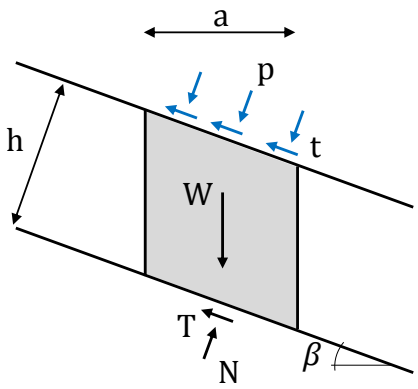


Figure 1.14: Geometrical scheme of the infinite slope model proposed in [30, 31].

only exception of a brief reference reported in a soil nailing technical guide published in the UK [83]. This has led different manufactures as well as independent researchers to propose various design methodologies (a critical review of existing methods can be found in [13]), and at the present time, a generally accepted design procedure does not exist. The common point between the different methodologies is that they are all based on the limit equilibrium method (i.e. referred then to an Ultimate Limit State approach). They instead differ with regard to the choice of the failure mechanism and in the schematisation of the mesh stabilising action. Another substantial difference concerns the unstable process considered in the design, namely the sliding of a rock block or the instability of the shallow layer of a soil slope. An overview of the commonly adopted design methods is reported in the following.

Infinite slope model

This model was proposed by da Costa [30] and da Costa and Sagaseta [31]. It applies to secured drapery interventions in soil slopes. It is based on the classic infinite slope failure mechanism and schematises the mesh action with a normal pressure p and a tangential pressure t evenly distributed on the slope face. The tangential action of the mesh is related to the normal pressure p by using a mesh-slope interface friction angle δ (i.e. $t = p \tan(\delta)$). The value of the pressure p is computed imposing the equilibrium of the system shown in Fig. 1.14 and adopting a Mohr-Coulomb failure criterion

for the soil. The required pressure p is therefore given by:

$$p = \frac{\gamma h[\sin(\beta) - \cos(\beta)\frac{\tan(\phi)}{FS}] - \frac{c}{FS}}{\frac{\tan(\phi)}{FS} + \tan(\delta)} \tag{1.9}$$

where γ represent the unit weight of the soil, ϕ and c the friction angle and the cohesion of the soil respectively and FS the factor of safety. Water pressure forces can be considered in the model.

Finite height slope model 1

This model was proposed by da Costa [30] and da Costa and Sagaseta [31]. It applies to secured drapery interventions in soil slopes. It is based on a global planar failure mechanism parallel to the slope and adopts a Mohr-Coulomb failure criterion for the soil. The decomposition of the unstable layer in several wedges (see Fig. 1.15) permits the finite height of the slope to be accounted for. An evenly distributed normal pressure p is used to schematised the mesh retaining action, moreover a tangential component can be added by using an interface friction angle δ as in the infinite slope model. The computation of the required pressure p is achieved by an iterative procedure starting from the slope crest and moving downwards. In each calculation step two blocks (see Fig. 1.15) are considered:

- block A, sliding on a plane parallel to the slope;
- block B, sliding on a plane inclined by an angle α with respect to the slope.

The forces considered in each of these steps are shown in Fig. 1.15. At each iteration a system of four unknowns (i.e. N_A, N_{AB}, N_B and p_j) is solved providing the pressure p_j. If a condition of the type $N_i < 0$ is encountered a value $N_i = 0$ is imposed and the system solution is recalculated accordingly ($N_i < 0$ is not physically meaningful). The full analytical formulation of the eight possible cases, here omitted for the sake of brevity, can be found in [30]. Water pressure forces can be considered in the model.

The iterative procedure is conducted as follows:

- i=1 $\rightarrow$ block A is formed by block 1, block B is formed by block 2 and $p_i = p_1 = 0$:
  - solving equilibrium of block A $\rightarrow$ N_A, N_{AB}
  - solving equilibrium of block B $\rightarrow$ N_B, $p_j = p_2$

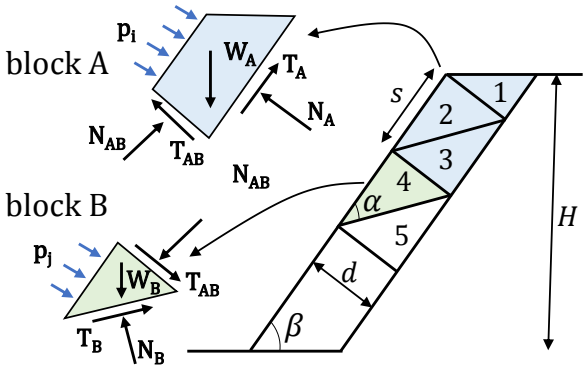


Figure 1.15: Geometrical scheme of the finite slope model proposed in [30,31].

- i=2 → block A is formed by block 1+2+3, block B is formed by block 4 and $p_i = p_2$ is known:
  - solving equilibrium of block A → N_A, N_{AB}
  - solving equilibrium of block B → N_B, $p_j = p_4$
- i=j → block A is formed by block 1+2+3+4+...+2j-1, block B is formed by block 2j and $p_i = p_{2j-2}$ is known:
  - solving equilibrium of block A → N_A, N_{AB}
  - solving equilibrium of block B → N_B, $p_j = p_{2j}$

The maximum pressure p is obtained for the wedge located at the toe of the slope and this values should be used in the design of the mesh system. For high slopes the solution obtained by the present method is approximately the same of the one obtained by using the infinite slope approximation.

Finite height slope model 2

This model was proposed by the manufacturer IberoTalud [61]. It applies to secured drapery interventions in soil slopes. It assumes a failure mechanism composed of an upper wedge sliding parallel to the slope and a lower wedge, sliding on a planar surface inclined by an angle α with respect to the horizontal ground as shown in Fig. 1.16. A Mohr-Coulomb failure criterion is adopted for the soil. The mesh stabilising action is schematised with a normal pressure p and a tangential pressure t evenly distributed on the slope face. In this case, the tangential contribution of the mesh is unknown (i.e. considered independent from the normal pressure p). The problem is

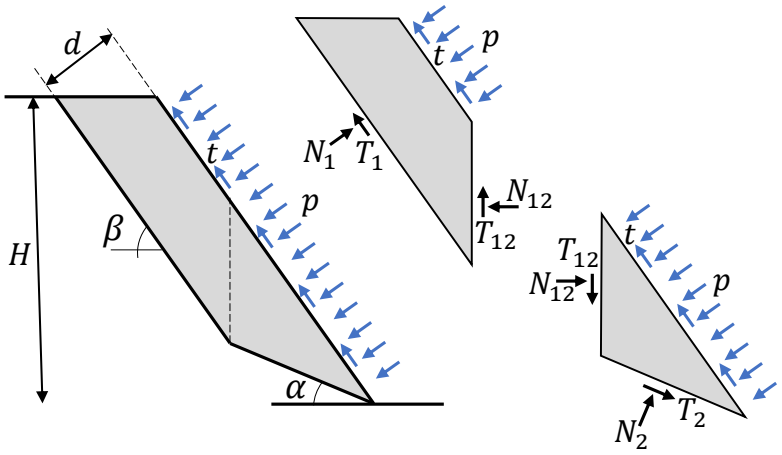


Figure 1.16: Geometrical scheme of the finite slope model proposed in [61].

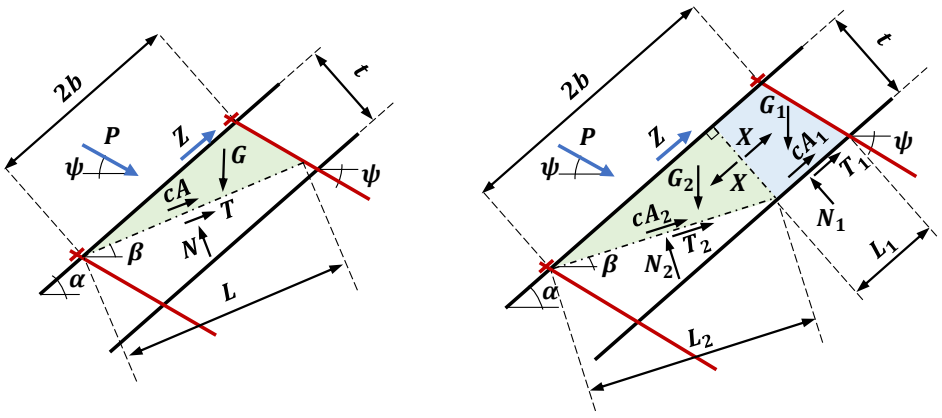
therefore characterised by five unknowns (i.e. p, t, N_1, N_{12}, N_2), so the four equations deriving from the equilibrium equations of the system are not enough to compute the value of the required stabilising pressure. In order to obtain p, the expression of p obtained from the solution of the equilibrium equations is maximised as a function of α. The full analytical formulation, here omitted for the sake of brevity, can be found in [61]. Water pressure forces can be considered in the model. For high slopes the solution obtained by the present method is approximately the same of the one obtained by using the infinite slope approximation.

Local failure between two individual nails

This model was proposed by Guasti [59] and Flum et al. [41] and is used by the manufacturer Geobrugg as a part of the Ruvolum®design method [19]. It applies to secured drapery interventions in soil slopes. It is based on the hypothesis that superficial instabilities parallel to the slope are prevented if the nails are correctly designed [19]. The design of the mesh is therefore conducted with regards to local instabilities between two individual nails. A Mohr-Coulomb failure criterion is adopted for the soil.

Two different local failure mechanism are considered:

- a wedge-shaped failure mechanism, referred as “mechanism A” (see Fig. 1.17a);
- a two-bodies failure mechanism, referred as “mechanism B” (see Fig. 1.17b).



(a) (b)

Figure 1.17: Geometrical scheme of the local failure mechanism between two bolts rows: (a) mechanism A, (b) mechanism B [19]

The mesh stabilising action is schematised with a concentrated force P, inclined as the anchor nails, and a slope-parallel force Z. The force Z represents the slope-parallel tensile force supportable by the mesh and is experimentally defined [19]. These forces are applied on the lower body when considering a failure mechanism of type B (see Fig. 1.17b). The unstable local volumes are characterised by the dimensions $2b$ and a_{red}, where the former is the vertical anchor spacing and the latter a reduced value of the horizontal anchor spacing a. The adoption of the reduced value a_{red} derives from the assumption that the pretension applied on the anchor plate, during the system installation, generates a pressure cone that locally stabilises the soil [19].

The force P_A is computed imposing the equilibrium of the failure mechanism A, and is given by (γ_m represents a model uncertainty coefficient):

$$P_A = \frac{G[\gamma_m \sin(\beta) - \cos(\beta)\tan(\phi)] - Z[\gamma_m \cos(\alpha - \beta)]}{\gamma_m \cos(\beta + \psi) + \sin(\beta + \psi)\tan(\phi)} + \ldots + \frac{Z[\sin(\alpha - \beta)\tan(\phi)] - cA}{\gamma_m \cos(\beta + \psi) + \sin(\beta + \psi)\tan(\phi)} \tag{1.10}$$

In order to determine the decisive failure mechanism the force P_A has to be maximised as a function of the inclination of the sliding surface β.

For the computation of the force P_B, in a first step the equilibrium of the

upper body of the failure mechanism B is imposed determining the inter-wedge force X, which is given by:

$$X = \frac{1}{\gamma_m}\{G_1[\gamma_m \sin(\alpha) - \cos(\alpha)\tan(\phi)] - cA_1\} \tag{1.11}$$

then P_B can be computed by imposing the equilibrium of the lower body. The force P_B is given by:

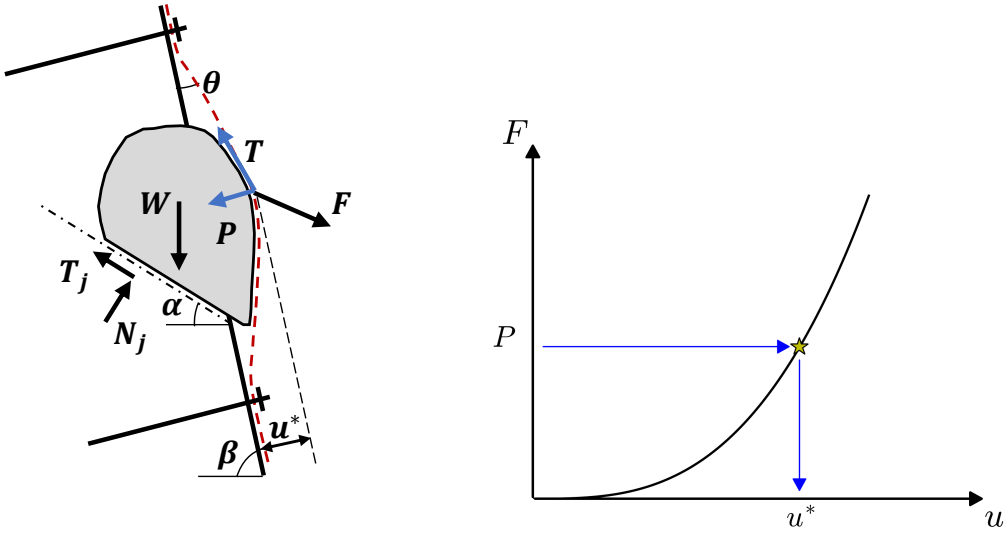
$$\begin{aligned} P_B = & \frac{G_2[\gamma_m \sin(\beta) - \cos(\beta)\tan(\phi)] + (X - Z)[\gamma_m \cos(\alpha - \beta)]}{\gamma_m cos(\beta + \psi) + \sin(\beta + \psi)\tan(\phi)} + \dots \\ & + \frac{(Z - X)[\sin(\alpha - \beta)\tan(\phi)] - cA_2}{\gamma_m cos(\beta + \psi) + \sin(\beta + \psi)\tan(\phi)} \end{aligned} \tag{1.12}$$

In order to determine the decisive failure mechanism the force P_B has to be maximised as functions of the unstable layer thickness t and the inclination of the sliding surface β.

Finally, the design value of P is determined as the maximum between P_A and P_B. Water pressure forces as well as seismic actions (i.e. pseudo-static method) can be considered in the model.

Local sliding block between two individual bolts (method 1)

This method was proposed by Grimod and Giacchetti [57] and is used by the manufacturer Maccaferri [68]. It applies to secured drapery interventions in rock slopes. It is based on the assumption of a local unstable block, comprised in-between two individual bolts, sliding along the most critical joint as shown in Fig. 1.18a. The block induces a force F on the mesh that is inclined as the joint by an angle α on the horizontal; the mesh reaction is characterised by a force P orthogonally oriented to the slope face and a force T inclined by an angle θ with respect to the slope face (this angle represents the angle between the deformed upper half profile of the mesh and the slope face). Both the forces P and T are determined from equilibrium considerations adopting a Mohr-Coulomb failure criterion at the sliding plane. This method assumes that the mesh system is characterised by a passive behaviour, namely the activation of a certain amount of retaining force P is associated to a deflection u^* of the system as schematically reported in Fig. 1.18b. The force-displacement relationship is derived from the results of laboratory punch tests. For the design of the mesh system, two conditions



(a) (b)

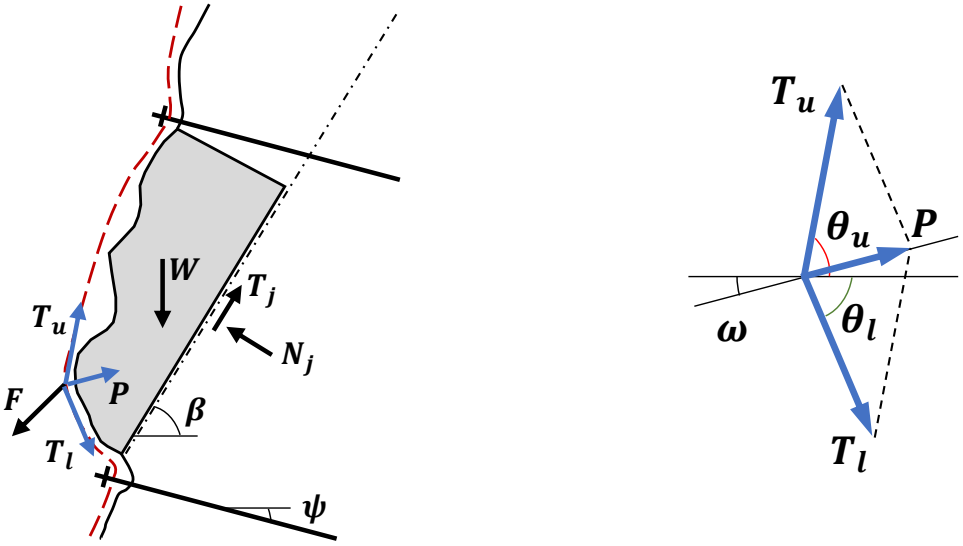
Figure 1.18: (a) Geometrical scheme of the local sliding block considered in the model proposed in [57]. (b) Conceptual scheme of the utilisation of the force-displacment relationship.

have to be satisfied: (i) the force T should be lower than the maximum tensile strength of the mesh, (ii) the deflection u^* (obtained on the basis of the required force P) should be lower than the maximum deflection allowed in serviceability conditions.

An interesting characteristic of this methodology is that it considers the passive behaviour of the drapery system, thus permitting an evaluation of the expected deformations in serviceability conditions. In this sense, this method can be seen as a "hybrid" approach. Nevertheless, the force-displacement relationship used for characterising the behaviour of the mesh derives from laboratory punch tests in which the mesh is fixed along its outer boundary. As already mentioned, this condition strongly differs from the field one (i.e. anchored mesh panel), and therefore affects the representativeness of the force-displacement relation obtained in the laboratory characterisation.

Local sliding block between two individual bolts (method 2)

This method was proposed by the manufacturer Geobrugg [49]. Similarly to the previous, it applies to secured drapery interventions in rock slopes. It



(a) (b)

Figure 1.19: (a) Geometrical scheme of the local sliding rock volume considered in the model proposed in [49] and (b) mesh force diagram.

considers the instability of the rock volume, comprised in-between individual rock bolts, sliding along the most critical joint characterised by a dip angle β as shown in Fig. 1.19a. The mesh reaction is schematised with a local force P, which direction is a function of the amount of force transferred to the upper (force T_u) and lower (force T_l) part of the mesh (see Fig. 1.19b). The value of P is calculated from an equilibrium analysis adopting a Mohr-Coulomb failure criterion at the sliding plane. The ratio between T_u and force T_l is varied in order to obtain the most critical value for P. A range of variation for this ratio is provided by the manufacturer on the basis of laboratory tilting tests [49].

For the design of the mesh system the tensile forces T_u and force T_l should be lower than the tensile resistance of the mesh. Water pressure forces as well as seismic actions (i.e. pseudo-static method) can be considered in the model.

1.4 Conclusive remarks

In this chapter, the main concepts related to drapery mesh systems were described, and a brief review of the available experimental tests (laboratory and field tests) was reported. Moreover, an overview on the commonly adopted design methodologies was presented. It was chosen to omit numerical works dealing with drapery system (a very limited number), because they will be reported in Chapter 3.

This introductory chapter permits some critical aspects related to drapery applications to be pointed out, these are listed below:

- despite the large utilisation of these systems, the comprehension of their mechanical behaviour is limited. In particular, a significant lack of knowledge regarding the load transfer mechanism inside the mesh and between the system elements, as well as concerning the system ultimate capacity still exist. This negatively reflects on the field performances of drapery applications, leading to an over-design of system elements in some case, or causing unsafe or poorly efficient interventions in others;
- the strong unknowns on the mechanical behaviour mentioned in the previous point are mainly related to the poor representativeness of the standard test procedures adopted for the mechanical characterisation of wire meshes. The commonly adopted test configurations, namely the tensile and the punch test, are strongly affected by the boundary conditions imposed to the mesh panel (i.e. fixed outer boundary) and provides a mechanical response of the mesh that is not representative of the field conditions. In this perspective, the need of new testing procedures that are more representative of the field conditions clearly emerges. The adoption of a punching test procedure in which the mesh panel is locally anchored (with the same anchor plates adopted in field applications), instead of being fixed to the testing frame, may represent a (relatively easy) first step in this direction;
- conversely to what done for rockfall fences, field or large-scale tests are not used to characterise the mechanical behaviour of drapery applications. Even if the implementation and execution of field tests may entail economic and technical issues, they should lead to a great improvement of the comprehension of the mechanical behaviour of drapery mesh systems. Moreover, a systematic monitoring of existing in-

terventions may provide further fundamental information;

- the nowadays adopted design methodologies are, generally, based on oversimplified assumption and do not consider the passive behaviour (with the only exception of [57]) that characterises this kind of structures. Considering the design methodologies for soil-retaining applications, the failure mechanism is arbitrarily defined and it varies between the different methods; moreover, the choice of a specific failure mechanism is not supported by any experimental or numerical evidences. The adoption of limit equilibrium analyses (Ultimate Limit State approach) in the design procedures does not allow an estimation of the system deformation in serviceability conditions. Considering that limitations on the system deformations are commonly imposed in the practice, a proper design methodology should consider the force-displacement behaviour of the mesh system (e.g. hybrid or displacement-based approaches [46,47]), thus permitting a control on the system deformation directly from the calculation phase.

Chapter 2

Experimental tests for model calibration

In this chapter the experimental data that will be used in Chapter 3 for the validation of the numerical mesh model, and successively in Chapter 4 and in Chapter 5 when analysing a specific test configurations, are presented. The mesh mechanical response obtained from the different test configurations will not directly discussed in this chapter, since it will be analysed in detail in the following of the thesis, also in the light of the data deriving from the numerical simulation of the same tests. Three mesh typolgies have been considered: the standard 8x10 double twisted hexagonal mesh, a prototype mesh (referred as "mesh type 1") in which longitudinal high resitance steel ropes are inserted in the standard double twisted mesh, a prototype mesh (referred as "mesh type 2") in which longitudinal and transversal high resitance steel ropes are inserted in the standard double twisted mesh. In particular, five different tests are considered:

(i) standard UNI punch tests on the 8x10 double twisted hexagonal mesh;

(ii) standard UNI punch tests on the "mesh type 1"and the "mesh type 2";

(iii) tensile tests on the "mesh type 1" and the "mesh type 2";

(iv) anchor-punch tests on the 8x10 double twisted hexagonal mesh;

(v) punch tests against soil on the 8x10 double twisted hexagonal mesh.

The experimental data of all the above reported tests were provided by Officine Maccaferri SpA (OM) and Maccaferri Innovation Center (MIC). For

the sake of brevity the different mesh types will be referred using the following abbreviations: DT indicates the 8x10 double twisted hexagonal mesh, MT1 indicates the prototype "mesh type 1", MT2 indicates the prototype "mesh type 2". It is worth mentioning that the test campaign (ii) was conducted by MIC contemporary to the study presented in this thesis, thus it was possible to participate in the experimental campaign. The other tests were instead conducted before to the beginning of this research work, or it was not possible to directly participate (tests were conducted abroad), thus the related information is obtained from the test reports. For each test campaign, all the available experimental data are reported in the following.

2.1 Standard UNI punch test on DT mesh type

The standard UNI punch test is a worldwide used test procedure for characterising the resistance of a wire mesh panel when subjected to an out-of-plane puncture force. The latter condition is imposed by applying the puncture load via a punch device (or punching element). The punch test procedure here considered is regulated by the standard UNI 11437:2012 [99] (other test guidelines are possible as for instance the ASTM A975 [4] or EN 10223-3 [37]). This standard imposes the dimension of the tested mesh panel and of the punching element. The former has to be a rectangular panel, which sides, namely L_1 and L_2, must present a nominal length of $3 \pm (0.2 \times 3)$m. The mesh panel is fixed to a rigid external frame along its outer boundary and the distance between the mesh boundary and the rigid frame (i.e. the space in which the constraining system is placed) has to be $\leq 0.15 \times \frac{L_1+L_2}{2}$. Finally, a "planarity condition" of the mesh panel has to be reached before the beginning of the test; this condition is respected when the panel deflection is $\leq 0.2 \min(L_1, L_2)$ (the reference plane is the one of the rigid frame). The punch device is represented by a half-dome shaped element, which must present a perfectly smooth surface. This element is placed at the intersection of the diagonals of the mesh sample, namely in correspondence with the centre of the mesh panel. Moreover, it has to respect the following geometrical conditions:

- curvature radius of the half-dome equal to 1200mm;

- projection on the mesh plane of diameter $\leq$ 1000mm (i.e. the punching element diameter);
- curvature radius of the edges equal to 50mm.

Finally, in order to apply the puncturing force on the mesh panel, the punching element is moved, orthogonally to the mesh plane, with a controlled velocity that has to be $\leq$ 10mm/s. The test output is a force-displacement relation, where the former is computed registering the contrasting force that the mesh panel opposes to the movement of the punching element (through a load cell connected with the punching device), while the latter is represented by the relative displacement of the punching element from the "reference" plane (i.e. the plane of the rigid frame). The mesh resistance is determined as the maximum force registered during the test. The test ends when the failure of the mesh is reached, namely when the mesh panel is no more able to support the movement of the punching element. If the test is arrested before the failure of the mesh, for instance, because of technical limitation of the testing device, the maximum resistance of the mesh is assumed equal to the maximum force reached during the test. The geometrical schemes taken directly from the standard UNI 11437 documentation are reported in Fig. 2.1 for the sake of clarity. The experimental campaign here summarised was conducted by OM [80]. In this experimental campaign, both the panel sides have a nominal dimension of 3m and the DT mesh is characterised by a nominal wire diameter of 2.7mm (i.e. diameter of the single wire). Five tests were performed obtaining the force-displacement curves reported in Fig. 2.3a; furthermore the deflection and force values at failure (δ^* and F^* respectively) are summarised in Tab. 2.1. Finally, two views of the experimental test setup are reported in Fig. 2.2.

In addition to the results of the standard UNI punch test, OM provided also the result of a modified version of the punch test, in which the mesh panel dimension as well as the dimension of the punching element were smaller than the ones imposed by the standard UNI 11437. Both were reduced by a factor of 3, therefore the mesh panel presents a nominal dimension 1m$\times$1m, while the punching element is characterised by a diameter equal to 0.33m. This modified version of the punch test permits a first estimation of scale effects on the puncture resistance of the considered mesh. The force-displacement relation obtained from this test is reported in Fig. 2.3b, while the force and deflection values at failure are reported in Tab. 2.1.

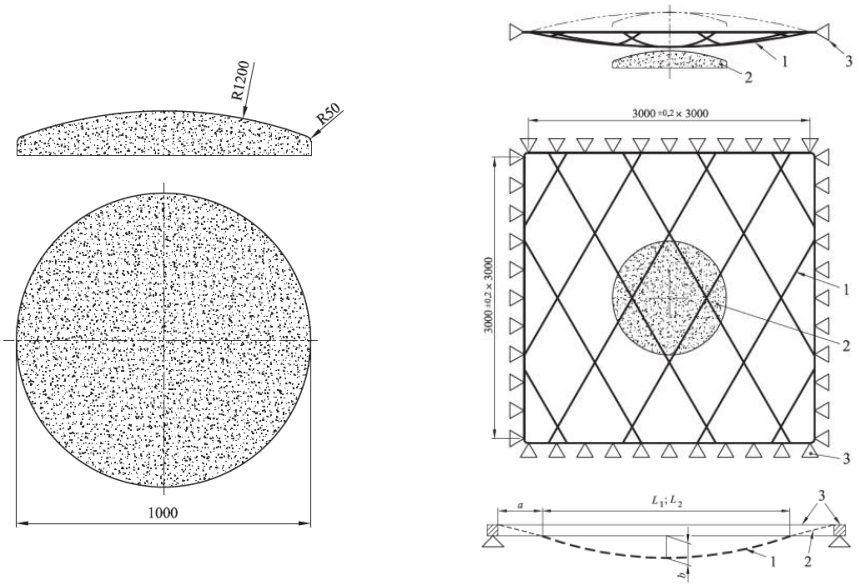
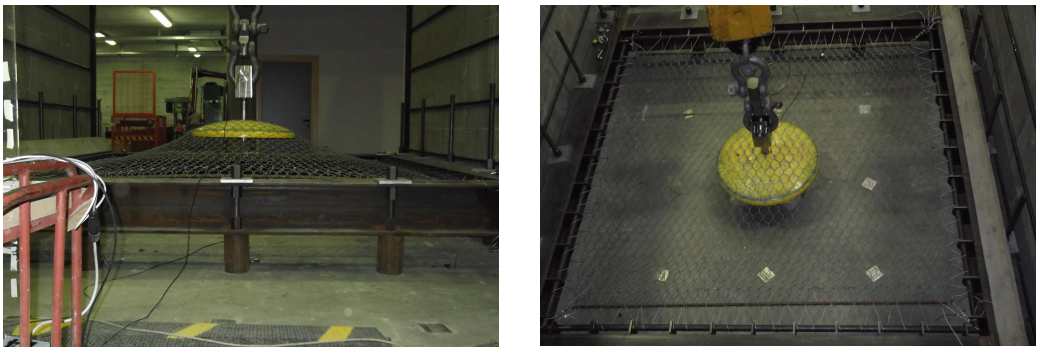
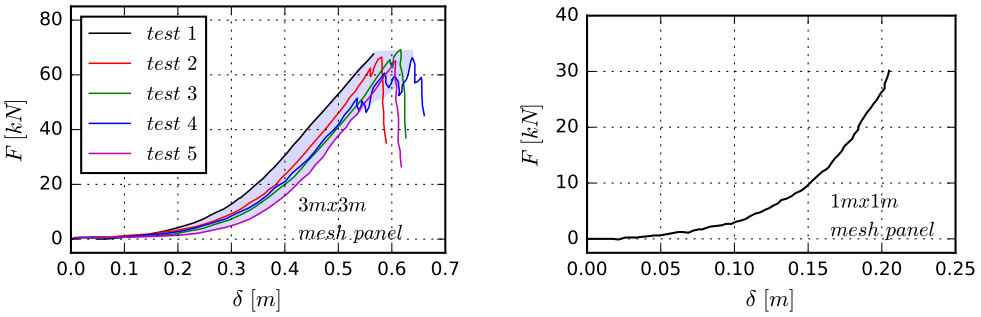


Figure 2.1: Geometrical dimensions (in millimiters) required by the standard UNI 11437:2012 (after [99]).



(a) (b)

Figure 2.2: (a) Lateral view and (b) overhead view of the standard UNI punch test (courtesy of Officine Maccaferri SpA).



(a) (b)

Figure 2.3: Experimental force-displacement curves obtained from the punch tests on the DT mesh for a test characterised by: (a) panel dimension of 3m×3m and punching device diameter of 1m, (b) panel dimension of 1m×1m and punching device diameter of 0.33m.

test (panel dim.)	F^* [kN]	δ^* [m]
test 1 (3m×3m)	67.6	0.57
test 2 (3m×3m)	66.5	0.58
test 3 (3m×3m)	69.3	0.62
test 4 (3m×3m)	66.3	0.64
test 5 (3m×3m)	65.1	0.61
average	67.0	0.60
test 6 (1m×1m)	30.4	0.21

Table 2.1: Experimental results of the standard UNI punch test (the panel nominal dimension in reported in round brackets). The data refers to the values measured an instant prior to the mesh failure.

2.2 Standard UNI punch test on MT1 and MT2 mesh types

The test procedure adopted for characterising the puncture resistance of the MT1 and MT2 mesh types follows the standard UNI 11437 [99] already descripted in Sec. 2.1. The MT1 and MT2 mesh types are realised by inserting high resistance steel ropes in the standard 8x10 double twisted mesh with a regular spacing. In particular, in the MT1 mesh type, only longitudinal ropes, namely parallel to the double twisted wires direction, are inserted, while in the MT2 mesh type both longitudinal and transversal (i.e. orthogonally aligned with the double twisted wires direction) ropes are used. Both the longitudinal and transversal ropes are woven inside the mesh panel at the level of the double torsions. The geometric fabric of the two mesh types can be observed in Fig. 2.4a and 2.4c for the MT1 and the MT2 respectively.

The experimental campaign was conducted by MIC [72]. In this test campaign, the ropes have a nominal spacing of 32cm and a diameter of 8mm; the DT mesh has a nominal wire diameter of 2.7mm. For the sake of clarity, two views of a mesh panel, for both the mesh types, before the beginning of the punch test, are reported in Fig. 2.4b and 2.4d. The geometrical configuration was chosen in order to respect the symmetry of the ropes pattern in the MT1 and MT2 mesh types (ropes nominal spacing of 32cm in both directions) and contemporary having the central ropes (only one in the case of the MT1) in correspondence to the centre of the punching element. The mesh panels are connected to the external rigid frame by looping a steel rope on a bordering cable (F-BC connection in Fig. 2.5). The latter is connected to the mesh panel's boundary by passing it inside loops made with the panel ropes (R-BC connection in Fig. 2.5). The loops are closed by using clamps as shown in Fig. 2.5. This particular constraining condition permits a slight rearrangement of the mesh panel during the test and, in particular, it allows a better redistribution of the stresses on the ropes, thus avoid a premature failure of the mesh panel. In contrast to the "rigid connection" condition obtained by directly fixing the mesh to the external frame, the adopted condition can be seen as a "soft connection" condition. For the sake of clarity, a view of the connection system adopted during the experimental campaign (i.e. "soft connection") is reported in Fig. 2.5. Before the beginning of each test, the mesh panel is tensioned in order to obtain a planar configuration

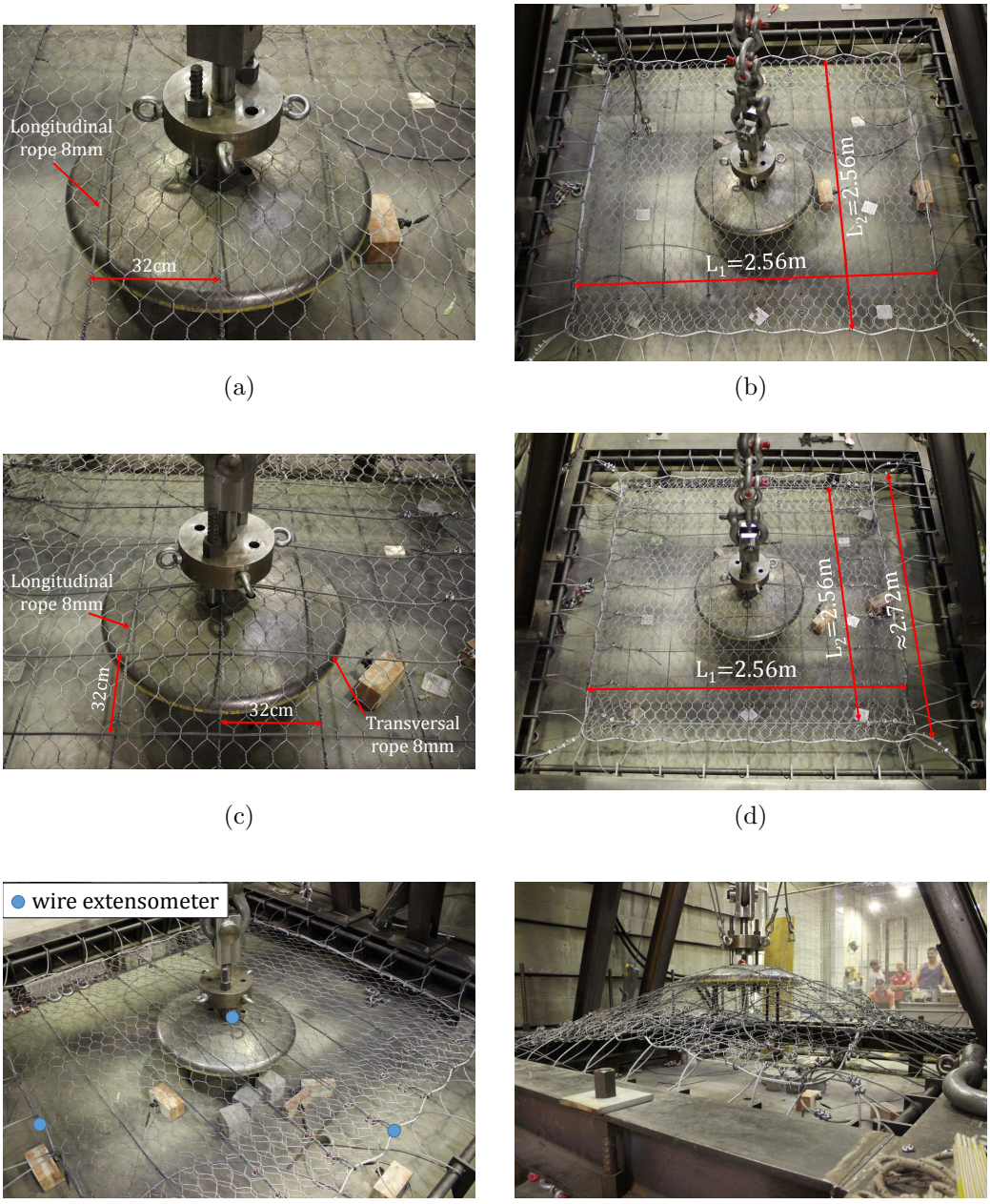


Figure 2.4: Particular of the mesh panel and overhead view of the initial configuration of the standard UNI punch test for (a,b) the MT1 mesh type and (c,d) the MT2 mesh type. (e) Positions of the wire extensometers used for computing the differential displacement between the mesh border and the one at the centre of the mesh panel. (f) A view of the MT2 mesh panel during the test (courtesy of Maccaferri Innovation Centre).

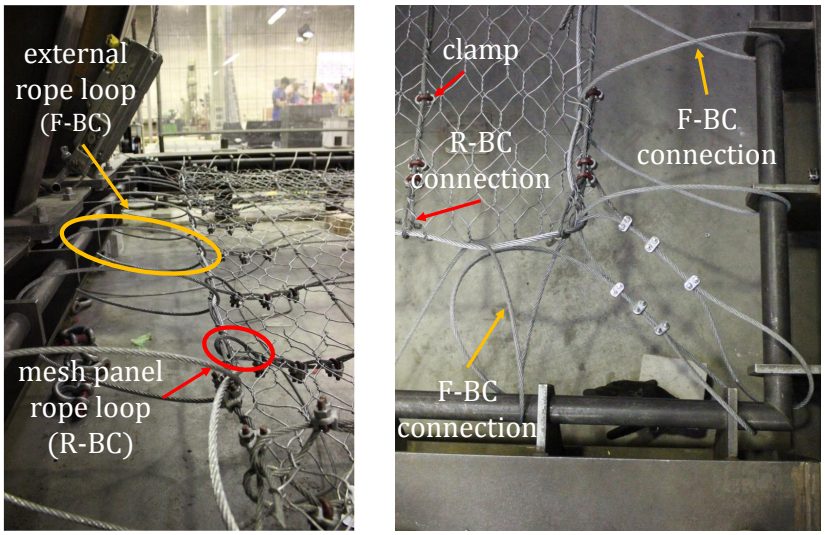


Figure 2.5: Particular of the "soft connection" with the external frame: the connection between the rigid frame and the bordering cable (external cable loop) is indicated by F-BC, while the connection between the panel ropes and the bordering cable (rope loop) is indicated by R-BC (courtesy of Maccaferri Innovation Centre).

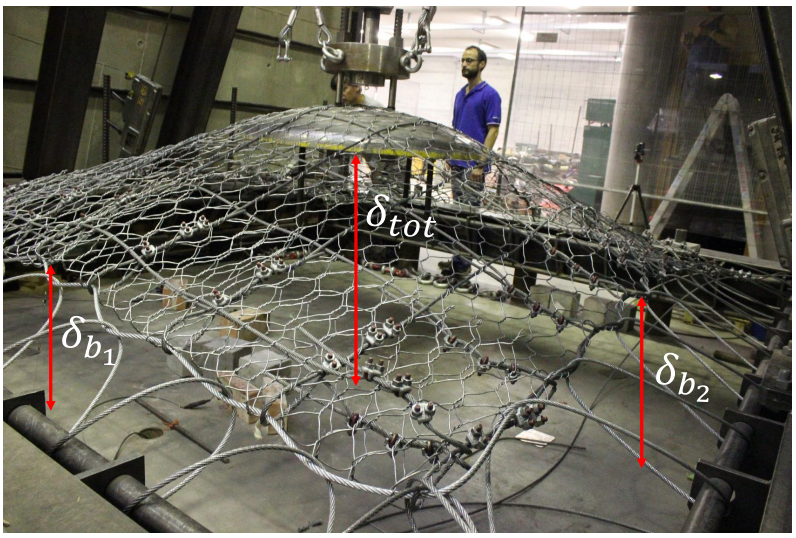
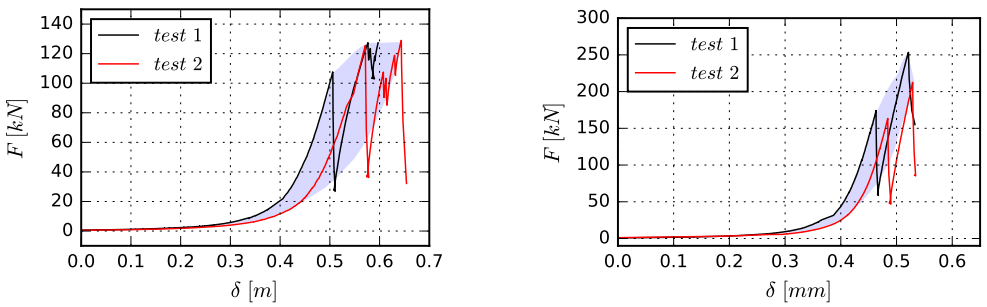


Figure 2.6: Schematic representation of the displacements measured during the test used to compute the displacement considered in the definition of the force-displacement curve $\delta_b = (\delta_{b_1} + \delta_{b_2})/2$ (courtesy of Maccaferri Innovation Centre).



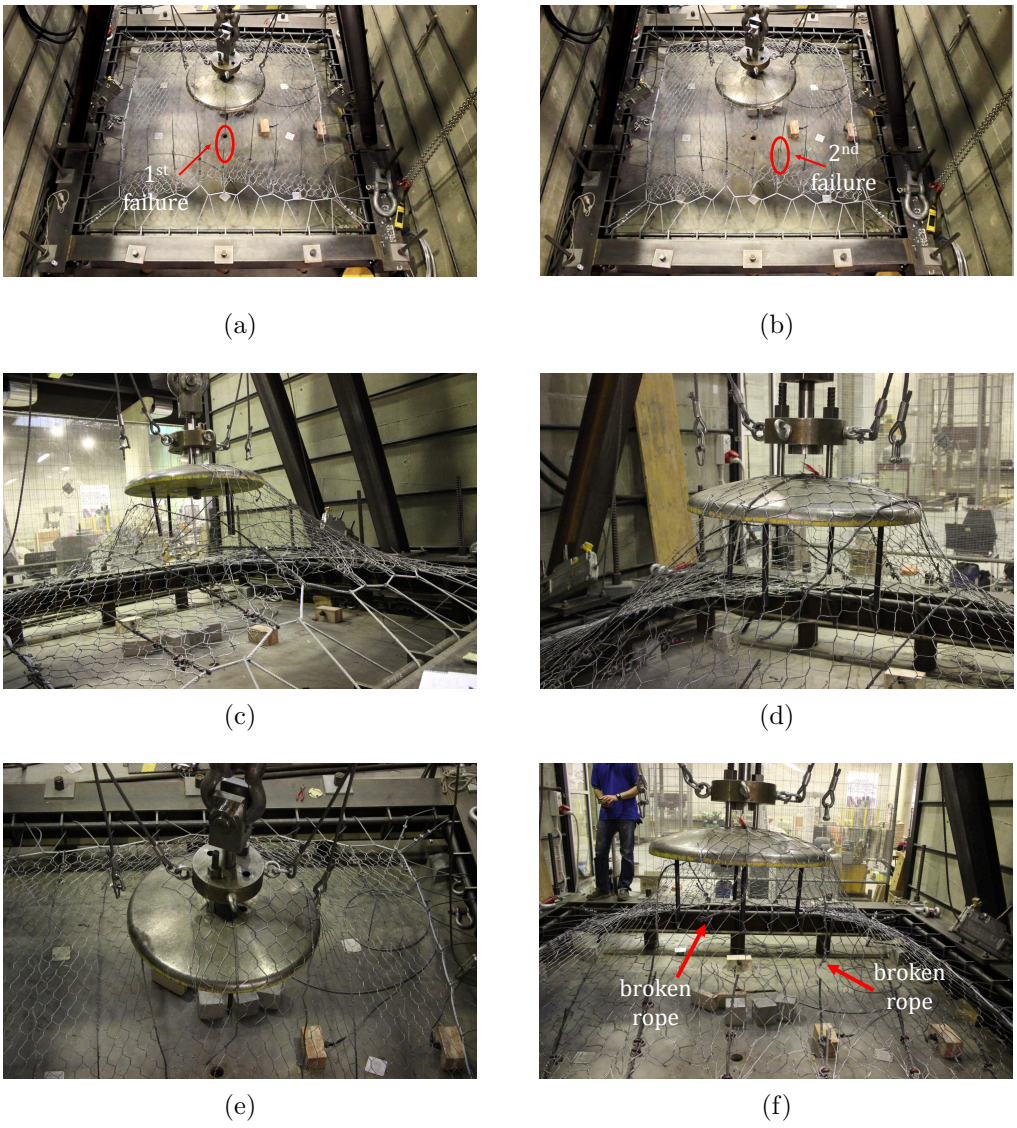
(a) (b)

Figure 2.7: Experimental force-displacement curves obtained from the punch test on the (a) MT1 mesh type and (b) MT2 mesh type.

by slightly moving upwards the punching element.

The test output is a force-displacement relation characterising the mesh response to the thrust force imposed by punching element displacement. In this case, in order to account for the displacement of the mesh border δ_b due to the deformability of the "soft connection", only the relative displacement between the mesh border and the mesh centre is considered. For doing that, wire extensometers are placed in correspondence to the middle point of the mesh sides, as shown in Fig. 2.4e. A schematic representation of these displacements, at a generic step of the test, is instead provided in Fig. 2.6. The displacement δ considered in the definition of the force-displacement relationships of the mesh panels is therefore calculated as the difference between the total displacement of the punching element δ_{tot}, and the one measured at the mesh boundary δ_b (i.e. $\delta = \delta_{tot} - \delta_b$). The latter is considered equal to the mean value of the measurements obtained from the two lateral wire extensometers (i.e. $\delta_b = (\delta_{b_1} + \delta_{b_2})/2$).

Two tests were conducted for each mesh type; the force-displacement curves thus obtained are reported in Fig. 2.7, while the panel deflection and force values at failure (δ^* and F^* respectively) are summarised in Tab. 2.2. From the observation of the F-δ curves reported in Fig. 2.7 it is possible to note that these are characterised by local peaks before reaching the complete failure of the mesh panel (i.e. the latter is no more able to contrast the punching element movement). These peaks are related to the breakage of a rope; indeed, during the experimental tests a sequential failure of the



(a) (b)

(c) (d)

(e) (f)

Figure 2.8: (a,b) Sequence of the rope failures during the experimental test. (c-f) Post-failure view of the mesh panel. The pictures refers to the test 2 on the MT1 mesh type (courtesy of Maccaferri Innovation Centre).

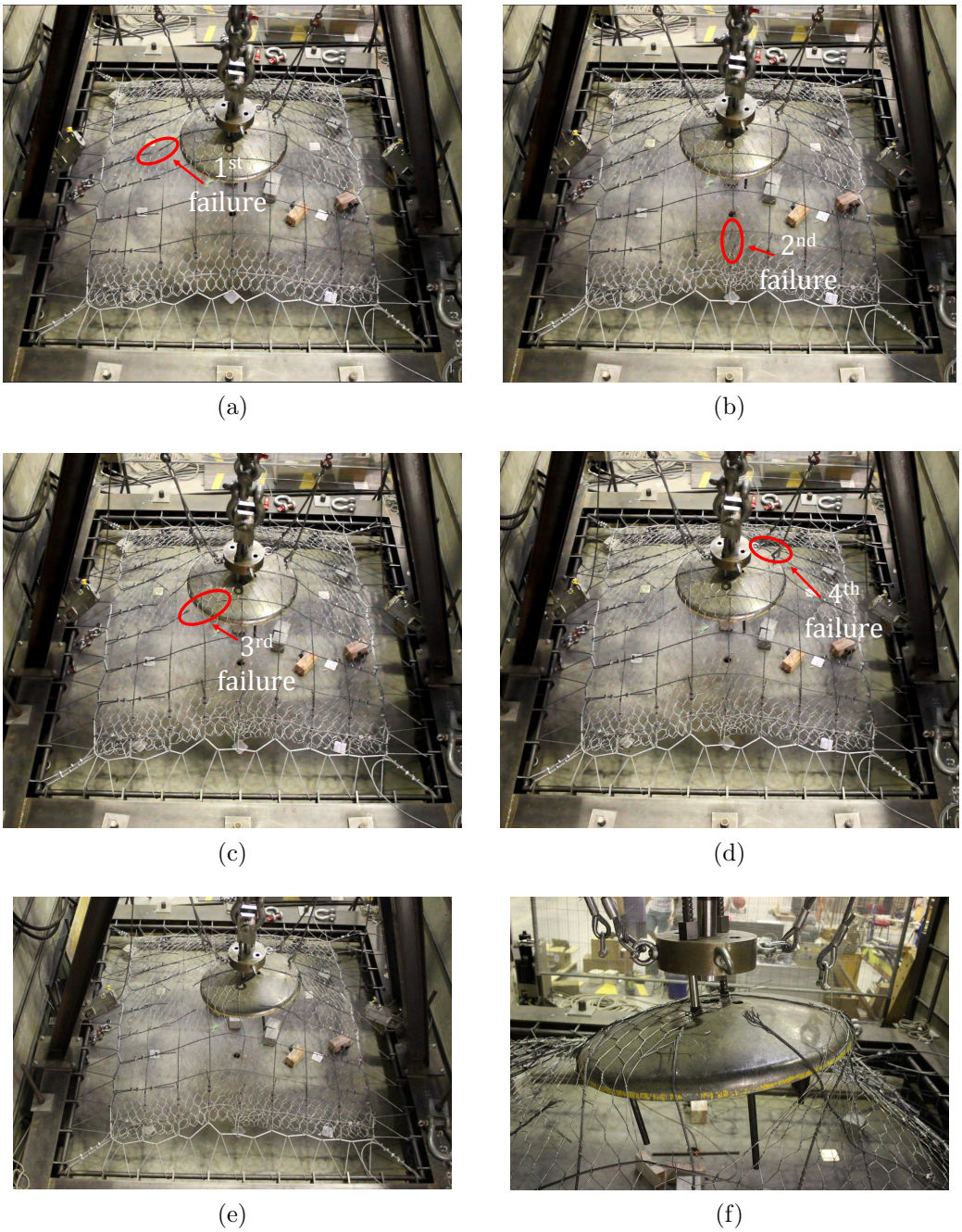


Figure 2.9: (a-d) Sequence of the rope failures during the experimental test. (e,f) Post-failure view of the mesh panel. The pictures refers to the test 1 on the MT2 mesh type (courtesy of Maccaferri Innovation Centre).

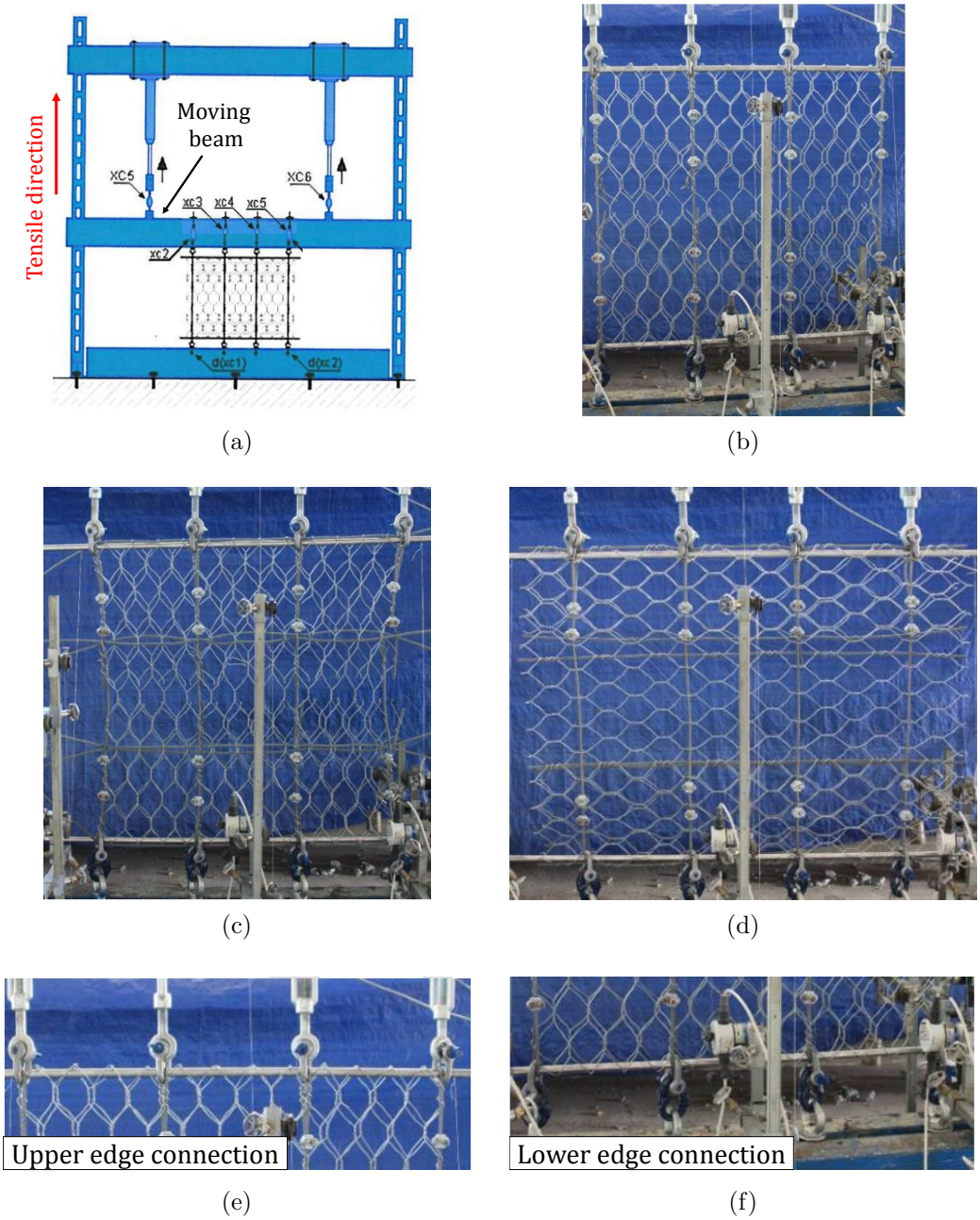
mesh type	test	F^* [kN]	δ^*_{tot} [m]	δ^*_b [m]	δ^* [m]
MT1	test 1	127.4	0.81	0.23	0.58
MT1	test 2	129.0	0.85	0.21	0.64
MT1	average	128.2	0.83	0.22	0.61
MT2	test 1	253.3	0.82	0.30	0.52
MT2	test 2	212.6	0.91	0.38	0.53
MT2	average	233.0	0.87	0.34	0.53

Table 2.2: Experimental results of the standard UNI punch test for the MT1 and MT2 mesh types. The data refers to the values measured an instant prior to the mesh failure.

ropes is observed. After the first failure of a rope, a temporary drop of the force acting on the punch device (i.e. the mesh reaction) is registered, however the external load is rapidly redistributed between the other ropes permitting the mesh panel to sustain a further increment of the external force. The failure of a further rope can lead to the mesh failure or to another phase of redistribution between the other ropes of the mesh panel; the former behaviour was observed for the MT1 mesh type, while the latter was observed for the MT2 mesh type. The sequence of the ropes failure as well as some post-failure views of the mesh panel are reported in Fig. 2.8 and Fig. 2.9 with reference to the MT1 (test 2) and the MT2 (test 1) mesh panel respectively.

2.3 Tensile test on MT1 and MT2 mesh types

The experimental campaign for determining the tensile resistance of the MT1 and MT2 mesh types was conducted directly by MIC [73]. The characteristic of the MT1 and MT2 mesh types are the same of the ones of the mesh panels adopted in the experimental characterisation reported in Sec. 2.2, namely a spacing between the ropes of 32cm, a diameter of the ropes equal to 8mm and a nominal wire diameter of the DT mesh of 2.7mm. The nominal dimension of the tested panels is equal to 0.96m×0.96m. The tensile test setup is schematised in Fig. 2.10a. In the test setup, a mesh panel is fixed at its lower edge to the rigid frame, connecting the ropes to the latter by means of specific fastening devices as shown in Fig. 2.10f; the upper edge of the



(a) (b) (c) (d) (e) (f)

Figure 2.10: (a) Scheme of the tensile test setup. View of the mesh panel at the beginning of the tensile test: (b) LL test, (c) LT test, (d) TT test. Particular of the connection (e) at the upper edge of the mesh panel and (f) at the lower edge of the mesh panel (courtesy of Maccaferri Innovation Centre).

panel is instead connected to the moving part of the testing rig as shown in Fig. 2.10e. Displacement gauge sensors are placed in correspondence to the rope-framework connection in the lower part of the system in order to measure the displacement of the moving part of the testing ring ($d(xc1)$ and $d(xc2)$ in Fig. 2.10a). A load cell is connected to each of the two jacks in the upper part of the testing rig permitting the tensile force imposed to the mesh panel to be measured ($XC5$ and $XC6$ in Fig. 2.10a). Finally, load cells are installed at the connections between the ropes and the moving beam, allowing the measurements of the tensile force acting on each rope ($xc2$ to $xc5$ in Fig. 2.10a). Before each test, a slight pre-tension is applied to the mesh panel in order to minimise the initial geometrical irregularities and distortions in the panel, thus permitting a prompt tensile reaction of the latter from the beginning of the tensile test.

The tensile test is performed in both the longitudinal and transversal direction (i.e. parallel and orthogonal to the double twisted orientation respectively) for the two mesh types (MT1 mesh and MT2 mesh). However, since the transversal tensile test on the MT1 mesh type will not be used for the validation of numerical mesh model reported in Chapter 3, this test is not reported. In the experimental nomenclature a specific test configuration is associated with two capital letters:

- the first letter indicates the direction of the applied tensile load. The letter L refers to a test in which the tensile load is applied along a direction parallel to the orientation of the double twisted wires, while the letter T refers to a test in which the tensile load is applied along a direction orthogonal to the orientation of the double twisted wires.
- the second letter indicates the type of tested mesh panel. The letter L is used to refer to a test in which a MT1 mesh panel is adopted, while the letter T is used when a MT2 mesh panel is considered.

For instance, the test LT refers to a tensile test in which the tensile load is applied along the direction of the longitudinal ropes (i.e. direction of the double twisted wires) and a MT2 mesh panel is adopted. A view of the mesh panels for the three test configurations, namely LL, LT and TT, are reported in Fig. 2.10b, 2.10c and 2.10d respectively. In the experimental campaign, several tests (from three to five) were conducted for each of the test configurations. The experimental results are reported in Fig. 2.11a, Fig. 2.11b and Fig. 2.11c, in terms of force-displacement curves for the LL, LT and TT test configurations respectively. Moreover the envelope of the

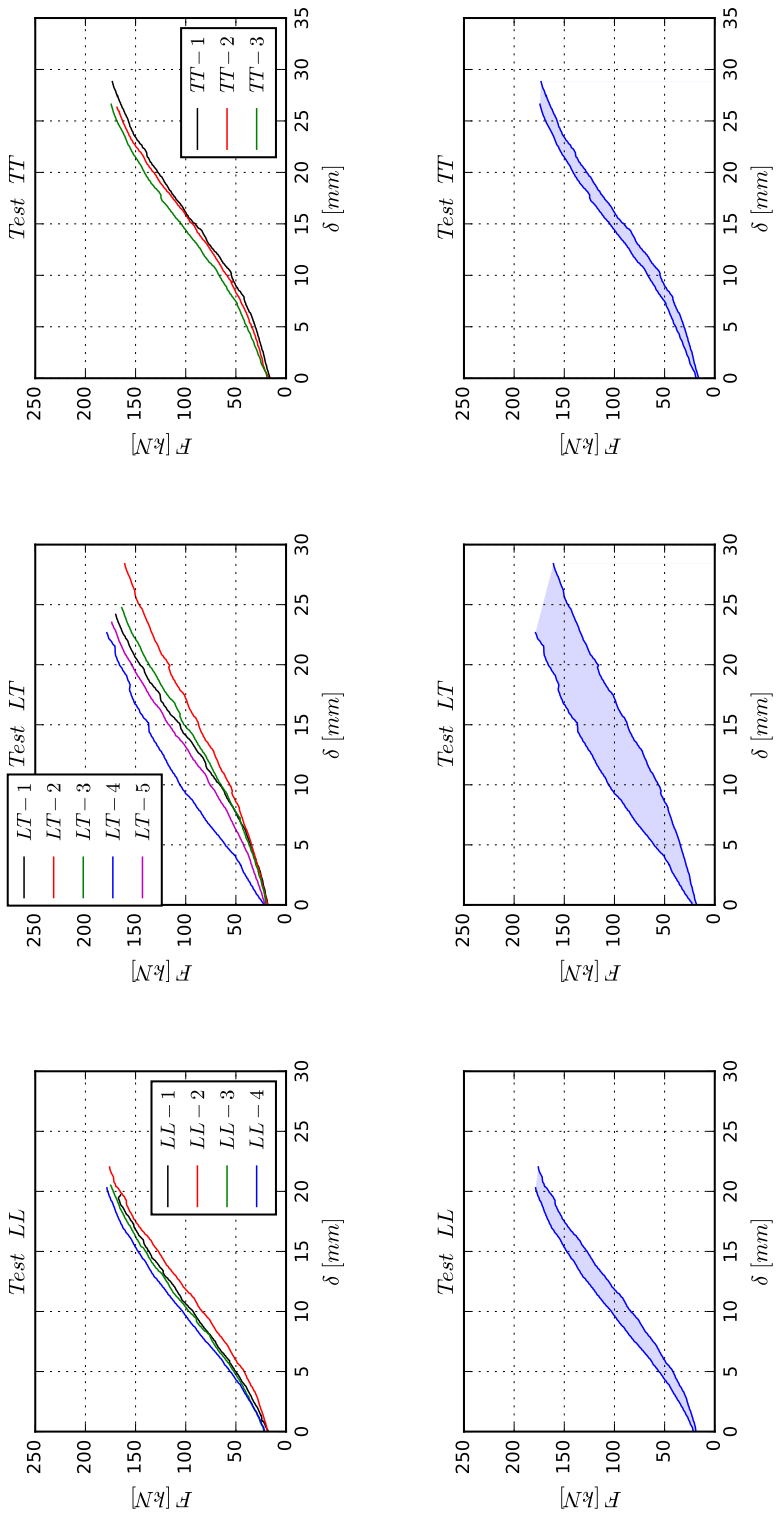


Figure 2.11: Experimental force-displacement curves and envelope of the experimental results obtained from the tensile test configuration: (a) LL, (b) LT and (c) TT.

test	F^* [kN]	δ^* [mm]	F_r^{mean} [kN]	F_r^{min} [kN]	F_r^{max} [kN]†
LL-1	170.5	19.4	41.8	36.2	44.7
LL-2	180.0	22.1	44.1	40.4	45.8
LL-3	178.8	20.7	43.8	41.1	47.3
LL-4	182.2	20.3	44.6	43.5	45.8
average	177.9	20.6	-	-	-

† the nominal ultimate strength of a high resistance 8mm steel rope is ≈45.8kN

Table 2.3: Experimental results of the tensile test for the LL configuration.

test	F^* [kN]	δ^* [mm]	F_r^{mean} [kN]	F_r^{min} [kN]	F_r^{max} [kN]†
LT-1	170.1	24.2	42.5	38.4	46.8
LT-2	161.2	28.5	40.3	31.2	45.8
LT-3	163.9	24.9	41.0	33.7	46.6
LT-4	179.5	22.8	44.9	42.7	46.7
LT-5	174.2	23.6	43.6	42.0	46.0
average	169.8	24.8	-	-	-

† the nominal ultimate strength of a high resistance 8mm steel rope is ≈45.8kN

Table 2.4: Experimental results of the tensile test for the LT configuration.

experimental results is reported in the same figures permitting the variability observed in the experimental characterisation to be highlighted. Finally, the displacement at failure and the maximum force registered in the tests (δ^* and F^* respectively) are summarised in Tab. 2.3, Tab. 2.4 and Tab. 2.5 for the LL, LT and TT test configurations respectively. In all the experimental tests, the force sustained by the different ropes, aligned with the tensile direction, is almost equally distributed between them. Moreover, an instant prior to the panel failure, the mean force (on the four ropes aligned with the tensile direction) supported by a single rope is greater than 40kN in all the test, showing that their resistance is efficiently exploited (the nominal ultimate strength of a high resistance 8mm steel rope is approximately 45.8kN). For the sake of completeness, the minimum (F_r^{min}) and maximum (F_r^{max}) force registered on a single rope as well as the mean force (F_r^{mean}) acting on the ropes are reported in Tab. 2.3, Tab. 2.4 and Tab. 2.5 for the related tests.

test	F^* [kN]	δ^* [mm]	F_r^{mean} [kN]	F_r^{min} [kN]	F_r^{max} [kN]†
TT-1	173.4	28.9	43.4	41.2	44.6
TT-2	168.9	26.4	42.2	40.1	43.2
TT-3	174.5	26.7	43.6	42.9	44.5
average	172.3	27.3	-	-	-

† the nominal ultimate strength of a high resistance 8mm steel rope is ≈45.8kN

Table 2.5: Experimental results of the tensile test for the TT configuration.

2.4 Anchor punch test on the DT mesh type

An alternative characterisation of the puncture resistance of a mesh panel (to the one deriving from the standard UNI punch test) can be provided performing a punch test in which the punching device is represented by an anchor plate [15, 22]. In fact, in a secured drapery system, the maximum force supportable by a mesh panel is generally controlled by the available resistance at the connection between the mesh and the anchor plate (this aspect will be further discussed in the following of this thesis). The latter can be efficiently estimated from the maximum puncture force, associated to an anchor plate, that a mesh panel can support.

The test procedure is analogous to the one of the standard UNI punch test. The mesh panel is fixed along its boundary to a rigid frame and a slight pre-tensioning is applied to the mesh panel prior to the beginning of the test in order to reach a "planarity condition" of the panel. In the test campaign, a square plate of side 250mm is adopted as punching device (this represents one typology of the anchor plates associated to this mesh type in field applications). The nominal dimension of the mesh panel is equal to 1.70m×1.60m and the DT mesh is considered. In this case, two different typologies of the DT mesh are considered, namely a DT mesh characterised by a nominal wire diameter of 3.0mm and a DT mesh characterised by a nominal wire diameter of 3.9mm. During the experimental test, the plate is moved downwards with a fixed velocity, and its displacement and the force acting on it, due to the contrast imposed by the mesh, are registered. In Fig. 2.12 some views of the experimental tests are reported in order to provide a better understanding of the test geometry. Moreover, a particular of the punching device (i.e. square anchor plate with cutted vertexes) and of the

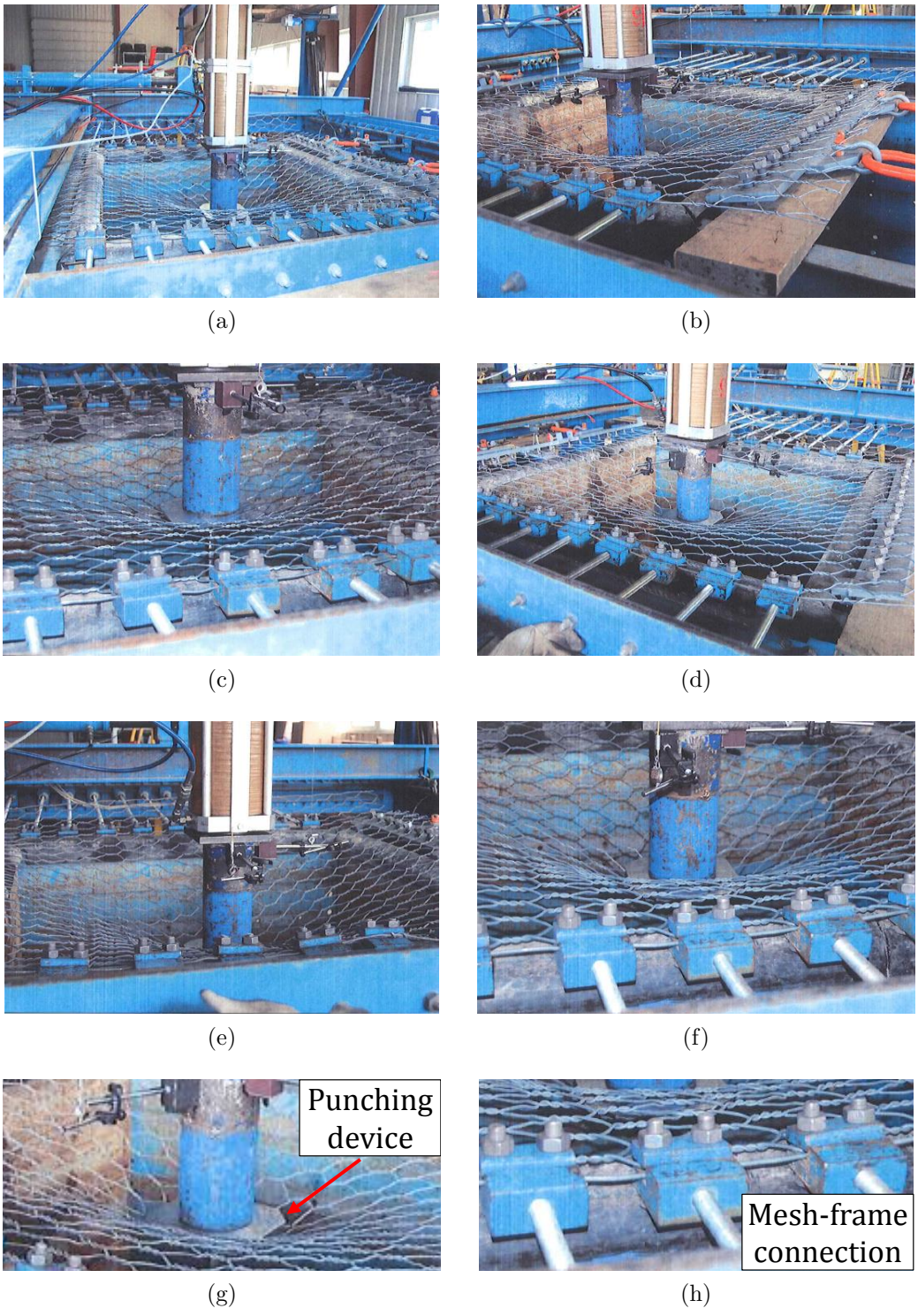
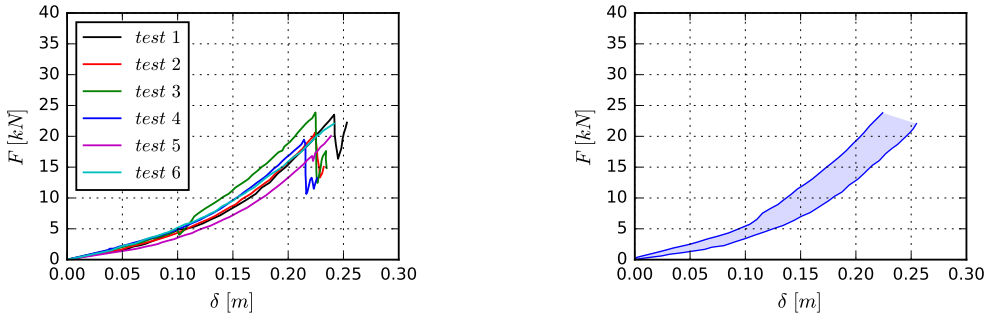


Figure 2.12: Views of the anchor punch test for (a,c,e) the 3.0mm DT mesh and (b,d,f) the 3.9mm DT mesh. Particular of (g) the punching device and of (h) the connection between the mesh panel and the external frame (courtesy of Maccaferri Innovation Centre).



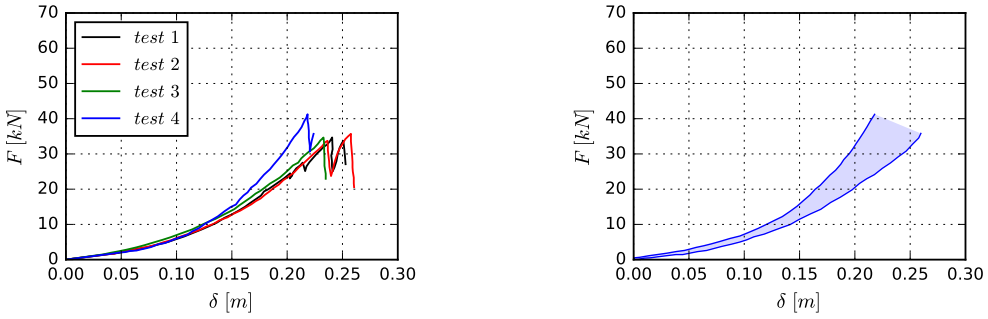
(a) (b)

Figure 2.13: (a) Experimental force-displacement curves and (b) envelope of the experimental results obtained from the anchor punch test on the 3.0mm DT mesh.

test (panel dim.)	F^* [kN]	δ^* [m]
test 1 (1.71mx1.60m)	23.5	0.24
test 2 (1.72mx1.60m)	20.6	0.22
test 3 (1.72mx1.60m)	23.9	0.22
test 4 (1.76mx1.60m)	19.5	0.21
test 5 (1.74mx1.60m)	20.1	0.24
test 6 (1.70mx1.60m)	22.1	0.24
average	21.6	0.23

Table 2.6: Experimental results of the anchor punch test on the 3.0mm DT mesh.

connection system between the mesh boundary and the external rigid frame are reported in Fig. 2.12g and 2.12h for the sake of clarity. Unfortunately, no post-failure views of the mesh panel were available; however, in the test report is specified that the failure of the mesh panel was observed in the area around the plate, for all of the performed tests. The test output is given in terms of force-displacement relationships, thus characterising the puncturing resistance, associated to an anchor plate (square plate of side 250mm in the present case), of the mesh panel. Several tests were performed for both the mesh types (6 for the 3.0mm DT, 4 for the 3.9mm DT). The experimental



(a) (b)

Figure 2.14: (a) Experimental force-displacement curves and (b) envelope of the experimental results obtained from the anchor punch test on the 3.9mm DT mesh.

test (panel dim.)	F^* [kN]	δ^* [m]
test 1 (1.72mx1.60m)	34.7	0.24
test 2 (1.71mx1.60m)	35.7	0.26
test 3 (1.71mx1.60m)	34.7	0.23
test 4 (1.72mx1.64m)	41.3	0.22
average	36.6	0.24

Table 2.7: Experimental results of the anchor punch test on the 3.9mm DT mesh.

data were provide by MIC [69, 70].

The experimental results are reported in Fig. 2.13 and Fig. 2.14 in terms of force-displacement curves for the 3.0mm DT and the 3.9mm DT respectively. Furthermore, the force and deflection values at failure (F^* and δ^*) are reported in Tab. 2.6 and Tab. 2.7 for the 3.0mm DT and the 3.9mm DT respectively.

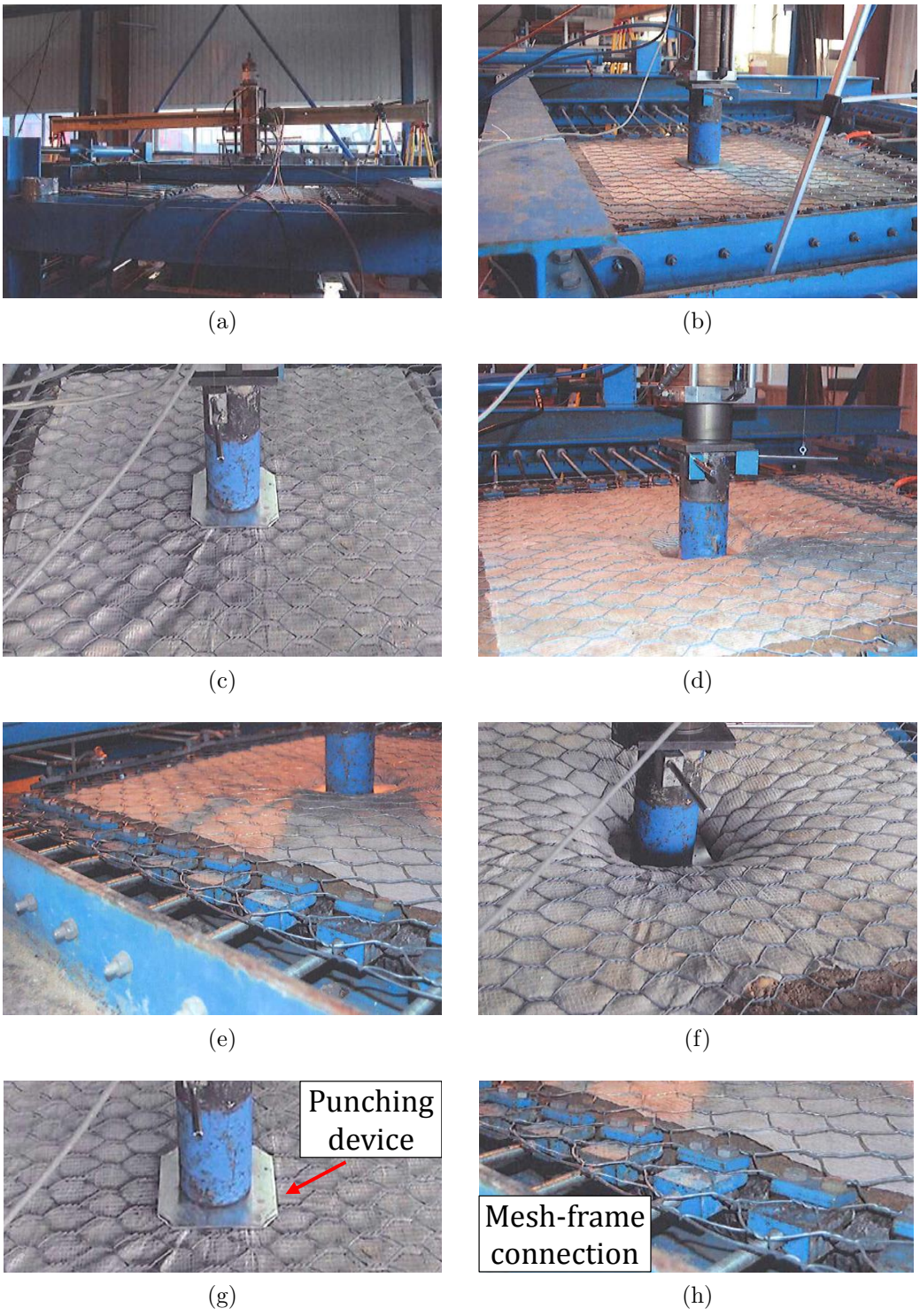
2.5 Punch test against soil

The punch test against soil is an experimental procedure that can be useful to estimate the relationship between the applied load to an anchor plate and

the settlement of the latter. Moreover, it permits the evaluation of the bearing capacity of the mesh-plate-soil system, thus estimating an upper limit for the force that is possible to apply to the anchor plate in field applications. The experimental setup is similar to the one of the test campaign presented in Sec. 2.4. However, in this case, the mesh panel is placed on the top of a granular soil layer, which provides a further contrast to the punching element displacement. In the experimental campaign a geotextile is lied in-between the soil and the mesh panel to avoid the passage of soil particles through the openings of the mesh; nevertheless, the structural role of this geotextile is negligible (the geotextile is let free to move at its boundary). The punching device is represented by the same square plate of side 250mm adopted in the test campaign reported in Sec. 2.4. The soil layer is contained in a parallelepiped caisson, and in the test report, is characterised as a sandy gravel (0/32mm), optimum compacted material. No data about the mechanical properties of the soil were available from the test report. The nominal dimension of the mesh panel is equal to 1.80m×1.70m (the dimension of the caisson, in the mesh plane, is the same) and a DT mesh with a nominal wire diameter of 3.0mm is considered. Several views prior and during the test of the experimental setup are shown in Fig. 2.15. Moreover, a zoomed view of the punch device, and one of the connection between the mesh boundary and the external rigid frame, are reported in Fig. 2.15g and 2.15h for a sake of clarity.

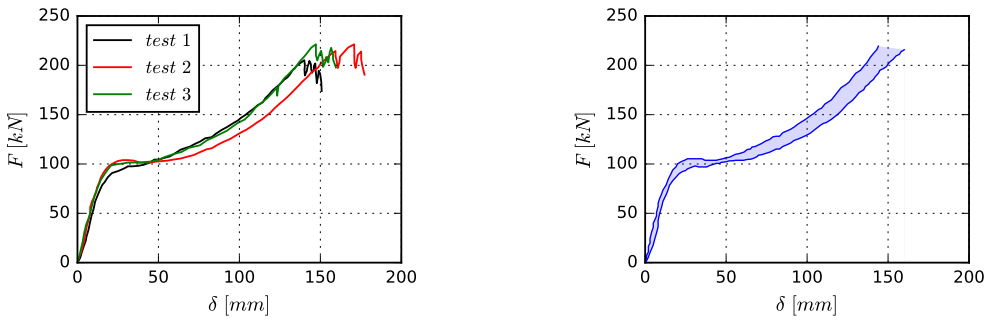
The testing procedure is analogous to the one presented in Sec. 2.4, namely the punching device is moved downwards (at a fixed displacement rate) and the force acting on it, this time deriving from the contrasts of both mesh and soil, is registered providing, at the end of the test, a force-displacement relation. The test is continued until the failure of the mesh panel, which occurs, for all the tests, in the area surrounding the anchor plate (as specified in the test report [71]). The experimental data were provide by MIC [71].

The experimental data obtained from the three tests performed in the experimental campaign are reported in Fig. 2.16. Moreover, the panel deflection and the maximum force registered during the tests (δ^* and F^* respectively) are summarised in Tab. 2.8. It is worth noting that, the mechanical response obtained in this test configuration is more complex than the one obtained when considering the solely mesh without the presence of the soil (Sec. 2.4). This is due to non-trivial effects deriving from the mesh-soil interaction



(a) (b) (c) (d) (e) (f) (g) (h)

Figure 2.15: Views of the punch against soil test setup (a,b,c) prior and (d,e,f) during the loading phase. Particular of (g) the punching device and of (h) the connection between the mesh panel and the external frame (courtesy of Maccaferri Innovation Centre).



(a) (b)

Figure 2.16: (a) Experimental force-displacement curves and (b) envelope of the experimental results obtained from the punch test against soil.

test (panel dim.)	F^* [kN]	δ^* [mm]
test 1 (1.80mx1.70m)	205.2	140
test 2 (1.80mx1.70m)	221.3	171
test 3 (1.80mx1.70m)	221.4	147
average	216.0	153

Table 2.8: Experimental results of the punch test against soil.

and to the further contrast imposed by the soil to the punching element's displacement. Moreover, the soil type, its mechanical properties, as well as the initial conditions of the soil volume (e.g. degree of compaction) may strongly influence the overall response of the system. A detailed mechanical analysis of the behaviour of the mesh-plate-soil system will be presented in Chapter 5.

Chapter 3

Numerical methodology

In this chapter, the numerical methodology adopted in this thesis is presented. In the first part of the chapter, the fundamental concepts of the Discrete Element Method (DEM) are briefly recalled, then a detailed description of the different strategies used for modelling wire meshes in a DE framework is reported. In the second part, the numerical mesh model is validated against the results of the laboratory tests presented in Chapter 2. Finally, the two numerical strategies adopted in this thesis for the modelling of the mesh, are compared in terms of mechanical response with reference to different loading conditions, as well as considering the possible differences in terms of computational efficiency.

3.1 Discrete element method

The Discrete Element Method was introduced by Cundall [28] and successively extended by Cundall and Strack [29]. This method permits one to efficiently simulate the evolution of a discrete assembly of bodies from the treatment of the binary interactions between the particles that compose the assembly. The attractive of a discrete method is that it gives access, at any time, to quantities that are hardly measurable in experimental tests (e.g. contact forces, contact distribution). Moreover, the description of a granular medium at the particle scale permits the physics of natural materials to be reproduced by using a relatively low number of parameters. The DEM is based on an explicit scheme for the numerical integration of the equations of dynamics. The interaction between the bodies are expressed explicitly

according to the rate of deformation (schematised with a rigid interpenetration) at the contact. Even if the method was originally meant to describe the evolution of granular materials, it has been efficiently applied to many geomechanical problems in which discontinuities and the interactions between soil particles and structural elements are relevant. Some examples of applications can be found in [21, 24, 25, 45, 74, 86, 91, 101].

For the sake of completeness, it should be noted that another method, for the simulation of granular materials, called Contact Dynamics (CD) [63, 64] exists. This method is substantially different from the formulation of Cundall and Strack [29]. In this method, particles are strictly indeformable (i.e. no interpenetration at the contact level) and their interaction is controlled by shock laws. The CD method is based on an implicit scheme for the computation of the particles motion and of the interaction forces between the particles. For further details refer to [63, 88].

3.1.1 DEM cycle

The standard cycle of a generic step of the DEM is reported in Fig. 3.1. The equations of the dynamics are integrated in time, starting from the information on particle interactions governed by the contact laws. The stability of the explicit scheme is ensured solving the problem at small time scales (i.e. smaller than the typical time of a collision); this ensure that the particles motions are smooth, and so twice differentiable. Details on the integration time step are given in Sec. 3.1.3. For a better understanding of the method, let us consider a calculation step for the case of spherical bodies. In an oriented tri-dimensional space it is possible to characterise the motion of a particle by its position x_i, and its translational and rotational velocities $\dot{x}_i$ and ω_i respectively. Moreover, its mass is indicated by m_i and its moment of inertia by I_i. The Newton's second law imposes that the translation and rotational accelerations are given by:

$$\ddot{x} = F_i/m_i \tag{3.1}$$

$$\dot{\omega} = M_i/I_i \tag{3.2}$$

where F_i and M_i are the force and the moment applied to the considered particle. The in-time evolution of the particulate system is reconstructed by the integration, over a time step Δt, of the accelerations $\ddot{x}_i$ and $\dot{\omega}_i$ using a

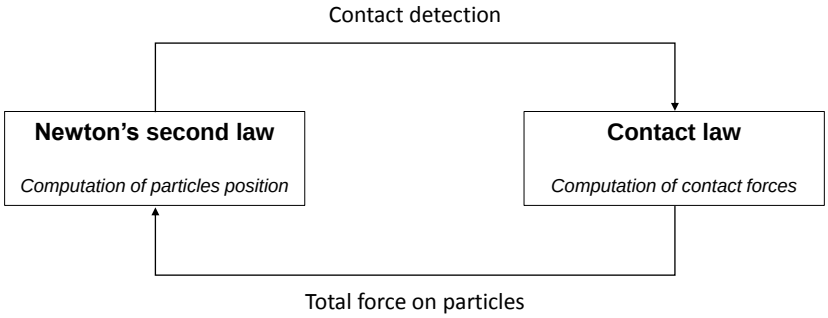


Figure 3.1: Scheme of a DEM cycle.

first-order centred finite difference scheme. Assuming that the accelerations are constant over the interval $t - \Delta t/2$, $t + \Delta t/2$, the velocities at time $t + \Delta t/2$ are given by:

$$\dot{x}_i^{[t+\Delta t/2]} = \dot{x}_i^{[t-\Delta t/2]} + \ddot{x}_i^{[t]} \Delta t \tag{3.3}$$

$$\omega_i^{[t+\Delta t/2]} = \omega_i^{[t-\Delta t/2]} + \dot{\omega}_i^{[t]} \Delta t \tag{3.4}$$

The position of the particle are finally computed at time $t + \Delta t$:

$$x_i^{[t+\Delta t]} = x_i^{[t-\Delta t]} + \dot{x}_i^{[t+\Delta t/2]} \Delta t \tag{3.5}$$

The updated positions of the particles are used to update the list of interactions (i.e. contact between bodies), then the new contact forces and so the force and moment acting on each particle can be computed. The updated values of $F_i^{t+\Delta t}$ and $M_i^{t+\Delta t}$ are used to compute the new accelerations, and these are used for the next cycle.

3.1.2 Contact law

A fundamental ingredient of a discrete element model is the definition of the contact law. This choice determines the information exchanged at the contact between two bodies (i.e microscopic behaviour) and so it will affect the macroscopic behaviour of the system. The contact force, in the case of a frictional interaction, can be decomposed into two components: one acting along the normal to the contact plane and the other acting onto the contact

plane. The definition of the contact forces is based on the assumption that the deformation at the contact can be schematised as a rigid interpenetration between the two particles in contact ("soft-contact" approach). The interpenetration δ_c is defined as reported in Fig. 3.2a. Using this approach the force components at the contact are described as function of the local geometry and of the contact stiffnesses k_n (normal) and k_t (tangential). A simple but widely adopted choice is to assume constant values for k_n and k_t as in the original method [29]. In cases in which a precise modelling of the contact interaction is needed more refined contact models can be used as, for instance, the Hertz-Mindlin [75] and the JKR [65] contact models.

In the original method [29], the normal component F_n of the contact force is given by:

$$F_n = k_n \delta_c \hat{\mathbf{n}} \tag{3.6}$$

where $\hat{\mathbf{n}}$ is the unit normal vector to the contact plane. The tangential component F_t is computed at each time step as a function of the increment of the relative tangential displacement Δu_s:

$$\Delta F_t = k_t \Delta u_s \hat{\mathbf{t}} \tag{3.7}$$

$$F_t^{[t]} = F_t^{[t-\Delta t]} + \Delta F_t^{[t]} \tag{3.8}$$

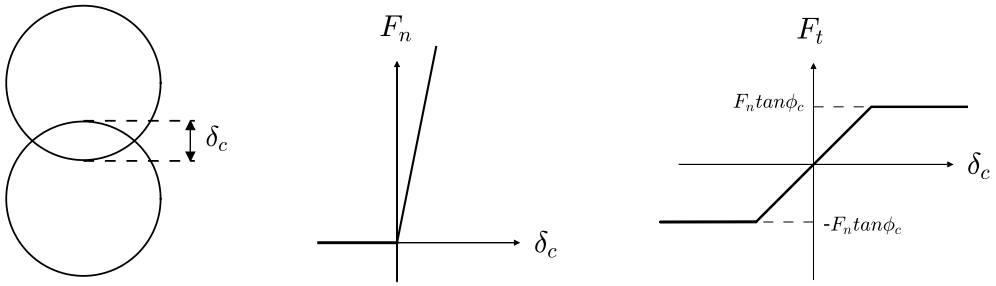
where $\hat{\mathbf{t}}$ is the unit tangential vector on the contact plane. A Coulomb plastic criterion is associated to the tangential contact as schematised in Fig. 3.2c. Therefore, an upper limit is imposed to the tangential contact force F_t, which is associated to the normal force F_n and the contact friction angle ϕ_c as given by:

$$\parallel F_t \parallel \leq F_n \tan \phi_c \tag{3.9}$$

A schematic representation of the contact model is reported in Fig. 3.2.

3.1.3 Time step

In the DEM an explicit scheme is used to find the solution at each time step. This implies that the integration time step Δt has to be smaller than a critical time step Δt_{cr} in order to avoid energy drifts and unphysical solutions caused by the numerical instability of the simulation. The critical time step is calculated considering the maximum eigenfrequency ω_{max} of the system. Considering a single degree of freedom system (i.e. single DEM particle),



(a) (b) (c)

Figure 3.2: (a) interpenetration between two grains. Contact model: (b) normal and (C) tangential interaction law.

the critical time step of the central difference integration scheme is given by:

$$\Delta t_{cr} = 2/\omega_{max} = 2\sqrt{m/K} \tag{3.10}$$

where m is the mass of the particle and K is the stiffness governing the particle's motion. Considering a generic assembly of particles, Itasca [62] defines a critical step idealising the system with an infinite series of point masses and springs, thus calculating the critical time step (the system is equivalent to a single mass-spring system with a stiffness equal to $4K$) as given by:

$$\Delta t_{cr} = \sqrt{m/K} \tag{3.11}$$

Moreover, Itasca suggests to apply a safety factor to the critical time step value and proposes a default value of 0.8. A more refined computation of the critical time step was proposed by O'Sullivan and Bray [81] considering regular dense packings (i.e. face-centred-cubic and rhombic packing) of homogeneous spheres (i.e. equal mass m and stiffness K) in an isotropic compression state. In these conditions, they shown that the critical time step proposed by Itasca [62] was unconservative, and proposed to adopt a critical time step $\Delta t_{cr} \leq 0.17\sqrt{m/K}$ for simulations involving uniform-sized spheres. For a generic assembly of spherical particles the critical time step has to be defined considering the minimum natural period obtained in the assembly. This condition is defined as given by:

$$\Delta t_{cr} = min\left(\sqrt{m_i^j/K_i^j}\right) \tag{3.12}$$

where K_i^j represents the equivalent stiffness (translational and rotational) computed considering all the real contacts of particle i, for each degrees of freedom j ($m_i^1 = m_i^2 = m_i^3 = m_i$, $m_i^4 = m_i^5 = m_i^6 = I_i$). Finally, a factor α ($\alpha < 1$) is applied to the critical time step, thus defining the simulation time step as a fraction of the critical one as given by:

$$\Delta t = \alpha \Delta t_{cr} \tag{3.13}$$

3.1.4 Non-viscous damping

A generic action applied to a particulate system will generate a wave inside the system itself. For waves of small amplitude, the system behaves in a purely elastic manner and therefore frictional effects may not be able to dissipate energy. In this condition, waves may continue to propagate indefinitely inside the system. In order to prevent this phenomenon, which may disturb the solution, damping can be introduced. The damping can be of different types. A first and common choice is to use a viscous damping at the level of particles contact; this will result in a further force (proportional to the rate of solicitation) which will be added to the elastic force. Alternatively, Cundall proposed a non-viscous damping [29] which acts on each particle and is not related to the solicitation rate. Considering the resultant force on a particle, this damping has the effect to reduce the force when it induces the particle motion and to increase the forces when it opposes to the particle motion. It should be noted that this damping is a purely numerical trick, then it is necessary to verify that it does not influence the results of the numerical calculation.

3.1.5 YADE DEM code

In this thesis the open-source discrete element code YADE [93] (*Yet Another Dynamic Engine*, `https://yade-dem.org`) is used. The computation parts of YADE are written in C++ using object-oriented programming, allowing independent implementation of new algorithms and interfaces. Python is used for rapid and concise scene construction, simulation control, postprocessing and debugging.

3.2 Discrete element modelling of wire meshes

The first works adopting the discrete element method for the study of steel wire mesh structures were carried out by Hearn et al. [60], and successively by Nicot et al. [78]. In these works the DEM was applied to study the dynamics of a flexible barrier impacted by a boulder. In the last two decades, the adoption of the DEM to the study of wire mesh structures has seen a large growth. More refined models have been implemented [10, 98] and they have been applied to analyse wire meshes in laboratory conditions [36, 42, 43] as well as in large scale applications. The dynamics of a single rock block impacting on wire mesh structures was studied in [11, 17, 26, 96]. Moreover, the impact of a dry granular flow on a flexible barrier was analysed in [1, 2], while an impacting debris flow (using a CFD-DEM coupled scheme) was considered in [66]. Only very recently, this approach was extended to the study of secured drapery systems in field conditions [44, 85, 105, 106]. The latter is also the main focus of the present thesis.

In a discrete elements framework, a wire mesh is generally represented by a regular pattern of bodies joined to each other or connected by long-range remote interactions. The force-displacement relationship between two connected mesh bodies is governed by a specific "contact" law. The latter is used to describe the mechanical behaviour of a mesh element as, for instance, a wire of the mesh. In this perspective, the contact law takes the meaning of a contact wire model. A detailed description of the existing contact wire models is reported in Sec. 3.2.1.

Different approaches can be used to represent a wire mesh in the framework of discrete element, depending on the combination of elementary particle types and on the pattern of remote interactions used to represent the mesh. They can be divided in:

- **Cell Based approach (CB)**: the mesh surface is described by spherical particles. Particles are connected by a specific geometrical pattern of remote interactions, which does not coincide with the real geometrical pattern of the wire elements, to reproduce the mechanical behaviour of the mesh (see Fig. 3.3a). The pattern of the interactions can be based on the geometry of a mesh elementary cell (e.g. a single ring of a ring net) or several mesh elementary cell (e.g. several connected rings of a ring net). This approach permits a minimal discretisation of the mesh structure improving the computational efficiency; however, the

interaction laws require a specific calibration. Furthermore, since the mesh geometry is, in general, not faithfully reproduced, this approach is not recommended in cases for which the geometrical details may have a strong influence (e.g. soil-inclusion problem, interaction of the mesh with external elements as selvedge/diagonal ropes). Examples of application of this approach can be found in [27, 78]

- **Node-Wire Based approach (NWB)**: the mesh surface is described by spherical particles placed at the physical nodes of the mesh (i.e. intersection between different wires). Particles are connected by a specific geometrical pattern of remote interactions, which coincides with the real geometrical pattern of the wire elements, to reproduce the mechanical behaviour of the mesh (see Fig. 3.3b). A remote interaction being related to a wire element, only a calibration of the mechanical behaviour of the wire is needed. This approach is detailed in Sec. 3.2.2. Examples of application of this approach can be found in [10, 44, 96, 98, 105].
- **Cylinder-Wire Based approach (CWB)**: the mesh surface is described by cylindrical particles. These cylindrical particles coincide with the real geometrical pattern of the wire elements, and can deform according to specific interaction laws reproducing the mechanical behaviour of the mesh (see Fig. 3.3c). An interaction being related to a wire element, only a calibration of the mechanical behaviour of the wire is needed. This approach is detailed in Sec. 3.2.3. Examples of application of this approach can be found in [2, 36, 85].

3.2.1 Contact wire model

The basic contact wire model is represented by the Elementary Wire Model (EWM) based on the work of Bertrand et al. [9] and implemented into YADE by Thoeni et al. [97]. The contact law is defined using a piece-wise linear force-displacement curve, in tensile direction, as reported in Fig. 3.4a. This curve is derived from an user-defined stress-strain relationship (e.g. experimentally derived) by using the specific wire diameter and the distance between the connected nodes (i.e. wire length). It should be noted that the wire diameter used in this step, represents a "contact parameter", and therefore can be defined independently of the nodal particle or the cylindrical particle diameter. The contact wire model is thus represented by

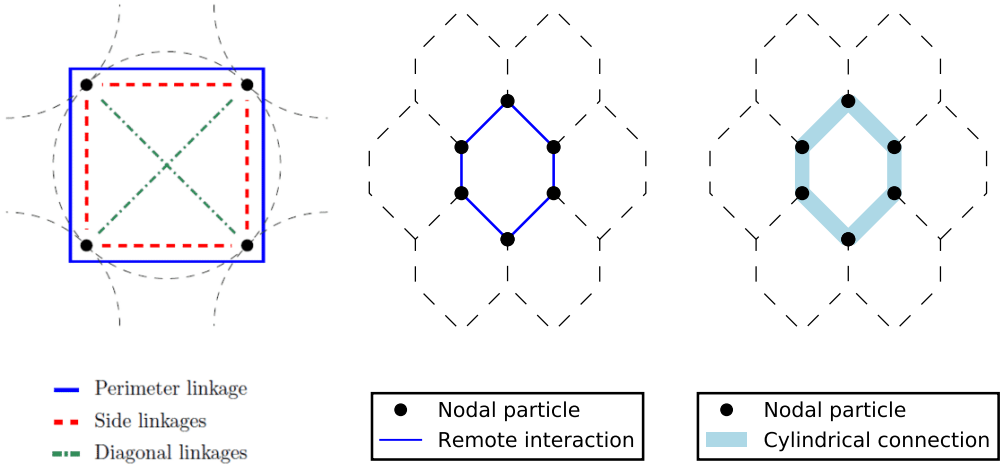
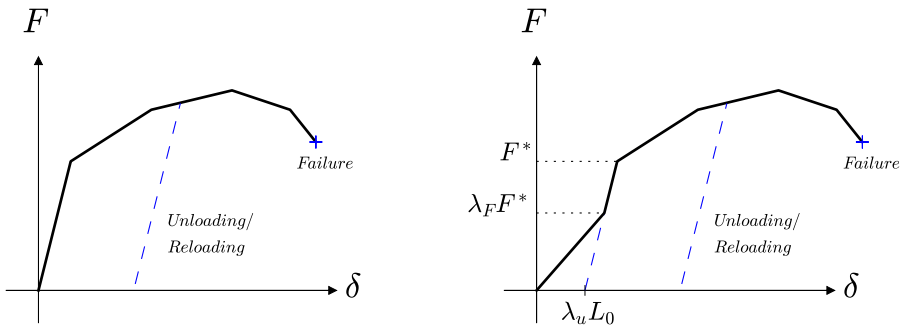


Figure 3.3: Graphical scheme of the modelling approaches: (a) CB (after [27]), (b) NWB and (c) CWB.

a force-displacement relationship. It considers normal tensile forces, while compressive forces are neglected because of their low magnitude related to the effect of buckling [9]. Unloading and reloading conditions are considered assuming a stiffness corresponding to the initial elastic stiffness (see Fig. 3.4). Finally, the interaction fails when the maximum admissible displacement is reached. A schematic representation of the EWM is reported in Fig. 3.4a. Different EWMs can be used in the same simulation in order to describe different wire types as, for instance, the single and double twisted wires that compose the commonly used hexagonal double twisted wire mesh. Hence, each wire is described by a specific force-displacement curve corresponding to its wire type. The EWM represents, in this sense, a deterministic contact wire model. It is worth mentioning that, for the hexagonal double twisted mesh type, a specific contact wire model which derives the contact law of the double twisted from the one used for the single wire has been defined in [9]. It is based on the definition of two local parameters λ_k and λ_ϵ acting on the initial stiffness and on the maximum deformation respectively. This model can be useful when a tensile characterisation of the double twisted wire is not available.

Starting from the EWM and considering that a physical mesh panel generally presents some distortions and irregularities (i.e. wires are not perfectly



(a) (b)

Figure 3.4: Contact wire models: (a) elementary wire model EWM and (b) stochastically distorted wire model SDWM (modified from [98]).

straight) Thoeni et al. [98] defined a stochastically distorted wire model (SDWM). In the SDWM these irregularities are accounted introducing two parameters:

- λ_u ($0 \leq \lambda_u \leq 1$) which defines a horizontal shift of the force-displacement curve.
- λ_F ($0 \leq \lambda_F \leq 1$) which modifies the stiffness of the wire in the shifted part.

The irregularities are randomly distributed on the mesh panel according to a triangular distribution with the average value equal to $0.5\lambda_u L_0$, where L_0 is the undistorted length of the considered wire. A schematic representation of the SDWM is reported in Fig. 3.4b.

3.2.2 Node-Wire Based modelling approach

In the NWB approach each physical node of the mesh is represented by a fictitious spherical particle that concentrates the mass of the related wires, while the wires are substituted by user-defined remote long-range tensile interactions (i.e. contact wire model in Sec. 3.2.1). This implies that the wires are not explicitly described in the numerical model, thus the contact with external bodies is handled only at the level of the nodal particles. The latter are treated as generic spherical elements when in contact with external elements. A simple example of the possible interaction between a wire element

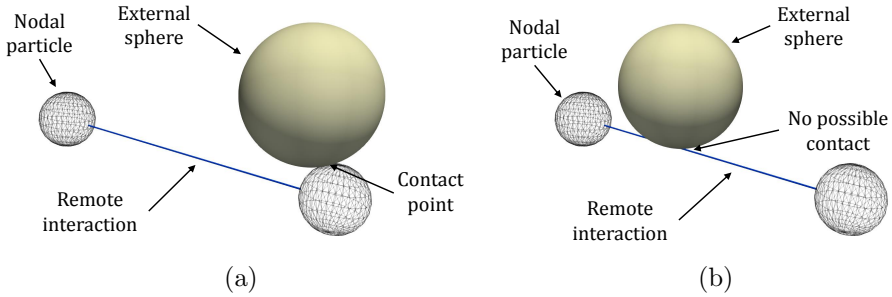


Figure 3.5: Example of interaction between a numerical wire (NWB approach) and an external sphere: (a) contact is detected, (b) contact is not detected.

described with the NWB approach and an external sphere is reported in Fig. 3.5 for the sake of clarity. The density of the nodal particles is calibrated to match the total mass of the mesh panel, thus the inertial properties of the mesh are correctly conserved permitting dynamic problems such as impacts to be analysed. It should be noted that, the wire contact model being independent of the dimension of the nodal spheres, the latter can be arbitrarily defined permitting one to optimise the computational time. The adoption of the NWB approach permits a reduction the computational effort in terms of contact detection and rigid body dynamic as it will be shown in Sec. 3.4. However, in some cases, the interaction between the wires surface and external elements may be relevant, and a more refined mesh description, as the one obtained with the CWB approach, should be preferred.

3.2.3 Cylinder-Wire Based modelling approach

The CWB approach is based on a special cylindrical discrete element developed by Bourrier et al. [16] for simulating plant roots, and successively extended by Effeindzourou et al. [35] for modelling mesh-like structures. Recently, it was applied to wire mesh structures [2,36,85]. A cylindrical element can be seen as a classical discrete element, but it can deform along its longitudinal direction according to a specific contact law. Cylinders can be combined together permitting the representation of any geometrical shape of mesh-like structure. The cylindrical element is defined as the Minkowski sum of a sphere and a segment [16, 35]; this permits the cost of the contact

detection to be kept low thanks to the simplicity of the elements representation. Furthermore, this description does not introduce any numerical roughness [1, 35]. A detailed description of the interaction between a cylindrical element and a spherical element, and between two cylindrical elements is reported afterwards. In the CWB approach, the wire mesh is therefore represented as a connection of cylindrical elements. Each cylinder (referred as "gridConnection" in YADE) connects two spherical particles (referred as "gridNode" in YADE) that are placed in correspondence of the physical nodes of the mesh. Thus, each mesh wire is described by using a cylindrical element (an exception is represented by meshes composed of complex elementary elements as, for instance, a ring net for which many cylinders may be used to discretise a single ring). The deformation of a cylinder is determined starting from the position and orientation of the nodes. The interaction between the nodes is ruled by a user-defined tensile interaction (i.e. contact wire model of Sec. 3.2.1). In this perspective, the CWB approach can be seen as an extension of the NWB one. In fact, the mechanical behaviour of the mesh is determined by the nodal interactions in both approaches. The enhancement introduced with the CWB is related to the more detailed description of the mesh physical shape, which allows the contact with external bodies to be handled also along the wires surface. This possibility may be of great importance when dealing with complex mesh-soil interaction problems or when other elements are superimposed over the mesh (e.g. high-resistance external ropes).

Sphere-Cylinder interaction

The sphere-cylinder interaction defines the interaction between an external spherical body (e.g. soil grain, rock block) and a cylinder belonging to the mesh (e.g. mesh wire). The contact mechanics is addressed using a virtual sphere, with the same radius of the cylinder, centred at the projection of the contact point on the segment connecting the nodes of the cylinder. A graphical example is reported in Fig. 3.6a for the sake of clarity. The displacement of the cylinder's body is assumed to vary in a linear manner between its nodes. Translational and rotational velocities of the virtual sphere are interpolated between the cylinder's nodes, and forces and moments are distributed to the cylinder's nodes. The normal and tangential forces acting at the sphere-cylinder contact can be computed using equations (3.6) and

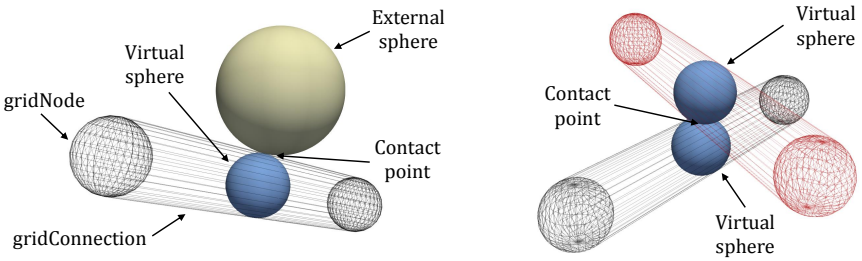


Figure 3.6: Example of interaction between: (a) a numerical wire (CWB approach) and an external sphere, (b) two numerical wires (CWB approach).

(3.7). The normal k_n and tangential k_t stiffness are defined as follow:

$$k_n = 2\frac{E_s r_s E_c r_c}{E_s r_s + E_c r_c} \tag{3.14}$$

$$k_t = \nu k_n \tag{3.15}$$

where E_s and E_c represent the micromechanical elastic moduli and r_s and r_c represent the radii of the sphere and of the cylinder respectively. The contact parameter ν represents the tangent to normal stiffness coefficient.

Cylinder-Cylinder interaction

The cylinder-cylinder interaction defines the interaction between a mesh element and an external cylindrical element in contact with the mesh as, for instance, external ropes (also the interaction between mesh wires, however this interaction is extremely unlikely, in well-posed boundary problems, before the mesh failure). Let us consider two generic cylinders C_1 and C_2 and their extremities nodes $N_0^{C_1}$, $N_1^{C_1}$ and $N_0^{C_2}$, $N_1^{C_2}$ as represented in Fig. 3.7. The cylinders could be represented by the segments A and B, A and B being defined as follows:

$$A = \| \, N_0^{C_1} N_1^{C_1} \, \| \tag{3.16}$$

$$B = \| \, N_0^{C_2} N_1^{C_2} \, \| \tag{3.17}$$

The parametric equations of segments A and B are given by [35]:

$$A(s) = N_0^{C_1} + s\hat{\mathbf{a}} \qquad \forall s \in [0,1] \tag{3.18}$$

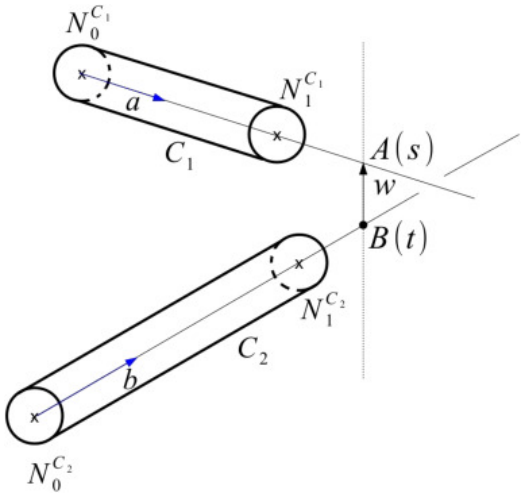


Figure 3.7: Distance between two cylinders (after [35]).

$$B(t) = N_0^{C_2} + t\hat{\mathbf{b}} \qquad \forall t \in [0,1] \tag{3.19}$$

where $\hat{\mathbf{a}}$ and $\hat{\mathbf{b}}$ are the unit vectors of the segment A and B direction respectively. If the two cylinders are in contact, the vector w at the contact point is defined as:

$$w_c = \min_{(s,t)\in[0,1]\times[0,1]} w(s,t) = w(s_c,t_c) = A(s_c) - B(t_c) \tag{3.20}$$

For A and B neither parallel nor intersecting each other, the segment w_c is uniquely perpendicular to the unit direction vectors $\hat{\mathbf{a}}$ and $\hat{\mathbf{b}}$, thus it can be written:

$$\begin{cases} w_c = A(s_c) - B(t_c) \\ \hat{\mathbf{a}} \cdot w_c = 0 \\ \hat{\mathbf{b}} \cdot w_c = 0 \end{cases} \tag{3.21}$$

and the solution of Eq. 3.21 is given by:

$$\begin{cases} s_c &= \frac{(\hat{\mathbf{a}}\cdot\hat{\mathbf{b}})(\hat{\mathbf{b}}\cdot w_0) - \|\hat{\mathbf{b}}\|(\hat{\mathbf{a}}\cdot w_0)}{\|\hat{\mathbf{a}}\|\|\hat{\mathbf{b}}\| - (\hat{\mathbf{a}}\cdot\hat{\mathbf{b}})^2} \\ t_c &= \frac{\|\hat{\mathbf{a}}\|(\hat{\mathbf{b}}\cdot w_0) - (\hat{\mathbf{a}}\cdot\hat{\mathbf{b}})(\hat{\mathbf{a}}\cdot w_0)}{\|\hat{\mathbf{a}}\|\|\hat{\mathbf{b}}\| - (\hat{\mathbf{a}}\cdot\hat{\mathbf{b}})^2} \end{cases} \tag{3.22}$$

where $w_0 = N_0^{C_1}$, $N_0^{C_2}$. The contact is then treated associating a virtual sphere to each cylinder at the contact point. A graphical example is reported

in Fig. 3.6b for the sake of clarity. The contact laws are formally identical to the ones used for the sphere-cylinder interaction.

3.3 Validation of the mesh numerical model

In this paragraph the numerical predictions obtained from the discrete element mesh models are compared against the results of the experimental tests presented in Chapter 2. The stress-strain relationships used as input in numerical model to characterise the EWMs of the different types of the elements of the mesh, namely the single wire (SW), the double twisted wire (DT) and the high resistance steel rope, are reported in Fig. 3.8. The stress-strain curves of the SW and the DT wires are taken from [98], while the one characteristic of the high resistance steel rope has been provided by Maccaferri Innovation Center. It is worth noting that in the numerical model the experimental relationships are introduced as deterministic curves, thus a numerical calibration of the wire contact parameters is, in general, not needed (this is true when a fully deterministic model as the EWM is used for describing the numerical wires). For the validation of the numerical model of the mesh the NWB approach was used. A scheme of the numerical representation of an elementary cell of the mesh is reported in Fig. 3.12. The NWB approach allows optimisation of the time-efficiency of the simulation with any differences in terms of mechanical behaviour of the mesh, if compared to a more refined approach as the CWB [43]. This aspect will be discussed in detail in Sec. 3.4, where a comparison between the NWB and CWB will be reported. In the following, the validation of the numerical models of the 8x10 double-twisted hexagonal mesh (DT), and of the prototype meshes MT1 and MT2 are presented.

3.3.1 Punch test on DT mesh

The standard UNI punch test configuration (described in details in Chapter 2) is chosen for a first validation of the discrete element model of the DT mesh. This test represents a complex loading condition in the sense that it permits the reaction of the mesh to an out-of-plane loading condition to be evaluated; therefore it is well adapted to analyse if the mesh mechanical behaviour is correctly reproduced by the model (tensile curves are the only input data). The geometry of the standard UNI punch test is faithfully re-

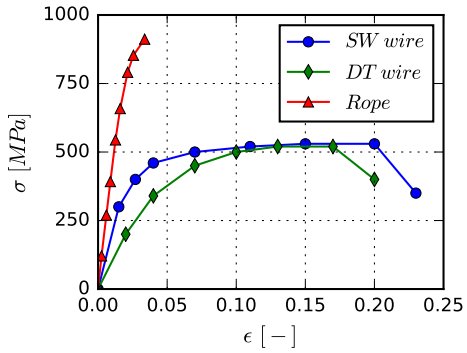
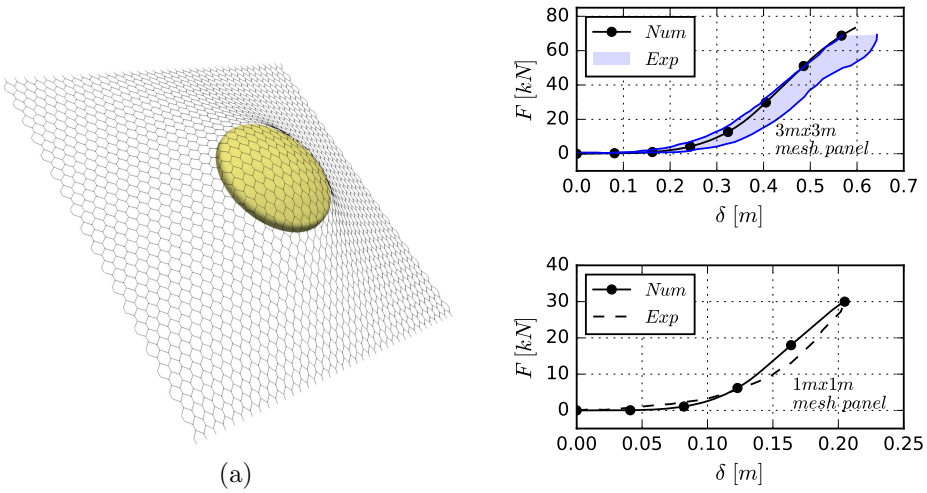


Figure 3.8: Stress-strain tensile relationships used for the definition of the EWM for the different elements of the mesh, namely the single wire (SW) the double twisted wire (DT) and the high resistance steel rope.

produced in the numerical model. A 8×10 DT hexagonal wire mesh with a nominal diameter of 2.7mm (i.e. diameter of the single wires) is considered. The 3m×3m mesh panel is described by using 2890 spherical particles ($\approx$ 322 particles/m^2), and its four edges are fixed by blocking all the degrees of freedom of the nodal spheres that belongs to the mesh boundary. In the model the particles diameter is set equal to $d_w = 10.8$mm which corresponds to four times the one of the single wires. This entails a benefit in the computational time without influencing the mechanical response of the mesh. Their density is thus adjusted in order to maintain the inertial properties of the mesh panel (≈ 1.43kg/m^2). The punching element is described by using 694 triangular elements (Facets). A 3D view of the numerical model during the test is shown in Fig. 3.9a. Following the experimental test procedure, the punching element is moved with a constant velocity; in the model this velocity is set equal to 0.1m/s (in the experimental the velocity has to be < 0.01m/s) to optimise the computational cost of the simulation (no difference in the results were observed increasing the punch velocity with respect to the experimental one). The numerical parameters for the punch-mesh contact used in this study are $k_n = 6.5 \cdot 10^5$N/m, $k_t = 0.3k_n$, and a frictionless contact (i.e. $\phi_c = 0$). It should be noted that these parameters have a negligible effect on the numerical results, being the problem controlled by the tensile behaviour of the mesh (this aspect will be further discussed in Chapter 4). Finally, the time step is set equal to $dt = 3 \cdot 10^{-5}$s which respects the



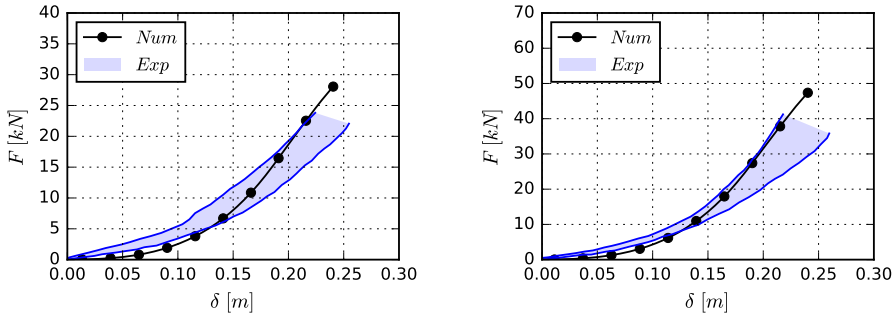
(a)

(b)

Figure 3.9: (a) 3D view of the numerical model of the punch test on the 3m side mesh panel. (b) Comparison between experimental and numerical results with reference to the 3m×3m and the 1m×1m panels respectively.

stability condition proposed in [10]. The thrust force and the punching element displacement are measured during the simulation providing as output a force-displacement curve. The numerical results are reported in Fig. 3.9b; the numerical predictions are in good agreement with the experimental data, showing the capability of the model to correctly reproduce the mechanical behaviour of the mesh.

In order to evaluate if the mesh model is able to reproduce scale effects, a "reduced version" of the standard UNI punch test is considered. In this case the mesh panel has a dimension of 1m×1m and the diameter of the punching element is equal to 0.33m (i.e. the problem "dimension" is scaled by a factor of three). The same numerical parameters as before are used. Also in this case a good agreement between experimental and numerical results is obtained as reported in Fig. 3.9b confirming the effectiveness of the mesh model. The mechanical behaviour of a wire mesh panel in punching condition is worth of interest, thus it will be analysed in details in Chapter 4.



(a) (b)

Figure 3.10: Comparison between experimental and numerical results of the punch test with the square anchor plate: (a) 3.0mm wire mesh and (b) 3.9mm wire mesh.

3.3.2 Anchor punch test on DT mesh

After the validation against the results of the standard UNI punch test, a different punch test configuration, in which a 250mm side square anchor plate is used as punching element, is considered. The test is conducted for two mesh panels, characterised by a nominal wire diameter of 3.0mm and 3.9mm. The details of these tests have been already reported in Chapter 2. The test geometry (i.e. anchor and mesh panel) is faithfully reproduced in the numerical model. The mesh panel (1.68m×1.56m in the model) is described by using 862 spherical particles and it is fixed along the outer boundary by blocking all the degrees of freedom of the nodal spheres that belongs to the mesh boundary. The punching element is schematised by using 12 triangular elements and it is moved with a constant velocity equal to 0.02m/s. The numerical results are reported in Fig. 3.10a and in Fig. 3.10b for the 3.0mm and 3.9mm mesh respectively. The numerical mesh shows a slightly stiffer response and a bit higher maximum resistance than in the experimental characterisation. These differences may be due to imperfections in the real mesh and to a local cutting of the wires in correspondence to the anchor plate edges in the experimental test. However, the numerical predictions are globally in good agreement with the experimental data confirming again the validity of the numerical model.

In Fig. 3.11 a 3D view and the lateral views of the mesh panel an instant

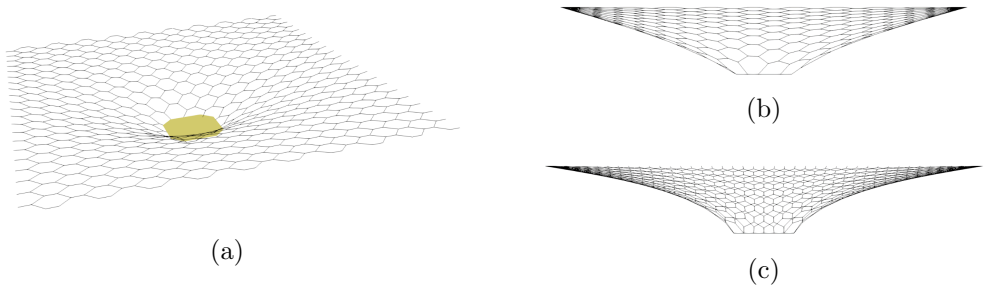
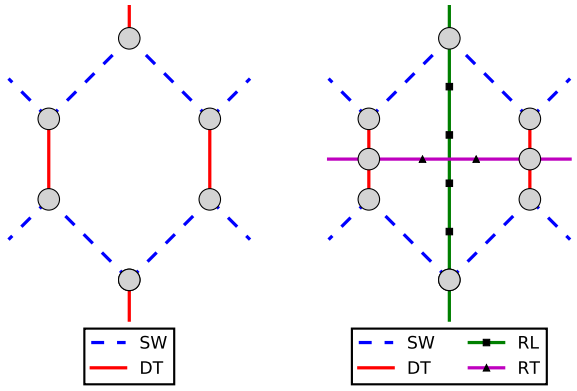


Figure 3.11: (a) 3D View of the numerical model of the anchor punch test (3.0mm case) and lateral view in the direction (b) orthogonal to the DT wire, and (c) parallel to the DT wire

prior to the failure are reported. It is worth noting that the deformation of the mesh panel is not the same for the two considered directions, namely the directions parallel and orthogonal with respect to the double twisted wires. This highlights the intrinsic anisotropy of the DT mesh that derives from the geometry of the hexagonal elementary cell and the different mechanical behaviour of the two wire types. The anisotropy of DT mesh will be analysed in details in Chapter 4.

3.3.3 Tensile test on MT1 and MT2 meshes

The results of the tensile test campaign reported in Chapter 2 are used for a first validation of the numerical model of the MT1 and MT2 mesh types. The numerical description of these mesh types, starting from the DT mesh model, is very straightforward. Some further nodal particles are created where the DT mesh is intercepted by the transversal ropes (i.e. at the middle point of some of double twisted wires), and the particles belonging to the high resistance steel ropes are connected between them, thus defining the interactions that simulate the ropes (longitudinal ropes RL and transversal rope RT) in the model as schematised in Fig. 3.12b. All the panels are composed of a 2.7mm DT mesh and have steel ropes of 8mm of diameter. Following the experimental nomenclature, the first capital letter indicates the direction of the applied tensile action, the second one the type of tested mesh panel, namely L for the MT1 mesh and T for the MT2 mesh. For instance, the test LT refers to a tensile test in which the traction is applied along the longitudinal direction (i.e. direction of the double twisted wire

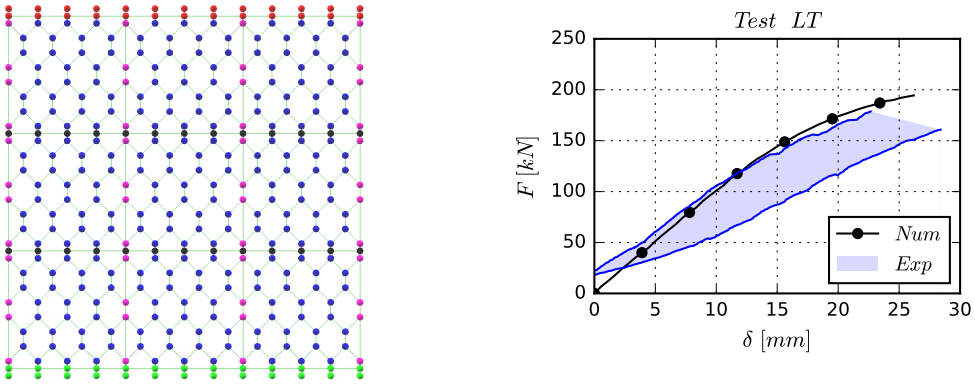


(a) (b)

Figure 3.12: Graphical scheme of an elementary cell: (a) DT mesh and (b) MT2 mesh (or the MT1 mesh if interactions RT are removed).

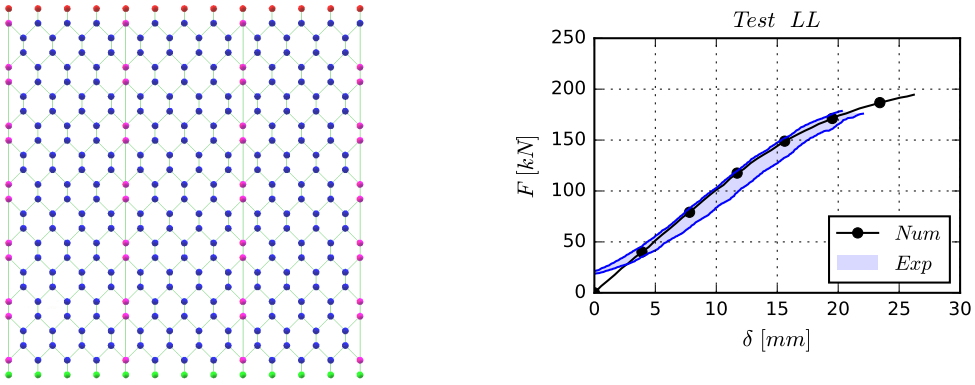
or equivalently of the longitudinal ropes) and considering a mesh panel of the MT2 type. The dimension of the panels used in the experimental tests (0.96m×0.96m) is reproduced with a very low discrepancy related to the periodicity of the model (0.96m×1.00m, 326 spherical particles were used for the MT1 and 378 for the MT2 mesh panels). To reproduce the experimental test, particles belonging to a panel's side are fixed (green particles in views of the models presented hereafter) and the ones belonging to the opposite panel's side are moved with a constant velocity of 0.05m/s (red particles in views of the models presented hereafter). The time step is set equal to $dt = 1 \cdot 10^{-6}$s. In the experimental procedure a pretension was applied to the mesh panels in order to minimise the initial irregularities and distortions. This phase is not necessary in the numerical model, the initial geometry being perfect in the model.

The comparison between experimental and numerical results are reported in Fig. 3.13, 3.14, 3.15, as well as a view of the related numerical models. The experimental and numerical values of the tensile force and displacement at failure are also reported in Tab. 3.1 in order to ease comparison. Some discrepancies between the numerical predictions and the experimental data exist. The difference in terms of maximum tensile strength is between 6% and 15%, between 6% and 27% in terms of maximum displacement (in both cases the model provides higher values). However, it should be considered that small discrepancies in the ropes length (always present in real panels)



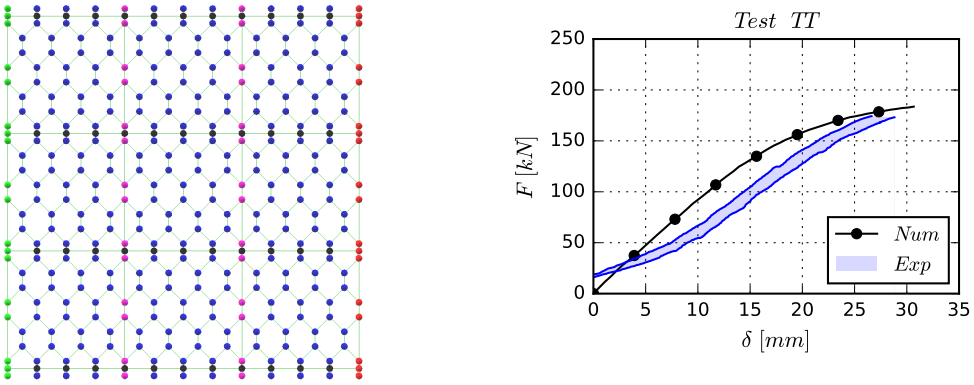
(a) (b)

Figure 3.13: Test LT: (a) view of the model and (b) comparison between numerical and experimental results.



(a) (b)

Figure 3.14: Test LL: (a) view of the model and (b) comparison between numerical and experimental results.



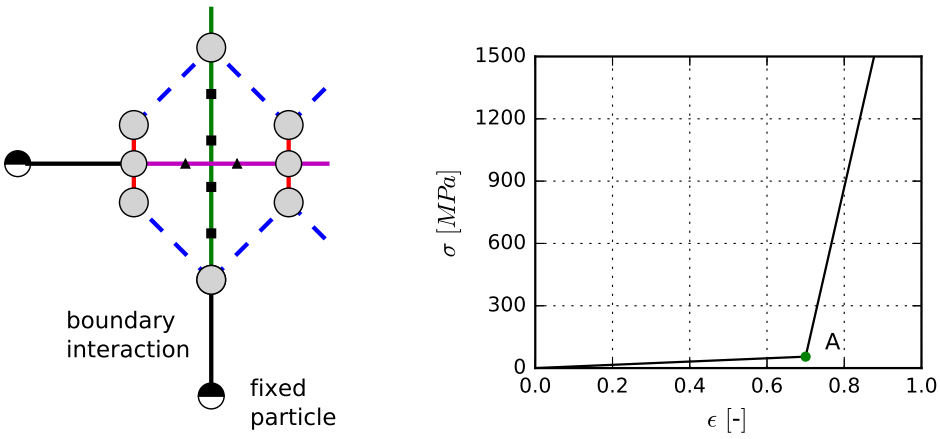
(a) (b)

Figure 3.15: Test TT: (a) view of the model and (b) comparison between numerical and experimental results.

Test	Exp		Num	
	F_{max} [kN]	δ_{max} [mm]	F_{max} [kN]	δ_{max} [mm]
LT	169.8	24.8	194.4	26.2
LL	177.9	20.6	194.5	26.2
TT	172.3	27.3	183.6	30.6

Table 3.1: Comparison between experimental (mean values) and numerical results of the tensile test.

may influence the results of tensile test leading to a different redistribution of the tensile load on the different ropes. This translates in a slight reduction of the theoretical maximum resistance. Thus, the ropes length being exactly the same for all ropes in the numerical model, the deriving mechanical characterisation of the mesh panel has to be seen as an upper bound of the mesh tensile strength. In this perspective, a global agreement, both in terms of tensile stiffness a maximum tensile strength, can be observed between experimental and numerical results.

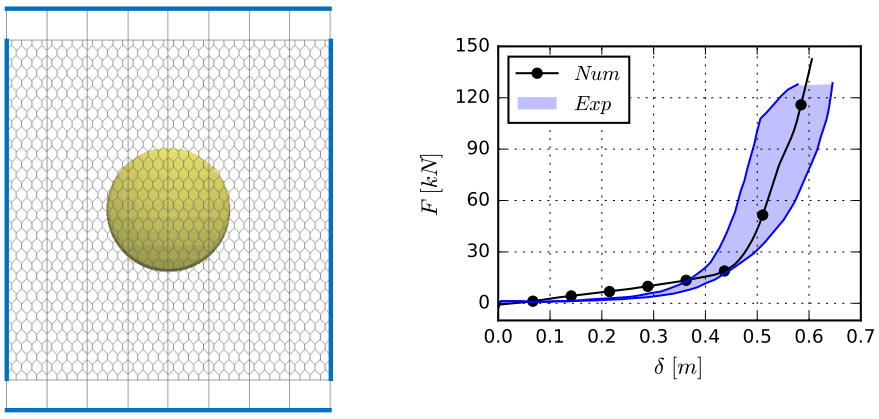


(a) (b)

Figure 3.16: (a) Graphical scheme of an elementary cell on the mesh boundary with the boundary interactions. (b) Stress-strain relationship of the interactions representing the "soft connection" at the ropes' extremities in the numerical model.

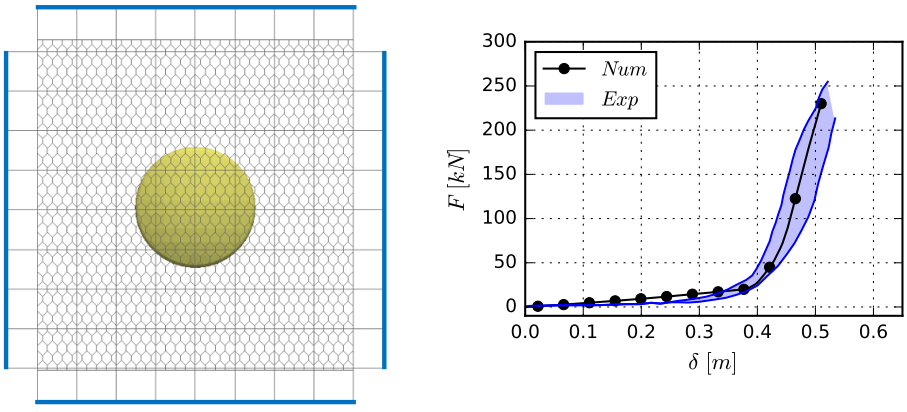
3.3.4 Punch test on MT1 and MT2 meshes

Finally, the punch test campaign on the MT1 and MT2 mesh types, presented in Chapter 2, is numerically simulated. The geometry of the mesh panels is faithfully reproduced in the models: the panels have a dimension of 2.56m×2.68m, and 9 high resistance ropes are considered in the longitudinal direction (for the MT1 mesh type) and both in longitudinal and transversal directions (for the MT2 mesh type). For the numerical description of the mesh 2212 spherical particles, of diameter equal to 10.8mm, are used. All the panels are composed of a 2.7mm DT mesh and have steel ropes of 8mm of diameter. The punching element is the same used for the DT mesh (see Sec. 3.3.1) and is moved with a constant velocity of 0.1m/s during the simulation. The time step is set equal to $dt = 1 \cdot 10^{-6}$s. In the experimental tests, the mesh panels were fixed to the rigid frame looping a rope on a bordering cable connected to the ropes of the mesh panel (see Chapter 2). This particular boundary condition ("soft connection") is simulated in the model by creating specific interactions between the extremities of the ropes and some fixed external particles, the latter representing the rigid frame, as



(a) (b)

Figure 3.17: (a) View of the numerical model (blue thick lines represent the fixed boundary) and (b) numerical results for the MT1 mesh type.



(a) (b)

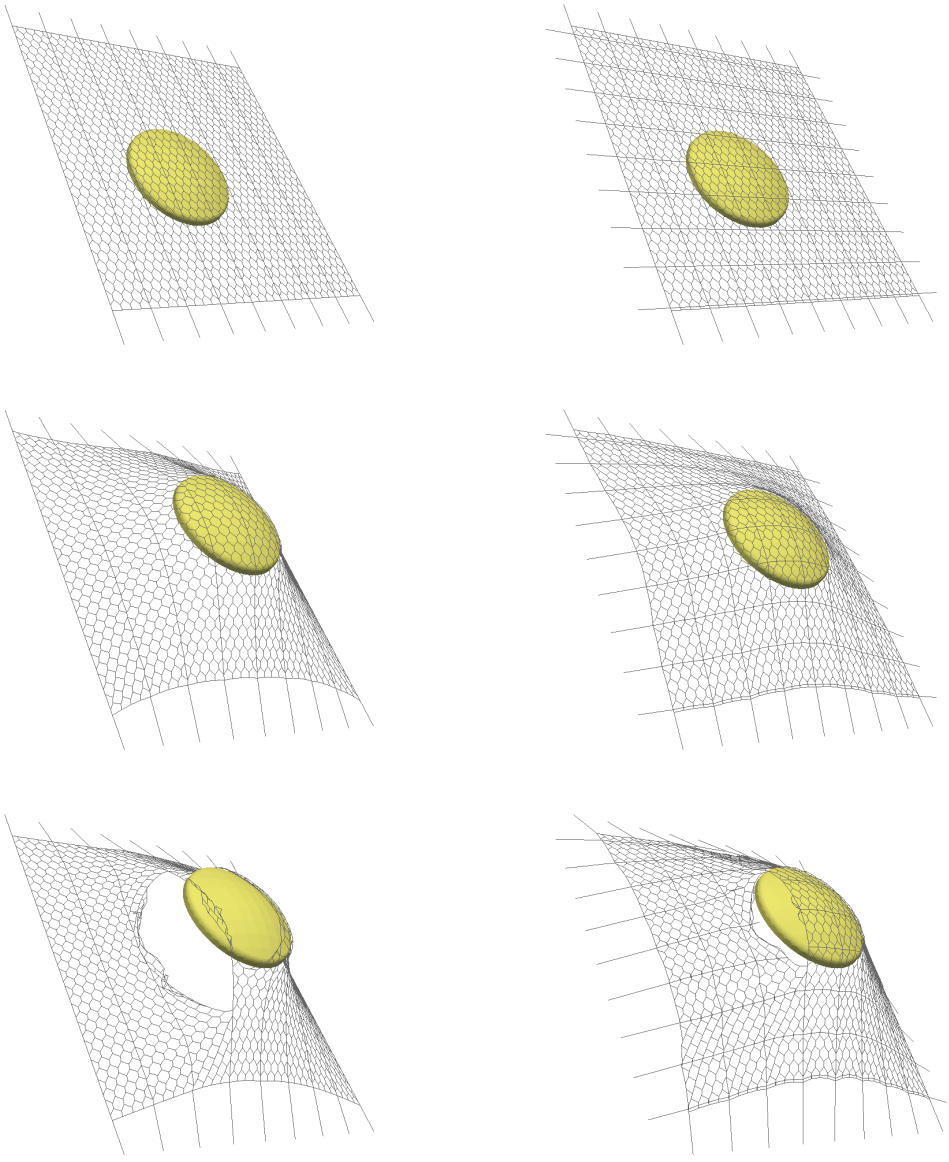
Figure 3.18: (a) View of the numerical model (blue thick lines represent the fixed boundary) and (b) numerical results for the MT2 mesh type.

Mesh type	Exp			Num	
	F_{max} [kN]	δ_{tot} [m]	δ [m]†	F_{max} [kN]	δ [m]†
MT1	128.2	0.83	0.61	143.6	0.60
MT2	233.0	0.87	0.53	239.4	0.51

† Corrected in order to account for the "soft connection" displacement δ_b

Table 3.2: Comparison between experimental (mean values) and numerical results of the punch test.

schematically reported in Fig. 3.16a. These interactions are mechanically described by the bi-linear stress-strain curve reported in Fig. 3.16. The bi-linear relationship aims to represent the low bending stiffness and the geometrical distortion/elongation of the loops in the first phase (i.e. low stiffness), then a material-based tensile stiffness in the second part of the test (i.e. high stiffness). Any limit is imposed to the maximum elongation for these interactions (i.e. line in Fig. 3.16 is not limited), thus they cannot break. The length of these interactions is set equal to 25cm, which is approximately equal to the distance between the mesh boundaries and the rigid frame in the experimental tests. The parameters defining the stress-strain curve of these boundary interactions are calibrated in order to fit the results of the experimental punch test on the MT2 mesh type. The point A in Fig. 3.16b is defined to fit the first part of the force-displacement curve ("geometric response"), while the stiffness of the second branch to fit the second part of the force-displacement curve ("material response"). The same values are used in the simulation of the MT1 mesh type. Following what has been done in the experimental characterisation, the displacement related to the "soft connection" δ_b (i.e. boundary ropes) is subtracted from the total displacement δ_{tot}. The displacement δ thus obtained represents the differential displacement between the mesh boundary and the mesh centre. The mean values of δ_b obtained in the model (0.23m for the MT1 mesh type, 0.33m for the MT2 mesh type) are applied to the numerical results. The comparison of the numerical predictions and the experimental measurements, reported in Fig. 3.17b and Fig. 3.18b, shows a good agreement between them. The force and displacement values at failure are also reported in Tab. 3.2 in order to ease comparison. In Fig. 3.19 3D views of the numerical model at different temporal steps of the simulation are reported for both mesh types.



(a) (b)

Figure 3.19: 3D views of the numerical punch test: (a) MT1 mesh type and (b) MT2 mesh type.

3.4 Comparison of the NWB and CWB modelling approaches

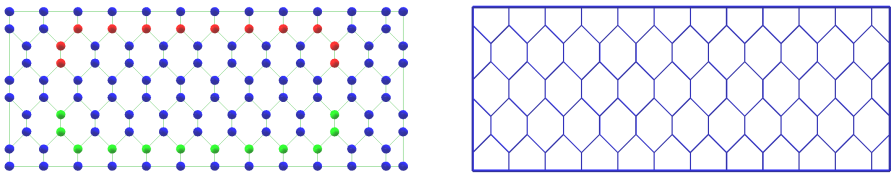
In this thesis, both the NWB and the CWB approaches are used. It is therefore useful to clarify when the NWB may be sufficient, and when a more refined approach, as the CWB, would be preferable. In this perspective, a comparison between these two approaches is reported in the following. Simple test configurations are used to analyse if differences exist, both in terms of mechanical behaviour of the mesh and/or in terms of interaction with external bodies. Finally, The computational cost of the two approaches is investigated. In this perspective, a fixed number of DEM cycles (function of the test configuration) was run for both the approaches and the time required by each phase of the DEM cycle was registered. These phases are:

- **ForceResetter**: reset forces on particles from the previous step
- **InsertionSortCollider**: approximate contact detection and update/ generation of the interactions (real and non-real)
- **InteractionLoop**: precise contact detection and computation of contact forces
- **NewtonIntegrator**: integration of Newton's laws of motion and update of the particles' position

For the sake of clarity the same terminology used in YADE was here adopted (for more detailed information one can refer directly to [93]).

3.4.1 Tensile Test

The first configuration adopted for comparing the NWB and the CWB approaches is the standard UNI tensile test [99]. A rectangular mesh panel of dimensions 92cm×36cm is used. The mesh panel is described by using 122 bodies in the NWB and 312 bodies (122 gridNodes, 156 gridConnections) in the CWB approach. In both cases, the diameter of the nodal particles is equal to 2.7mm, namely the diameter of a single wire. The boundary conditions typical of the test are applied by blocking the degrees of freedom of the nodal particles. The numerical mesh models are reported in Fig. 3.20. The particles ideally intercepted by the lower hooks are fixed (i.e. green particles in Fig. 3.20a), while a constant velocity, equal to 10mm/s, is imposed to the particles ideally intercepted by the upper hooks (i.e. red particles in Fig. 3.20a). The mechanical response of a mesh panel in tensile test



(a) (b)

Figure 3.20: View of the numerical model: (a) NWB and (b) CWB approach.

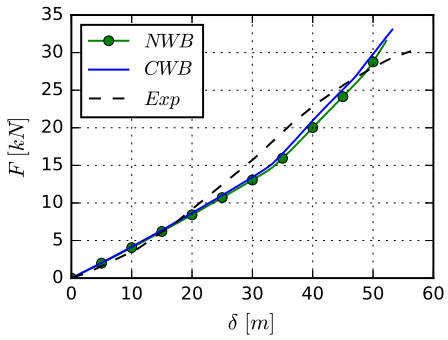


Figure 3.21: Comparison of the numerical result of the tensile test in terms of force-displacement curve (the dashed line represents the experimental results after [98]).

conditions is strongly affected by initial deformations of the wires and the hexagonal cells. In the numerical model, the initial mesh geometry being perfectly regular (i.e. wires are undistorted), this randomness is inserted into the constitutive relationships of the wires. The stochastically distorted wire model (SDWM), introduced in Sec. 3.2.1 is therefore used in this case. The values of the SDWM stochastic parameters used in the simulations are $\lambda_F = 1.0$ and $\lambda_u = 0.2$. Details about the numerical calibration of the SDWM parameters can be found in [98]. The numerical time step is set equal to $dt = 1.3 \cdot 10^{-6}$s which satisfies the stability condition for the integration scheme proposed by Bertrand et al. [10]. The results in terms of force-displacement curves are reported in Fig. 3.21, where the experimental data are taken from [98]. The mechanical response obtained by using the two approaches appears very similar. The slight discrepancy is compatible with the intrinsic randomness of the stochastic model. In fact, using the

DEM phases	NWB		CWB	
	t [s]	t_{rel} [s]	t [s]	t_{rel} [s]
ForceResetter	0.344	2.16%	0.779	2.58%
InsertionSortCollider	0.006	0.04%	0.139	0.46%
InteractionLoop	10.152	63.72%	20.064	66.50%
NewtonIntegrator	5.430	34.08%	9.191	30.46%
Total	15.993	100%	30.173	100%

Table 3.3: Time statistics of the tensile test.

deterministic model for the numerical wires no differences are observed as reported in [43].

In order to compare the computational cost of the two approaches the time statistics obtained running 350000 steps are reported in Table 3.3. The relative computational time of the different phases of the DEM algorithm is roughly the same for the two approaches. The total time instead is approximately 1.9 times higher for the CWB ($t_{NWB} = 15.93$s and $t_{CWB} = 30.17$s). In this case the contact with external bodies is not considered, therefore the difference between the NWB and the CWB is only related to the greater number of bodies required by the CWB approach.

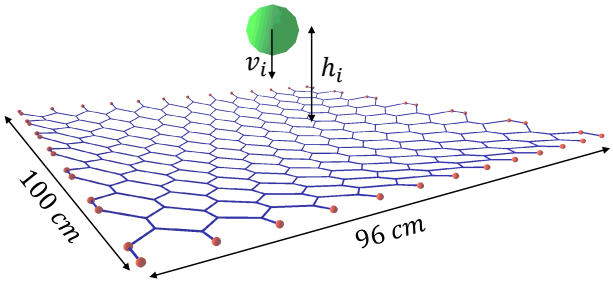
3.4.2 Drop Test

A simple test in which a dropping sphere interacts with the mesh is considered. A rectangular mesh panel of dimensions 96cm×100cm is used. It is numerically described by using 326 bodies in the NWB and 777 bodies (326 gridNodes, 451 gridConnections) in the CWB approach. In both cases, the diameter of the nodal particles is equal to 2.7mm. The mesh panel is fixed along its outer boundary. The mesh panel is characterised by the same total mass in the two approaches ($m \approx 1.43$kg). The numerical time step is set equal to $dt = 1.3 \cdot 10^{-6}$s. A sphere of density $\rho = 1500\text{kg/m}^3$ is placed in correspondence with the centre of the mesh panel at an initial height from the mesh panel of $h_i = 22.5$cm. Different diameters $d_s = 8, 9, 12, 16$cm of the sphere are used. In order to keep constant the impact energy, a initial velocity $v_i = \sqrt{\frac{2}{m}(E^* - mgh_i)}$ is imposed to the dropping sphere for the cases in

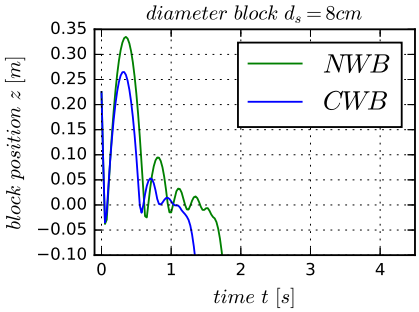
DEM phases	NWB		CWB	
	t [s]	t_{rel} [s]	t [s]	t_{rel} [s]
ForceResetter	4.635	2.17%	10.091	2.49%
InsertionSortCollider	1.583	0.74%	4.524	1.12%
InteractionLoop	141.580	66.32%	277.835	68.51%
NewtonIntegrator	65.682	30.77%	113.119	27.89%
Total	213.481	100%	405.569	100%

Table 3.4: Time statistics of the drop test.

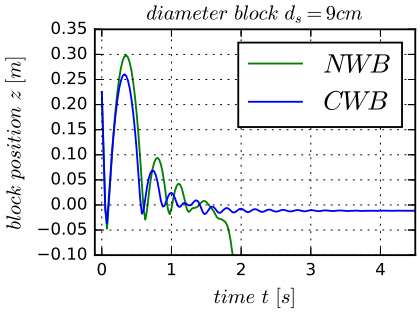
which $d_s < 16$cm. A 3D view of the model (CWB approach) is reported in Fig. 3.22a for a sake of clarity. As reported in Sec. 3.2.1 the mesh model accounts only for tensile forces, however during an impact energy is dissipated also through bending of the wires. An additional source of energy dissipation is therefore added to the model considering a non-viscous local damping (Sec. 3.1.4). As proposed by Thoeni et al. in [98], the damping force term is applied only to the mesh particles, while the block remains unaffected. The damping coefficient used in the numerical damping scheme of YADE [93] is set equal to $\lambda_d = 0.5$ in analogy with [98]. The evolution of the vertical position z of the sphere as a function of time is used to compare the two approaches. The numerical results reported in Fig. 3.22 show that there is a significant difference between the two approaches for the cases characterised by $d_s \leq 9cm$. In the case of $d_s = 9$cm (see Fig. 3.22c), it is worth noting that the sphere falls into a mesh hole (i.e. mesh cell) if the wires are not explicitly schematised. The sphere in fact, is retained only when using the CWB approach. When increasing the sphere diameter, some discrepancies between the two approach are still observable, but they decrease when increasing d_p and tend to become negligible for $d_p \geq 16$cm. These discrepancies can be related to differences in the contact dynamics: in the CWB the falling sphere can intercept the mesh at each point along the wires, while in the NWB the sphere can intercept the mesh only at the nodal sphere level. This implies that the contact between the falling sphere and the mesh can be detected before and more often using the CWB (e.g. consider the case in which the sphere is centred on a wire as reported in Fig. 3.5b and Fig. 3.6a). For the comparison of the computational time, the test characterised by a sphere of



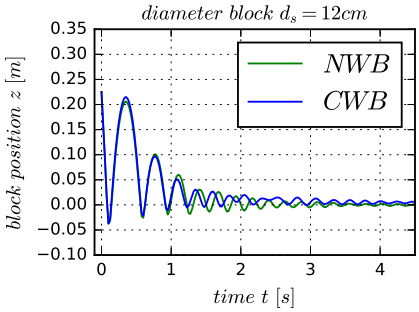
(a)



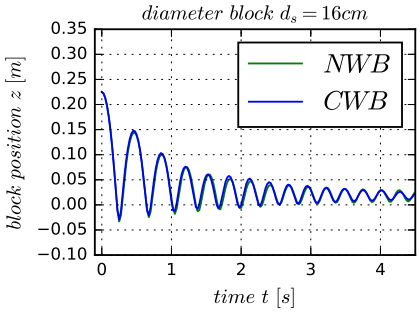
(b)



(c)



(d)



(e)

Figure 3.22: (a) 3D view of the initial configuration of the drop test with the CWB approach (orange particles indicate the fixed nodes on the mesh outer boundary). Evolution of the dropping sphere vertical position: (b) $d_s = 8$cm, (c) $d_s = 9$cm, (d) $d_s = 12$cm, (e) $d_s = 16$cm.

$d_p = 16$cm is considered in order to minimise the difference between the two approaches deriving from the different contact dynamics. The time statistics reported in Table 3.4 are obtained on 2000000 steps. Globally the total time required by the CWB is 1.9 times the one required by the NWB approach.

3.4.3 Retaining test

The drop test presented in Sec. 3.4.2 has shown that some differences between the NWB and the CWB are observable when the numerical mesh interacts with an external body, if the latter is sufficiently small. A natural further step is to analyse the interaction with multiple external bodies. The same mesh panel is therefore applied in order to retain an assembly of spherical bodies. The assembly is initially generated in a prismatic volume and then it is let to fall under gravity on the mesh panel (see Fig. 3.23). In the first phase the retaining capacity of the mesh panel is considered. A sample composed of 350 spheres is used in the tests. Different spheres diameters $d_s = 6, 7, 8, 9, 10$cm are used modifying the diameter of the particles of the original sample ($d_s = 10$cm). This permits the same geometrical distribution of the spherical particles to be used. The spheres density is equal to $\rho = 2500\text{kg/m}^3$ and the interparticle friction angle is set equal to $\phi_c = 40°$. The retention efficiency χ (i.e. ratio between the number of retained bodies n_{ret} over the total number of bodies n_{tot}) is used to compare the two modelling approaches. The results are reported in Table 3.5. The difference between the NWB and the CWB approach is notable for the cases in which the diameter of the spherical particles is similar to the minimum mesh opening, namely $d_s = 7$ and 8cm. In these cases, the geometrical description of the wire surface becomes significant and the adoption of the CWB approach permits a considerably higher amount of spherical particles to be retained. This difference is evident observing the time evolution of n_{ret} as reported in Fig. 3.24a. For bigger external bodies the difference between the two approaches is negligible; this is confirmed comparing the mesh deformed configuration at the end of the test as reported in Fig. 3.24b. In the second phase, the computational cost of the two approaches is addressed. In the previous cases it has been shown that the increment of the computational cost is mainly related to the higher number of bodies required by the CWB to represent the mesh. Here, the role of the number of external bodies is addressed in a simplified manner. The number of the sphere composing the

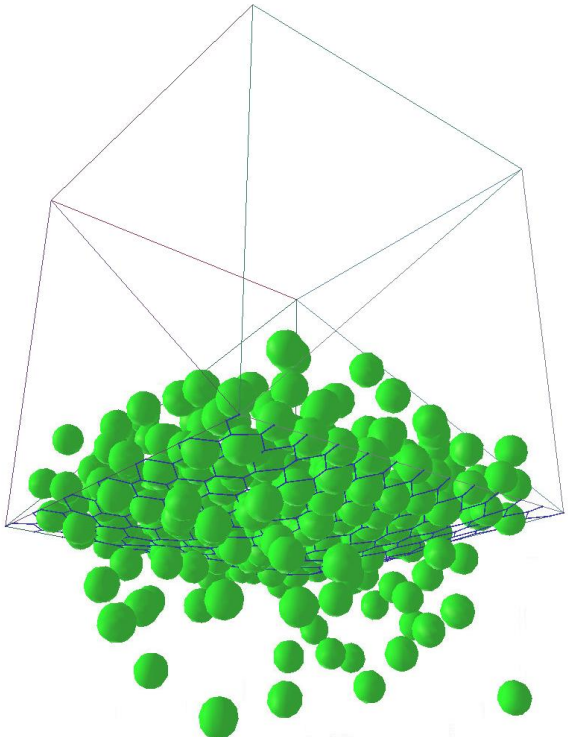


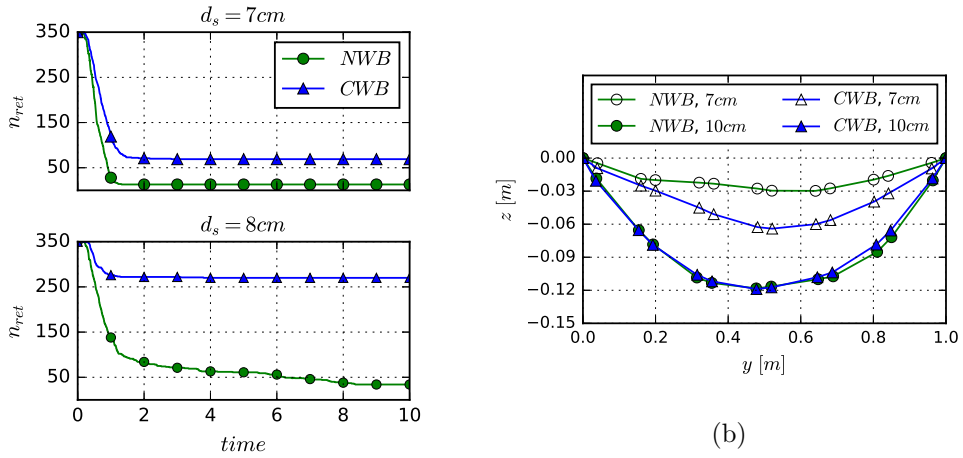
Figure 3.23: 3D view of an intermediate step of the retainig test simulation with the CWB approach (sphere diameter $d_s = 8$cm).

		NWB		CWB	
d_s [cm]	n_{tot}	n_{ret}	χ	n_{ret}	χ
6	350	2	0.01	18	0.05
7	350	13	0.04	69	0.20
8	350	34	0.10	270	0.77
9	350	319	0.91	350	1.00
10	350	350	1.00	350	1.00

Table 3.5: Comparison of the retention efficiency.

n_{tot}	468	1412	2338	3288	4033	4668
t_{NWB}	39.36	87.59	153.08	257.21	345.24	434.87
t_{CWB}	80.03	162.36	280.59	442.89	560.20	658.48
t_{CWB}/t_{NWB}	2.03	1.85	1.83	1.72	1.62	1.51

Table 3.6: Time comparison of the retaining test.



(a) (b)

Figure 3.24: Numerical results of the retainig test: (a) time evolution of n_{ret} for d_s = 7cm and 8cm, (b) mesh deformed configuration after 10s for d_s = 7cm and 10cm.

sample is varied modifying the height of the prismatic volume for the sample generation. A diameter of d_p = 10cm is considered in order to minimise the difference between the two approaches in terms of contact dynamics. The density of the particles is reduced to $\rho = 500\text{kg/m}^3$ to avoid the mesh failure for large samples. The total computational times for 100000 steps (time step $dt = 1.3 \cdot 10^{-6}$s) obtained with the two approaches are reported in Table 3.6. For both approaches, a linear increment of the computation time with the number of bodies is observed, however the difference in terms of total time between the two approaches decreases when increasing the number of external bodies. In fact, a gradually increment of the number of external bodies tends to reduce the relative weight of the greater number of bodies, required by the CWB in the mesh description, on a DEM cycle.

3.4.4 Punch test

The last configuration adopted in order to compare the NWB and the CWB modelling approaches is represented by the standard UNI punch test (see Sec. 3.3.1). The 3m×3m mesh panel is described by using 2890 bodies in the NWB and 7113 bodies (2890 gridNodes, 4223 gridConnections) in the

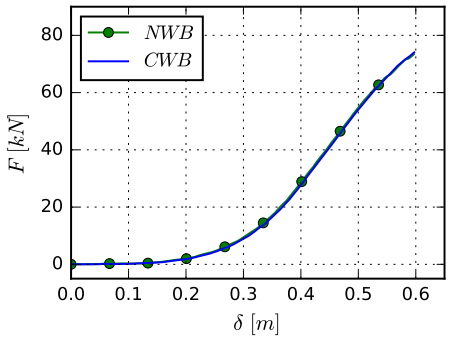


Figure 3.25: Comparison of the numerical results of the punch test in terms of force-displacement curve.

CWB approach. In both cases, the diameter of the nodal particles is equal to 2.7mm. The punching element has to be described differently according to the approach used for the mesh in order to ensure the contact compatibility between elements. It is described by using Facet elements [93] when adopting the NWB and using pFacet elements [93] when adopting the CWB approach. In the former case the punching element is composed of 694 elements, while in the latter case it is composed of 2084 elements (349 gridNodes, 1041 gridConnections, 694 pFacets). The force-displacement curves, obtained from the numerical simulations are reported in Fig. 3.25. No differences are observed between the two F-δ curves, thus showing that the mechanical behaviour of the mesh is not influenced by the modelling approach when loaded by a sufficiently large element (compared to the mesh cell). Concerning the computational cost, the time statistics of 250000 steps (time step $dt = 1.3 \cdot 10^{-6}$s) are reported in Table 3.6.

The relative weight on the total time of the contact detection phase is significantly greater for the CWB than for the NWB approach, this is due to the different description of the punching element (i.e. larger number of external bodies, thus larger number of possible interactions). The total time required by the CWB is 5.6 times the one required by the NWB approach. This strong increment of the computational time is related to both the greater number of bodies, and to a more computational demanding contact detection phase when adopting the CWB approach.

DEM phases	NWB		CWB	
	t [s]	t_{rel} [s]	t [s]	t_{rel} [s]
ForceResetter	6.831	1.75%	27.757	1.27%
InsertionSortCollider	1.027	0.26%	30.594	1.40%
InteractionLoop	260.229	66.65%	1759.630	80.36%
NewtonIntegrator	122.355	31.34%	371.750	16.98%
Total	390.441	100%	2189.732	100%

Table 3.7: Time statistics of the punch test.

3.5 Conclusive remarks

The results of the numerical tests above reported permit one to make some general observations regarding the NWB and CWB approaches. Both approaches use the same EWMs, thus the same mechanical behaviour of the mesh is expected when the latter is not interacting with external elements. This fact is confirmed by the results of the tensile test (discrepancies in Fig. 3.21 are related to the intrinsic randomness of the SDWM). The two approaches provide the same mechanical response also for a more complex loading condition as the one typical of the punch test. Concerning the cases in which the mesh interacts with relatively small external bodies (i.e. drop test and retaining test), differences between the NWB and the CWB are observed when these external bodies are smaller or equal to the mesh opening size. Under this condition, the numerical description of the wire surface may be important for precisely account for the mesh-soil interaction. The CWB should therefore be preferred when analysing problems in which the interaction between the mesh and the soil, at the particle scale, is important as, for instance, soil-inclusion and retaining problems. Conversely, if the focus of the study is on the macroscopic interaction between the mesh and the soil the NWB can also be adopted. Beside the condition on the external bodies dimension, the CWB approach should be preferred when using external elements of complex shape (e.g. angular or elongated blocks). Furthermore, the CWB permits one to efficiently simulate structural elements superimposed on the mesh (e.g. reinforcement cables [85]) or the connection between different elements (e.g. sliding rings [2]) and the relative motion between them.

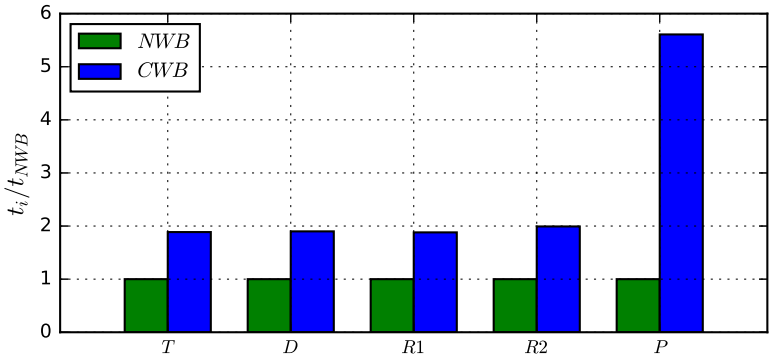


Figure 3.26: Time comparison between the NWB and CWB in different test configurations: T = tensile test, D = drop test, $R1$ = retaining test (only mesh), $R2$ = retaining test, P = punch test. The total time of each configuration is normalised on the value obtained with the NWB approach.

Regarding the computational cost, the total time obtained in the different test configurations is summarised in Fig. 3.26. In order to facilitate the comparison, the total time of each configuration is normalised on the value obtained with the NWB approach. When the difference is related only to the mesh descritpion (i.e. tensile, drop and retaining tests) the results show that the time required by the CWB approach can be considered two times higher than the one required by the NWB ($t_{CWB} \approx 1.9 t_{NWB}$). This difference can be mainly related to the higher number of bodies required by the CWB approach ($n_{CWB} \approx 2.5 n_{NWB}$ in the considered cases). No significant increments of the contact detection cost are observed, in these cases, using the CWB, confirming the efficiency of the adopted numerical representation. In the punch test instead, a different description of the punching element is necessary in order to ensure the contact compatibility between elements in the two approaches. This determines a larger number of external bodies (i.e. not belonging to the mesh) and a consequent increment of the computational cost of the contact detection phase which reflects on a strong increment of the total computational cost required by the CWB approach ($t_{CWB} \approx 5.6 t_{NWB}$). Finally, it is worth noting that a gradual reduction of the difference between the total simulation time required by the two approaches is observed when increasing the number of external bodies as reported in Tab. 3.6.

Chapter 4

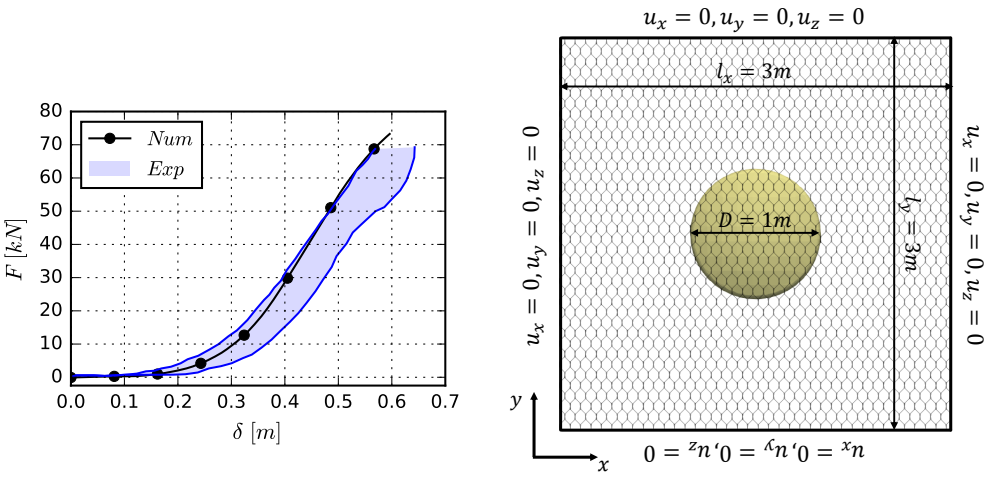
Punching behaviour of a secured drapery system

In this chapter, the mechanical behaviour of a mesh panel subjected to a local out-of-plane loading condition is addressed. This loading condition is typical when a secured drapery system is installed along rock slopes in order to prevent the detachment of potentially unstable rock blocks and/or to retain the ones that may become detached. The blocks can slide over the joint surface and push over the mesh, or being part of a bulged volume on which a mesh is installed to prevent its detachment and the subsequent free-fall. In both cases, the block can be schematised as a local punching condition on the mesh panel. The standard UNI punch test is extensively used in practice to characterise the resistance of a wire mesh to such a kind of loading conditions. The load applied by the punching element represents, in fact, a simple but effective schematisation of the action that an unstable block may exert on the mesh. This test configuration is therefore analysed in details in the first part of this chapter. The 8×10 hexagonal double twisted mesh type (DT mesh) with a nominal wire diameter of 2.7mm is used as the reference mesh. Initially, the laboratory test is faithfully simulated and the numerical results are used in order to investigate the internal force transmission mechanism of the mesh panel, as well as its deformation evolution during the test. After that, the main variables of the problem as the punching element dimension and position, as well as the panel dimensions are modified in order to quantify their effect on the mesh mechanical response. In the second phase, the mechanical behaviour of an anchored mesh panel is addressed. This will permit the mechanical behaviour of a

mesh panel to be analysed in a configuration that is more representative of the field conditions. A periodic single panel test configuration is defined, on the basis of the analysis of large-scale models. Referring to the latter test configuration, a parametric analysis is performed, considering the role of the dimension and position of the punching element, the anchor plate size and spacing, as well as the aspect ratio of the mesh panel. From the results of this analysis, simple analytical relationships are derived aiming to provide useful information to practitioners for the design phase of secured drapery systems as well as for the assessment of their safety conditions. Finally, the mechanical response of the DT mesh is compared with two prototype mesh typologies, namely the MT1 and the MT2 presented in Chapter 3. This will permit the investigation of the effect of introducing high resistance steel ropes in the standard DT mesh.

4.1 Laboratory standard UNI punch test

The experimental procedure characterising the standard UNI punch test has been described in details in Chapter 2, while the numerical model of this test has been already presented in Chapter 3. Anyway, the details of the numerical test are fundamental for a full comprehension of the analysis object of this chapter, and therefore they are briefly reported in the following. The 8×10 DT hexagonal mesh type with a nominal diameter of 2.7mm is considered. The 3m×3m mesh panel (see Fig. 4.1) is described adopting the NWB approach by means of 2890 spherical particles (in this test condition the NWB and the CWB approach provide the same result as reported in Chapter 3). The diameter of these nodal particles is set equal to four times the one of the real wires (i.e. $d_w = 10.8mm$); this permits the computational time to be reduced, without influencing the mechanical response of the mesh as shown in Fig. 4.2a. The particles' density is adjusted in order to maintain the inertial properties of the mesh panel ($\approx$1.43kg/m^2). The nodal particles belonging to the mesh outer boundary are fixed in order to represents the boundary conditions typical of the laboratory test. The punching element is described using 694 triangular elements (i.e. facets) and it is moved with a constant velocity equal to $v_z = 0.1$m/s. In order to reduce the computational time, the velocity imposed to the punching element in the numerical model is higher than the one used in the experimental procedure (i.e. $\leq$0.01m/s), however this does not modify the mechanical response of the mesh panel

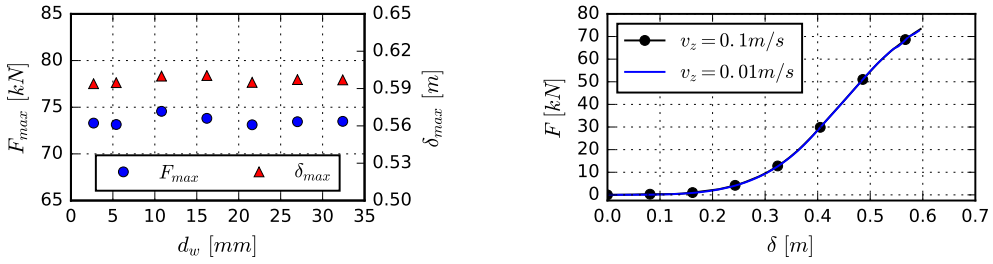


(a) (b)

Figure 4.1: (a) Mechanical response of the mesh panel and (b) geometrical scheme of the numerical model.

as reported in Fig. 4.2b. The EWMs used for the contact wire model are derived from the stress-strain relationships presented in Chapter 3. The contact parameters between a nodal sphere of the mesh and an element of the punching element are $k_n = 6.5 \cdot 10^5$ N/m, $k_t = 0.3k_n$ and $\phi_c = 0$ (i.e. frictionless contact). It should be noted that these parameters have a slight effect on the numerical results (i.e. F-δ curve) as it will be shown in the sensitivity analysis reported in Sec. 4.1.1. Finally, the time step is set equal to $dt = 3 \cdot 10^{-5}$s.

The standard output of this test is a force-displacement curve (F-δ), which characterises the mesh panel reaction to the external action applied by the displacement of the punching element. In the numerical model, this curve is computed registering the force acting on the punching element and the displacement of the latter. During the test also the force acting on the mesh fixed boundary was registered, and the latter results identical to the one registered with reference to the punching element. The DEM being well suited for studying dynamic problems, the equivalence between the force acting of the punching element and the one supported at the mesh boundary further confirms that the velocity imposed to the punching element is "sufficiently low" to avoid dynamic effects in the simulation. The numerical results are reported in Fig. 4.1 together with a graphical schematisation of



(a) (b)

Figure 4.2: (a) Effect of the nodal particle diameter d_w in terms of force F_{max} and deflection δ_{max} values at failure. (b) Effect of the punching element lifting velocity v_z on the mechanical response of the mesh.

the test geometry. The experimental data are reported in the same figure for facilitating the comparison. A 3D view of the time evolution of the numerical punch test is reported in Fig. 4.3, highlighting the failure modality and its propagation inside the mesh panel.

4.1.1 Sensitivity analysis of the mesh-punch contact parameters

Mesh-punch contact stiffnesses

The influence of the normal contact stiffness is analysed varying its value in the range 6.5×10^3N/m$\leq k_n \leq 2.6 \times 10^7$N/m. A variation of k_n induces a variation of k_t as well, however being the mesh-punch contact frictionless (i.e. $\phi_c = 0$) this does not influence the tangential behaviour at the mesh-punch contact. The numerical results reported in Fig. 4.4a show that for $k_n \geq 1 \times 10^5$N/m, this parameter does not significantly influence the mechanical response of the mesh (differences in terms of force and displacement values at failure are less than 1%.). For lower values of k_n, the interpenetration between the mesh particles and the facet elements, at a certain point of the simulation (depending on the k_n value), becomes too large, compromising the correctness of the simulation, namely the punching element passes through the mesh before the failure of the latter. However, before this moment the mechanical response of the mesh is the same independently of the value k_n (i.e. F-δ curves are superimposed).

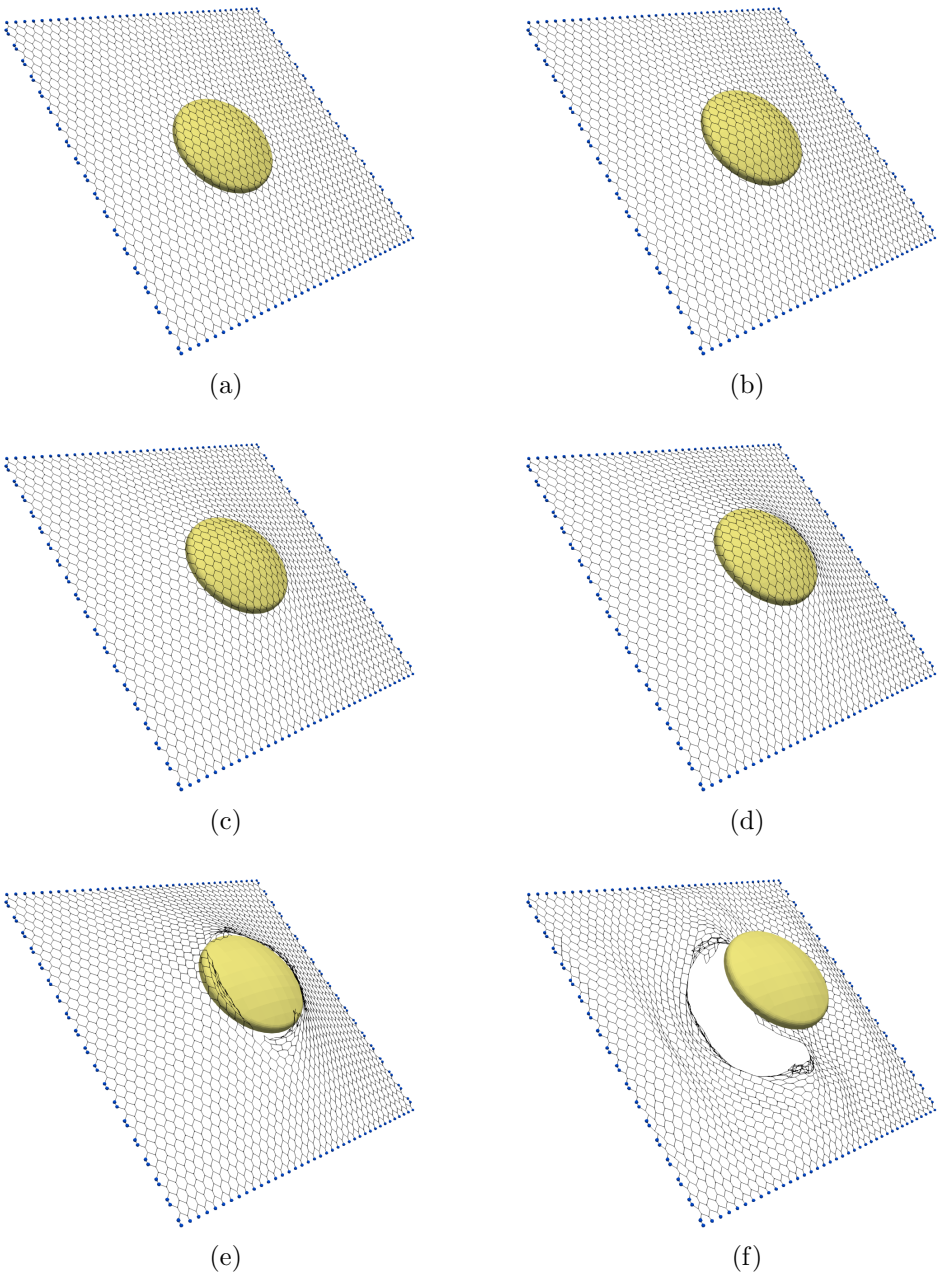
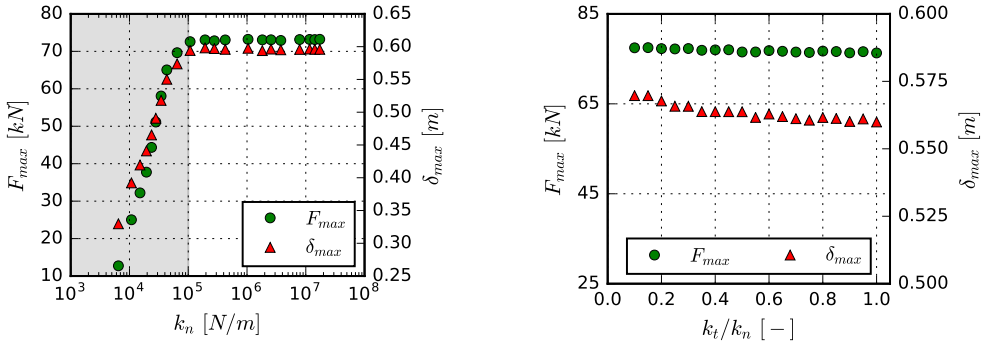


Figure 4.3: 3D View of the time evolution of the numerical punch test (the fixed nodes of the mesh are represented with blue spheres).



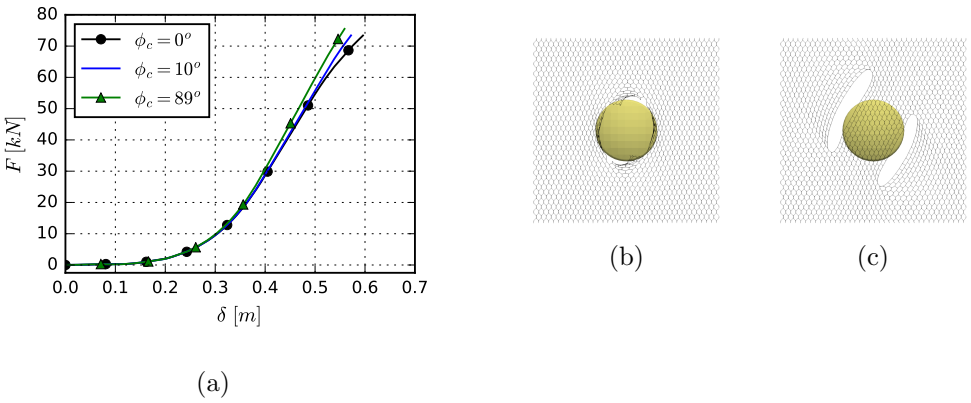
(a) (b)

Figure 4.4: (a) Effect of the mesh-punch (a) normal contact stiffness k_n and (b) tangential contact stiffness k_t in terms of force F_{max} and deflection δ_{max} values at failure.

For the analysis of the effect of the tangential contact stiffness k_t an extremely high value of the contact friction angle ($\phi_c = 89°$) is used in order to maximise the possible differences due to tangential effects at the mesh-punch contact. The value of k_t is varied in a wide range $0.1k_n \leq k_t \leq 1.0k_n$ ($k_n = 6.5 \times 10^5$N/m). The results reported in Fig. 4.4b show that the influence of k_t is also negligible (differences in terms of force and displacement values at failure are less than 1.3%.).

Mesh-punch contact friction angle

Finally, the mesh-punch contact friction angle ϕ_c is varied from a frictionless case up to the extremely high frictional condition $\phi_c = 89°$ ($k_n = 6.5 \times 10^5$N/m, $k_t = 0.3k_n$). The numerical results obtained for $\phi_c = 0°$, $\phi_c = 10°$, $\phi_c = 89°$ are compared in Fig. 4.5a. The mechanical response in the initial part of the force-displacement curve (i.e. $\delta \leq 0.35$m) is the same for all the three cases, then the curves diverge in a very slight manner. Considering the two extreme cases (i.e. $\phi_c = 0°$ and $\phi_c = 89°$), the difference is approximately equal to 4% and to 6% concerning respectively the force and the deflection values at failure. This shows the slight influence of the contact friction angle on the mesh response. This fact is ascribable to the particular testing conditions: on one hand the rounded shape of the punch limits the mesh sliding at the contact with the punching element, on the other hand the



(a) (b) (c)

Figure 4.5: (a) Effect of the mesh-punch contact friction angle on the mechanical behaviour of the mesh panel. Rupture mechanisms for (b) a frictonless contact and (c) a frictional contact.

loading direction (i.e. normally oriented to the mesh plane) entails that tangential forces have a marginal effect on the mesh mechanical behaviour.

From a numerical perspective, it is interesting to note that the failure modality is different moving from a frictionless to a frictional case as shown in Fig. 4.5b and Fig. 4.5c. In the former, the mesh starts to break just in the centre of the panel, while the failure occurs near the edges of the punching element for a frictional case. In the experimental test, the failure starts approximately from the centre of the mesh panel and propagates parallel to the double twisted wires orientation. This condition is similar to the one obtained adopting $\phi_c = 0$. Having said that, given the low influence of ϕ_c on the mesh response and the lack of knowledge of a precise value of the mesh-punch friction coefficient, a frictionless mesh-punch contact is adopted in the following of the analysis, this representing the most critical condition for the mesh (i.e. $\phi_c = 0$ minimises the force value at failure).

In light of the above reported results, it is evident that the mesh-punch contact parameters play a negligible role in the considered problem. Indeed, the problem is controlled by the tensile behaviour of the mesh, which is ruled by the contact laws governing the mesh particles interactions (i.e. EWMs). The EWMs are defined from stress-strain tensile relationships obtained from experimental tensile test. In this sense, since deterministic EWMs are used, a "calibration phase" of the numerical parameters is not needed.

4.1.2 Internal mechanical behaviour of the mesh panel

The effectiveness of the numerical model in reproducing the mesh response is evident from the observation of the F-δ curves reported in Fig. 4.1a. The numerical results can therefore be used to investigate in details the mesh mechanical behaviour. In particular, the possibility to monitor the stress and strain on each wire element permits one to analyse how the external load (i.e. thrust force applied by the punching element) is transmitted inside the mesh. In this perspective, in Fig. 4.6 and 4.7 the tensile stress and strain distributions on the wires are reported an instant prior to the mesh failure (contour plots are used for the sake of clearness). These distributions are computed from a linear interpolation of the tensile strain/stress acting on the wires on a regular dense grid (grid spacing of 4cm). In both cases, single wires and double twisted wires are analysed separately to highlight their different behaviour, and only for the stress a generalised distribution on the mesh panel (i.e. considering all the wires) is reported. Only the single wires $+45°$ oriented with respect to the x-axis (a counterclockwise rotation is considered positive) are considered in the plot. The stress and strain distribution on the other single wires (i.e $-45°$ oriented) are symmetrical with respect to the y-axis. The comparison of the stress distribution on the two wire types highlights that the double twisted wires experience less tensile stresses than single wires. In fact, they share the load over two wires (they are composed of two twisted single wires) and, as such, they are characterised by a higher tensile strength. In both wire types, the tensile stress distribution appears quite homogeneous above the punching element, while a stronger anisotropic distribution arises in the external domain. This reflects both, the specific deformation modality of the hexagonal elementary cells and the effect due to the difference in terms of stiffness and maximum strength of the two types of wires. The double twisted wires show a soft decay of tensile stresses along the y-direction while the stress significantly decays moving along the x-direction (see Fig. 4.6b). Concerning the single wires instead, they exhibit a preferential cross-shape distribution with inclined arms with respect to the y-direction (see. Fig. 4.6a). Finally, considering the overall stress distribution on the mesh wires (see Fig. 4.6c), a vertically oriented central slice characterised by the higher values of the stress is observed highlighting the existence of a preferential direction for the stress transmission. Considering the strain distribution (see Fig. 4.7), only

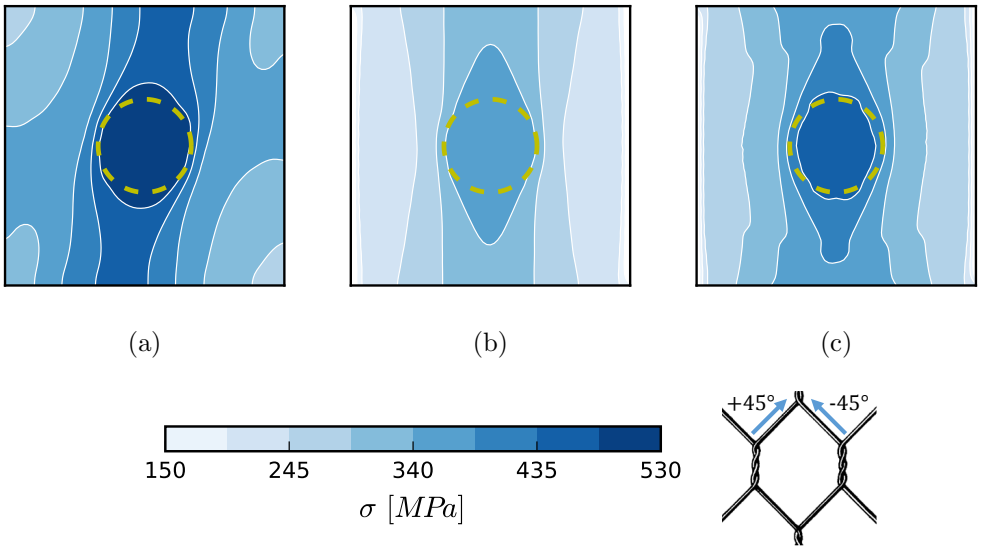


Figure 4.6: Tensile stress distribution, an instant prior to the mesh failure, on (a) single wires (+45° oriented), (b) double twisted wires and (c) both wire types.

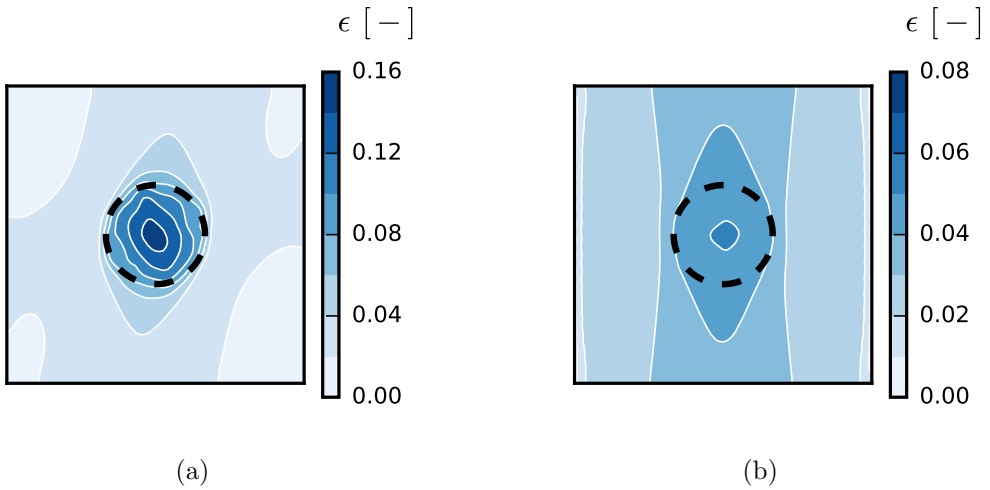
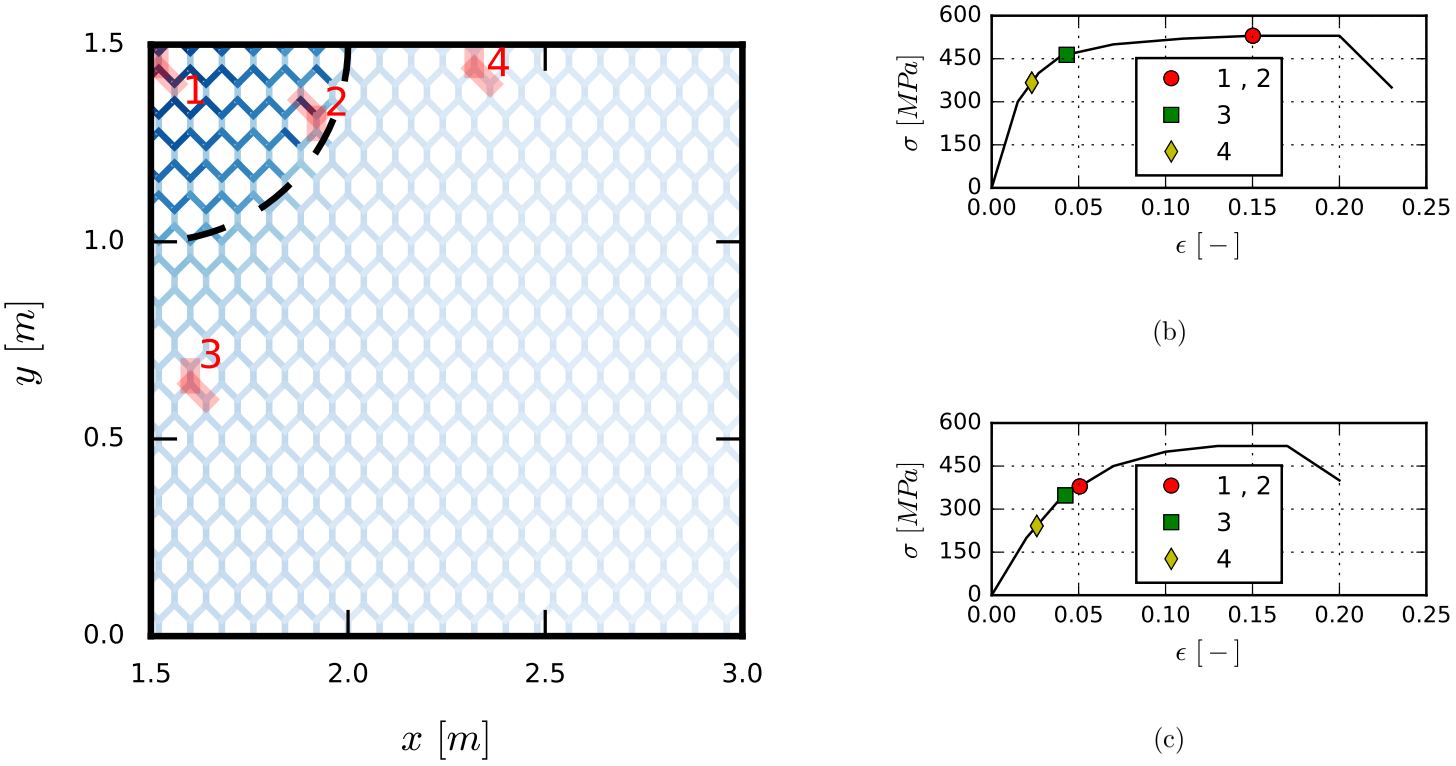


Figure 4.7: Tensile strain distribution, an instant prior to the mesh failure, on (a) single wires (+45° oriented) and (b) double twisted wires.

few single wires, in the centre of the mesh panel, are close to their maximum strain level (i.e. $\epsilon_{max} = 0.23$), and moving away from that zone a rapid decay of the deformation level is observed. The deformation level is instead significantly lower than the maximum deformation (i.e. $\epsilon_{max} = 0.2$) for all of the double twisted wires. The contour plots of Fig. 4.6 and Fig. 4.7 permit the qualitative stress and strain distribution on the mesh panel to highlighted. This is useful in order to provide a macroscopic characterisation of the mesh panel behaviour. Nevertheless, considering that the failure of a wire can rapidly lead to mesh panel failure, it can be interesting to analyse the wires separately to better understand their rate of work and to point out the critical zones of the mesh panel. In this perspective, a quarter of the mesh panel is reported in Fig. 4.8a in which the color of the wires represents the actual normalised strain level (ϵ/ϵ_{max}). The stress-strain condition for four couples of single/double twisted wires (highlighted in red in Fig. 4.8a) is also reported on the specific tensile curves in Fig. 4.8b and 4.8c. It is evident that the most critical wires are in correspondence to the centre of the mesh panel and near the edges of the punching element, as for instance the single wires of couples 1 and 2. However, it has to be considered that the wires are characterised by a significant plastic phase, thus even if most of the wires are far from the maximum elongation, the actual stress supported by them can be considerable. This condition is highlighted in Fig. 4.9a where the percentage of wires characterised by a stress level $\sigma \geq \sigma_{max}/2$, represented by the parameter n_{50}, is reported as a function of the normalised punching element displacement (i.e. ratio between the actual displacement δ and the one at failure δ^*). After that, in order to provide a measure of the increment of the tensile strain into the wires during the test, let us consider the geometric parameters $L_{DT}(\delta_i)$ and $L_{SW}(\delta_i)$ defined as the lengths of the double twisted and single wires of the panel for a displacement δ_i of the punching element. Moreover, considering the couples L^0_{DT}, L^0_{SW} and L^{max}_{DT}, L^{max}_{SW} as the corresponding initial lengths and the admitted maximum lengths of the wires respectively, the parameter Γ_k is defined as follows:

$$\Gamma_k = \frac{1}{n_k} \frac{\sum_{j=0}^{n_k} \frac{L_{k,j}(\delta_{i+1}) - L_{k,j}(\delta_i)}{L_k^{max} - L_k^0}}{(\delta_{i+1} - \delta_i)/\delta^*} \tag{4.1}$$

In Eq. 4.1 the subscript k indicates the wire type, namely DT (i.e. double twisted wire) or SW (i.e. single wire), and n_k the total number of k-type wires. The parameter Γ_k represents the normalised mean increment of ten-

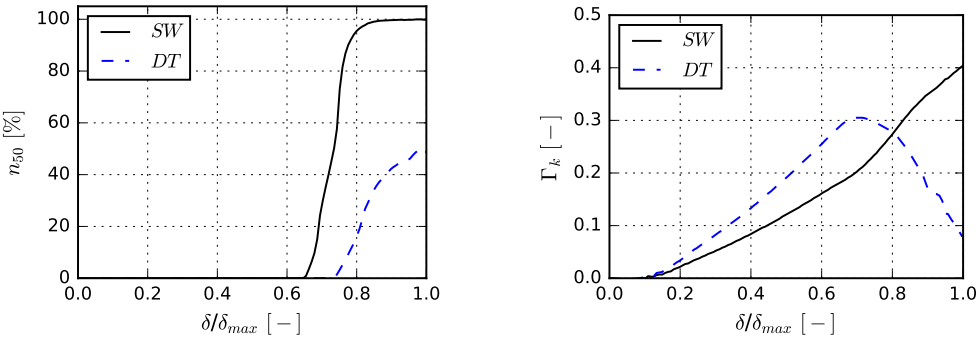


(a)

(b)

(c)

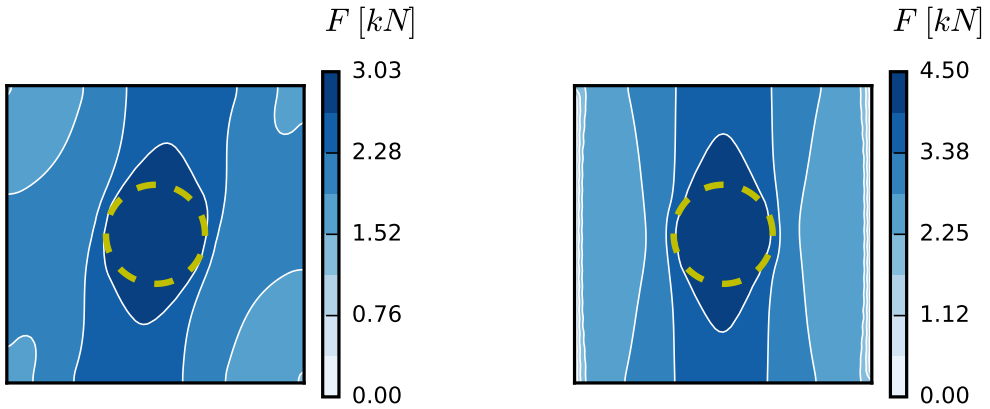
Figure 4.8: (a) Normalised tensile strains prior to failure on a quarter of mesh panel and stress-strain values related to four different positions for (b) single and (c) double twisted wires.



(a) (b)

Figure 4.9: (a) Percentage of wires n_{50} characterised by $\sigma \geq \sigma_{max}/2$ and (b) normalised mean increment of tensile strain Γ_k of the wires as a function of the normalised punching element displacement.

sile strain held by the k-type wires, for a given unit amount of "strain" of the punching element (i.e. normalised increment of punching element displacement). For low values of Γ_k, the displacement of the punching element produces only a geometrical strain of the hexagonal cells (e.g. rotations of the wires). Then, the higher this value, the higher the wire strain in comparison to the geometrical strain of the hexagonal cells. The evolution of Γ_k, as a function of the normalised punching element displacement, is reported in Fig. 4.9b. At the beginning of the test, the strain level on the wires is very low and most of the deformations are due to a geometrical distortion of the hexagonal cells. Successively, the rate of material strain increases for both wire types, with a preference for the double twisted ones, which are less stiff. For further increments of the punch displacement, more and more single wires reach the yielding point, varying consequently their stiffness and increasing plastic deformations. In the plastic region, the stiffness of the single wires becomes less than the one of the double twisted wires, leading to a reduction of the increment of strain (Γ_{DT}) for the double twisted wires (the descending part of the dashed line and the rising part of solid line in Fig. 4.9b). Summing up the two Γ_k functions, for single and double twisted wires, in the final part of the test, an approximately asymptotic trend for the Γ_k function can be observed. This may be considered as an indicator of the achievement of the maximum stress redistribution and of a "full plastic"



(a) (b)

Figure 4.10: Tensile force distribution, an instant prior to the mesh failure, on (a) single wires (+45° oriented) and (b) double twisted wires.

condition of the mesh panel.

Finally, the tensile force distribution on the mesh wires, for both single and double twisted ones, is considered. The force distribution is computed from a linear interpolation of the force acting on the considered wires on a regular dense grid (grid spacing of 4cm). Also in this case the wires are considered separately, the two wire types being characterised by a different maximum force (i.e. $\approx$ 3.03kN for the single wires and $\approx$ 5.95kN for the double twisted wires). The contour plots showing the tensile force distribution, an instant prior to the mesh failure, are reported in Fig. 4.10. They obviously reflect the related stress distributions (see Fig. 4.6), however they permit a better visualisation of the significant role of the double twisted wires on the mesh reaction. The double twisted wires intercept two single wires each, and being able to support a higher force, they determines a preferential direction for the load transmission inside the mesh. In fact, the thrust force imposed by the punching element is transmitted from the centre to the edges of the mesh panel following the double twisted wire direction as observable in Fig. 4.10. This points out the anisotropic behaviour of the DT mesh, which shows a higher stiffness in one direction (i.e. the direction parallel to the double twisted wires). Referring to the latter consideration, it is interesting to note as the mesh mechanical anisotropy reflects on the



(a) (b)

Figure 4.11: Lateral views of the numerical model of the punch test an instant prior to the mesh failure: (a) x-z plane and (b) y-z plane.

deformation modality of the mesh panel. In this perspective, two lateral views, along the x-z and the y-z plane, of the numerical mesh panel, an instant prior to the mesh failure, are reported in Fig. 4.11a and Fig. 4.11b respectively. Comparing these views the difference in terms of curvature along the two directions is evident. The deformed configuration of the mesh panel, with respect to the x-z plane (Fig. 4.11a), well adapts to the punching element and shows a strong curvature in correspondence to the edges of the latter (i.e. high deformability) which gently diminishes moving towards the mesh boundary. Referring to the y-z plane (Fig. 4.11b) instead, the mesh deformed configuration is almost linear from the centre to the edges of the panel. The hexagonal mesh elementary cells are less deformable in the direction parallel to the double twisted wires, consequently the mesh shows a higher stiffness along that direction. The intrinsic anisotropy of the DT mesh is related to both the particular geometry and orientation and the mechanical characteristic of the two wire types constituting the mesh. The internal force transmission mechanism follows the double twisted wires orientation. This peculiar mechanical behaviour of the DT mesh should be carefully considered in order to optimise the efficiency of this mesh typology.

4.1.3 Parametric analysis

In Sec. 4.1.2 the mechanical behaviour of the DT mesh panel has been analysed in details. This has permitted a better understanding of the force transmission mechanism typical of the considered mesh type with reference to a standard testing condition. In this section instead, the main variables that characterise the punch test configuration are varied in order to bring out how the different variables affect the performance of the mesh panel. In particular, size and position of the punching element, as well as the mesh

l_x [m]	l_y [m]	D [m]	*pos. punch* [m]	n_{sim}
3.0	3.0	1.0	$(1.5, 1.5)$	1
3.0	3.0	**0.1-2.5**	$(1.5, 1.5)$	48
3.0	3.0	1.0	(**0.5-1.5,0.5-1.5**)	1153
1.5-4.5	**1.5-4.5**	1.0	$(1.5, 1.5)$	196

Table 4.1: Summary of the parameter sets considered in the parametric analysis. The first row corresponds to the reference test. Bold font is used to mark the parameters that differ from the reference test providing their range of variation (n_{sim} represents the number of performed simulations).

panel dimension and aspect ratio are considered. All the results reported in the following are normalised with reference to the values of force F^* (73.3kN) and displacement δ^* (0.60m) at failure obtained from the numerical UNI punch test (see Fig. 4.1) in order to facilitate the comparison.

Effect of the size of the punching element

In the punch test, the punching element is used to schematise the action that an unstable block may impose on the mesh panel. In this perspective, the variation of its dimension permits one to investigate the possible scale effects related to the block dimension, as well as the effect of the block sharpness (i.e. the sharper the block, the lower the contact surface between the block and the mesh). However, due to the particular boundary conditions imposed to the mesh panel in the laboratory test configuration, scale effects are dominant and the effect related to the block sharpness is difficult to be appreciated. The latter will be analysed in Sec. 4.2.2, where a more realistic schematisation of the field boundary condition is adopted. Furthermore, even if the standard UNI punch test configuration is widely used other test configurations are adopted in practice [15, 22]. The difference between the test procedures, which is mainly related to the punching element dimension, makes direct comparison between the experimental results in the technical literature difficult. The understanding of how the punching element influences the mechanical response of a mesh panel may help to compare the results coming from different test configurations.

The size of the punching element is modified varying its diameter while

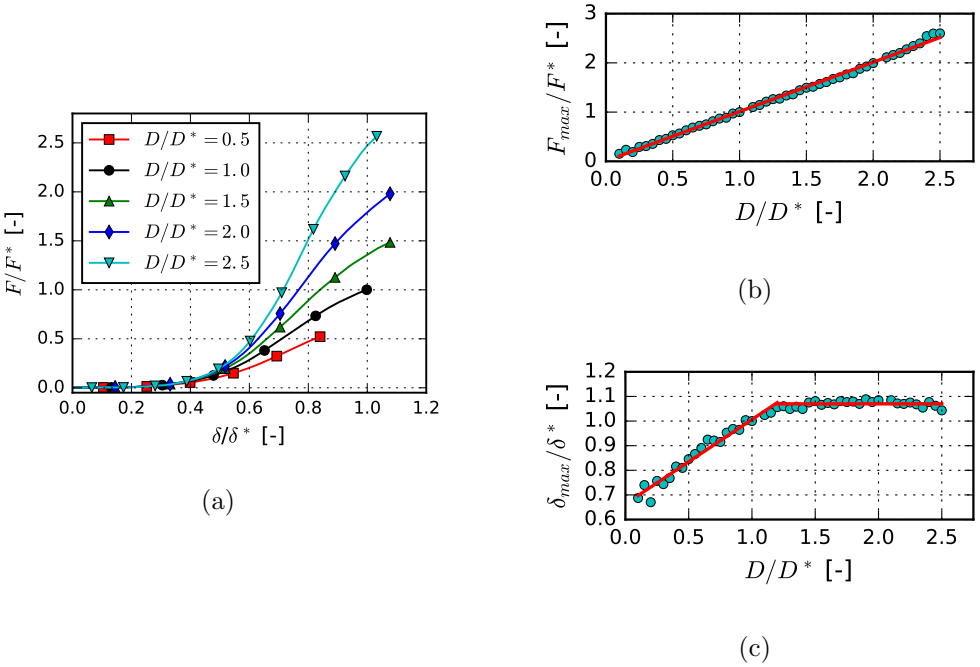


Figure 4.12: (a) Effect of the punching element size on the mechanical behaviour of the mesh panel, trend (b) of the maximum force F_{max} (fit Eq. 4.2) and (c) of deflection δ_{max} at failure (fit Eq. 4.3).

keeping constant the size of the mesh panel (i.e. 3×3m). The punch diameter is varied in a wide range, namely 0.1m$\leq D \leq$ 2.5m with an incremental step of 0.1m. In Fig. 4.12a the mechanical response of five sizes of the punching element (i.e. D/D^*=0.5, 1.0, 1.5, 2.0, 2.5) is reported. The numerical results show that an increment of the punching element dimension leads to a monotonic increment of the maximum sustainable force F_{max}, while the deflection value δ_{max} firstly increases with D, then seems to saturate for the higher values of D. Finally, the out-of-plane stiffness of the mesh panel (i.e. stiffness of the F-δ curves) increases when increasing the dimension of the punching element. This can be related on one hand to a better redistribution of tensile stress on the panel due to a larger mesh-punch contact surface, and on the other hand to the greater proximity of the punching element to the fixed boundary of the mesh.

In order to better understand the influence of D on the mesh panel response, the trends of the F_{max} and δ_{max}, obtained in the entire range of variation of D are reported in Fig. 4.12b and in Fig. 4.12c respectively.

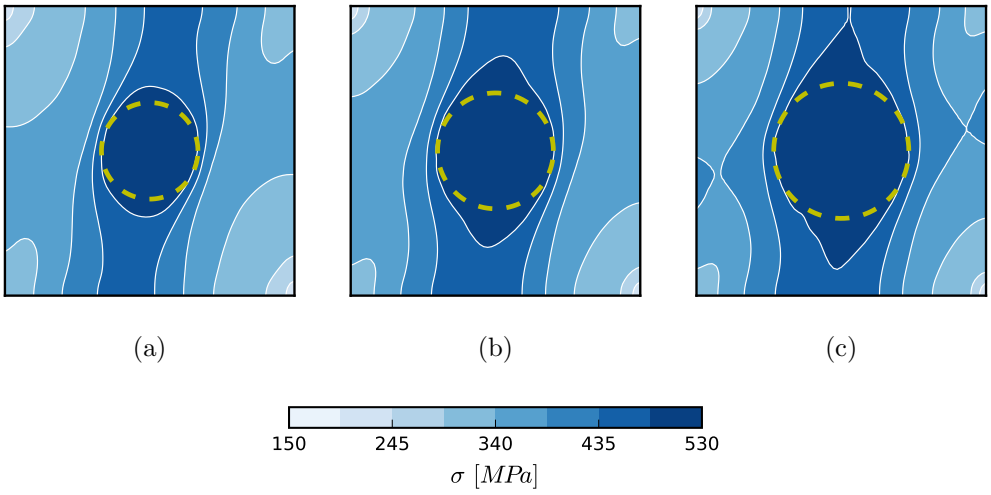


Figure 4.13: Tensile stress distribution, an instant prior to the mesh failure, on single wires (+45° oriented) for: (a) $D/D^* = 1.0$, (b) $D/D^* = 1.2$ and (c) $D/D^* = 1.4$.

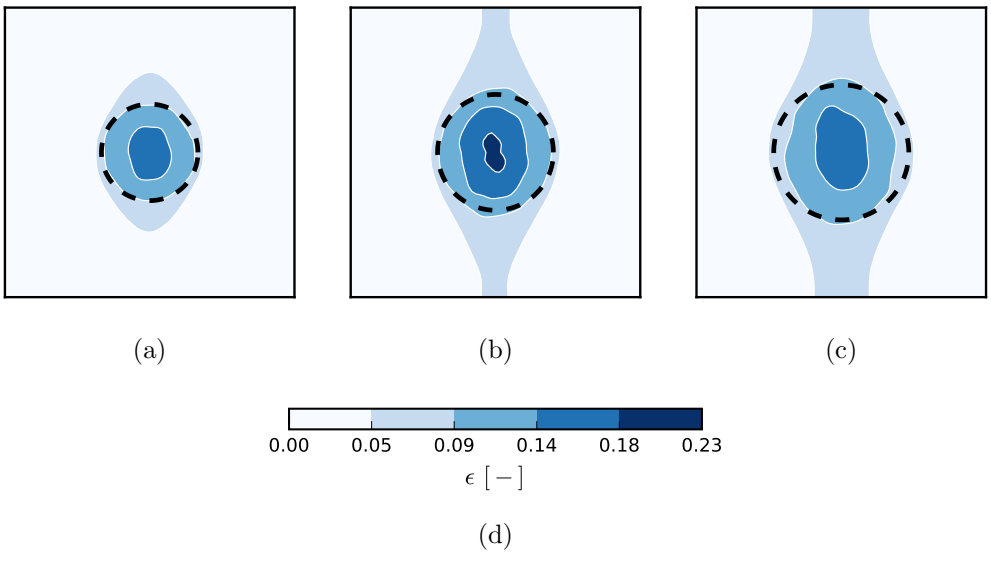


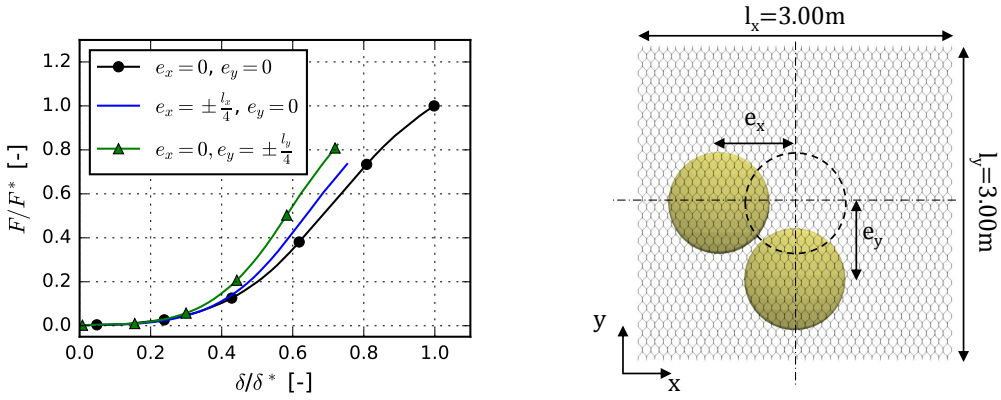
Figure 4.14: Tensile strain distribution, an instant prior to the mesh failure, on single wires (+45° oriented) for: (a) $D/D^* = 1.0$, (b) $D/D^* = 1.2$ and (c) $D/D^* = 1.4$.

The numerical results show that F_{max} and D are linearly related (see Fig. 4.12b); for instance, scaling the dome diameter by a factor of two results in a twice F_{max} value. The maximum retaining force can be viewed, in fact, as an integral of the tensile forces at failure along the dome boundary, which is a function of the number of wires intercepting the dome perimeter and, in turn, a linear function of the dome diameter. However, it should be noted that this result also depends on the tensile properties of the wires and on the ability of the mesh to redistribute loads (e.g. boundary conditions, shape of the punching element). In this case, just prior to the mesh failure all the single wires that lie above the punching element experience a stress value approximately equal to the maximum one as reported in Fig. 4.13. This happens independently of the value of D, thus determining the linearity between D and F_{max}. The relationship between the maximum force and the punching element dimension (D^* =1.0m) is well represented by the following expression (linear least squares fit):

$$F_{max} = \frac{D}{D^*} F^* \tag{4.2}$$

Eq. 4.2 allows the effect of the punching element dimension on the puncturing resistance of a mesh panel to be accounted for. This also permits one to extend the results obtained from different test configurations (i.e. different dimensions of the punching device) to a "common" dimension of the punching element, thus allowing a first comparison between the different data reported in the technical literature. It should be noted, that possible effects deriving from the shape of the punching device as well as from its orientation with respect to the mesh wires (wire meshes are generally characterised by an anisotropic behaviour in the two principal directions) were not considered in the definition of Eq. 4.2.

The value of the displacement at failure δ_{max} (see Fig. 4.12c) increases as a linear function up to D/D^*=1.2, then it reaches a plateau with a value $\delta_{max}/\delta^* \approx$1.07. This specific trend of δ_{max} proves that the finite size of the mesh panel acts as a limiting factor. In this perspective, the emergence of the plateau for the trend of δ_{max} should be related to the ratio of D over the length of the vertical side of the mesh l_y (the load is transmitted along the y-direction). In particular, the ratio D/l_y affects the strain distribution in the wires. For $D/l_y \geq 0.4$ some of the wires along the mesh outer boundary are characterised by a high tensile strain (i.e. $\epsilon \geq 0.05$) and start to experience plastic deformations as reported in Fig. 4.14 (the contour plots are obtained



(a) (b)

Figure 4.15: (a) Effect of the punching element position on the mechanical behaviour of the mesh panel. (b) Sketch of the geometry of the cases with an eccentric position of the punching element.

from a linear interpolation of the strain acting on the wires on a regular spaced grid of 4cm). From this moment, the mesh panel cannot redistribute the load coming from the punching element and a further displacement leads to a localisation of strains in the centre of the mesh panel triggering the failure of the latter. The numerical results permit the definition of a relationship between the panel deflection at failure and the punching element dimension ($D^* = 1.0$m). This is well represented by the following expression (linear least squares fit):

$$\begin{cases} \delta_{max} = \left(0.34\frac{D}{D^*} + 0.66\right)\delta^*, & \text{if } \frac{D}{l_y} < 0.4 \\ \delta_{max} = 1.07\delta^*, & \text{if } \frac{D}{l_y} \geq 0.4 \end{cases} \tag{4.3}$$

Effect of the position of the punching element

In order to analyse the influence of the position of the punching element, the latter has been shifted from the standard centred case (i.e. x_c=1.5m, y_c=1.5m). In Fig 4.15a the force-displacement curves obtained for two orthogonal shifts e_x, e_y, (symmetric shifts, namely $\pm e_j$, leads to the same behaviour), equal to the 25% of the panel side, of the punching element are compared with the standard centred case. It is remarkable that, when the mesh panel is not centrally loaded, both the maximum force and displace-

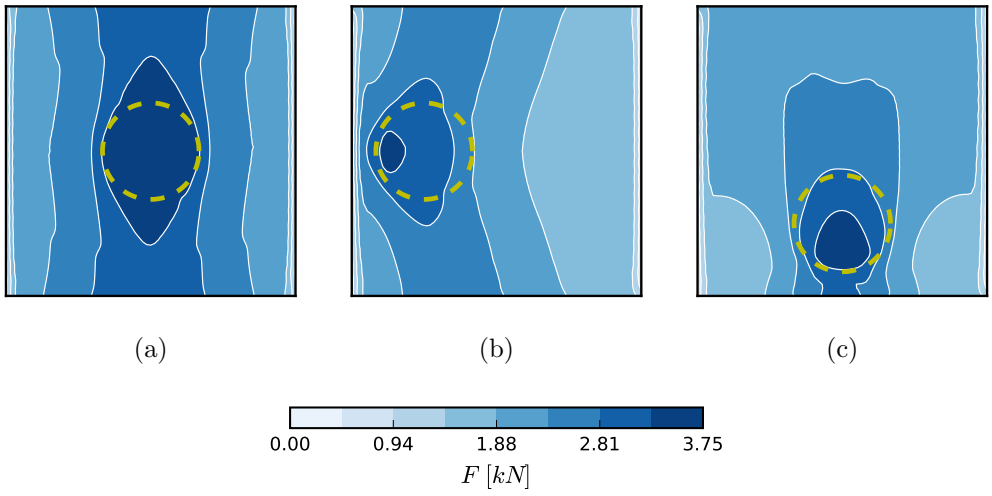
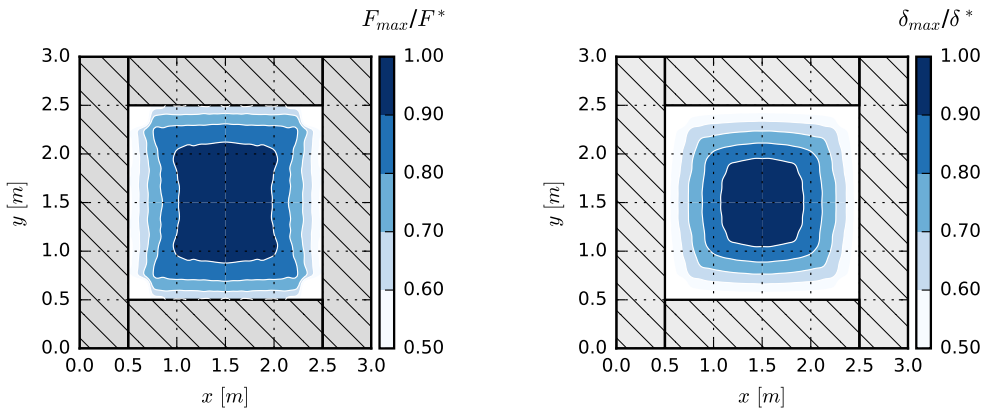


Figure 4.16: Tensile force distribution, an instant prior to the mesh failure for: (a) $e_x = 0m, e_y = 0m$, (b) $e_x = \frac{l_x}{4}, e_y = 0m$ and (c) $e_x = 0m, e_y = \frac{l_y}{4}$.

ment decrease. For the former, the reduction can be associated with an asymmetric distribution of the tensile forces on the mesh panel as shown in Fig. 4.16. The reduction of the deflection value at failure δ_{max} instead, is caused by the greater proximity of the punching element to the fixed outer boundary of the mesh. In fact, the number of wires between the boundary of the punch and the mesh boundary is lower when the punch is not centred, and δ_{max} being related to the elongation of the wires, the shift reflects in a reduction of the possible deflection of the mesh panel. The greater proximity to the mesh fixed boundary entails also a more rapid transmission of the force inside the mesh and a consequent stiffer response to the applied out-of-plane loading condition. The direction of the shift is also relevant: for an eccentric load along y-direction (i.e. parallel to the direction of double twisted wires) the mesh shows a stiffer response than for the same eccentricity along x-axis. This reflects the anisotropic mechanical behaviour of the mesh panel: the preferential force transmission direction of the DT mesh is, in fact, oriented with the double twisted wires as reported in Sec. 4.1.2.

Finally, the punch was shifted on a dense regular grid in order to characterise the value of F_{max} and δ_{max} with reference to a generic shift e_x, e_y. In Fig. 4.17a and 4.17a the interpolated contour-plots of the maximum force



(a) (b)

Figure 4.17: Effect of the punching element position: (a) contour plot of maximum force value F_{max} and (b) contour plot of deflection values δ_{max} at failure. The contour plots are obtained from a linear interpolation of the numerical data on a regular grid with a spacing of 4cm.

and deflection values at failure are reported respectively. In these plots, a value of generic coordinates $(x, y) = (x_c \pm e_x, y_c \pm e_y)$ refers to a punch test in which the punching element is centred in the same (x, y) position. The external grey-filled area represents the zone where the punching element cannot be moved because of the interference with the fixed edges of the panel. A gentle asymmetric interpolation surface arises from the plot of the force at failure (see Fig. 4.17a). Higher values of the maximum force F_{max} are observed when shifting the punch along the vertical direction than for the same shift along the horizontal one. Instead, for the deflection value δ_{max} (see Fig. 4.17b) the effect of the shift direction is negligible. As a general comment both, the values of force and deflection at failure, decrease when increasing the eccentricity of the punching element, and abruptly drop when the punch is close to the edges of the panel.

Effect of the panel dimension and aspect ratio

In the standard UNI punch test a square mesh panel is considered, however it is interesting to analyse the effect of a variation of the panel dimension and

of the ratio of the lengths of the two panel's sides. The latter will be referred as the aspect ratio $AR = l_x/l_y$ in the following. In this perspective, the mesh side's length is varied in the range 1.5m $\leq l_i \leq$ 4.5m (incremental step of 0.25m) considering one side at a time. Initially, the mechanical response of three equiareal panels (i.e. 2m×4.5m, 3m×3m, 4.5m×2m), characterised by a different aspect ratio, is reported in Fig. 4.18. The F-δ curve obtained for $AR = 2.25$ (i.e. $l_x = 4.5$m, $l_y = 2.0$m) shows a slightly higher maximum force ($F_{max} \approx 1.08F^*$) and a significant reduction of the deflection at failure ($\delta_{max} \approx 0.78\delta^*$) with respect to the reference case (i.e. $AR = 1.0$). Conversely, for $AR = 0.45$ (i.e. $l_x = 2.0$m, $l_y = 4.5$m) a reduction of the maximum force is observed ($F_{max} \approx 0.90F^*$); this premature failure determines also a reduction of the deflection value ($\delta_{max} \approx 0.90\delta^*$). This behaviour is caused by the existence of a preferential direction, oriented with the double twisted wires, for the force transmission inside the mesh as already mentioned in Sec. 4.1.2. When considering an $AR > 1$, for equiareal panels, the distance between the punching element and the upper and lower sides of the mesh decreases, and so does the transmission force path, determining a prompter response of the mesh panel. Furthermore, considering a panel characterised by $AR < 1$ leads to a reduction of the number of double twisted wires along the upper and lower sides. As these sides are the ones on which the external force is mainly sustained, a reduction of their length negatively reflects on the maximum sustainable force by the mesh panel. It is worth mentioning that these considerations refer to equiareal panels.

In the second phase, the dimension of the mesh panel is varied without any constraint on its area. The effect of a generic variation of the panel aspect ratio on the mesh mechanical response can be observed in the contour plots of Fig. 4.19a (obtained from a linear interpolation of the numerical data). The solid yellow lines indicate equiareal panels. The effect of a variation of AR on F_{max} is reported in Fig. 4.19a. The increase of the maximum force supportable by the mesh panel when increasing AR is confirmed. Moreover, the mesh panel resistance seems to be more influenced by a variation of the side length l_x rather than by a variation of the side length l_y. Finally, considering a fixed value of AR, adopting a larger panel leads only to a slight increment of the F_{max} value.

The effect of a variation of AR on the deflection value δ_{max} is shown in Fig. 4.19b. Considering equiareal panels, a non-monotonic trend of δ_{max} is observed, and its value seems to be maximised for mesh panels characterised

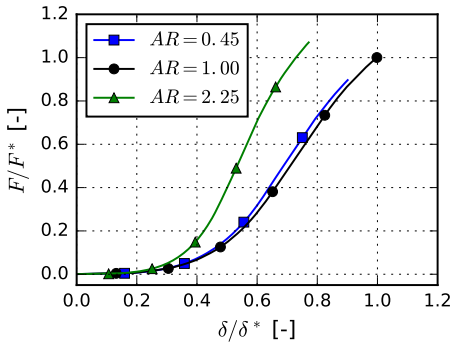


Figure 4.18: Effect of the panel aspect ratio on the mechanical behaviour of the mesh panel.

by $0.85 \leq AR \leq 1.0$. Nevertheless, the adoption of panels that are more elongated along the horizontal direction (i.e. $AR > 1$) is more effective than using panels more elongated along the horizontal one in order to reduce the deflection value at failure. Having said that, from the observation of Fig. 4.19b it is evident that the deflection δ_{max} of the mesh panel is mostly controlled by the size of the mesh panel, while the effect of AR is more limited.

Finally, it is interesting to consider the effect of a variation of the mesh panel dimension and of its aspect ratio on the stiffness of the mechanical response of the mesh as reported in Fig. 4.19c. A measure of the out-of-plane stiffness is here given by the parameter k_{75}. This is defined as the stiffness of the F-δ curve calculated at the 75% of the maximum force registered in the same simulation. The choice of the reference force value (i.e. $0.75F_{max}$) is arbitrary, in fact, if the second part of the F-δ curve is considered (for $F \gtrsim 0.3F_{max}$), other values of the reference force provide an analogous result in terms of the stiffness parameter above defined. The second part of the F-δ curve is characteristic of the mesh mechanical response ("material response") and the F-δ curve is almost linear in this part as can be observed in Fig. 4.18. Conversely, the first part of the F-δ curve is related both, to a geometrical rearrangement of the mesh wires ("geometrical response") and to the development of a sufficient out-of-plane mesh deformation in order to activate the mesh response against a load in the same direction (activation of the membrane-like resistance). In this part, the stiffness of the F-δ curve progressively increases with the deformation, and it is strongly related to the

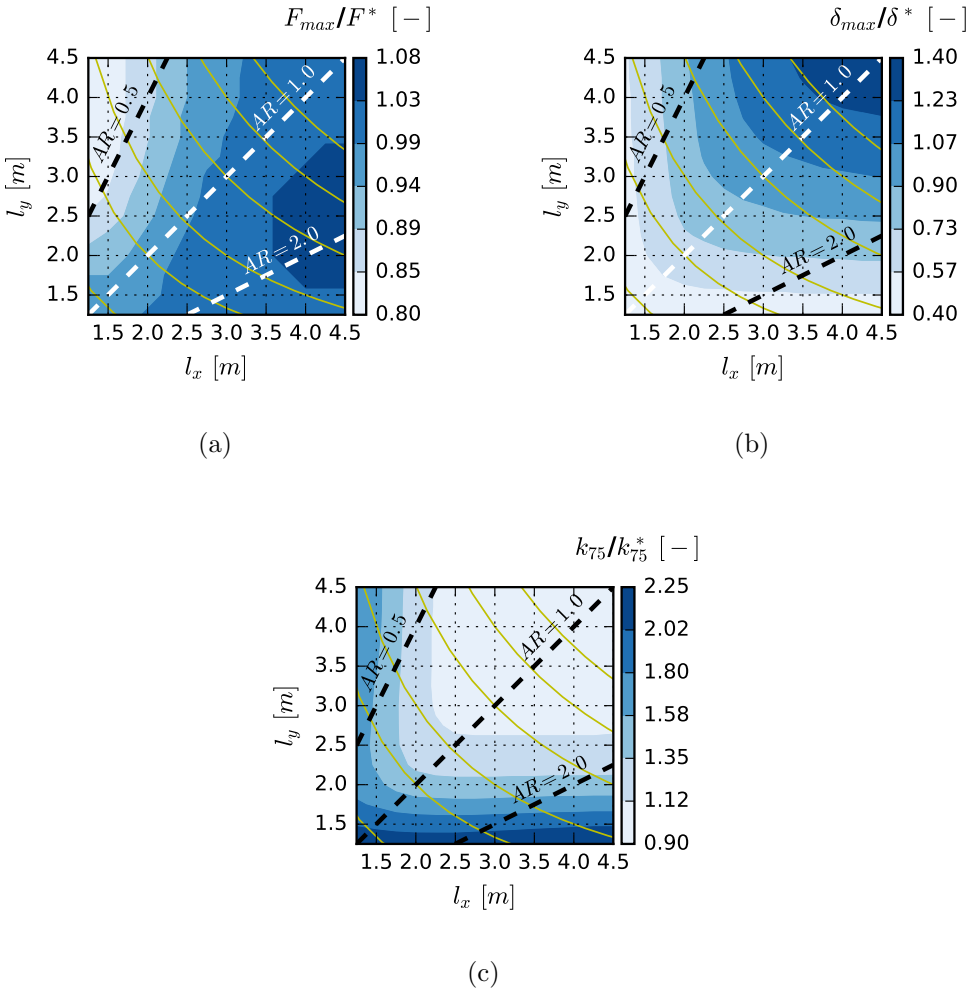


Figure 4.19: Effect of the panel aspect ratio ($AR = l_x/l_y$) in terms of: (a) force F_{max}, (b) deflection δ_{max} values at failure, (c) out-of-plane stiffness k_{75}. The plots are obtained from a linear interpolation of the numerical data and the solid yellow lines indicate equiareal panels.

initial configuration of the panel; therefore it cannot provide a parameter that can be considered as characteristic of the mesh mechanical response. For a fixed size of the mesh panel, the stiffness parameter k_{75} shows a non-monotonic trend and the lower values are obtained for $0.85 \leq AR \leq 1.0$ confirming what has also been observed with reference to the panel deflection δ_{max}. Nevertheless, a reduction of the side length l_y seems more effective in

order to increase the out-of-plane stiffness of the mesh panel. Even if the effect of the AR on the stiffness of the out-of-plane response of the mesh panel cannot be neglected, the numerical data reported in Fig. 4.19c evidence that the panel stiffness is mostly controlled by the size of the mesh panel.

The results above discussed have pointed out that the aspect ratio of the mesh panel can significantly influence its mechanical response, highlighting the effect related with the anisotropy that characterises the mechanical behaviour of the DT mesh. Nevertheless, it should be noted that the effect of the aspect ratio on the panel mechanical response may significantly vary when changing the boundary conditions of the panel because of the possible variation of the force transmission mechanism. This will be discussed in Sec. 4.2.2 when considering the mechanical behaviuor of an anchored mesh panel.

4.2 Punch test on an anchored panel: an idealisation of the in-situ conditions

The standard UNI punch test procedure is used as an informative test for the design of secured drapery interventions. Nevertheless, as already mentioned, the constraint conditions applied on the panel (i.e. fixed outer boundary), substantially differ from the ones characterising field applications in which the panel is only locally fixed by means of anchor plates. This difference determines a characterisation of the mesh mechanical behaviour that is not representative of the field conditions, which, if not duly considered, may negatively reflect on the performance of the mesh system. While the implementation of an field test setup may be difficult (a field test setup was implemented by Bertolo et al. [8]), the use of a numerical approach allows this problem to be overcome [44, 105].

In order to move towards typical field conditions two large-scale configurations were simulated in the first phase. In both configurations the mesh has dimensions 12m×12m (45152 nodal particles) and is subdivided into 9 square mesh panels (3m×3m each); the distance between the borders of the lateral mesh panels and the outer boundary of the mesh system was set equal to 1.5m to limit possible boundary effects (see Fig. 4.20). The presence of the anchor plates is simulated by fixing all the degrees of freedom of the nodal particles ideally intercepted by the anchor plates. Square anchor plates of side $d_p = 0.32$m are considered in the model, which represents a standard

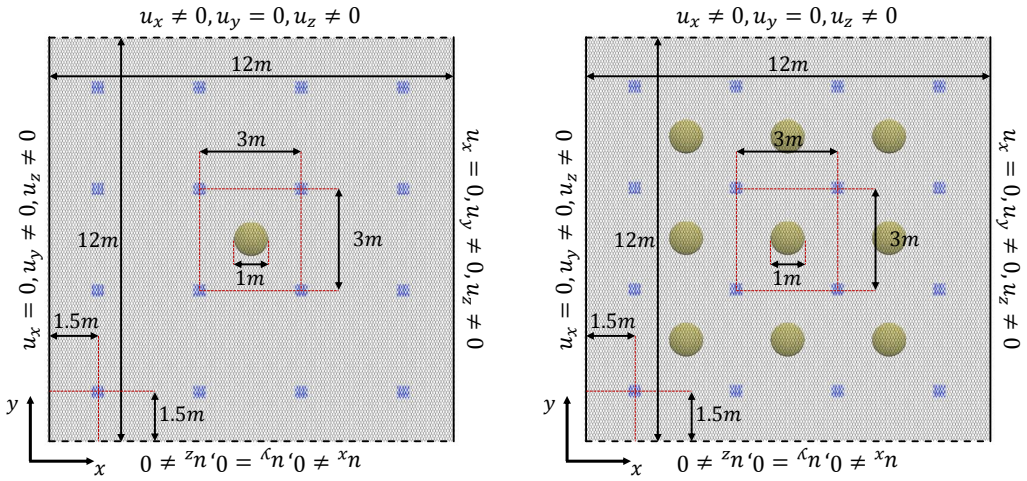


Figure 4.20: View of the large-scale test configuration: (a) *Test A* (b) *Test B* (the fixed nodes are represented with blue spheres)

plate dimension in practice. The loading condition is simulated by using the same punching element (or several punching elements) and the same contact parameters adopted in Sec. 4.1. The punching element is moved with a constant velocity (i.e. $v_z = 0.1$m/s) in a direction perpendicular to the mesh plane until the complete failure of the mesh. In this case, the failure condition is determined by the tear of the mesh at the level of the anchor plates. In the first configuration (*Test A*) a single punching element is considered, acting in the centre of the mesh system as shown in Fig. 4.20a. This condition ideally simulates the load caused by a single unstable block similarly to what was considered in [105]. In the second configuration (*Test B*), a punching element is considered acting on each mesh panel (i.e. 9 punching elements are simulated) as shown in Fig. 4.20b. This condition ideally simulate the restrictive case in which each mesh panel has to support a single block and cannot share the external load with neighbouring panels, as instead happens in *Test A*. In both configurations, the output is represented by the force-displacement curve referred to the punching element acting on the central mesh panel (in *Test B* differences in terms of maximum force are lower than 10% between the different panels); the final point of the force-displacement curve refers to the maximum force value measured during the test. The mechanical response obtained in *Test A* and *Test B* is reported in Fig. 4.21.

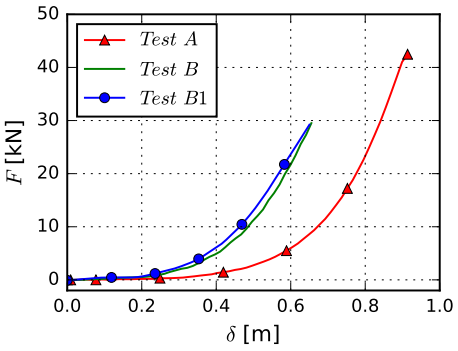
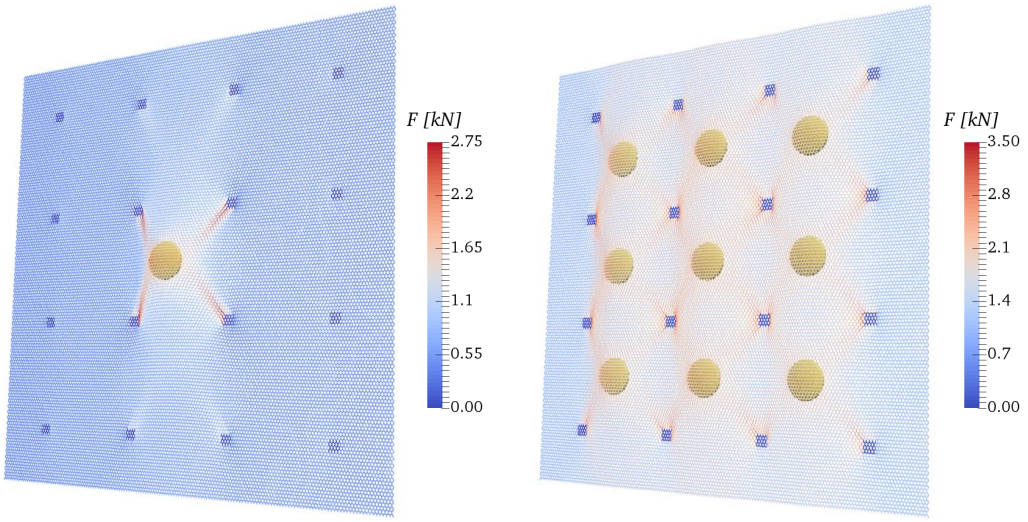


Figure 4.21: Comparison of the mechanical response obtained from the different test configurations (*Test A*, *Test B*, *Test B1*)

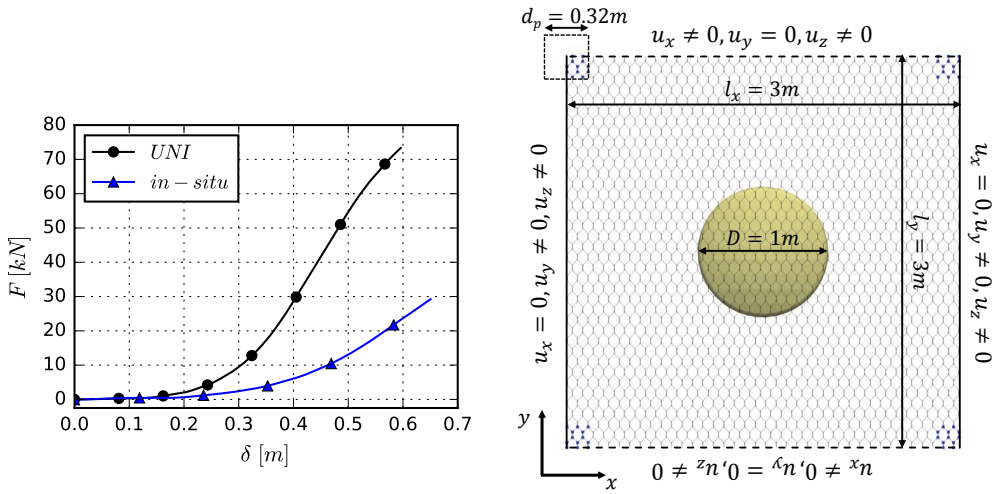
In the former configuration a higher localised force can be sustained by the mesh (F_{max} = 43.3kN in *Test A*, F_{max} = 31.3kN in *Test B*), because the load can be shared between the different panels (see Fig. 4.22a). In *Test B* instead, the load imposed by the punching element is entirely sustained by a single panel, the loading condition being the same for each mesh panel (see Fig. 4.22b). Even if a condition similar to *Test B* configuration may be unlikely in practice, it provides a lower bound estimation of the puncturing resistance of an anchored mesh panel. From the perspective of characterising the mesh resistance to be used in the design phase of secured drapery systems, the adoption of *Test B* configuration is more conservative. Finally, the *Test B* configuration is schematised by using a "periodic" single panel test configuration (*Test B1*). In this a quarter of a square anchor plate of side length d_p is considered at the panel corners and periodic boundary conditions are imposed on the panel edges (i.e. the displacement along the direction parallel to the mesh side is fixed). For the sake of clarity, a sketch of the model of the *Test B1* configuration is reported in Fig. 4.23b. This approximation permits a significant reduction of the computational cost of the simulation, and entails a negligible effect on the mechanical response of the mesh as observable comparing the force-displacement curves reported in Fig. 4.20b. Therefore the "periodic" single panel configuration (*Test B1*) is adopted in the following in order to analyse the mechanical response of an anchored mesh panel. This configuration permits a more representative schematisation of the field conditions, and in this sense, it will be referred as "in-situ" punch test configuration in the following. In order to quantify the



(a) (b)

Figure 4.22: Tensile force distribution on wires for the test configuration: (a) *Test A* and (b) *Test B*. The mechanical condition refers to an instant before the failure of the mesh.

difference in terms of mechanical response of the mesh panel, moving from the laboratory to "idealised" field conditions (i.e. anchored mesh panel), the force-displacement curve obtained from the standard UNI punch test is compared with the one obtained in the "in-situ" punch test configuration as reported in Fig. 4.23a. A significant reduction of the maximum sustainable force is observed when considering more realistic boundary conditions: $F^* = 73.3$kN in the standard UNI configuration, $F_a^* = 29.1$kN in the "in-situ" configuration. This is due to the lower number of wires that can sustain an out-of-plane force (i.e. fixed nodal particles in the model). In the standard UNI punch test all the wires converging to the panel outer boundary are able to sustain an out-of-plane load; considering an anchored panel, the number of wires that can sustain such a kind of loading condition is significantly lower (i.e. only the wires intercepted by the anchor plates). The failure modality is also different in the two cases: in the standard UNI punch test the failure is observed in correspondence with the punching element (see Fig. 4.3), while it occurs in proximity to the anchor plates considering the "in-situ" punch test configuration (see Fig. 4.24). A 3D view of the time evolution of the numerical punch test is reported in Fig. 4.24 highlighting



(a) (b)

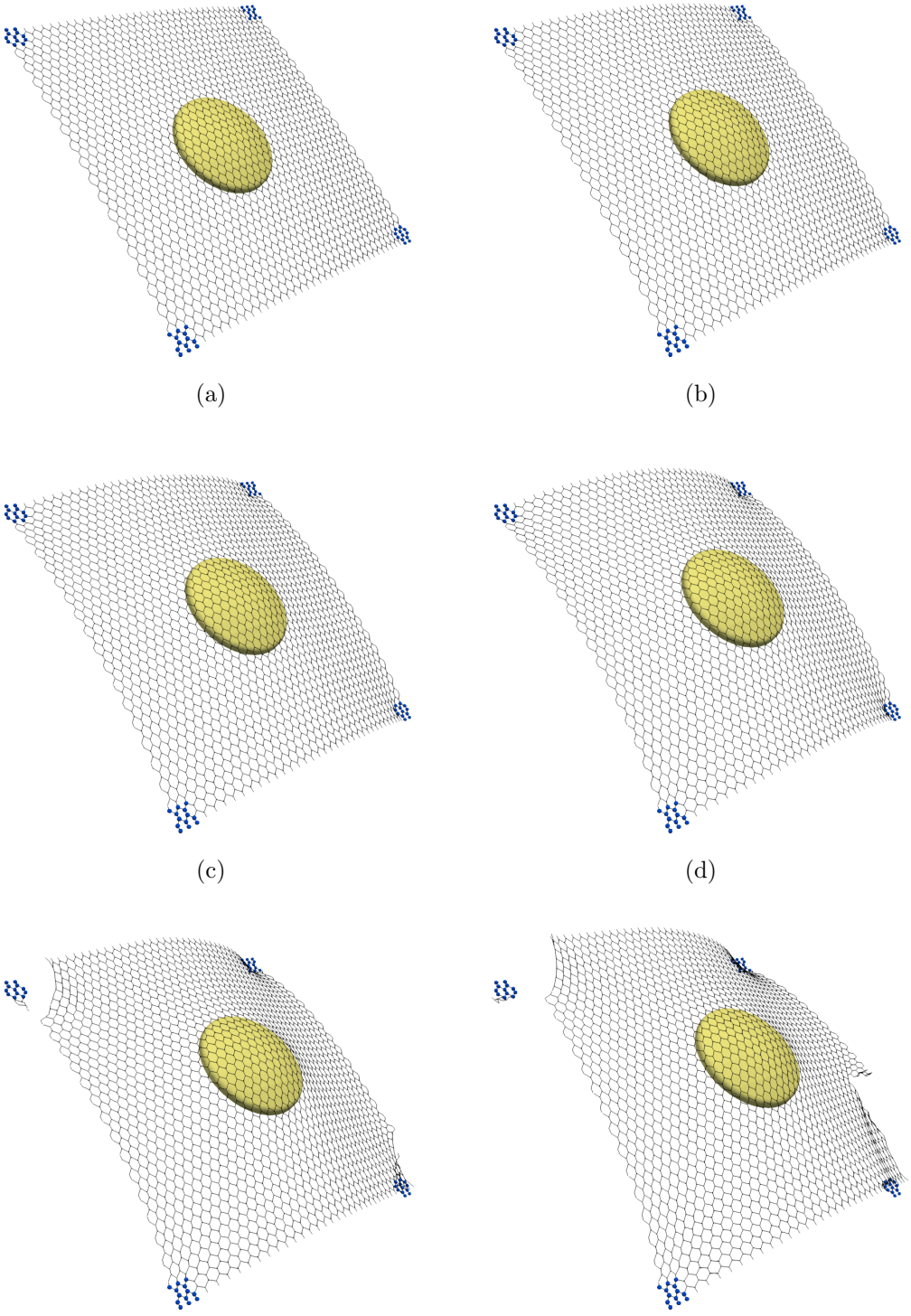
Figure 4.23: (a) Mechanical response of the mesh panel and (b) geometrical scheme of the idealised "in-situ" configuration numerical model.

the failure modality and its propagation inside the mesh panel.

The ratio between the maximum force obtained in standard UNI conditions and the one obtained considering an anchored mesh panel ($\alpha_F = F_a^*/F^* \approx 0.40$) can be used, to a first approximation, in order to estimate the reduction of the panel's ultimate strength moving from laboratory to field conditions. The same reasoning can be applied for the maximum deflection ($\alpha_\delta = \delta_a^*/\delta^* \approx 1.08$). From the comparison of the F-δ curves of Fig. 4.23a it is also evident that the out-of-plane stiffness of the mesh is significantly lower when considering an anchored panel. However, these results are significantly influenced by the geometry of the problem (e.g. anchor size and spacing, punching element size and position) and the mesh mechanical properties, therefore should be carefully considered. Moreover, the panel deformability in field application is strongly related to the installation phase and to the slope morphology that may affect the adherence between the mesh and the slope surface.

4.2.1 Internal mechanical behaviour of the mesh panel

The internal mechanical behaviour of the mesh panel in the "in-situ" punch test configuration is investigated in analogy with what has been done with



(a) (b) (c) (d) (e) (f)

Figure 4.24: 3D View of the evolution of the "in-situ" punch test (the fixed nodes of the mesh are represented with blue spheres).

reference to the standard UNI punch test condition in Sec. 4.1.2. In particular, the tensile stress distribution on the wires and the transmission mechanism of the external force inside the mesh panel are addressed. The tensile stress distribution is reported in Fig. 4.25, firstly for the single wires (+45° oriented) and the double twisted wires separately, then considering a generalised stress distribution. They are referred to the mesh mechanical condition an instant prior to its failure. In analogy with what has been observed in the standard UNI punch test configuration, the single wires experience a higher stress than the double twisted wires. Moreover, for both the wire types, the stress distribution appears homogeneous in correspondence with the punching element. Considering the single wires (Fig. 4.25a), a pronounced cross-shaped with 45° oriented arms stress distribution is observed (the stress distribution of -45° oriented single wires is symmetrical with respects to the y-axis). The stress migrates following the shortest path, namely along the ±45° oriented directions that connect the centre of the panel to the anchor plates. Furthermore, a strong localisation of tensile stresses is observed in the zones surrounding the anchors plates. These are in fact the zones from which the failure of the mesh starts (see Fig. 4.24). An analogous distribution can be observed for the generalised tensile stress (computed considering both wire types), while the stress level acting on the double twisted wires is too low to permit the shape of the distribution to be appreciated.

The role of the double twisted wires can be better understood considering the tensile force distribution as reported in Fig. 4.26. Also in this case the plots refer to an instant prior to the mesh failure. A cross-shaped distribution is observed for both the wire types, showing that the internal force transmission mechanism is significantly different from the one observed in the standard UNI punch test. In this case, the thrust force imposed by the punching element is transmitted diagonally from the centre of the panel to the anchors. In the standard UNI punch test instead, the force was mainly transmitted vertically following the direction of the double twisted wires. This difference in the internal force transmission permits the reduction of the stiffness of the mesh mechanical response (i.e. F-δ curve), observed by adopting the "in-situ" testing conditions, to be explained. In Sec. 4.1.2 it has been shown that the DT mesh is characterised by a higher tensile stiffness in the direction parallel to the double twisted wires. In the "in-situ" test, the load is only partially transmitted along this direction, and thus the anisotropic behaviour of the DT mesh is not optimally exploited leading

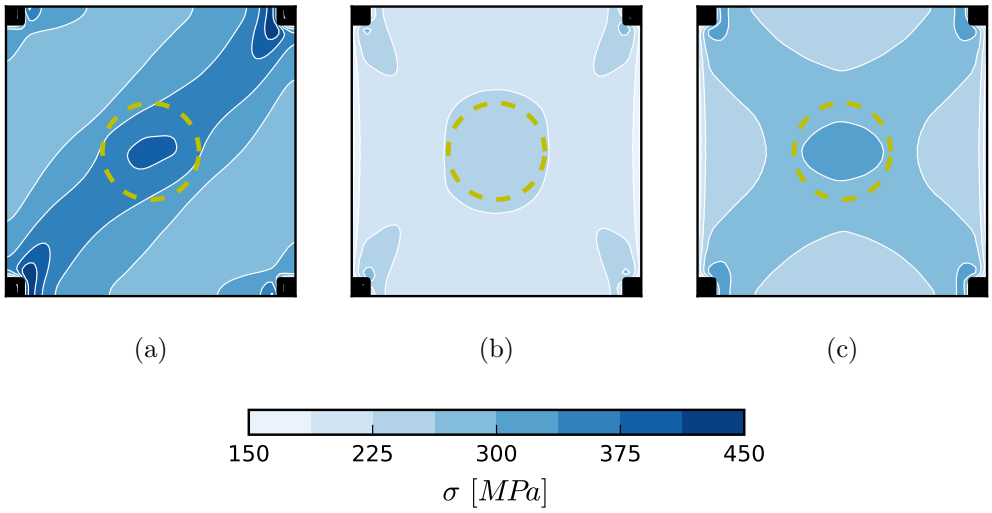


Figure 4.25: Tensile stress distribution, an instant prior to the mesh failure, on (a) single wires (+45° oriented), (b) double twisted wires and (c) both wire types.

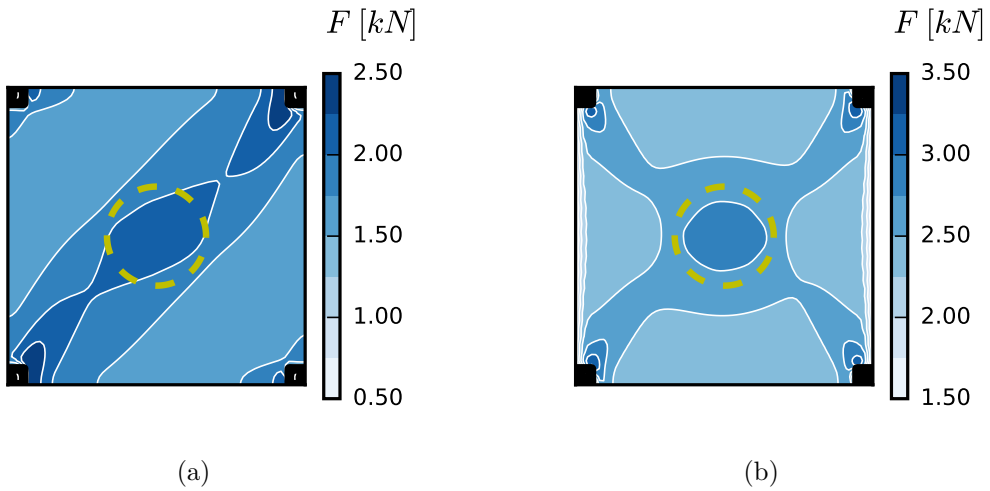
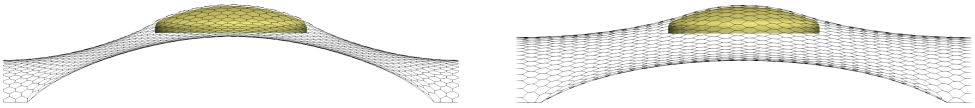


Figure 4.26: Tensile force distribution, an instant prior to the mesh failure, on (a) single wires (+45° oriented) and (b) double twisted wires.



(a) (b)

Figure 4.27: Lateral view of the numerical model of the "in-situ" punch test an instant prior to the mesh failure: (a) x-z plane and (b) y-z plane.

to a "softer" response of the mesh panel. This condition is confirmed by considering the lower tensile forces registered in the double twisted wires in the "in-situ" test conditions than in the UNI test conditions (compare Fig. 4.10b and Fig. 4.26b). Finally, two lateral views of the mesh panel along the x-z plane and the y-z plane, an instant prior to its failure, are reported in Fig. 4.27a and Fig. 4.27a respectively. Comparing the lateral views, a difference in the deformed configurations is observed, highlighting the effects of the anisotropy of the DT mesh. As already observed in Sec. 4.1.2, the deformability of the mesh is higher in the direction orthogonal to the double twisted wires, and this causes a different profile of the deformed configuration of the mesh with respect to the two considered planes.

4.2.2 Parametric analysis

In analogy with what has been done for the standard UNI test, a parametric analysis is performed also with reference to the "in-situ" punch test. The influence of the size and position of the loading element, as well as the role of anchors plate dimension and spacing are discussed in the following. Finally, the dependency of the mechanical response on the aspect ratio of the mesh panel is investigated. The results of the parametric analysis will permit information for helping the practitioners to extend the standard mesh characteristic values, derived from laboratory tests, to field conditions to be provided. Furthermore, they give useful information in order to account for the different variables of the problem during the design phase. For facilitating the comparison, all the results are normalised on the values of the force F_a^* (29.1kN), the deflection δ_a^* (0.65m) at failure and the stiffness parameter $k_{75,a}^*$ (105kN/m) obtained for the 3m×3m "in-situ" punch test configuration with a centred punching element and square anchor plates of side $d_p = 0.32$m.

l_x [m]	l_y [m]	D [m]	*pos. punch* [m]	d_p [m]	n_{sim}
3.0	3.0	1.0	(1.5, 1.5)	0.32	1
3.0	3.0	**0.1-2.5**	(1.5, 1.5)	0.32	48
3.0	3.0	1.0	(**0.0-1.5,0.0-1.5**)	0.32	2118
3.0	3.0	1.0	(1.5, 1.5)	**0.08-0.64**	8
1.5-4.5	**1.5-4.5**	1.0	(1.5, 1.5)	0.32	196

Table 4.2: Summary of the parameter sets considered in the parametric analysis. The first row corresponds to the reference test. Bold fonts are used to mark the parameters that differ from the reference test providing their range of variation (n_{sim} represents the number of performed simulations).

Effect of the size of the punching element

In the design phase of a secured drapery system, the expected dimension and sharpness of the unstable blocks should be carefully accounted to optimise the system's mechanical performances. The knowledge of how the geometry of the unstable block influences the mechanical response of the mesh panel is therefore of great importance. In this perspective, dimension D of the punching element is varied ranging from 0.1m to 2.5m with an incremental step of 0.1m. As introduced in Sec. 4.1.3, the variation of the dimension of the punching elements permits one to consider, in addition to scale effects related to the block dimension, also the impact of block sharpness on the mesh mechanical response. The main effect of block angularity is to vary the contact surface between the block and the mesh, thus a reduction of the punching element dimension may represent a simple but effective way to consider the reduction of the contact surface associated with an increment of block angularity. In other words, the sharper the assumed block, the lower the punching element dimension considered in the model. Having said that, in order to have a complete mechanical characterisation of the mesh panel, the failure condition is reached independently of the considered dimension of the punching element. The numerically obtained F-δ curves are reported in Fig. 4.28a for five different values of D (i.e. D/D^*=0.1, 0.2, 0.4, 1.0, 2.0). For the lower D/D^* ratios (i.e. $D/D^* \leq$0.40) an increment of the punching element dimension leads to a significant increase of the maximum sustainable force F_{max}, while further increments of D seem to have a negligible effect on

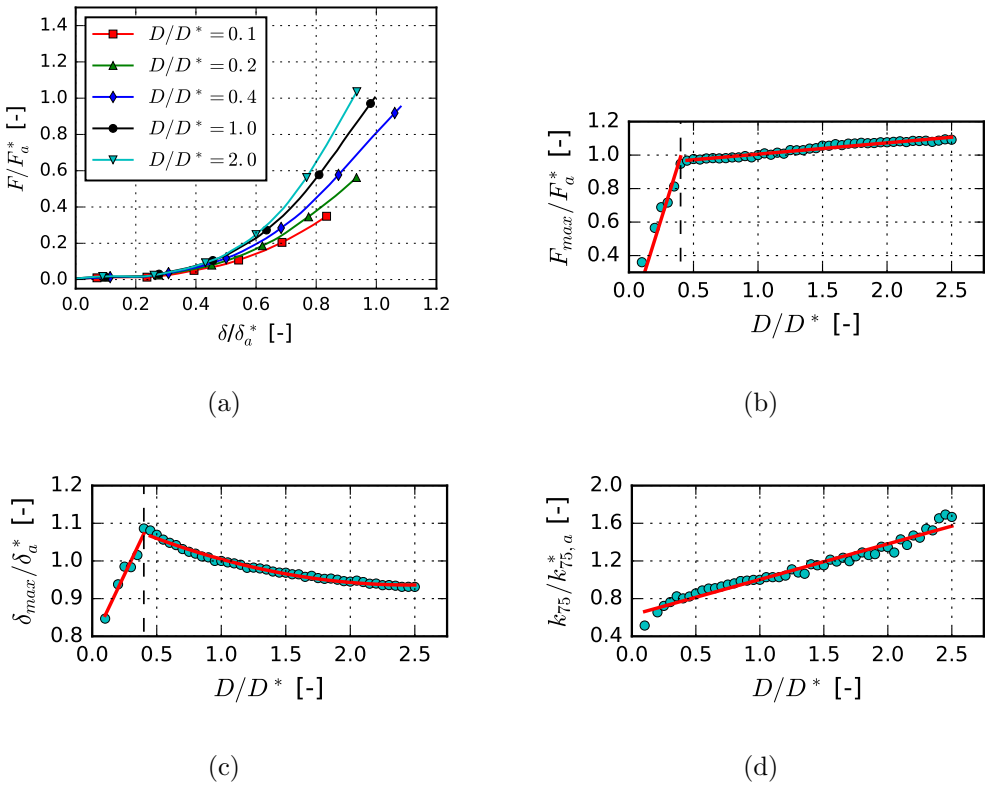
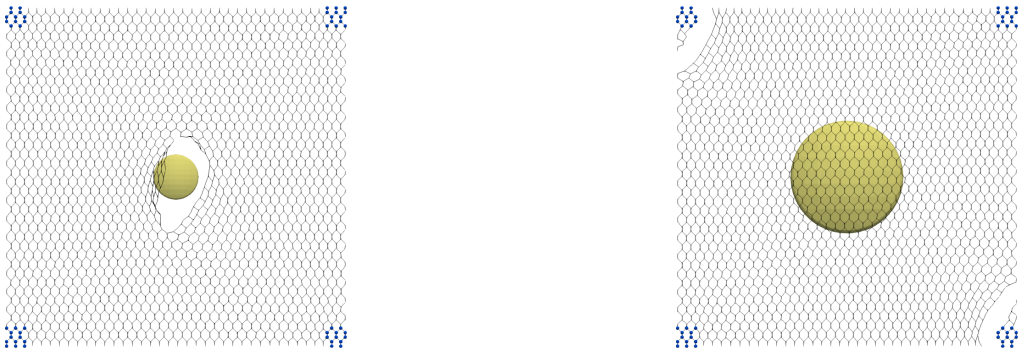


Figure 4.28: (a) Effect of the punching element size on the mechanical behaviour of the mesh panel, trend (b) of the maximum force F_{max} (fit Eq. 4.4), (c) of deflection δ_{max} at failure (fit Eq. 4.5) and (d) of stiffness parameter k_{75} (fit Eq. 4.6).

the F_{max} value. Considering, the deflection at failure δ_{max} instead, this firstly increases with D, then tends to decrease for the higher values of the punching element dimension. Finally, the stiffness (i.e. k_{75} stiffness parameter) of the mesh mechanical response seems to monotonic increase when increasing the punching element dimension. These preliminary results are confirmed analysing the trends of the above mentioned parameters in the entire range of variation of D as reported in Fig. 4.28b, 4.28c and 4.28d. Considering the value of F_{max}, this considerably increases when increasing the punching element dimension for $D/D^* \leq 0.4$. After this threshold, the increase of F_{max} with D is greatly reduced as shown in Fig. 4.28b. Such a change of behaviour is related to the variation of the failure modality of the mesh panel. In the former case (i.e. $D/D^* \leq 0.4$), the mesh failure starts at the centre

of the panel, namely in correspondence with the punching element. This failure modality is similar to the one observed in the standard UNI punch test, and in fact a similar trend of F_{max} is observed (strong increase of F_{max} with D). In the latter case (i.e. $D/D^* > 0.4$) instead, the failure moves close to the anchor plates. For the sake of clarity, the two failure modalities, observed in the simulations, are shown in Fig. 4.29. The variation of the failure modality is observed for a threshold value of D that is very close to the anchor plate dimension ($D = 0.4$m and $d_p = 0.32$m). The maximum force of an anchored mesh panel is limited by the available resistance at the mesh-plate connection, which can be considered a function of the number of wires intercepted by an anchor plate. In this perspective, when considering a punching element characterised by a dimension lower than the anchor plate dimension, the former intercepts a lower number of wires (small interacting surface), and thus the mesh fails in correspondence of the punching element. In the opposite case (i.e $D \gtrsim d_p$), the larger interacting surface between the mesh and the punch permits avoidance of a premature failure, and the mesh fails at the mesh-plate connection when the maximum available resistance of the latter is overcome. In this case, the anchor plate can be seen as the "new punching element". The two observed failure modalities can be characterised on the basis of where the local punching mechanism takes place. In this sense, it is possible to define a "block-punching" failure mechanism when $D \lesssim d_p$ and an "anchor-punching" failure mechanism when $D \gtrsim d_p$. Finally, the slight increment of the maximum force observed when increasing the punching element dimension over the threshold values $D = 0.4$ may be attributable to a better redistribution of the forces inside the mesh panel. The effect of the two different failure mechanisms is also observable with regard to the trend of the deflection at failure δ_{max} as reported in Fig. 4.28c. An increase of δ_{max} with D is observed if the mesh failure is characterised by the "block-punching" mechanism. In fact, under this condition an increase of D permits a delay of the failure of the mesh panel related to the puncturing at the punch-mesh contact. Conversely, if the mesh failure is characterised by the "anchor-punching" mechanism, a reduction of δ_{max} when increasing D is observed. In this case, a larger punching element determines a prompter response of the mesh, the distance between the punching element edges and the anchor plates being lower, thus determining a reduction of the mesh panel deflection. Furthermore, the effect of a larger contact surface between the punch and the mesh permits the external load to be better redistributed



(a) (b)

Figure 4.29: Failure mechanism observed in the numerical simulation for a punch dimension of (a) $D = 0.40$m, (b) $D = 1.0$m (reference case).

on the mesh panel. Finally, it is interesting to analyse the influence of the punching element dimension on the mesh panel out-of-plane stiffness; also in this case the stiffness of the mesh panel mechanical response is represented with the stiffness parameter k_{75}. The data reported in Fig. 4.28d, show a linear increase of the stiffness parameter k_{75} with the punching element dimension D, and no significant differences are observed moving from one to the other failure mechanism. The stiffness of the mechanical response therefore can be considered as independent of the failure modality. The increase of the stiffness parameter k_{75} is related to greater proximity of the punching element edges to the anchor plates, which shortens the mesh-internal transmission force path. Almost identical results were found considering stiffness parameters defined with reference to other force values (e.g. k_{40}, k_{50}, k_{60}, ect.).

In conclusion, the effects of a variation of the punching element dimension, namely the influence of block-mesh interaction surface, can be summarised as follows. The failure of the mesh may occur in correspondence with the punching element (i.e. the unstable block) or near the anchor plates. The transition between the two failure mechanisms is governed by the anchor plate dimension d_p, which determines the available resistance at the mesh-plate connection. For small values of D (i.e. sharp block assumption), the mesh fails in correspondence with the punching element because the local puncturing resistance at the mesh-punch contact is lower than the resistance at the mesh-plate connection ("block-punching" failure mecha-

nism). For further increments of D (i.e. rounded large block assumption), the puncturing resistance at mesh-punch interface becomes larger than the one at the mesh-plate connection and thus the failure moves close to the anchor plates ("anchor-punching" failure mechanism). In practical applications, both of the above mentioned failure modalities can be observed. The former mechanism is the most likely when a sharp block interacts with the mesh panel, and therefore the contact surface with the mesh is reduced. The "anchor-punching" mechanism is instead typical when dealing with a rounded and/or large block interacting with the mesh system (this failure mechanism is the most likely also when considering retaining applications in soil or highly fragmented rock slopes as will be analysed in Chapter 6).

Finally, from the numerical results, the influence of D on the mesh mechanical response can be described by the following relationships. The relation between the maximum force supportable by the mesh panel F_{max} and the punching element dimension D can be expressed as follows (linear least squares fit):

$$\begin{cases} F_{max} = 2.47\frac{D}{D^*}F_a^*, & \text{if } D \lesssim d_p \\ F_{max} = \left(0.06\frac{D}{D^*} + 0.94\right)F_a^*, & \text{if } D \gtrsim d_p \end{cases} \tag{4.4}$$

The relation between the panel deflection at failure δ_{max} and the punching element dimension D can be expressed as follows (second order polynomial least squares fit):

$$\begin{cases} \delta_{max} = \left(0.72\frac{D}{D^*} + 0.78\right)\delta_a^*, & \text{if } D \lesssim d_p \\ \delta_{max} = \left[0.03\left(\frac{D}{D^*}\right)^2 - 0.16\frac{D}{D^*} + 1.13\right]\delta_a^*, & \text{if } D \gtrsim d_p \end{cases} \tag{4.5}$$

The relation between the stiffness parameter k_{75}, representing the out-of-plane stiffness of the mesh panel, and the punching element dimension D can be expressed as follows (linear least squares fit):

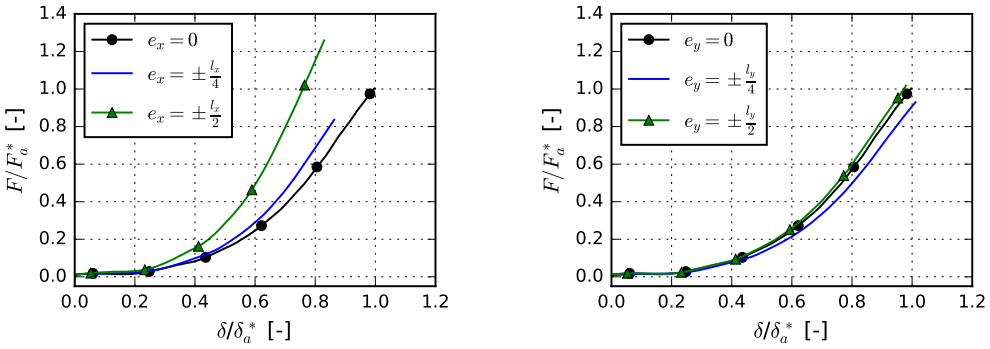
$$k_{75} = \left(0.38\frac{D}{D^*} + 0.62\right)k_{75,a}^* \tag{4.6}$$

It should be noted that the above reported relationships were obtained considering a square anchor plate of dimension $d_p = 0.32$m; the adoption a different shape and dimension of the anchor plates may introduce a variation of the numerical coefficients.

Effect of the position of the punching element

The position of a possible unstable block on the mesh panel, or more precisely, the relative position between the block and the anchors, can somehow be controlled during the installation of a secured drapery system. Therefore, it may be interesting to investigate its effect on the mechanical response of an anchored mesh panel. In the first phase, the effect of a shift of the punching element along the central axes of the mesh panel is analysed similarly to what has been done in Sec. 4.1.3. This permits the effects related to the DT mesh mechanical anisotropy to be highlighted. Successively, the punching element is "freely" moved on the mesh panel (a dense grid spaced by 4cm is considered) in order to characterise the value of F_{max} and δ_{max} with reference to a generic shift e_x, e_y.

In Fig. 4.30 the force-displacement curves obtained by shifting the punching element along the panel central axes are reported. The same shifts are applied along both axes, namely $e_j = \pm l_j/4$ and $e_j = \pm l_j/2$ (subscript j represents the shift direction). The results relating to a shift along the x-axis (i.e. $e_x \neq 0$) are reported in Fig. 4.30a, while the results relating to a shift along the y-axis (i.e. $e_y \neq 0$) are reported in Fig. 4.30b. In the former case, a significant variation of the mechanical response is observed both in terms of maximum sustainable force and out-of-plane stiffness of the F-δ curve. Furthermore, a non-monotonic effect on the F-δ curve is observed: for $e_x = \pm l_x/4$ a decrease of the maximum force is observed ($F_{max} \approx 0.85F_a^*$), while for $e_x = \pm l_x/2$ the maximum force is greater than the one obtained from a centred case ($F_{max} \approx 1.25F_a^*$). The shift $e_x = \pm l_x/2$ also determines a significant increase of the stiffness of the mesh panel response (i.e. $k_{75}\,(e_x = \pm l_x/2, e_y = 0) \approx 1.6k_{75,a}^*$). Conversely, a shift along the y-axis has a very low influence on the mesh panel response, and the F-δ curves obtained are almost coincident, as shown in Fig. 4.30b. The significant difference in the mesh mechanical response, associated to the direction of the punching element shift, can be explained by observing the force distribution on the mesh panel as reported in Fig. 4.31. The contour plots represent the tensile force distribution (computed considering both wire types) an instant prior to the mesh failure, and they refer to the centred case and the two extreme ones, namely $(e_x = \pm l_x/2, e_y = 0)$ and $(e_x = 0, e_y = \pm l_y/2)$. Comparing the force distributions, it is evident that the internal force transmission mechanism is significantly different when the punch is placed in-between two anchor rows

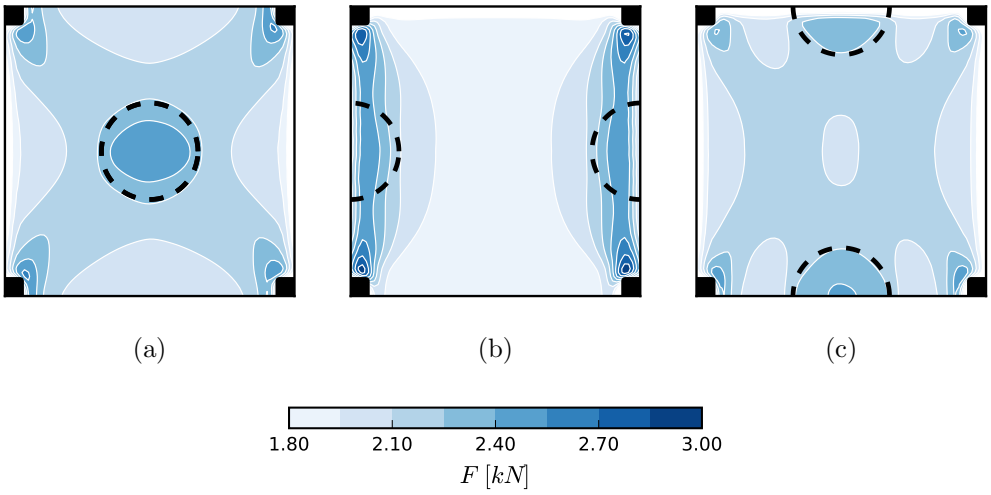


(a) (b)

Figure 4.30: Effect of the punching element position on the mechanical behaviour of the mesh panel for a shift along (a) the x-axis and (b) the y-axis.

($e_x = \pm l_x/2, e_y = 0$) from the one observed in the others two configurations. In this case, the thrust force imposed by the movement of the punching element is transmitted vertically, and the transmission path is shorter than in the other two cases. A lower transmission path determines a stiffer response of the mesh, while the vertical direction of the force transmission permits a better exploitation of the double twisted wires, which reflects on an increase of the maximum sustainable force.

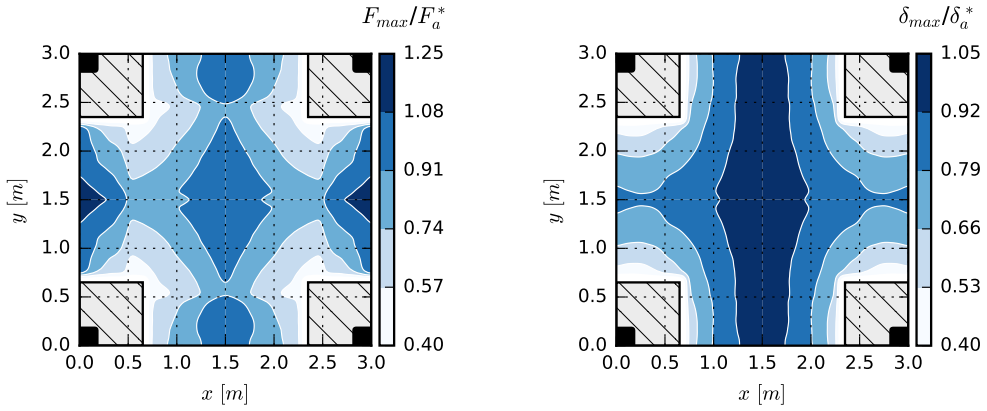
The effect of a generic shift (e_x, e_y), on the maximum sustainable force and on the deflection value at failure, can be observed in the contour plots of Fig. 4.32a and Fig. 4.32b respectively. They are obtained by a linear interpolation of the numerical data on the same grid used for defining the punch shift. The light grey areas at the corners represent the zones where the punching element cannot be placed because of the interference with the edges of the anchor plates, while latter are represented by the smaller black areas. The contour plots show that the effect of the position of the punching element, on the mechanical behaviour of the mesh is not trivial. The anisotropy of the mesh mechanical response is particularly evident observing the trend of the deflection at failure. A very slight influence is observed moving the punching element in the vertical direction, while a shift along the horizontal direction entails a significant variation of δ_{max}. In particular, in the latter case, the deflection at failure diminishes when moving towards the boundary of the mesh panel. Concerning the trend of the maximum



(a) (b) (c)

(d)

Figure 4.31: Tensile force distribution (on both wire types), an instant prior to the mesh failure, for different position of the punching element: (a) (x_c, y_c), (b) $\left(x_c \pm \frac{l_x}{2}, y_c\right)$ and (c) $\left(x_c, y_c \pm \frac{l_y}{2}\right)$.



(a) (b)

Figure 4.32: Effect of the punching element position: (a) contour plot of maximum force value F_{max} and (b) contour plot of deflection values δ_{max} at failure. The contour plots are obtained from a linear interpolation of the numerical data on a regular grid with a spacing of 4cm.

force F_{max}, it is useful to consider the central part of the panel, namely $0.5m \leq x \leq 2.5m$ and $0.5m \leq y \leq 2.5m$, separately from the remaining four parts, which are comprised between the anchor plates.

In the central part, shifting the punch along the y-direction leads to a slight variation of the F_{max}, while the effect on F_{max} is more significant moving it along the x-direction. Three zones of local maximum of F_{max} are observable, they are approximately located corresponding to a symmetric position of the punching element with reference to the anchor plates, namely (x_c, y_c), $(x_c \pm l_x/2, y_c)$ and $(x_c, y_c \pm l_y/2)$. The global maximum of force is observed for a punching element aligned in-between two anchors rows $(x_c \pm l_x/2, y_c)$; furthermore this position presents also the highest overall mesh stiffness (i.e. $k_{75}\left(x_c \pm l_x/2, y_c\right) \approx 1.6 k^*_{75,a}$).

From this analysis it can be argued that the relative position between the punching element and a possible unstable block influences the mechanical behaviour of an anchored mesh panel. In particular, a significant gain in terms of both maximum sustainable force and out-of-plane stiffness of the mesh panel is observed when the block is comprised in-between two anchor rows. It is therefore advisable, when possible, to consider the position of the unstable blocks on the slope face during the design and the installation phases of a secured drapery system in order to optimise its mechanical behaviour in terms of retaining capacity and panel deformability.

Effect of the anchor plate size

The dimension of the anchor plate is one of the controllable design parameters of a secured drapery system together with the mesh type, the anchor spacing and the panel aspect ratio (these latter two will be analysed in the following of the parametric analysis). It was already observed that the maximum force sustainable by an anchored mesh panel is limited by the available resistance at the mesh-anchor connection and that the latter is mainly controlled by the anchor plate dimension (for the same mesh type). Nevertheless, a quantitative estimation of the effect of a variation of the dimension d_p of the anchor plate was not provided. In order to characterise a relationship between the maximum sustainable force and the plate dimension, the latter is varied in the range $0.16\text{m} \leq d_p \leq 0.64\text{m}$ with an incremental step of 0.08m. It is worth mentioning that in practical application the anchor plate size is limited to $0.16\text{m} < d_p < 0.40\text{m}$, however larger values are adopted in

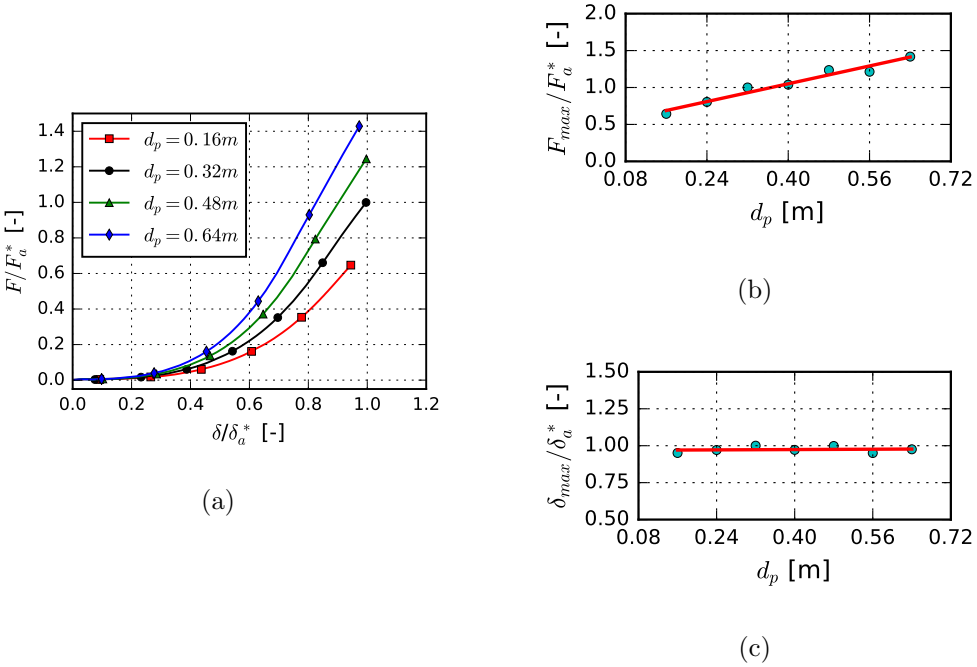


Figure 4.33: (a) Effect of the punching element size on the mechanical behaviour of the mesh panel, trend (b) of the maximum force F_{max} (fit Eq. 4.7) and (c) of the deflection δ_{max} at failure (fit Eq. 4.8).

the numerical model to obtain a wider range of values for the definition of a relationship between F_{max} and d_p.

The numerical results are reported in Fig. 4.33a in terms of force-displacement curve, while the trends of the maximum force and of the deflection at failure are shown in Fig. 4.33b and Fig. 4.33c respectively. Considering the F_{max} value a linear increasing trend is observed when increasing the plate dimension d_p. In fact, an increase of d_p leads to a higher number of wires intercepted by the anchor plate, thus a higher force can be sustained by the mesh panel. It is also interesting to note that the linear trend is in analogy to what is observed when increasing the punching element size; in fact in this case the failure of the mesh is characterised by an "anchor-punching" mechanism ($d_p < D$), and so the anchor plate can be seen as the punching element. The relation between the maximum sustainable force F_{max} and the anchor plate dimension d_p can be expressed as follows (linear least squares fit):

$$F_{max} = \left(0.48\frac{d_p}{d_p^*} + 0.45\right) F_a^* \qquad d_p \geq 0.16m \tag{4.7}$$

The non-null value of the intercept in the linear fit is associated to the fact that a value of $d_p = 0$ m is meaningless, thus this value is related to the minimum dimension of the anchor plate that can be realistically considered in the model (i.e. $d_p = 0.16$m). Conversely, the deflection at failure δ_{max} is almost unaffected by a variation of the anchor plate dimension. The fit of the numerical data reported in Fig. 4.33c (linear least squares fit) gives the following fit equation:

$$\delta_{max} = \left(0.02\frac{d_p}{d_p^*} + 0.98\right) \delta_a^* \qquad d_p \geq 0.16m \tag{4.8}$$

Finally, an increment of the stiffness of the F-δ curve is observed when increasing the anchor plate dimension (see Fig. 4.33a). The steps trend observed in Fig. 4.33b and 4.33c may be related to the discrete nature of the mesh model. In the latter, in fact, the anchor plate embraces a finite number of nodal particles, which is dependent of the mesh cell geometry.

Effect of the anchor spacing

The anchor spacing i, or equivalently for a square panel, the panel side length (i.e. $i = l_x = l_y$), can be controlled during the design phase of a secured drapery system. It can be argued that the spacing i controls the out-of-plane deformability of the mesh panel (and thus δ_{max}), however it is not trivial to give a quantitative estimation of the effect of i on the mesh panel performance without performing a specific analysis. In this perspective, the anchor spacing is varied ranging from $i = 1.25$m to $i = 4.5$m with an incremental step of 0.25m. Initially, the force-displacement curves obtained for four different values of the anchor spacing (i.e. i =1.5m, 2.0m, 3.0m, 4.0m) are compared in Fig. 4.34a. The numerical results confirm the assumption of an increment of the panel deformability when increasing the anchor spacing, as well as of the maximum deflection at failure.

In order to have a more precise overview of the influence of the anchor spacing on the mesh mechanical response, the trends of F_{max} and δ_{max} as a function of i are reported in Fig. 4.34b and in Fig. 4.34c respectively. The effect of a variation of the anchor spacing i on the maximum force F_{max} can

be estimated by the following relationship (linear least squares fit):

$$F_{max} = \left(0.16\frac{i}{i^*} + 0.84\right) F_a^* \tag{4.9}$$

A variation of i seems to have a slight effect on the maximum force sustainable by the panel. The small increase of the F_{max} value observed when increasing i may be related to a better redistribution of stresses for larger panels. The effect on the deflection at failure is instead significant, and a linear increment of the value of δ_{max} with i is observed in Fig. 4.34c. The trend of δ_{max} is well represented by the following relation (linear least squares fit):

$$\delta_{max} = 0.98\frac{i}{i^*}\delta_a^* \tag{4.10}$$

In light of the obtained results, for practical applications, the maximum force that a mesh panel can sustain may be assumed as independent from the anchor spacing. For instance, considering the two extreme values of the anchor spacing here considered, namely $i = 1.25$ m and $i = 4.5$ m, the increment in terms of F_{max} is approximately equal to the 16%. This increment is very limited, considering that the panel is more than three times larger in the second case. However, the role of the anchor spacing on the mesh panel performance, namely the relationship between the activated force for a given deflection of the panel, cannot be neglected.

In order to better understand this concept, let us define the force F_δ as the force value that can be mobilised for a panel deflection $\delta \leq \delta^d$, where δ^d represents the maximum admissible deflection in serviceability conditions. It should be noted that δ^d is here intended as a design parameter and, generally, does not coincide with the deflection δ experienced by the system. Therefore, if $\delta^d \leq \delta^i_{max}$ (δ^i_{max} is the maximum deflection related to a specific anchor spacing i observed in the numerical characterisation as reported in Fig. 4.34c), the system retaining capacity is only partially mobilised, namely $F_\delta < F^i_{max}$ (F^i_{max} is the maximum force related to a specific anchor spacing i observed in the numerical characterisation as reported in Fig. 4.34b). Conversely, if $\delta^d \geq \delta^i_{max}$ then the system retaining capacity is fully mobilised even for a deflection $\delta < \delta^d$ and therefore one can consider $F_\delta = F^i_{max}$. Finally, the mobilised rate of the system retaining capacity is indicated as $f_m = F_\delta / F^i_{max}$. In Fig. 4.34d, the latter is reported as a function of the anchor spacing i, considering four different values of admissible deflection δ^d. The f_m-i curves thus defined permit evaluation of the system performance, quantifying the

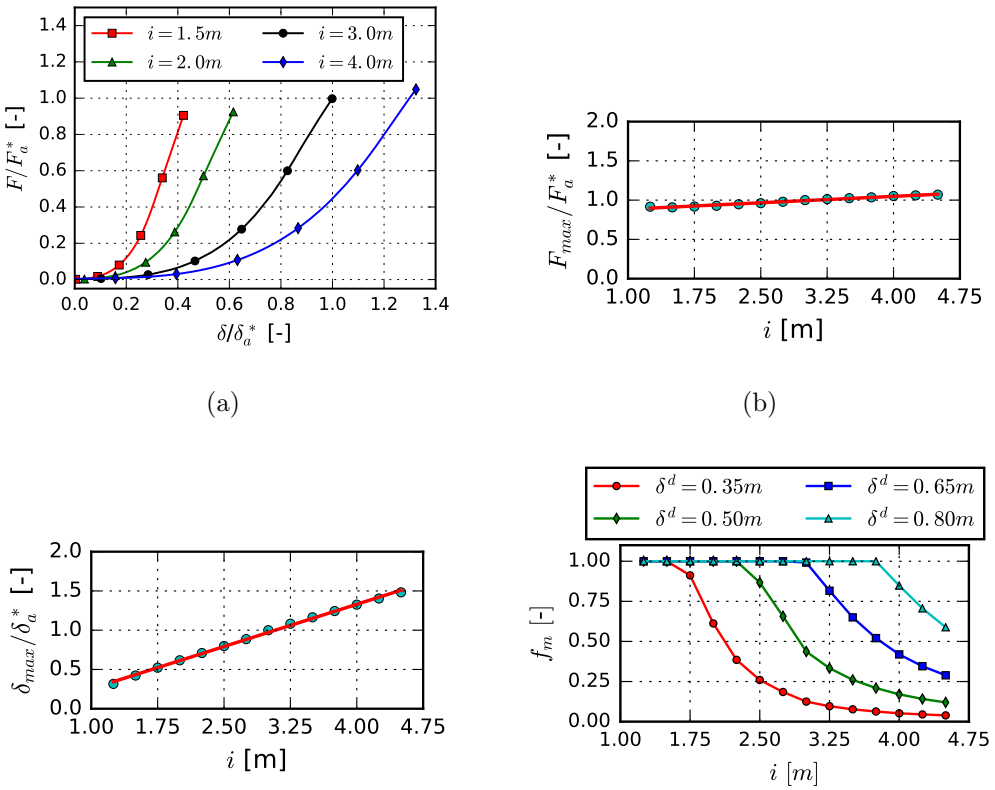


Figure 4.34: (a) Effect of the punching element size on the mechanical behaviour of the mesh panel, trend (b) of the maximum force F_{max} (fit Eq. 4.9) and (c) of the deflection δ_{max} at failure (fit Eq. 4.10). (d) Evolution of the mobilised rate of the retaining capacity f_m as a function of the anchor spacing.

mobilised retaining capacity associated to a given limit condition on the maximum deflection of the system (i.e. $\delta \leq \delta^d$). They represent a useful design tool considering that limitations of system deformations, in serviceability conditions, are generally required, especially when secured drapery systems are applied along railways or other infrastructures. In fact, by means of the f_m-i curves, it is possible to characterise the maximum anchor spacing that permits the required rate of system retaining capacity to be mobilised, and fulfilling at the same time the condition $\delta \leq \delta^d$ on the system deformations.

For instance, if a limit deflection $\delta^d = 0.50$m is imposed in serviceability conditions, the f_m-i curve characterised by $\delta^d = 0.50m$ (green line with

diamond marker in Fig. 4.34d) shows that the mesh panel retaining capacity is fully mobilised for $i \leq 2.25$m (i.e. $f_m = 1.0$, with $\delta \leq \delta^d$), while the retaining efficiency of the intervention is very low for $i \geq 3.0$m (i.e. $f_m < 0.5$, with $\delta = \delta^d$). Furthermore, considering that a reduction of the anchor spacing entails a significant increment of the cost of the system, the benefit related to the use of f_m-i curves also has an effect in financial terms.

Effect of the panel aspect ratio

In order to extend the results related to a simple variation of the mesh panel dimension (i.e. the same variation of the anchor spacing along both directions), the aspect ratio $AR = l_x/l_y$ is varied. The length of the panel sides is varied in the range $1.25\text{m} \leq l_j \leq 4.5\text{m}$ (incremental step of 0.25m) considering one side at a time. Firstly, the effect of AR on the mechanical response of three equiareal panel (i.e. 2m×4.5m, 3m×3m, 4.5m×2m) is considered. From the comparison of the force-displacement curves reported in Fig. 4.35, it is evident that the adoption of a panel which is more elongated along the horizontal direction (i.e. $AR = 2.25$), leads to a significant increment of the panel deformability ($\delta_{max} \approx 1.37\delta_a^*$) and also determines a reduction of the maximum sustainable force with respect to the square panel case ($F_{max} \approx 0.91F_a^*$). Conversely, for $AR = 0.45$, the panel deformability is almost unaffected and an increase of the force sustainable by the mesh panel is observed ($F_{max} \approx 1.11F_a^*$). It is interesting to highlight that the effect of the AR on the mesh mechanical behaviour is the opposite of the one that has been observed when considering the standard UNI punch test condition (Sec. 4.1.3). This is related to the difference in the internal force transmission mechanism, due to the different boundary conditions imposed to the mesh panel. It has been shown that, if the mesh is fixed along its outer boundary, the external force is transmitted vertically (Sec. 4.1.3), and therefore increasing the panel AR determines a reduction of the force transmission path and so a consequent increment of the stiffness of the mesh response. Furthermore, the direction of the force transmission remains unchanged. Considering an anchored panel (idealised "in-situ" conditions) instead, a variation of the panel AR determines a variation of the direction of the force transmission inside the mesh panel. The latter becomes more and more vertical decreasing AR, and being the DT mesh characterised by a higher tensile resistance along the direction of the double twisted wires (the

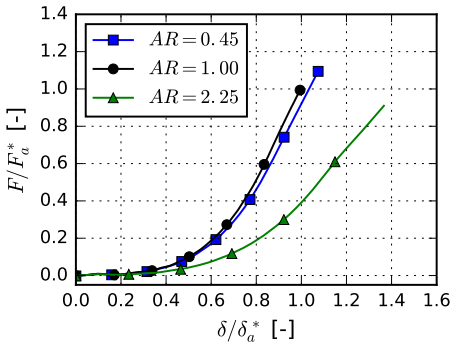


Figure 4.35: Effect of the panel aspect ratio on the mechanical behaviour of the mesh panel.

vertical one in the considered case), this "rotation" of the force transmission direction permits a better exploitation of the double twisted wires resistance. This consequently reflects in an enhanced mechanical response of the panel. It should be noted that the previous considerations are obtained considering equiareal panels.

The effect of a generic variation of the panel aspect ratio on the mesh mechanical response can be observed in the contour plots of Fig. 4.36. The solid yellow lines indicate equiareal panels. The effect of a variation of AR on F_{max} can be observed in Fig. 4.36a. It is evident that, for equiareal panels, an increment of AR leads to a decrease of the maximum sustainable force by the mesh panel. This highlights the anisotropy that characterises the mechanical behavoiur of the hexagonal double twisted wire mesh indicating that a square mesh panel may not be the optimal configuration. For a fixed value of AR instead, increasing the panel size leads to an increase of the maximum sustainable force, which may be related to a better redistribution of the stress on larger mesh panels. This was also observed when considering a uniform variation of the anchor spacing. Considering a generic variation of AR, a reduction of the latter determines an increase of F_{max}. Nevertheless, the effect on panel resistance seems to be controlled by the side length l_y (side oriented with the double twisted wires), a variation of l_x having a negligible effect on F_{max}. In fact, an increment of the side length l_y, while keeping constant l_x, permits a more efficient transmission of the force inside the mesh. The internal transmission mechanism is more and more oriented with the direction of the double twisted wires; the mesh being characterised by a

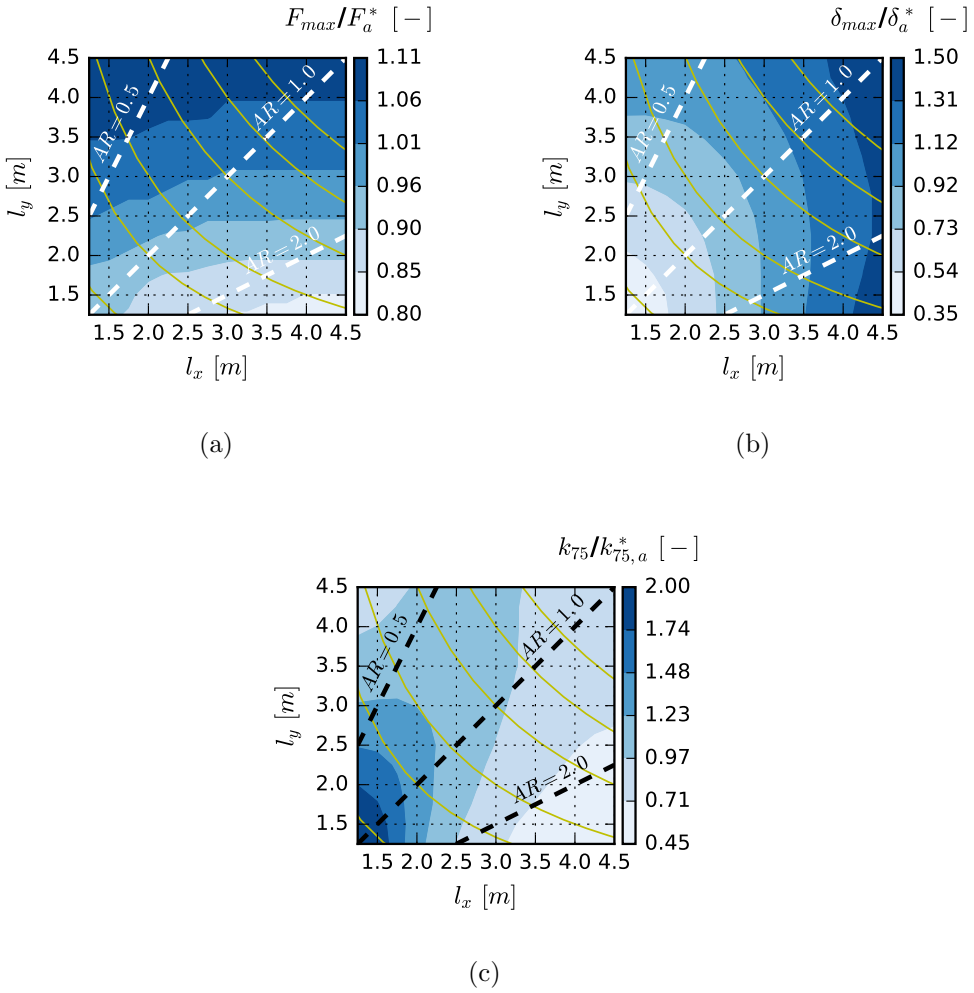


Figure 4.36: Effect of the panel aspect ratio ($AR = l_x/l_y$) in terms of: (a) force F_{max}, (b) deflection δ_{max} values at failure, (c) out-of-plane stiffness k_{75}. The plots are obtained from a linear interpolation of the numerical data and the solid yellow lines indicate equiareal panels.

better tensile resistance in such direction, this reflects in an enhancement of the mechanical response of the mesh in terms of sustainable force.

The effect of a variation of AR on the deflection value at failure δ_{max} is reported in Fig. 4.36b. Considering equiareal panels, δ_{max} increases when increasing AR; however, the panel deformability seems to be more affected by a variation of the side length l_x rather than a variation of the side length l_y. A

	F_{max} [kN]	δ_{max} [m]
UNI characteristic values	73.3 (F^*)	0.60 (δ^*)
Field boundary conditions	29.1 ($\alpha_F F^*$)	0.65 ($\alpha_\delta \delta^*$)
Block dimension D	28.4 (Eq. 4.4)	0.68 (Eq. 4.5)
Anchor plate dimension d_p	23.4 (Eq. 4.7)	0.68 (unaffected)
Anchor spacing i	22.8 (Eq. 4.9)	0.56 (Eq. 4.10)
Design characteristic values	**22.8**	**0.56**

Table 4.3: Application example of the analytical relationships (i = 2.5m, d_p =0.25m and D =0.60m).

general increment of δ_{max} is also observed when increasing the dimension of the mesh panel (i.e. panel area) confirming what observed when considering a uniform variation of the anchor spacing.

Finally, the influence the panel aspect ratio on the out-of-plane stiffness of the mesh panel is analysed. As before, this is quantified by using the stiffness parameter k_{75}. Observing the results reported in Fig. 4.36c, an increasing trend of k_{75} is observed when decreasing the AR, however the out-of-plane stiffness seems mostly controlled by the dimension of the mesh panel (i.e. panel area). It is interesting to note that the stiffness parameter k_{75}, for a given panel area, is greatest when the panel aspect ratio is in the range $0.65 \leq AR \leq 0.75$.

Application example

A calculation example is reported in the following in order to show the use of the analytical relations presented in the previous paragraphs. The secured drapery system that is here considered is characterised by an anchor spacing i=2.5m (a square anchor pattern is adopted, thus $l_x = l_y = 2.5$m) and the dimension of the anchor plates is equal to d_p =0.25m. Finally, the nominal dimension of the unstable block considered is equal to D=0.60m. The wire mesh is the hexagonal double twisted mesh with nominal wire diameter of 2.7mm. The characteristic values provided by the manufacturer (obtained from a experimental characterisation in standard UNI punch test conditions) are F^*=73.3 and δ^*=0.60m.

The analytical relationships derived from the numerical analysis, starting from the values obtained from the standard UNI laboratory characterisation,

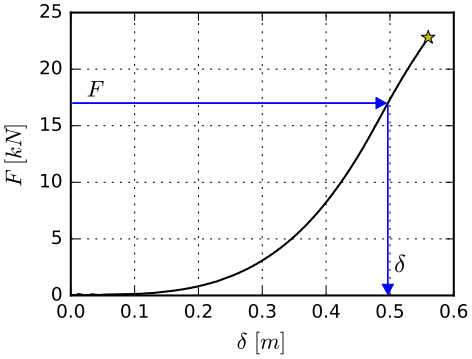


Figure 4.37: Force-displacement response obtained from the numerical simulation of the mesh panel considered in the application example. The simulation is characterised by $l_x = l_y = 2.5$m, d_p =0.25m and D =0.60m. The star marker indicates the couple F_{max}, δ_{max} obtained from the analytical relationships (see Tab. 4.3).

can be applied in sequence in order to estimate the characteristic values to be used in the design phase of the mesh system (F_{max}=22.8kN and $\delta_{max} = 0.56m$). The procedure is summarised in Tab. 4.3.

A simulation characterised by the same parameters considered in the calculation example (i.e. $i = l_x = l_y = 2.5$m, d_p =0.25m and D =0.60m) was performed for an ex-post verification of the analytical relationships derived in the parametric analysis. The obtained values of the force and deflection values at failure are F_{max}=22.5kN and δ_{max}=0.56m. The very slight difference between these values and the one obtained from the application of the analytical relationships confirms the validity of the latter. Moreover, the force-displacement curve (obtained from the simulation) permits the expected panel deflection to be estimated with reference to a given force value (e.g. the latter can be obtained from limit equilibrium analysis [57]) as schematically reported in Fig. 4.37.

4.3 Comparison of the mechanical behaviour of different mesh typologies

In this chapter, the 8x10 hexagonal double twisted wire mesh with a nominal diameter of 2.7 mm was used as the reference mesh type. In this section, the

two prototype mesh typologies presented in Chapter 2 (i.e. MT1 and MT2) are considered. Their mechanical response, in both standard UNI laboratory and "in-situ" punch test conditions, is analysed in order to characterise the main differences in their mechanical behaviour. For both of them the nominal diameter of the high resistance steel ropes is equal to 8mm and the nominal spacing between them is equal to 32cm.

4.3.1 Laboratory standard UNI punch test conditions

The three mesh typologies are firstly tested with reference to the standard UNI punch test condition. In order to respect the periodicity of the MT1 and MT2 mesh types, the punch test is conducted on a panel of nominal dimension 2.56m×2.56m, for all the three mesh types instead of the 3 m side panel previously considered. This condition respects the limits imposed by the UNI 11437 standard [99] which requires a nominal dimension of the panel sides $l_i = 3 \pm (0.2 \times 3)$ m. Moreover, differently from what has been done in the experimental campaign for the MT1 and MT2 mesh types (see Chapter 2), in this analysis the mesh panels are directly fixed along their outer boundary in order to have a perfect similarity with the testing conditions used for the DT mesh. Furthermore, this will permit the influence of the "soft connection" condition, adopted in the experimental characterisation, to be observed. The numerical parameters are the same of those used for the simulations reported in Chapter 3.

The obtained force-displacement relationships are reported in Fig. 4.38. The comparison of the three F-δ curves permits the effect of the insertion of the high resistance steel ropes on the mesh mechanical response to be understood. In this perspective, it has to be considered that the steel ropes are characterised by a maximum resistance much greater than the wires, and that their mechanical response in tensile direction is much stiffer than the ones of the wires (see the tensile relationships reported in Fig. 3.8 of Chapter 3). This implies that, in the MT1 and MT2 mesh types, the mechanical response is mainly controlled by the reaction of the steel ropes to the applied load.

Considering the MT1 mesh type, the addition of the ropes in the longitudinal direction determines a considerable increment of the out-of-plane stiffness of the mesh panel, while the maximum sustainable force remains almost unchanged from the one observed considering the DT mesh (however

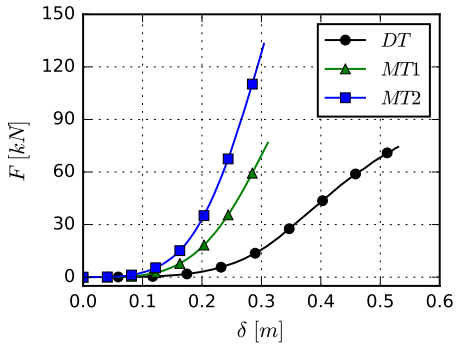
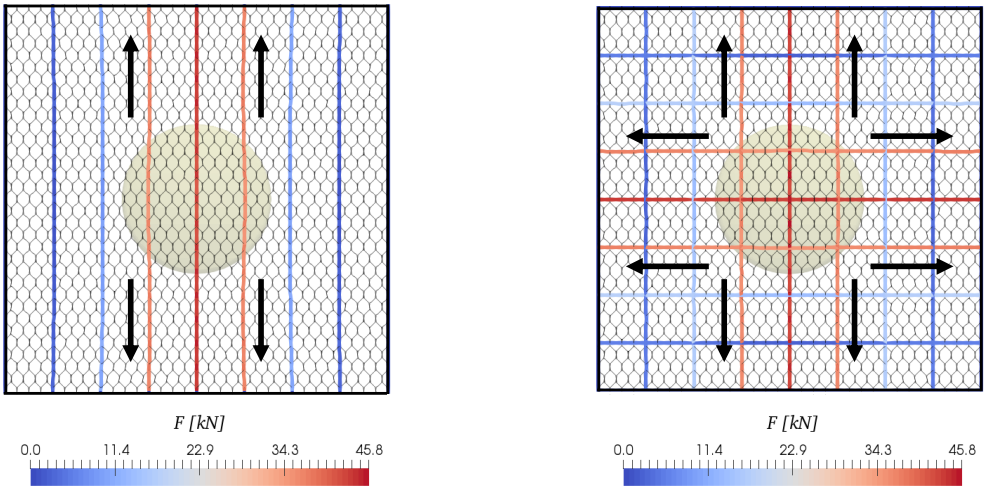


Figure 4.38: Mechanical behaviour of the different mesh typologies in standard UNI punch test conditions.

the resistance of the MT1 mesh may be even lower if ropes characterised by a smaller diameter are used). The ropes being stiffer than the DT wires, their presence permits a prompter response of the mesh panel to an out-of-plane loading condition, thus limiting the deformation of the panel. The resistance of the latter is in this case controlled by the ropes intercepted by the punching element. During the test, the ropes above the punch contrast its displacement, vertically transmitting the external load to the rigid frame to which the mesh panel is fixed (upper and lower mesh edges) as shown in Fig. 4.39a. Once the force acting on the central rope reaches the rope maximum resistance, this fails triggering the rupture of the other ropes in rapid succession, and thus leading to the failure of the entire panel. The resistance of the mesh panel is therefore linked to the capacity of redistributing the load between the ropes. The MT1 mesh type is characterised by a highly anisotropic mechanical behaviour: the internal force transmission mechanism is perfectly vertically oriented, namely it follows the ropes orientation. The existence of this preferential direction for the load transmission affects the possibility to redistribute the external load between the ropes, which mostly act as independent elements. This is even more evident when considering an anchored panel as it will be shown in Sec. 4.3.2.

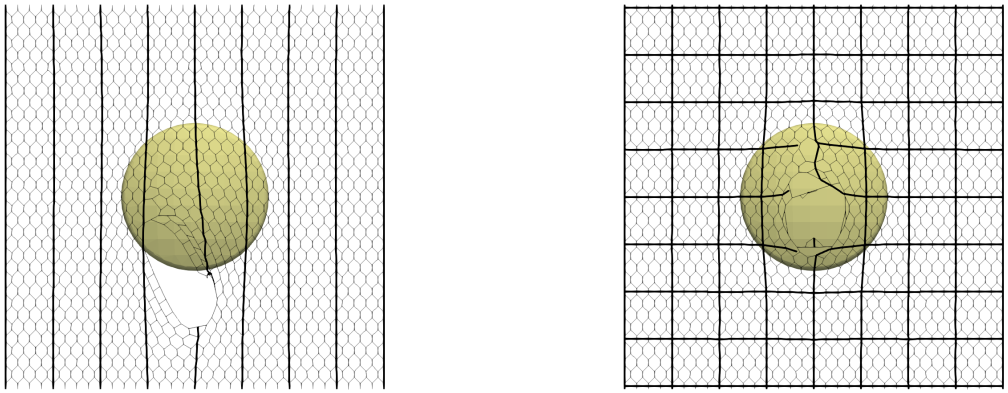
Considering the MT2 mesh type, the further introduction of the ropes along the transversal direction leads to a considerable increment of the force sustained by the panel, as well as a further increment of the out-of-plane stiffness. Hence, the addition of the transversal ropes dramatically improves the mechanical behaviour of the mesh panel. These ropes, in fact, permit the



(a) (b)

Figure 4.39: Tensile force distribution on the mesh ropes in standard UNI punch test conditions for (a) the MT1 and (b) the MT2 mesh type (the black thick line represents the fixed mesh boundary).

mesh panel to contrast an external load also reacting in the horizontal direction, and the mesh resistance in that direction is now approximately the same that the one in the orthogonal one. This introduce the fundamental possibility of transmitting the external load in both the longitudinal and transversal directions, hence leading to an almost homogeneous mechanical response of the mesh in the two directions. Moreover, this permits the load transfer between the different ropes, thus allowing a partial interaction between them. During the punch test, a higher number of ropes are actively opposing to the punching element displacement as reported in Fig. 4.39b. Furthermore, the bi-directionality of the ropes permits the force to be equally transmitted to the four fixed edges of the mesh panel leading to a better redistribution of the tensile forces inside the mesh panel (i.e. between the ropes). The central longitudinal and transversal ropes, an instant prior to the failure, are sustaining approximately the same force (see Fig. 4.39b) and their rupture is almost contemporary, confirming the homogeneous distribution of forces in the two directions. After the failure of the central ropes, the neighbouring ropes fail in rapid succession determining the failure of the entire mesh panel. The failure modality (with reference to the first rope failure) is shown



(a) (b)

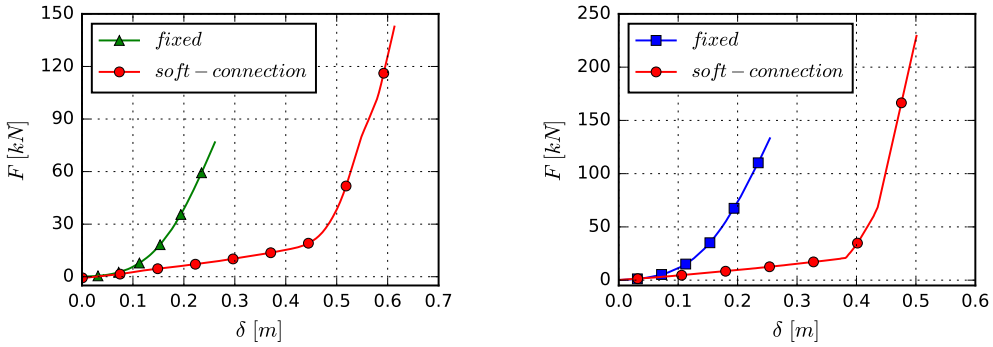
Figure 4.40: Failure modality observed in the standard UNI punch test conditions, for (a) the MT1 and (b) the MT2 mesh type.

in Fig. 4.40 for both the mesh types.

It is interesting to note that both the MT1 and the MT2 mesh types are characterised by the same deflection value at failure. This is related to the maximum elongation that the central longitudinal (and transversal for the MT2) rope can undergo before breaking. This limit value for the rope elongation together with its free length, determines also the maximum inclination of the rope in the out-of-plane direction. At this point, considering that a rope can transmit the force only along its axial direction, the more inclined the rope is in the out-of-plane direction, the more efficient its reaction in the same direction will be. Finally, the ropes being the elements that control the mechanical behaviour of the MT1 and MT2 mesh types, the latter considerations can be extended to the mesh panel. In this perspective, the maximum out-of-plane force that the MT1 and MT2 can sustain may be significantly increased if the panel has the possibility to undergo larger deformations. This aspect will be analysed in the next paragraph.

Effect of the "soft connection" condition

In the experimental campaign for the mechanical characterisation of the MT1 and MT2 mesh types, the mesh panel was fixed to the external rigid frame by looping a cable on the bordering ropes of the mesh panel as described in Chapter 2. This determines that the connection between the mesh and the



(a) (b)

Figure 4.41: Effect of the adoption of the "soft connection" boundary condition on the mechanical response of the mesh panel for (a) the MT1 and (b) the MT2 mesh types.

external frame is not rigid, and thus can deform; in this sense, this condition was referred as "soft connection" in Chapter 2. The "soft connection" condition was also reproduce in the numerical simulation of these tests by using special interactions as reported in Chapter 3. In order to understand the influence of the "soft connection" condition on the mesh panel mechanical response, the force-displacement curves obtained in the latter case and by directly fixing the mesh outer boundary, are compared in Fig. 4.41a and in Fig. 4.41b for the MT1 and the MT2 mesh types respectively. The adoption of the "soft connection" condition leads to a significant increment of the maximum force sustained by the mesh panel. The maximum force measured using the "soft connection" is approximately 1.85 and 1.80 times greater than the one obtained considering the panel directly fixed along its outer boundary, for the MT1 and the MT2 mesh typology respectively. This constraining condition permits a larger deformation of the mesh panel in the out-of-plane direction, which translates in an enhancement of the capacity to contrast an out-of-plane external load. As already mentioned, the efficiency of the mesh reaction to an out-of-plane load is related to how much the mesh is curved in that direction (membrane-like mechanical behaviour). In this perspective, the greater deformability of the mesh panel associated to the transition from the standard UNI laboratory (i.e. fixed outer boundary) to the "in-situ" (i.e. anchored panel) boundary conditions may act favourably,

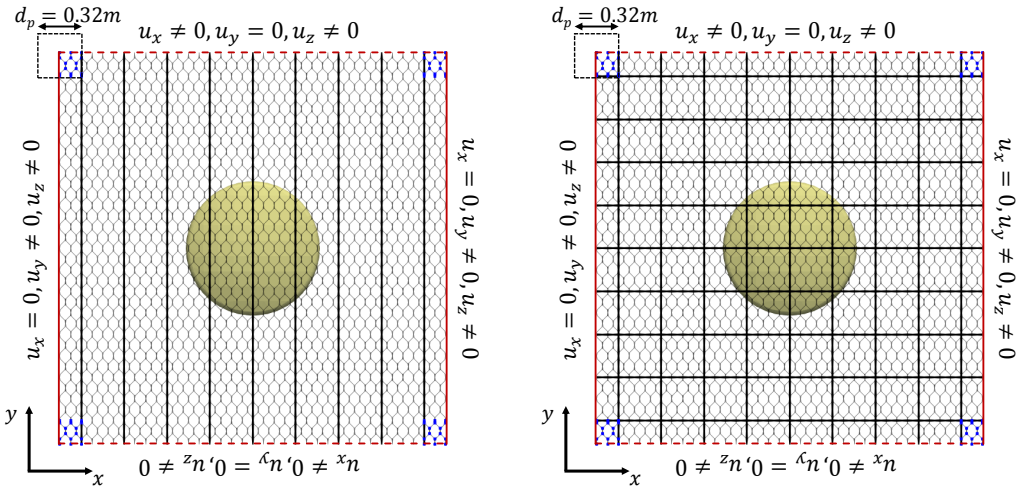


Figure 4.42: Sketch of the boundary conditions imposed to (a) the MT1 and (b) the MT2 mesh type with reference to the "in-situ" punch test configuration.

and the reduction of the maximum sustainable force can be limited.

4.3.2 Idealised "in-situ" punch test conditions

The three mesh types are finally tested with reference to the "in-situ" punch test configuration already presented in Sec. 4.2. In this case, the periodicity of the problem has to be respected with the further constraint of the mesh-plate connection. For this reason the dimension of the generic mesh panel was slightly modified, and a panel of nominal dimension 2.88m×2.92m was considered in the simulations. The boundary conditions imposed to the mesh panels are shown in Fig. 4.42. The obtained force-displacement curves are reported in Fig. 4.43 considering a square pattern for the anchors. In Fig. 4.44, the force acting on the ropes for the MT1 and MT2 mesh types, an instant before the failure of the mesh panel, is reported. It is interesting to observe that the reduction of the maximum force sustainable by the MT2 mesh type moving towards the "in-situ" condition is very limited. A more consistent reduction is instead observed for the MT1 mesh type; in this case, the reduction of the maximum force is due to the fact that the panel fails because of the tear of the DT mesh in correspondence to the two lateral ropes

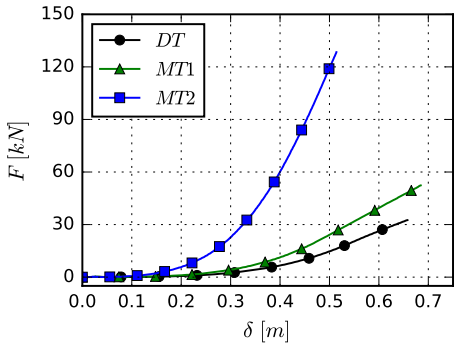
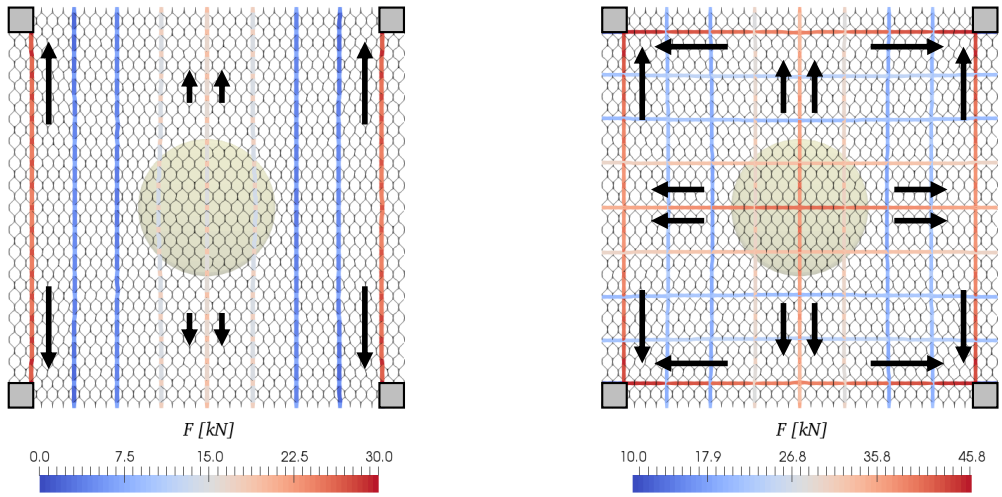


Figure 4.43: Mechanical behaviour of the different mesh typologies with reference to the "in-situ" punch test conditions.

as reported in Fig. 4.45a. The failure is therefore prematurely reached, and the resistance of the ropes is not optimally exploited as observable from the low force level acting on the constrained ropes (i.e. ropes intercepted by the anchor plates) an instant prior to the mesh failure as shown in Fig. 4.44a). In this particular case, the panel resistance is limited by the resistance of DT mesh rather than by the one of the ropes. This explains the similarity between the mechanical response of the MT1 and the DT mesh types observable in Fig. 4.43. In analogy to what has been obtained with reference to the laboratory test condition, the introduction of the transversal ropes seems fundamental, also considering more realistic in-situ conditions, in order to increase the retaining capacity of the mesh panel.

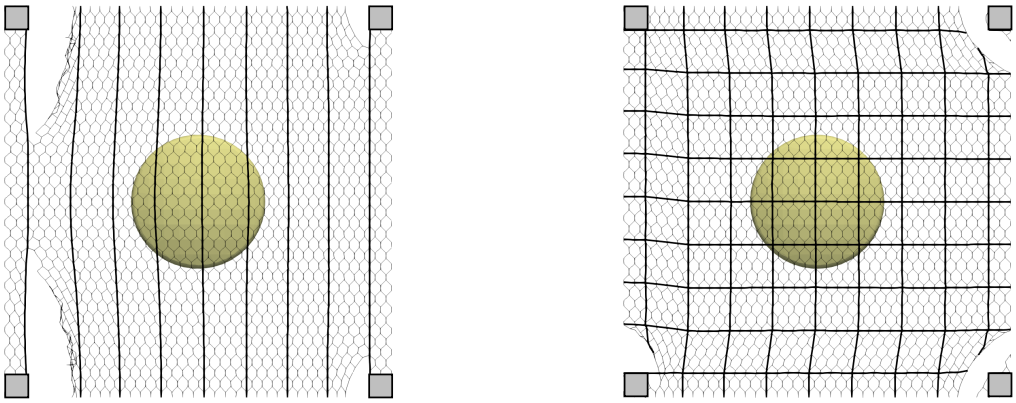
4.4 Conclusive remarks

In this chapter the punching behaviour of a double twisted hexagonal wire mesh panel was investigated. In the first phase, the mesh mechanical behaviour was analysed with reference to standard UNI laboratory punch test conditions. Successively, a periodic anchored mesh panel test configuration was defined on the basis of the results obtained from large-scale models. This had permitted an extension of the characterisation of the mesh panel response to more realistic field conditions. The performed analyses shown that mechanical response to a local punching condition is controlled by the mesh internal force transmission mechanism. The latter is, on one hand



(a) (b)

Figure 4.44: Tensile force distribution on the mesh ropes, with reference to the "in-situ" punch test conditions, for (a) the MT1 and (b) the MT2 mesh type.



(a) (b)

Figure 4.45: Failure modality observed in the "in-situ" punch test conditions, for (a) the MT1 and (b) the MT2 mesh type.

related to the mechanical characteristics of the mesh elements, namely the force tends to be transmitted along the strongest elements (e.g. double twisted wires in the DT, ropes in the MT1 and MT2); on the other hand, it is influenced by the boundary conditions imposed to the mesh panel. It was shown that the DT mesh is characterised by a preferential force transmission direction, which is oriented with the double twisted wires. However, considering the "in-situ" punch test configuration (i.e. anchored panel) the internal load transfer is differently oriented and follows the shortest path between the loading point and the anchors. This reflects in a reduction of the mesh mechanical performance, stressing the fact that the internal force transmission mechanism has to be carefully considered in order to optimise the mechanical behaviour of the mesh. Moreover, for both the standard UNI and the "in-situ" punch test configurations, a parametric analysis was performed in order to quantify the effect of the different variables of the problem on the mesh mechanical response. From the obtained numerical data, simple relationships permitting estimation of the effect of the considered variables on the mesh mechanical response were proposed. Referring to the "in-situ" punch test configuration the effect of the single variables can be summarised as follows:

- **the size of the punching element** controls the amount of the mesh-punch interacting surface, and determines the failure modality occurring in the mesh. Two different failure mechanisms were observed, namely a "block-punching" and an "anchor-punching" mechanism. The transition between the two is controlled by the available resistance at the mesh-plate connection, which is a function of the anchor plate dimension d_p (for the same mesh type). The former mechanism occurs when the resistance at the mesh-block contact is lower than the mesh-plate connection resistance (a condition likely when the mesh is retaining a sharp block). In this case, a significant increment of the maximum sustainable force is observed when increasing the punching element size (Eq. 4.4 for $D \lesssim d_p$). When instead the mesh failure is caused by the overcoming of the mesh-plate connection resistance (a condition likely when the mesh is retaining large and/or rounded blocks), the panel resistance is very slightly affected by a variation of the block size (Eq. 4.4 for $D \gtrsim d_p$). Concerning the out-of-plane stiffness of the mesh panel, this monotonic increases when increasing the block dimension as described by Eq. 4.6;

- **the position of the punching element** influences the orientation of the force transmission mechanism inside the mesh, thus the mechanical performance of the mesh as well. The effect of an eccentric load is strongly related to the anisotropy that characterises the DT mesh; in particular, an eccentricity along the direction parallel to the double twisted wires orientation has a negligible effect on the mesh response, while an eccentricity along the orthogonal direction strongly influences the mesh response. Three zones of local maximum for the sustainable force were observed, namely for a block centred on the mesh panel and when the block is in-between two anchor plates. The global maximum is observed when the block is located in-between two anchor rows and vertically aligned with them. Concerning the panel's maximum deflection, this reduces when increasing the proximity between the retained block and the anchor plates in a direction orthogonal to the orientation of the double twisted wires;
- **the anchor plate dimension** controls the maximum resistance of the mesh panel (i.e. mesh-plate connection resistance). Considering the case in which the mesh failure is characterised by the "anchor-punching" mechanism, the panel resistance linearly scales with the anchor plate dimension as described by Eq. 4.7. Instead, the maximum deflection of the panel, can be considered to be independent of the anchor plate dimension;
- **the anchor spacing** controls the deformability of the mesh panel. The maximum deflection linearly scales with the anchor spacing as described by Eq. 4.10, while the effect on the maximum force is very limited. As the deformability of the mesh panel is ruled by the anchor spacing, the latter can be use in a performance perspective, namely to control the rate of system retaining capacity associated to a certain deflection level of the mesh panel (e.g. maximum admitted deflection in serviceability conditions). This can be achieved by using the f_m-i curves as defined in Sec. 4.2.2;
- **the panel aspect ratio** has a significant role in the mechanical response of the mesh panel. In particular, considering equiareal panels, an enhancement of the mechanical behaviour was observed when considering panels that are more elongated along the double twisted wires direction (i.e. $AR < 1$). Moreover, it was shown that the side length l_y has a significant effect on the puncturing resistance of the mesh

panel, while the side length l_x mostly influences the panel deformability. Finally, the adoption of $0.65 \leq AR \leq 0.75$ seems to maximise the out-of-plane stiffness of the mesh panel.

It is important to note that the mesh panel is tested up to its failure. This permits the entire mechanical response (i.e. F-δ curve) to be provided and to define the ultimate limit condition of an anchored mesh panel. The analytical relationships presented in Sec. 4.2.2 permit extension of the mesh characteristic values provided by manufacturers (obtained from standard laboratory tests) to field conditions (i.e. anchored mesh panel) as reported in the application example of Sec. 4.2.2. Such information can be of great importance in practice, providing a more realistic mechanical characterisation of mesh resistance in field conditions. Moreover, knowledge of the entire force-displacement behaviour permits estimation of the system deformations in serviceability conditions at the design phase.

Finally, the punching response of the DT mesh was brielfy compared with the one of the MT1 and the MT2 prototype meshes in order to understand the effect of the introduction of high resistance steel ropes on the DT mesh type. From the obtained results, the introduction of the transversal ropes appears fundamental in order to increase the retaining capacity of the mesh panel. These, in fact, introduce a further resistance in the horizontal direction and also permit the load transfer between the different ropes, thus allowing a better exploitation of the resistance of the latter.

Some findings of this chapter have been accepted for publication in Acta Geotechnica journal [84].

Chapter 5

Punching behaviour at the mesh anchor plate connection: punch test against soil

In this chapter, the local punching mechanism between the mesh anchor plate connection and a granular soil is addressed. The experimental punch test against soil presented in Chapter 2 is used as reference test in the following analysis. This test configuration is used by manufactures in order to characterise the relationship between the load applied during the installation phase to the anchor plate and the settlement of the latter [32]. Furthermore, it permits an insight into the force transmission mechanism between the soil and the retaining system in the zone surrounding the anchor plates. In this thesis work, the punch against soil test is also used in order to prove the effectiveness of the adopted approach in reproducing problem involving the interaction between the mesh and a granular layer. In the first phase, the experimental test is numerically reproduced and the model parameters are calibrated in order to fit the experimental results. The numerical results are then used for an in-depth analysis of the problem. In the second phase, the boundary conditions of the problem are relaxed to move towards a more faithful schematisation of the field conditions. In the latter configuration a parametric analysis is performed considering the role of the mechanical characteristics of the soil, the mechanical characteristics of the mesh and the anchor plate dimension.

5.1 Numerical modelling of the experimental test

The punch test against soil aims to analyse the force transmission mechanism between the anchor plate and the soil volume under it, and the macroscopic interaction between the mesh and the soil. In this perspective, a precise description of the wire geometry is not needed in the numerical model, therefore the NWB approach is adopted in the numerical schematisation of the mesh. In order to reproduce the experimental test presented in Chapter 2, a mesh panel of dimension of 1.76m×1.64m (DT mesh with a nominal diameter of 3mm) is discretised by using 946 spherical particles in the model. The scaling of the diameter of the nodal particles d_w (equal to 12mm) is adopted also in this case to reduce the computational cost (see Chapter 3). According to the experimental test procedure, in the model the mesh is fixed along its outer boundary by fixing all the degrees of freedom of the nodal particles belonging to the mesh panel edges. The square anchor plate of side $b = 250$mm, used as punching element, is represented by 12 triangular elements (i.e. facets). In the experimental campaign, the puncturing resistance of the solely mesh was analysed before to conduct the test with the soil layer. The same tests have been reproduced numerically and they have been already reported in Chapter 3. Hence, they are here omitted for the sake of brevity. Due to the presence of the soil layer, in the experimental campaign, the mesh panel was not tensioned prior to the test (as instead was done for the test with the solely mesh) and so the wires were initially slightly distorted and deformed. In order to account for this initial condition, the SDWM is used. The stress-strain curve used as input for the SDWM are the ones reported in Chapter 3 (see Fig. 3.8), while the stochastic parameters are set equal to $\lambda_u = 0.05$ and $\lambda_F = 1.00$. They have been calibrated in order to fit the experimental results as it will be described in Sec. 5.1.1. The geotextile used in the experimental procedure does not have a structural function, hence it is not discretised in the numerical model to optimise the computational cost of the simulation. The soil volume ($1.76\times1.64\times1.0$m^3) is composed of approximately 47k spherical particles. It is laterally contained by four walls, while a layer of particles (layer thickness equal to 10cm) at the bottom of the soil volume is fixed to simulate the base of the soil volume. A 3D view of the numerical model is reported in Fig. 5.1 for the sake of clarity. The mean diameter of the soil particles is set equal to d_{50}=4.0cm (polidispersity

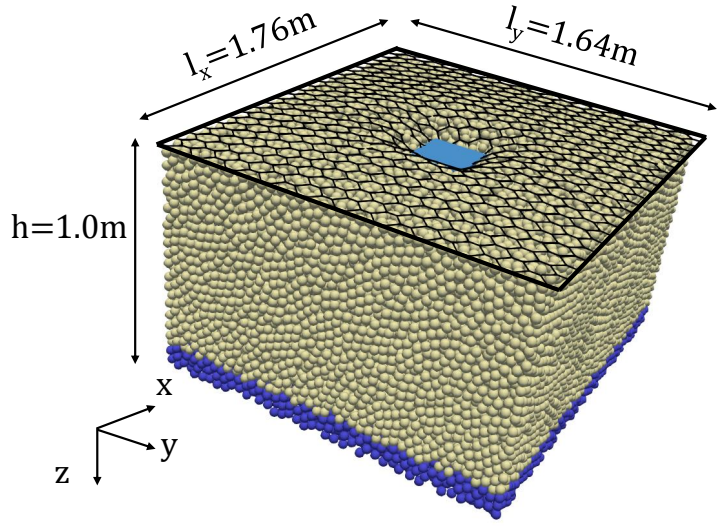


Figure 5.1: 3D view of the numerical model of the punch test against soil: the black thick line represents the fixed boundary of the mesh, while the fixed soil layer is highlighted in blue.

of 5%), which is slightly higher than the experimental maximum grain size (i.e. d_{50}^{exp}=32mm, the size distribution was not available). This choice was dictated on one hand to have representative number of particles under the anchor plate and keep their dimension similar to the experimental one, on the other hand to optimise the computational cost of the simulation. The contact model applied for the soil grain interactions is the standard linear force-displacement model for the normal contact and linear with a frictional plastic limit for the tangential contact. The general forms of the normal force and the incremental tangential force are given by Eqs. 3.6, 3.7, where the normal and tangential contact stiffnesses are given by [93]:

$$k_n = 2\,\frac{E_i r_i E_j r_j}{E_i r_i + E_j r_j} \tag{5.1}$$

$$k_t = 2\,\frac{E_i r_i \nu_i E_j r_j \nu_j}{E_i r_i \nu_i + E_j r_j \nu_j} \tag{5.2}$$

In Eqs. 5.1, 5.2, i, j represent the i-th and j-th particles in contact (for a facet-sphere contact an ideal radius equal to two times the one of the sphere is considered for the facet element in the contact stiffness computation

/	E_i [Pa]	ν_i [-]	ϕ_i [°]	ρ_i [kg/m^3]	β_r [-]	η_r [-]	λ_u [-]	λ_F [-]
mesh	2e10	0.30	35.0	15.5e3	-	-	0.05	1.00
soil	1e9	0.30	47.5	2.5e3	0.02	0.06	-	-
plate	1e9	0.30	35.0	-	-	-	-	-
box	1e9	0.30	0.0	-	-	-	-	-

Table 5.1: Numerical parameters used in the simulation.

[93]). An additional rotational resistance is introduced to fit the typical range values of real granular materials, since the macroscopic friction angle of spheres, allowing their free rotation, is physically limited to 24-26° [20, 94]. The rotational law in YADE [93] (rolling and twisting are here unified for simplicity) is controlled by two dimensionless parameters, namely the rotational stiffnesses coefficient β_r and the rotational resistance coefficient η_r. The rotational moment at the contact is linearly related to the relative rotation by means of the rotational contact stiffness k_r. Finally, a plastic limit condition is imposed on the rotational moment at the contact. The expressions of the rotational stiffness and of the plastic condition for the rotational moment are given by [93]:

$$k_r = \beta_r r_i r_j k_t \tag{5.3}$$

$$\parallel M_r \parallel \leq \eta_r \parallel F_n \parallel min(r_i, r_j) \tag{5.4}$$

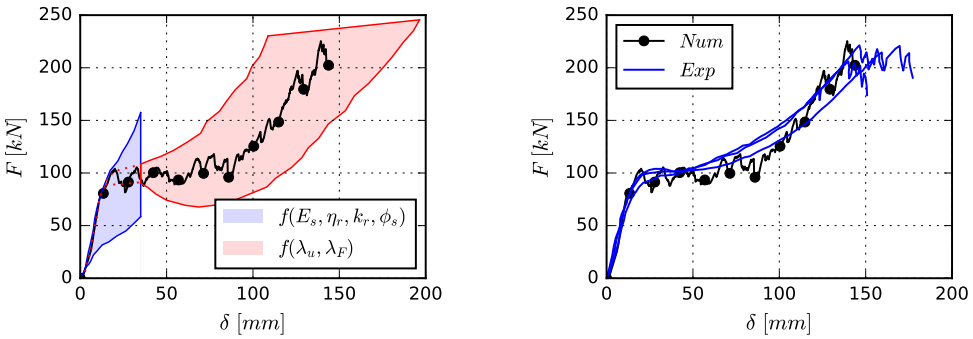
For the soil-mesh and the soil-anchor plate contact no rotational resistance is applied. No specific tests were carried out in the experimental campaign to characterise the soil. The calibration of the numerical parameters is therefore made in order to fit the experimental results of the punch against soil test as it will be described in Sec. 5.1.1. The calibrated parameters are reported in Tab. 5.1.

The simulation is divided in the following steps. The assembly of spheres representing the soil volume was generated by pluviation inside the prismatic box. In this phase the contact friction angle was set equal to zero and the rotational resistance was not applied in order to obtain a dense sample. After the stabilisation under gravity, the top of the soil sample was regularised in order to obtain an almost planar initial surface of the soil layer. The calibrated contact parameters are then assigned to the soil particle (existing

interactions are modified accordingly). After this preliminary phase, the mesh panel is created in adherence with the top layer of the soil and it is let settle on the soil layer under gravity. Once the equilibrium is reached (this condition is considered achieved when the ratio of the mean unbalanced force acting on bodies over the mean contact force is lower than $1 \cdot 10^{-2}$), a constant velocity of v_z=0.02m/s, in the direction perpendicular to the mesh plane, is imposed to the anchor plate, thus starting the test. It should be noted that a lower velocity will not lead to significant differences in the system mechanical response. Displacements of the plate in x and y directions, as well as plate rotations are not allowed. The test ends once the failure of the mesh is reached, namely when the maximum tensile strength of the wires surrounding the anchor is overcome. This determines the rupture of these wires, and leads to the consequent tear of the mesh in correspondence to the plate boundary. During the simulation, the force acting on the anchor plate and its displacement, as well as the force acting on the mesh are registered in order to characterise the mechanical response of the system. The numerical time step is set equal to $dt = 3 \cdot 10^{-5}$s.

5.1.1 Calibration phase of the numerical model

The calibration of the numerical parameters is based on the peculiar mechanical behaviour of the system (i.e. F-δ curve) as described in the following. For low displacements ($\delta \leq$ 35mm in this case) the force is controlled by the soil reaction and the mesh reaction is negligible. The first part of the curve is therefore used to calibrate the soil numerical parameters. Firstly, the value of the micromechanical elastic modulus E_s is selected in order to fit the stiffness of the elastic part of this branch of the F-δ curve. Secondly, the rotational resistance coefficient η_r (controlling the plastic moment, see Eq. 5.4) is used to fit the value of the force plateau. Finally, the rotational stiffness coefficient β_r and the contact friction angle ϕ_s are selected in order to optimise the agreement with the experimental measurements. It should be noted that the calibrated values of these parameters were obtained from a trial and error procedure, therefore they represent only one of the possible sets of value permitting one to reproduce the soil behaviour under the considered test conditions. For further increments of the anchor plate displacement a strong variation of the trend of the F-δ curve is observed. This is related to the occurrence of a first failure mechanism in the soil (i.e. soil bearing



(a) (b)

Figure 5.2: (a) Graphical schematisation of the effect of the numerical parameters: blue and red envelopes represent the bounds of the system mechanical response when modifying the numerical parameters in the brackets. These results were used to split the calibration in two phases. (b) Comparison between experimental and (calibrated) numerical results.

capacity is exceeded). This induces a lateral flowing of the soil, which starts to interact with the mesh. From this moment, the mesh mechanical response is progressively activated, partially by the soil, and partially by the anchor plate displacement. The system mechanical response, here summarised with the F-δ, will be significantly influenced by the mesh reaction in this second part of the test, hence the parameters associated with the numerical mesh (i.e. λ parameters of the SDWM) are calibrated with reference to second part of the experimental F-δ curve ($\delta \geq 35$mm in this case). A graphical schematisation of these observations and of the calibration procedure is reported in Fig. 5.2a. The numerical F-δ curve is reported in Fig. 5.2b where it is compared with the experimental data. A good agreement between the numerical predictions and the experimental data is obtained for both the test phases, namely the initial soil reaction (first part of the curve) and the one characterised by the interaction between the mesh and the soil. It is worth mentioning that the system failure is triggered by the local ruptures of wires around the plate, then the nearby wires start to break in rapid succession until the complete tear of the mesh around the anchor plate. This was observed in both numerical and experimental tests.

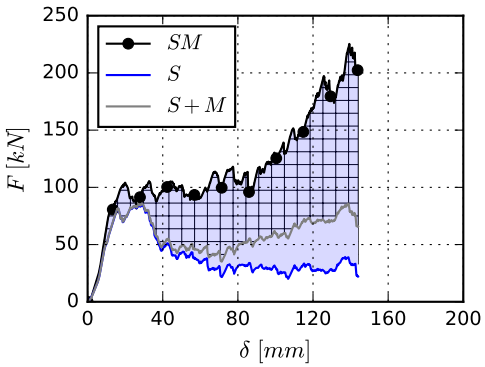
5.2 Investigation of the mechanical behaviour of the system

5.2.1 Evaluation of the mesh-soil interaction

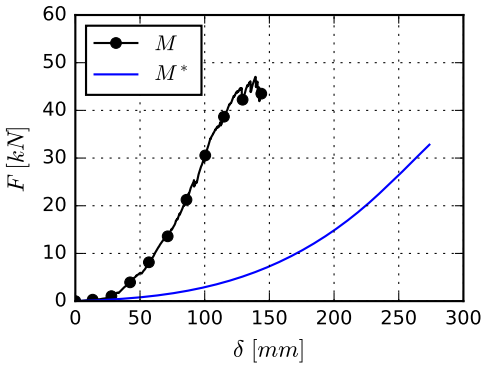
Once the numerical contact parameters of the soil and of the mesh calibrated, the model can be used to perform an in-depth analysis of the problem. From the numerical results, it is in fact possible to isolate the mesh mechanical behaviour from the overall system response, thus being able to quantify the role of the mesh, as well as that of the mesh-soil interaction. In this perspective, the contribution of the different parts of the system is separately considered using the following definition of the forces (see also Fig. 5.3):

- the overall force sustained by the system (soil-mesh, SM), given by the total force acting on the anchor plate;
- the force sustained by the mesh (M), given by the tensile forces acting on the wires intercepted by the anchor plate only (i.e. sum of the interaction forces between mesh nodal particles);
- the force sustained by the mesh without the presence of the soil layer (M^*). This force is derived from a further simulation in which the soil layer was removed (same stochastic parameters of the case M were used);
- the force sustained by the soil without the presence of the mesh (S). This force is derived from a further simulation in which the mesh was removed.

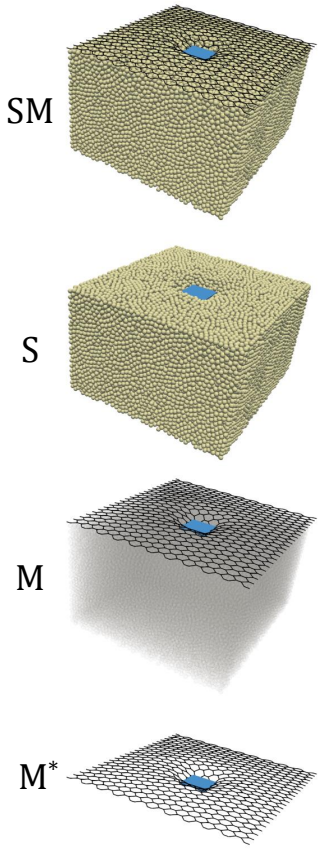
These forces can be finally combined with each other in order to analyse the effect deriving from the possible interaction between the mesh and the soil. In Fig. 5.3a the force-displacement curve of the overall system (SM) is compared with the one obtained from a punch test on the solely soil volume (S). A first observation is that the two curves are almost identical for low displacements ($\delta \leq 35$mm), confirming that the mechanical response in the first part of the test is controlled uniquely by the soil reaction. A further confirmation of this aspect is given by comparing the curve $S + M$, obtained by the algebraic sum of the contribution of the mesh (M) and of the solely soil (S). Indeed, the two curves are almost coincident for low displacements, showing that the mesh reaction is negligible in this phase. This part of the test can be therefore seen as a particular plate bearing test on the soil layer. Considering instead the entire F-δ curves, and comparing the cases SM and



(a)



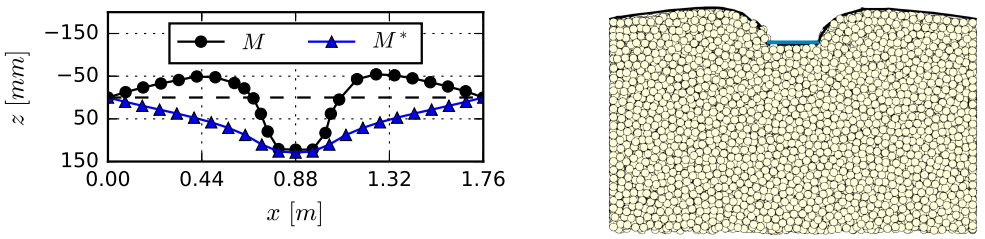
(b)



(c)

Figure 5.3: (a) Comparison of the system mechanical response with (SM) and without (S) the presence of the mesh. (b) Comparison of the mesh mechanical response with (M) and without (M^*) the presence of the soil layer. (c) Graphical explanation of the legend (elements considered in the force definition are highlighted).

S as reported in Fig. 5.3a, it is notable that the system bearing capacity (i.e. admissible initial load on the anchor plate) strongly increases with the introduction of the mesh. From a quantitative point of view, the bearing capacity goes from 84.8kN (maximum S force) to 225.4kN (maximum SM force). Moreover, the introduction of the mesh permits higher displacement levels to be reached (e.g. settlement of the anchor plate during the installation phase). The blue-filled area in Fig. 5.3a (difference between SM and S curves) highlights the benefit provided by the introduction of the mesh to the mechanical response of the system during the entire test. It is worth mentioning that this increment is only partially due to the mesh mechanical resistance, and a larger contribution is provided by the interaction between the mesh and the soil. To better understand this aspect, it is useful to refer to the force-displacement curve $S + M$ reported in Fig. 5.3a. Following its definition, this curve describes the mechanical contribution provided by the soil and by the mesh, if taken separately (some effects related to the mesh-soil interaction are still present in the mesh mechanical response actually, and this aspect will be analysed afterwards). The contribution related to the mesh soil interaction is therefore given by the difference between the force-displacement curve SM and $S+M$ and it is highlighted by the hatched area in Fig. 5.3a. The contribution provided by the mechanical resistance of the mesh is thus represented by the difference between the hatched and the blue-filled area in the same figure. Considering the maximum force registered during the test (i.e. system bearing capacity), the mesh-soil interaction provide the 62% of its value ($\approx$ 140kN), while the pure mesh contribution is only responsible for the 20% ($\approx$ 47kN) of its value. As above mentioned, also the mesh mechanical response (M), measured in the punch against soil test, is influenced by its interaction with the soil. This is particularly evident comparing the force-displacement curves reported in Fig. 5.3b. The mesh mechanical response obtained in the punch test against soil (M) shows a higher stiffness than the one obtained without the presence of the soil (M^*). The soil layer contrasts the displacement of the mesh panel, and therefore the effect of the soil, on the mesh mechanical response, can be seen as a "soft constraint" opposing to the mesh "free" displacement. This effect is particularly significant in the area surrounding the anchor plate where the soil flows against the mesh. Moreover, the upwards pressure generated by the soil on the mesh panel leads to a better redistribution of the external load, which translates in an enhancement of its retaining capacity. Finally,



(a) (b)

Figure 5.4: (a) Mesh centred section and (b) 2D view of the numerical model in the x-z plane for a plate displacement $\delta = 140$mm. The section is derived linearly interpolating the position of the nodal particle (schematised by the markers in the figure).

the mesh deformed configuration, with reference to the mesh centred section in the x-z plane (the one in y-z is analogous), for the case M and M^*, for a displacement level of $\delta \approx 140$mm of the anchor plate (i.e. an instant prior to the mesh failure in the punch test against soil), are compared in Fig. 5.4 to better visualise the effect of the presence of the soil on the mesh deformation.

5.2.2 Evaluation of the force transmission mechanism

In Sec. 5.2.1, the mesh-soil interaction and its effect on the mechanical behaviour of the system have been analysed from a macroscopic point of view, namely considering the force-displacement curves. In the following instead, the discrete nature of the numerical model is exploited. The numerical model gives access to micromechanical information, as for instance the contact forces between the soil grains. The spatial and temporal evolution of the contact force network (normal contact forces) is analysed in order to provide a better understanding of the force transmission mechanism between the anchor plate and the soil. Moreover, from the contact force network it is possible to visualise the retaining effect that the mesh applies on the soil. From studies on the contact force distribution in granular media [3, 87], it is known that, when a granular medium is subjected to an external load, the grains tend to rearrange and to form oriented aligned chains that permit the external load to be sustained. Dividing the contact forces into two net-

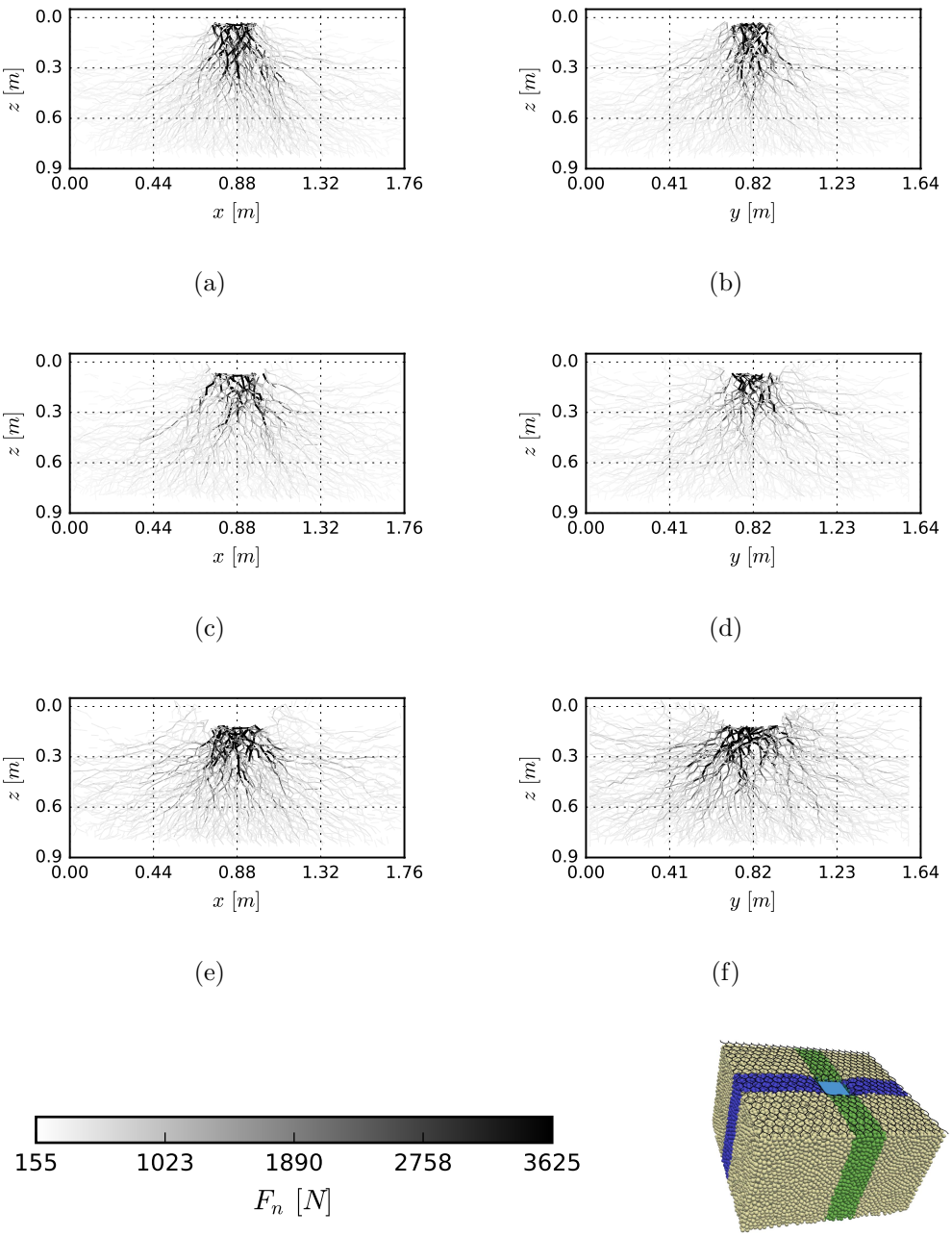
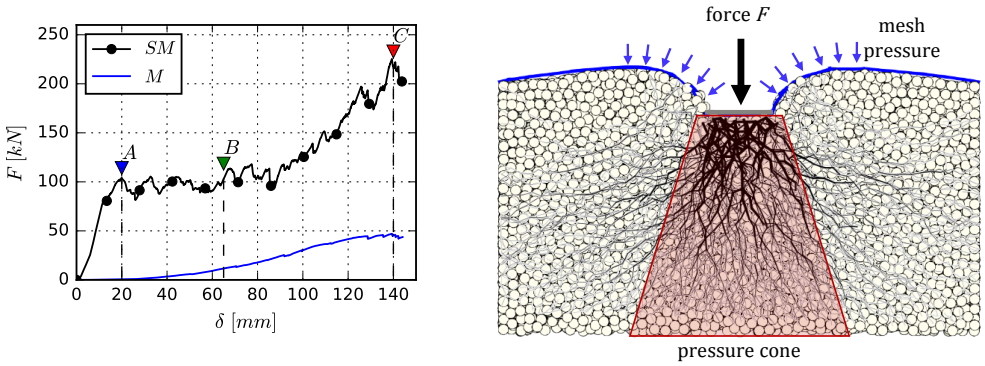


Figure 5.5: Contact force network (strong network) at different displacement levels of the anchor plate: (a,b) $\delta \approx 20$mm, (c,d) $\delta \approx 65$mm and (e,f) $\delta \approx 140$mm. The colorbar upper limit is set equal to $\max(F_n)/4$, the blue and green volumes highlight the slices of the soil domain considered in the plots (x-z and y-z plane respectively).



(a) (b)

Figure 5.6: (a) Mechanical response of the system (SM) and of the mesh (M) and indication of the point considered in the analyis of the force network. (b) Graphical scheme of the different actions on the soil volume.

works, depending on their magnitude, namely a strong (forces greater than the mean force amplitude) and a weak network, it is possible to observe that the orientation of these grain alignments is not arbitrary, and, more precisely, the strong network is oriented with the direction of the applied external load. The strong network permits the medium to sustain the applied load, while the weak network provides for the stability of the strong network (i.e. it prevents the buckling of the grains alignments). This analysis aims to study the force transmission mechanism, from the plate to the soil, therefore only the strong network will be considered in the following.

In Fig. 5.5 the contact network is reported with reference to three displacement levels of the anchor plate, namely $\delta \approx$ 20mm, 65mm and 140 mm. The plots show the force network with reference to two slices of thickness equal to the anchor plate side (b=250mm) of the soil domain (blue and green volumes in Fig. 5.5) and then condensed in a 2D plot in the x-z and y-z plane respectively. The considered values of δ define some characteristics points of the force-displacement response of the system (quantitative values of δ are representative of this specific case). Considering the force network, at each of these plate displacement levels, and linking it to the F-δ relationships (SM and M), as reported in Fig. 5.6a, may help to understand the effect the application of an initial load to the anchor plates at the installation phase. Three different behaviours can be distinguished:

- $\delta = 20$mm (point A in Fig. 5.6a), the applied force (can be view as load imposed to the anchor plate at the installation phase) permits the creation of a pressure cone in the soil (area interested by the thick black lines in Fig. 5.5a and 5.5b), which partially stabilises the soil volume under the anchor plate. The anchor plate settlement is instead not sufficient to tensioning the mesh, thus the mesh does not apply any stabilising pressure on the soil layer. This condition is evident observing that the mesh reaction is almost negligible (curve M in Fig. 5.6a), and so the system reaction is controlled solely by the soil reaction. Moreover, observing the force network, one may note that the external force is transmitted only to the soil immediately under the anchor plate, in fact the sides of the pressure cone are almost vertical. If applied, such an initial load level allows the (partial) stabilisation of a soil volume under the anchor plate, however it is not sufficient to activate the mesh; before being able to provide a retaining action, the mesh needs to undergo further deformations and thus displacements of the mesh system in serviceability conditions are expected.
- $\delta = 65$mm (point B in Fig. 5.6a), the applied force permits a larger soil volume to be interested by the stabilising pressure cone with reference to the previous point (see Fig. 5.5c and 5.5d). The anchor plate settlement is now sufficient to tensioning the mesh, nevertheless the mesh applies a low retaining action on the soil layer. This condition is evident observing the low mesh reaction value (curve M in Fig. 5.6a) and that the point B is placed on the plateau of the curve SM. From the force network it is possible to observe a larger pressure cone in the soil layer, and that it extends also outside the vertical projection of the anchor plate (i.e. sides of the pressure cone are more inclined). Moreover, contact forces starts to appear also in the upper-lateral zones with respect to the anchor plate (see Fig. 5.5c and 5.5d) showing that the mesh starts to contrast the soil movement. If applied, such an initial load level allows the increment of the (partially) stabilised soil volume under the anchor plate. It permits the mesh to be tensioned hence, even if its retaining action is initially low, the mesh reacts promptly reducing the displacements of the system in serviceability conditions.
- $\delta = 140$mm (point C in Fig. 5.6a), the applied force permits the soil volume interested by the stabilising pressure cone to be even more increased with reference to the previous points (see Fig. 5.5e and 5.5f).

The anchor plate settlement is now sufficient for tensioning the mesh and also for activating its retaining action. This condition is evident observing that the mesh reaction is completely activated (curve M in Fig. 5.6a) and that the point C is placed on the ascending part of the curve SM. From the force network it is possible to note that the stabilising pressure cone interests a significant portion of the soil volume and that it largely extends outside to the anchor plate vertical projection. In this condition, relevant contact forces are observed in the upper-lateral zones with respect to the anchor plate (see Fig. 5.5e and 5.5f) showing that the mesh is applying a considerable retaining pressure on the soil surrounding the anchor plate. If applied, such an initial load level, allows a (partial) stabilisation not only of the soil volume directly under the anchor plate, but also of a considerable portion in the area surrounding the latter. It permits the activation of the mesh retaining action, and thus the displacements of the system in serviceability conditions are strongly reduced.

Summarising what above mentioned, the application of an initial load to the anchor plate generates a pressure cone in the soil substrate, which permits a partial stabilisation of the soil volume in the zone surrounding the anchor plate. Initially (for $\delta \leq 20$mm in this case), this cone affects only the zone immediately under the anchor plate. Then (for $\delta \geq 65$mm in this case), the mesh starts to actively contrast the soil displacement and the pressure cone becomes wider and affects the soil also in a volume external to the vertical projection of anchor plate. Moreover, if the applied initial load is sufficient to activate the retaining action of the mesh, a further stabilising pressure is imposed to the soil volume directly by the mesh. A graphical representation of the different actions that may be applied on the soil volume is reported in Fig. 5.6b for the sake of expository clearness.

Finally, it is interesting to note that the pressure cone observed with reference to the y-z is wider than the one in the x-z. Furthermore, a larger number of contact forces in the lateral zones surrounding the anchor plate is also observed with reference to the y-z, as a results of a higher local mesh containment. Both these effects may be related to the intrinsic anisotropy of the DT mesh that, as already discussed in Chapter 4, determines a stiffer response along the direction parallel to the double twisted wires (i.e. y-direction in this case).

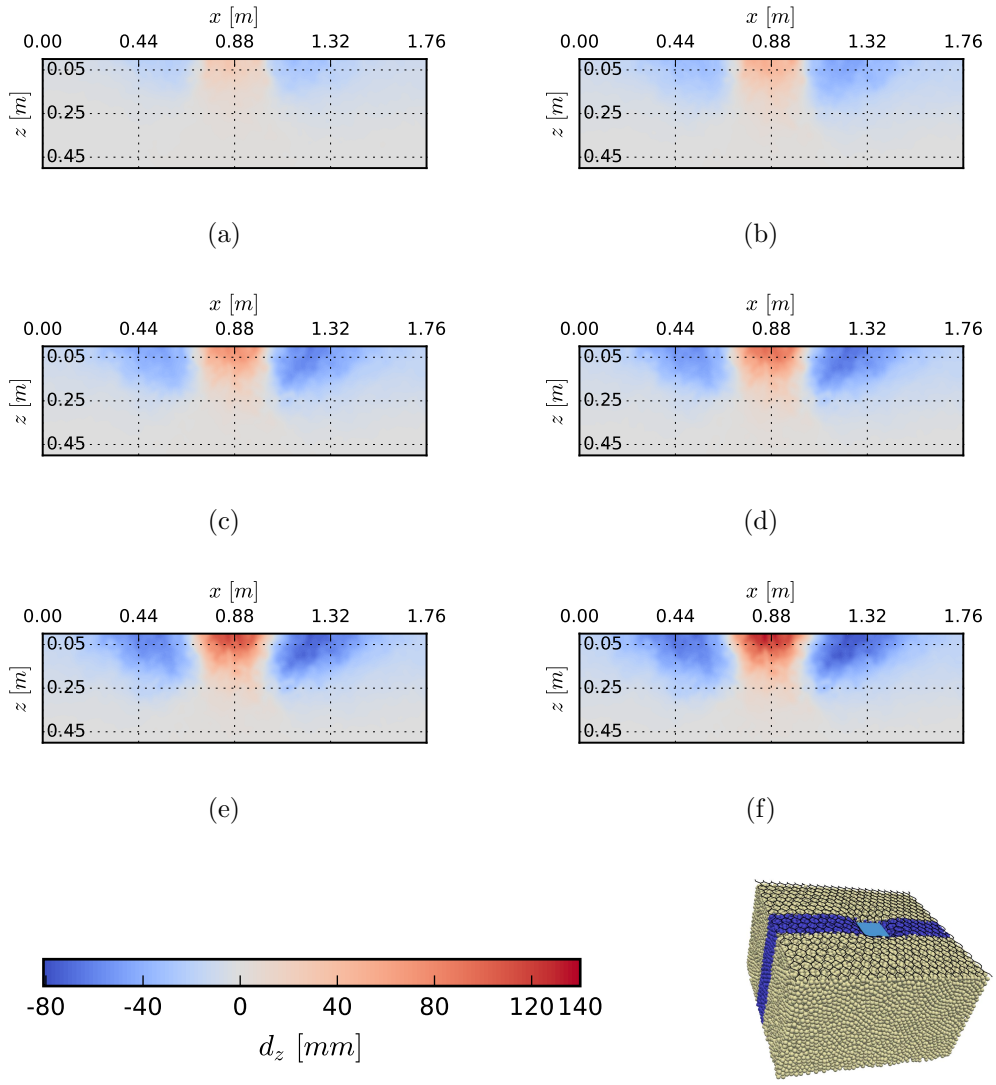


Figure 5.7: z-Displacement field at different displacement levels of the anchor plate: (a) $\delta \approx 20$mm, (b) $\delta \approx 42$mm, (c) $\delta \approx 65$mm, (d) $\delta \approx 92$mm, (e) $\delta \approx 110$mm, and (f) $\delta \approx 140$mm. The blue volume highlights the slice of the soil domain considered in the computation of the displacement field.

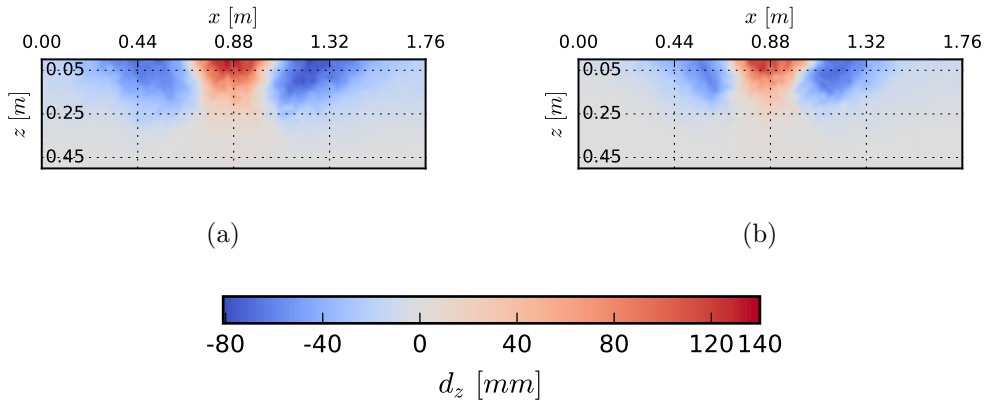


Figure 5.8: z-Displacement field at $\delta \approx 140$mm for the test (a) with and (b) without the presence of the mesh.

5.2.3 Evaluation of the soil displacement field

The displacement field of the soil volume is finally investigated. Following the procedure adopted in the force network analysis, a slice of thickness equal to the anchor plate side ($b = 250$mm) of the soil is considered as reported in Fig. 5.7. The displacement field is computed by linearly interpolating the displacements in the z-direction of the soil particles on a regular grid. The thus computed z-displacement field is reported in Fig. 5.7, with reference to different displacement levels of the anchor plate ($\delta \approx 20$mm, 42mm, 65mm, 92mm, 110mm and 140 mm) and to the x-z plane (an analogous result was obtained with reference to the y-z plane). The time evolution of the displacement field highlights that the kinematic of the soil failure mechanism is well represented by the classical theories of shallow foundations [95, 100]. In fact, in Fig. 5.7 it is possible to identify a soil wedge, under the plate, that is following the plate movement (red zone), and two lateral zones that are bulging and sliding upwards (blue zones). This result is not surprising considering that the punch test against soil represents a "special configuration" of a bearing plate test. In this perspective, the mesh effect may be seen as a progressively increasing lateral pressure, which contrasts the lateral spreading of the soil in the area immediately surrounding the plate. This leads to move the soil emergence zones more laterally (with respect to the anchor plate) and the consequent increase of the soil volume involved by the bulging mechanism as observable comparing the displacement fields in Fig.

5.8, which are obtained from the tests with and without the presence of the mesh.

5.3 Punch test against soil: towards an in-situ condition

The test configuration analysed in Sec. 5.2 faithfully represents the laboratory testing conditions (i.e. mesh is fixed along its outer boundary) and was used for calibration purposes. However, these conditions are not representative of the field conditions, where the mesh is only locally constrained by the presence of the anchor plates. Therefore the boundary conditions of the punch test against soil are modified as described in the following. In the new test configuration (referred as "in-situ"), symmetric boundary conditions are imposed at the edges of mesh panel, namely only the displacements along the orthogonal direction to the considered side are blocked (the displacement of the nodal particles at the mesh corners is blocked along both x and y direction). This permits one to move towards an idealised in-situ condition considering, at the same time, realistic constraints for the mesh panel (i.e. presence of the anchor plate) and the effect of adjacent panels (i.e. periodicity along the mesh boundary). For the sake of clarity, a 3D view of the model is shown in Fig. 5.9 with emphasis on the "in-situ" boundary conditions.

5.3.1 Investigation of the mechanical behaviour of the system

In analogy with the previous analysis, the mechanical behaviour of the system is described considering different force-displacement curves (see Sec. 5.2.1). The results of the numerical simulation are reported in Fig. 5.10 where they are compared with the one obtained from the simulation without the mesh (S). From a qualitative point of view, the overall mechanical behaviour of the system is analogous to the one observed in laboratory testing conditions. Indeed, for a low displacement of the plate ($\delta \leq 35mm$) the presence of the mesh has a negligible effect on the system response, then further displacements progressively activate the mesh mechanical reaction, leading to a consequent increment of the system bearing capacity. In this configuration, the presence of the mesh permits the bearing capacity of the system

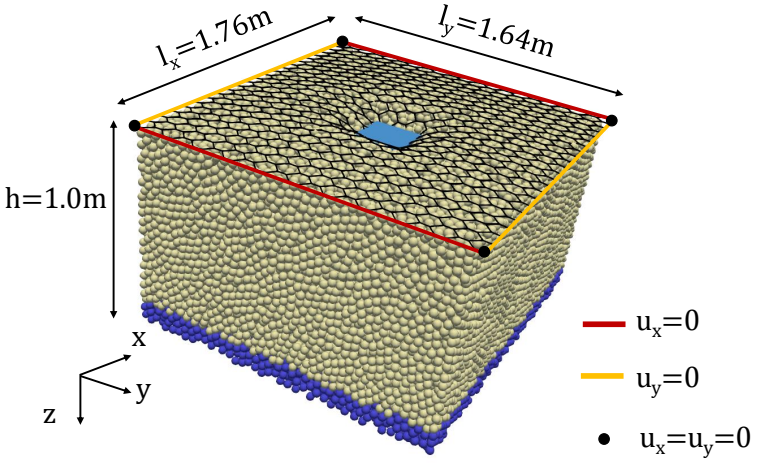


Figure 5.9: 3D view of the numerical model of the punch test against soil with the "in-situ" boundary conditions.

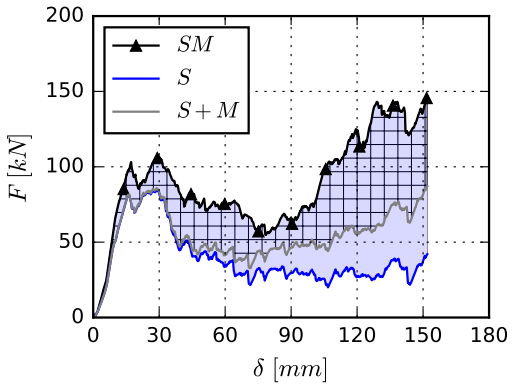
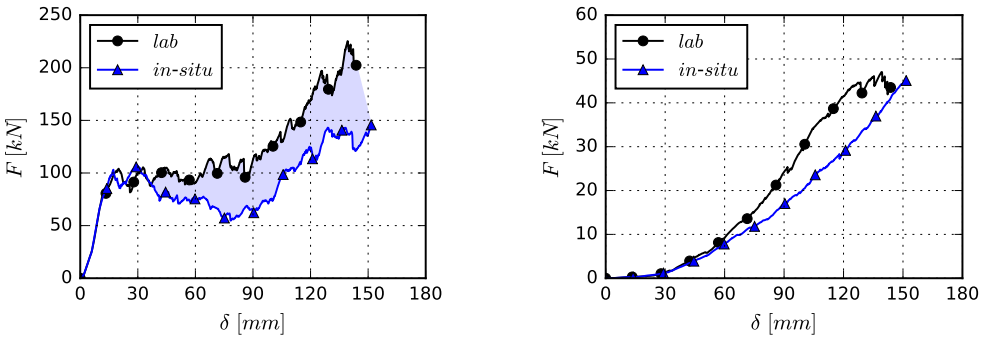


Figure 5.10: Comparison of the system mechanical response with (SM) and without (S) the presence of the mesh.

to be increased from 84.8kN to 147kN. As before the blue-filled area in Fig. 5.10 (difference between SM and S curves) highlights the benefit provided by the introduction of the mesh to the mechanical response of the system during the entire test. The hatched area represents instead the rate of this benefit solely related to the interaction between the mesh and the soil (i.e. subtracting the pure mechanical contribution of the mesh). Considering the maximum force registered during the test (i.e. system bearing capacity), the mesh-soil interaction provide 41% of its value ($\approx$ 60kN), while the pure mesh contribution is responsible for 31% ($\approx$ 45kN) of its value. In this case, the comparison between the mechanical response of the mesh with and without the presence of the soil layer is not possible because of, in the latter case, the mesh will freely follow the plate displacement, the soil being the only constraint to the mesh displacement along the z-direction.

5.3.2 Comparison with laboratory testing conditions

In order to quantify the influence of the boundary conditions on the system mechanical response, the results obtained in laboratory and idealised "in-situ" configurations are compared in the following. In Fig. 5.11a the overall mechanical response of the system (SM), obtained for the two above mentioned configurations, is compared. The two force-displacement relationships are almost identical in the first phase of the test ($\delta \leq$ 35mm), confirming once more that the system response is unaffected by the mesh response for low displacements of the anchor plate. In the second part of the test (i.e. $\delta >$ 35mm) instead, the relaxation of the boundary conditions leads to a decrease of the stabilising effect that the mesh has on the soil layer. This is particularly evident in the range 35mm$\leq \delta \leq$ 90mm of the plate settlement, namely in the phase in which the mesh is progressively tensioned. During this phase, the mesh is exerting a very low pressure on the soil, and its stabilising action is mostly due to the geometrical constraint that the mesh imposes to the upwards displacement of the soil, in the area surrounding the anchor plate. Considering the mesh fixed along its boundary, a more rigid constraint than in the "in-situ" configuration is imposed to the soil upwards-displacement, and this can limit the sliding of the bulging soil volumes in the zone external to the anchor plate. This prevents the drop of the F-δ curve which is instead observed for the "in-situ" configuration. It is worth mentioning that the temporary reduction of the system reaction, in the latter



(a) (b)

Figure 5.11: Comparison of (a) the system mechanical response (SM) and (b) of the mesh mechanical response (M) obtained with laboratory and "in-situ" boundary conditions.

configuration, occurs because of the low interaction between the mesh and the soil. In the general case, the interaction between the mesh and the soil may be sufficiently high to contrast the soil sliding also for low displacements, and thus the drop of the F-δ curve can be avoided. In the final part of the curve (i.e. $\delta > 90$mm), the mesh starts to apply a significant containment to the soil layer and approximately the same stiffness of the F-δ curve is observed in the two cases. The difference in terms of maximum force measured at the end of the test is imputable to the loss of the initial load due to the sliding of the soil volume under the anchor plate (i.e. 35mm$\leq \delta \leq$ 90mm). The difference in terms of system mechanical response between the laboratory and the "in-situ" configurations, during the entire test, is graphically represented by the blue-filled area in Fig. 5.11a. Finally, the pure mechanical reaction of the mesh is compared in Fig. 5.11b. It is interesting to note that the maximum z-force exerted by the mesh is almost the same in the two cases. The mesh being not directly constrained along the z-direction in the "in-situ" configuration, this implies that the mesh reaction is fully transmitted to the soil (no z-forces can be supported along the mesh boundary). The pure mechanical contribution that the mesh can provide to the system bearing capacity, seems therefore slightly influenced by the considered variation of the boundary conditions. Nevertheless, the more rigid condition obtained by fixing the mesh edges determines a prompter mesh response and permits

a limitation of the loss of the load initially applied to the anchor plate during the intermediate phase of the test (i.e. 35mm$\leq \delta \leq$ 90mm). This reflects a higher bearing capacity of the system as observed in the standard laboratory configuration.

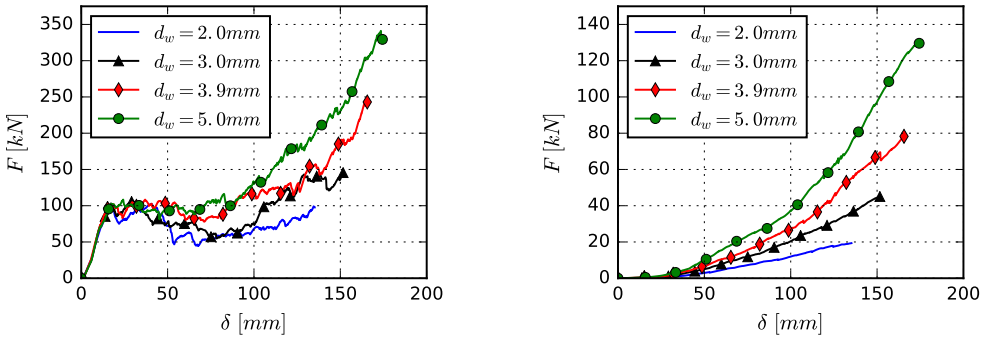
5.4 Parametric analysis

The analyses conducted in Sec. 5.2 and Sec. 5.3 have permitted the investigation of the main aspects related to the application of an initial load to the anchor plate. Moreover, the transmission mechanism of the initial load from the plate to the soil layer has been detailed. However, the system components, namely the mesh and the anchor plate, as well as the mechanical characteristics of the soil layer were kept constant and the effect of the variation of one of them was not considered. In this paragraph, a parametric analysis is conducted in order to understand the role of these variables on the system mechanical behaviour. The "in-situ" punch against soil test configuration (see Fig. 5.9) is considered in the following.

5.4.1 Mesh mechanical properties

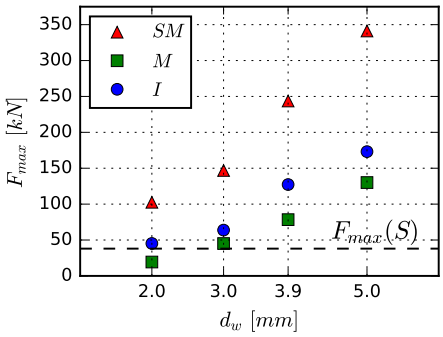
The mesh mechanical properties are modified varying the nominal diameter of the mesh wires. This allows the strength and the stiffness of the mesh to be modified, without changing the mesh typology. In fact, a variation of the mesh typology (e.g. internal geometry, type of elements) may lead to a strong modification of the mesh internal force transmission modality and thus to a strong variation of its interaction mechanism with the soil layer. Four different nominal wire diameters (i.e. SW diameter) are used, namely d_w =2.0, 3.0 (reference case), 3.9, 5.0mm. The latter value of d_w is higher than common commercial diameters; nevertheless, it is consider because it permits the role of the mesh mechanical properties to be highlighted. The same stress-strain curve are used for the definition of the contact wire model for all the considered diameters.

The mechanical response of the entire system is reported in Fig. 5.12a, while the mechanical response provided by the solely mesh is reported in Fig. 5.12b. As expected, the bearing capacity of the system increases when using a larger wire diameter. In fact, this entails an increase of the mesh mechanical resistance, as observable in Fig. 5.12a. Anyway, it is interesting



(a) (b)

Figure 5.12: (a) Comparison of (a) the system mechanical response (SM) and (b) of the mesh mechanical response (M) obtained with different wire diameters d_w.



d_w	F_{SM}	F_M	F_I
2.0mm	102 kN	19 kN	45 kN
3.0mm	146 kN	45 kN	64 kN
3.9mm	243 kN	78 kN	127 kN
5.0mm	341 kN	130 kN	173 kN

Table 5.2: Force values

Figure 5.13: Force values at failure for the overall system (F_{SM}) and partial contribution provided by the mesh (F_M) and by the mesh-soil interaction (F_I).

to note that the gain in terms of bearing capacity is provided, not only by the contribution given by a higher resistance of the mesh to local puncturing, but also in terms of mesh-soil interaction. The confining action that a stiffer mesh can exert on the soil, for the same amount of the plate displacement, is in fact higher, and this reflects in a higher contrast to the lateral spreading of the soil surrounding the anchor plate. If the mesh is sufficiently stiff to contrast the soil sliding immediately after the triggering of the failure mechanism, the loss of the initial load can be avoided (as in the case $d_w = 5.0$mm). In Fig.

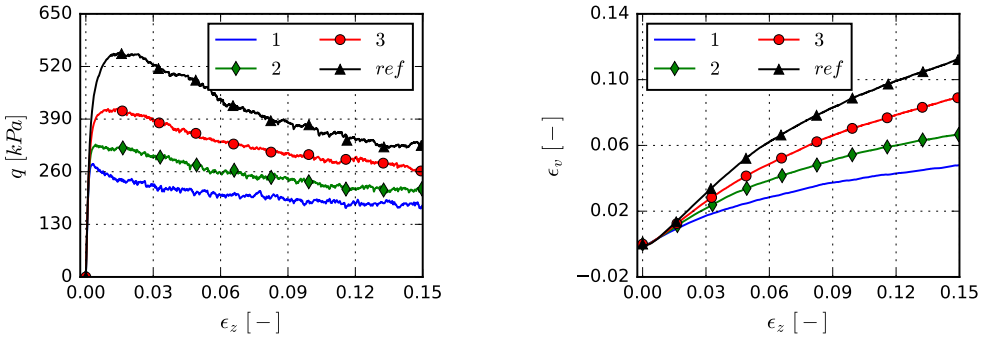
soil	E_i [Pa]	ϕ_i [°]	β_r [-]	η_r [-]	E_{50}^M [MPa]	ϕ_S^M [°]
1	1e9	47.5	0.000	0.00	218 (±8.5)	28.0 (±1.0)
2	1e9	47.5	0.005	0.01	220 (±6.5)	31.5 (±1.0)
3	1e9	47.5	0.010	0.03	209 (±5.0)	35.5 (±0.5)
ref.	1e9	47.5	0.020	0.06	204 (±5.0)	40.0 (±0.5)

Table 5.3: Numerical contact parameters used for the definition of the different soil types and macroscopic parameters obtained from numerical triaxial tests (the value in round brackets gives the range of variation observed by varying the confining pressure).

5.13 the bearing capacity obtained in the considered cases is reported, as well as the partial contribution given by the mesh and the one related to the mesh-soil interaction (I). The latter is calculated a posteriori subtracting from the overall bearing capacity of the system (SM), the rate provided by the mesh (M) and by the soil (S, which is constant and approximately equal to 38kN) at the system failure. From the observation of Fig. 5.13, the increase of the contribution provided by the mesh-soil interaction on the overall system bearing capacity is evident. The values are also reported in Tab. 5.2 to facilitate comparison.

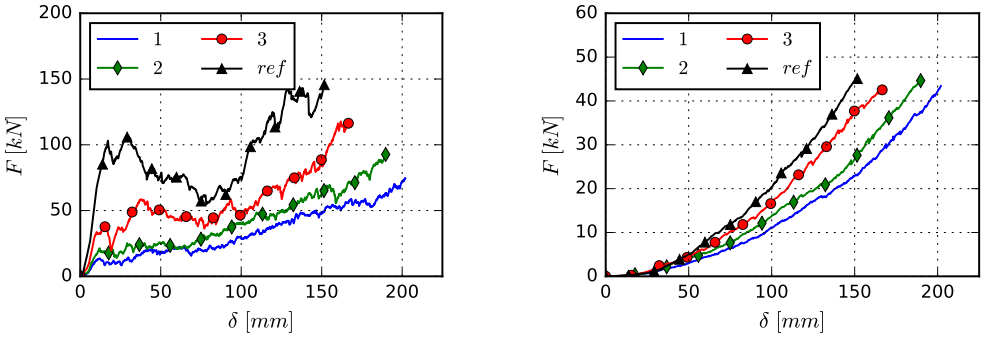
5.4.2 Soil mechanical properties

In order to vary the macroscopic mechanical behaviour of the numerical soil, and more precisely its macroscopic friction angle, different sets of the contact rolling parameters are considered. The considered numerical parameters together with the related macroscopic values (macroscopic elastic modulus E_{50}^M and the peak friction angle ϕ_S^M) that characterise the numerical soil are reported in Tab. 5.3. The macroscopic parameters are derived from 3D numerical periodic drained triaxial tests on sample of approximately 8500 particles. The triaxial tests were conducted with reference to four confinement pressures (50kPa, 75kPa, 150kPa and 225kPa) for each set of the considered numerical parameters (mean values of the resulting macroscopic parameters and the range of variation observed by varying the confining pressure are reported in Tab. 5.3). The same porosity (i.e. $n = 0.385$) that characterises the soil volume used in the punch test against soil is also



(a) (b)

Figure 5.14: DEM triaxial test results of the numerical soil: (a) deviatoric curve and (b) volumetric curve with reference to a confining pressure of 150kPa.



(a) (b)

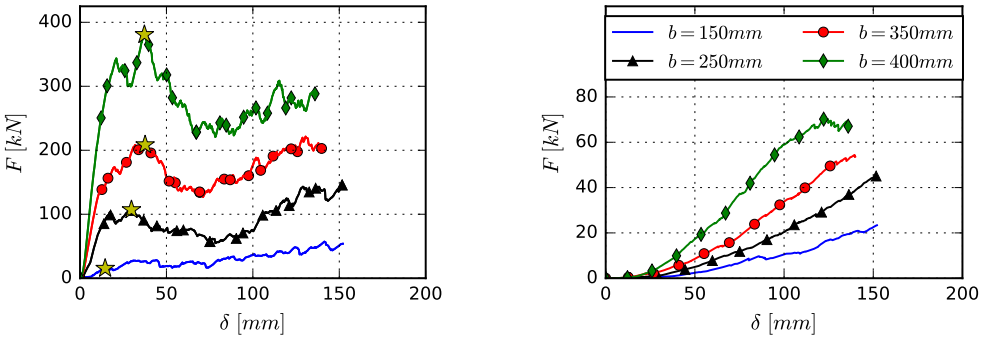
Figure 5.15: Comparison of (a) the system mechanical response (SM) and (b) of the mesh mechanical response (M) obtained with different mechanical characteristics of the soil layer.

reached before the deviatoric phase. The results of the triaxial test, with reference to a confining pressure of 150kPa, are reported in Fig. 5.14 where q represents the deviatoric stress, ϵ_z and ϵ_v the axial and volumetric strain respectively.

The numerical results obtained repeating the punch test against soil for each set of parameters are reported in Fig. 5.15. As expected a higher bearing capacity of the system is obtained when increasing the macroscopic soil friction angle. This increment is mostly related to the increase of the soil bearing capacity (i.e. reaction for low displacements), in fact the contribution provided by the mechanical resistance of the mesh is approximately the same in all the considered cases as observable in Fig. 5.15b. Only a slight difference in the stiffness of the mesh response is observed. From this simple analysis it is evident that the relationship between the force-displacement behaviour of the mesh-anchor-soil system, as well as its ultimate bearing capacity are strongly affected by the soil mechanical characteristics. Therefore, for a correct estimation of the force-displacement behaviour of the mesh-anchor-soil system, it is recommended to consider soil layers of different mechanical properties in the experimental characterisation.

5.4.3 Anchor plate dimension

Finally, the dimension b of the square anchor plate is varied in the range 150mm$\leq b \leq$400mm. The obtained force-displacement curves related to the entire system and to the solely mesh are reported in Fig 5.16a and 5.16b respectively. For the sake of clarity only four values of b are reported. The increase of the plate dimension leads to an increase of both the soil bearing capacity and the mesh maximum puncturing force as expected. This reflects in a significant gain in terms of ultimate force of the system. Having said that, it is interesting to analyse how the two contributions are influenced by a variation of the plate dimension. In this perspective, the initial soil failure mechanism (associated with the initial peak of the F-δ curve) and the mesh failure are investigated separately. The point of the F-δ curves associated with the occurrence of the former mechanisms is highlighted with a yellow star marker in Fig. 5.16a. The force values characteristic of the two mentioned failure processes, for different values of b, are reported in Fig. 5.17a. Firstly, it can be observed that the ultimate puncturing force of the mesh ($\bullet$) linearly scales with the plate dimension ($F_M = \alpha_M \frac{b}{b^*} F_M^*$,



(a) (b)

Figure 5.16: Comparison of (a) the system mechanical response (SM) and (b) of the mesh mechanical response (M) obtained with a different dimension b of the anchor plate.

with $\alpha_M = 0.90$ and the asterisk superscript indicates the reference case $b = 250$mm); this is in agreement with the assumption that the resistance of an anchored mesh panel is a function of the number of the wires intercepted by the anchor plate (see Chapter 4). Secondly, the trend of the force contribution given by the soil bearing capacity (★) is well fitted by a cubic function of b ($F_S = \alpha_S \left(\frac{b}{b^*}\right)^3 F_S^*$, with $\alpha_S = 0.78$), this being in perfect agreement with the classical theory of shallow foundations [95, 100]. Finally, the displacement fields obtained for $b = 150mm, 250mm, 350mm$ and 400mm, at a displacement level of the anchor plate approximately equal to 140mm, are reported in Fig 5.17. The comparison highlights that a larger soil volume is mobilised when a larger anchor plate is considered, or in other terms, a larger soil volume can be ideally stabilised through the application of an initial load at the anchor plate level. This condition is confirmed by the spatial distribution of the contact forces reported in Fig. 5.18. From the comparison of the contact force distributions, it is evident that the stabilising pressure cone generated by the same amount of plate displacement ($\delta \approx 140$mm) is wider, and can reach a deeper soil layer, when increasing the anchor plate dimension.

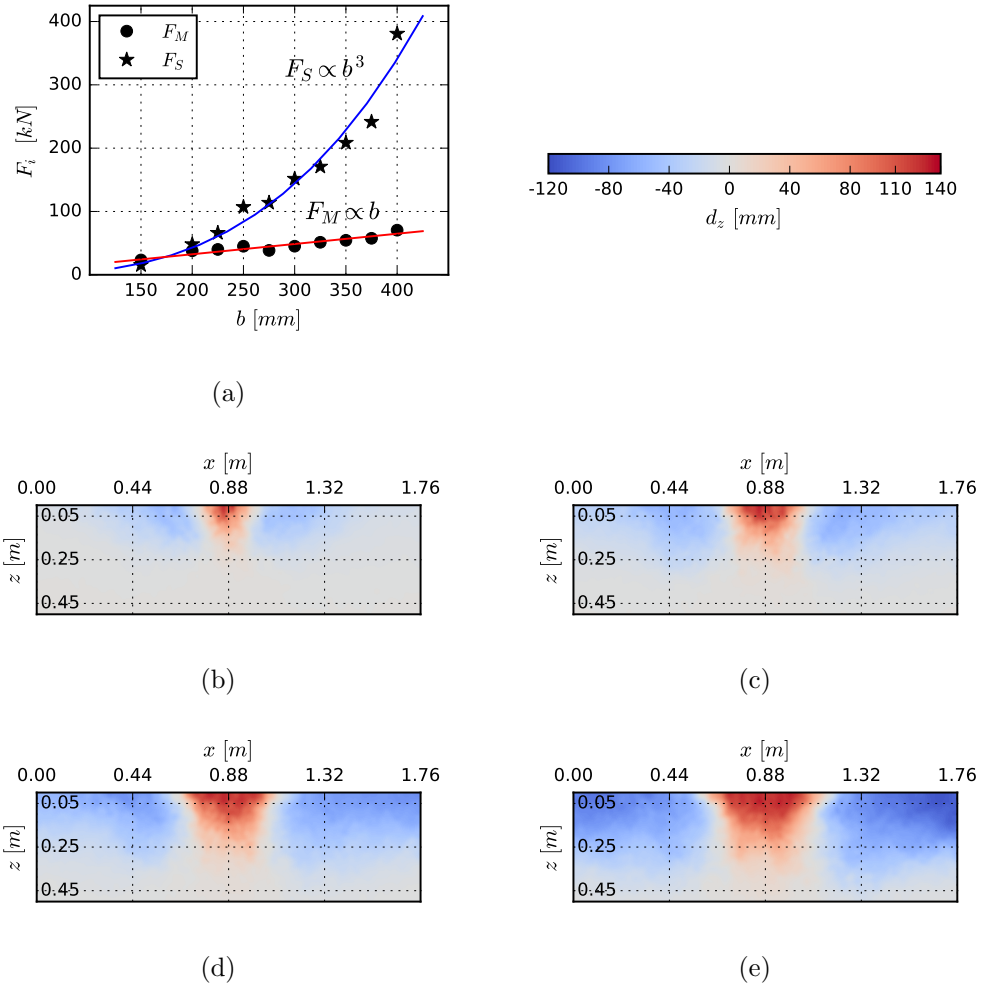


Figure 5.17: (a) Force values characteristic of the soil failure (★) and the mesh puncturing failure (•) mechanism. z-Displacement field at $\delta \approx 140$mm for different anchor plate dimension: (b) $b = 150$mm, (c) $b = 250$mm, (d) $b = 350$mm, (e) $b = 400$mm.

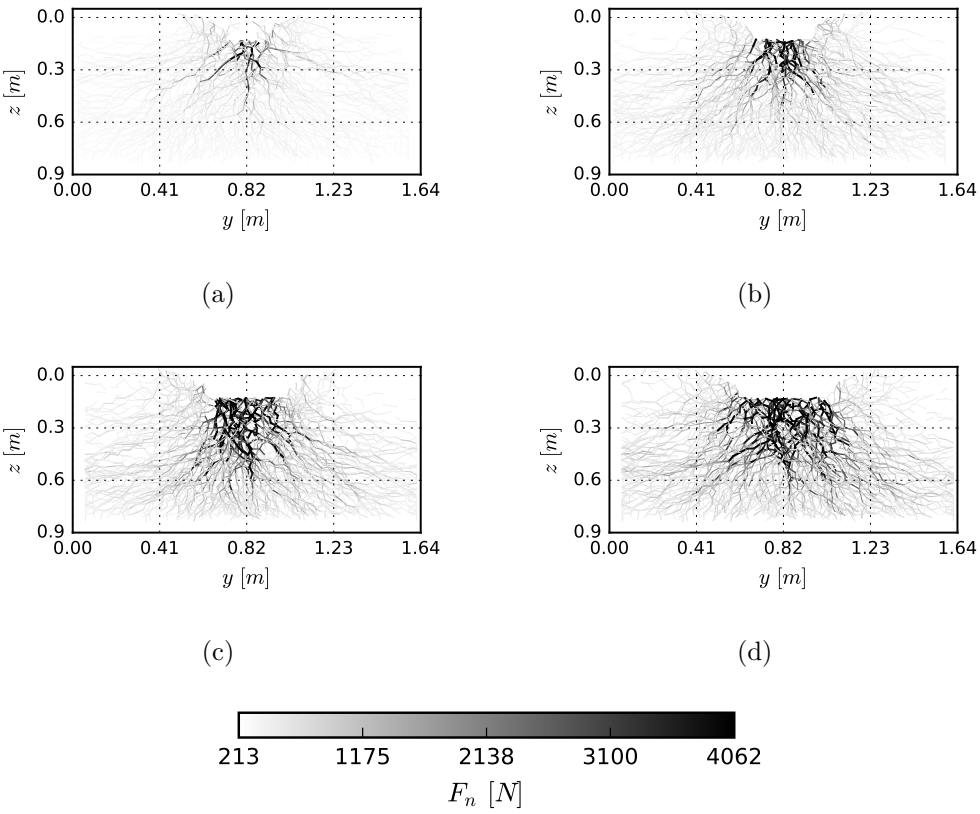


Figure 5.18: Contact force network (strong network) at $\delta \approx 140$mm for different anchor plate dimension: (a) $b = 150$mm, (b) $b = 250$mm, (c) $b = 350$mm, (d) $b = 400$mm (the colorbar upper limit is set equal to $\max(F_n)/4$).

5.5 Conclusive remarks

In this chapter, the effect of a loading phase, during the mesh system installation, of the anchor plate was investigated. The evolution of the relationship between the applied force and the anchor plate settlement was characterised and its peculiar behaviour was analysed in detail. This was done with reference to both laboratory testing conditions and idealised "in-situ" conditions. Furthermore, a parametric analysis was conducted in order to analyse the effect of the main variables of the problem. The main results are summarised as follows:

- the mechanical response of the system (i.e. applied force and anchor plate settlement relationship), represented by the F-δ curve, is characterised by two main phases. Firstly, for a low displacement, the system response is ruled by the soil reaction and the effect of the mesh is negligible. For further increments of the plate displacement, a failure mechanism occurs in the soil (soil bearing capacity is overcome), hence the mesh-soil interaction and the mesh reaction are progressively activated and the system response is mainly controlled by these contributions in this second phase of the test;
- the adoption of boundary conditions more similar to the "in-situ" ones leads to a decrease of the system bearing capacity, with respect to the one measured in laboratory configuration. This reduction of the bearing capacity is due to a "delayed activation" of the mesh-soil interaction, due to a "softer" constraining of the mesh. This translates in a partial loss of the initial force deriving from the sliding of the soil volume (surrounding the anchor plate) along the failure surface;
- the pure tensile contribution of the mesh (i.e. F_M) seems slightly affected by the considered variation of the boundary conditions. This highlights that the vertical load (i.e. along z-direction), applied by the plate displacement on the mesh, is directly transmitted from the mesh to the soil;
- the adoption of a mesh of enhanced mechanical characteristic leads to a considerable increase of the system bearing capacity. This is mainly related to the enhancement of the interaction between the mesh and the soil, and only in a minor part to the increase of the mesh puncturing resistance. A stiffer mesh permits the activation of the mesh-soil interaction for lower values of the anchor plate settlement,

thus reducing the loss of the initial load. In this perspective, the choice of the mesh mechanical characteristic should be made in order to activate the mesh-soil interaction immediately after the occurrence of the failure mechanism in the soil. In this way, the sliding of the soil volume along the failure surface is strongly limited, thus avoiding a significant loss of the load initially applied to the anchor plate;

- the soil mechanical characteristics (the macroscopic friction angle was here considered) considerably influence the bearing capacity of the system, and in particular its reaction for low anchor plate displacements. For a correct experimental characterisation of a specific mesh type different tests should by performed using soil layers of different mechanical characteristics;
- the adoption of a large anchor plate considerably increases both the soil bearing capacity and the mesh puncturing resistance; consequently, this determines a significant increase of the overall bearing capacity of the system. The increment can be estimated by using a linear function of the anchor plate side b concerning the mesh ultimate puncturing force, and by using a cubic function of b concerning the soil bearing capacity. Moreover, a larger anchor plate permits the stabilisation of a larger soil volume (larger stabilising pressure cone).

Besides the results directly related to the numerical analysis, some more general considerations are worth of mentioning. Firstly, the force-displacement relationship, obtained from the punch test against soil, is generally used to characterise the response of the system to an initial loading phase of the anchor plates. However, as observed by Di Prisco et al. [32] it is fundamental to keep in mind that the effect of an initial load may decrease over time due to the time dependency of the mechanical behaviour typical of geomaterials (e.g. creep effects). A monitoring program should be therefore considered if the effect of an initial load is accounted during the design of an anchored mesh system. Secondly, it has to be considered that this initial load is generally applied by operators, which manually tighten the bolts by means of a torque wrench. The maximum force that they can applied is therefore limited, and, in general, significantly lower than the force values obtained in a standard laboratory characterisation. Finally, in the laboratory characterisation as well as in the numerical analyses here presented the soil layer is lying on a horizontal plane. However, in real applications, the soil layer is inclined and gravitational effects affect the layer stability. Moreover, the

initial load applied to the anchor plates is generally not normally oriented with the sliding plane. These differences may lead to a decrease of the effectiveness of the load applied in the installation phase, which should be carefully considered when its effects are accounted in the design phase of an anchored mesh system.

Chapter 6

Secured drapery systems for slope stabilisation

In this chapter, the mechanical behaviour of a secured drapery system when loaded by an unstable soil (or debris) layer is addressed. This condition is typical when a secured drapery is installed along soil (or highly-fragmented rock) slopes in order to control and to retain the potential movement of its shallow portion (the unstable layer thickness is generally limited to 3m because of practical limitations as discussed in Chapter 1). In this shallow layer, as a consequence of a variation of the slope conditions (e.g. weathering and erosion, degradation of the material mechanical properties, seismic action, intense rainfalls), diffuse or localised instabilities may occur. Under such circumstances, the soil volume interested by the failure process slides, and it applies a pressure over the mesh system; consequently, the mesh deforms and contrasts the movement of the soil by applying a retaining action on the latter. The mesh reaction is progressively activated with its deformation which, in turn, is related to the soil displacements. The mutual interaction between the mesh and the soil plays, therefore, a major role in the evolution of the problem: the soil displacements are influenced by the retaining action exerted by the mesh system on the soil, and vice versa. Hence, it is fundamental to carefully considered the mesh-soil interaction, and the large deformations of both the mesh and the soil, for a correct characterisation of the mechanical response of the mesh system.

In order to represent the non-trivial loading condition above described, an idealised "in-situ" configuration is considered in the definition of the numerical model. In particular, a secured drapery system, composed of three

vertically stacked mesh panels, is loaded by an unstable granular column (this test configuration will be referred as "mesh-soil" problem in the following). The 8x10 hexagonal double twisted mesh type (nominal wire diameter of 2.7mm) is considered as the reference mesh.

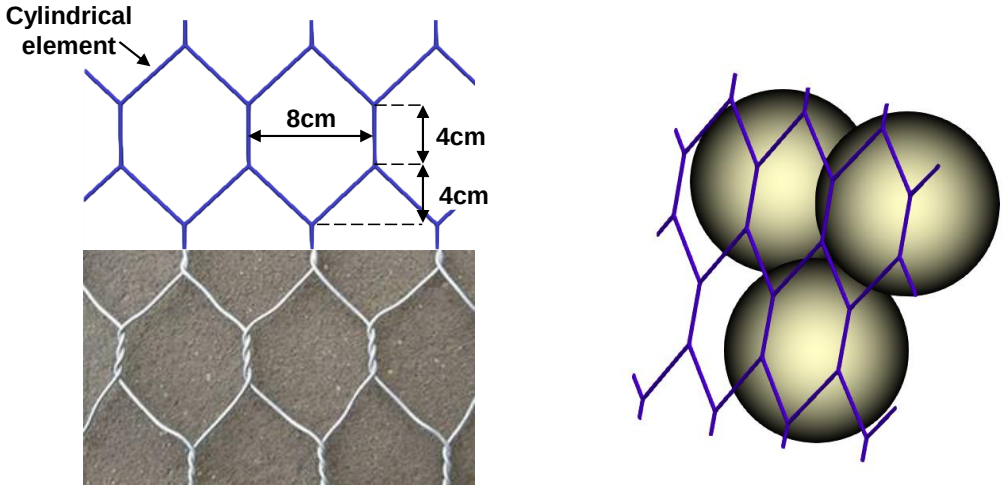
The discrete nature of the modelling approach adopted in this thesis ensures a "realistic" representation of the mesh-soil interaction. In fact, the evolution of the failure mechanism in the soil layer behind the mesh, as well as the activation of the mesh retaining action will spontaneously arise from the forces exchanged at the contact between the different elements (wires and soil particles) through the application of the contact laws.

In the first part of this chapter, the numerical model is presented in detail. Then, the mechanical behaviour of the mesh system is analysed considering its deformation evolution, and characterising its mechanical response in terms of force-displacement relationships of the system and of its different parts. Furthermore, a particular attention will be dedicated to the failure mechanism that characterises the instability that occurs in the soil layer. Successively, a parametric analysis is performed in order to understand the role of several problem's variables on the mesh system mechanical response. In particular, the soil properties (i.e. friction angle, stiffness), the interface mechanical properties (i.e. soil-mesh contact friction angle), the mechanical characteristic of the mesh (i.e. wire diameter d_w) and the geometrical characteristics of the problem (i.e. slope angle, thickness of the column, anchor plate dimension, anchors' pattern) are considered.

6.1 Numerical model

6.1.1 Mesh numerical modelling

In the mesh-soil problem, as above mentioned, the interaction between the mesh and the soil is extremely important and should be realistically considered in the simulation. In this perspective, a detailed description of the mesh geometry is needed, and thus the CWB approach (see Chapter 3) is adopted for the numerical representation of the wire mesh. In fact, the adoption of cylindrical elements allows the physical shape of the mesh wires to be considered in the numerical model, thus ensuring a precise computation of the mesh-soil contact. These cylindrical elements are characterised by the same length of the real wires and by a diameter of 2.7mm, which corresponds to



(a) (b)

Figure 6.1: (a) Comparison between the real and the numerical schematisation of the DT mesh. (b) Graphical example of the DT mesh interacting with external spherical particles.

the one of the single wires (the double twisted wires have therefore a slightly smaller diameter in the model than in the real mesh). A graphical comparison between the real and the numerical mesh is reported in Fig. 6.1; in the same figure a graphical example of a portion of the numerical mesh interacting with spherical particles is also reported for the sake of clarity. The tensile stress-strain relationships used for the definition of the EWMs adopted for the mechanical description of the wires in the model are the ones reported in Fig. 3.8 of Chapter 3. The validation of the numerical mesh model using the CWB approach has already been presented in Chapter 3 (with reference to standard UNI punch test). Finally, the numerical parameters adopted for the mesh elements are reported in Tab. 6.1 (a non-null friction contact angle is here adopted to consider a frictional contact between the mesh and the soil particles).

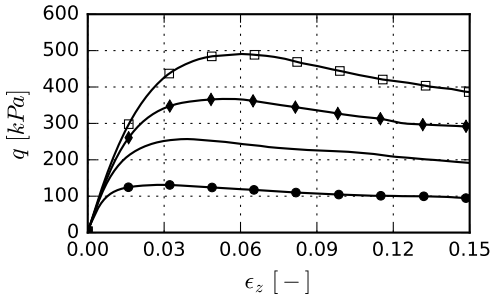
6.1.2 Soil numerical modelling

For the description of the granular soil column that represents the unstable layer, spherical particles are used (for the sake of computational efficiency). The mean diameter of the particles is set equal to $d_{50} = 12$cm (polidispersity in diameter of $\pm 10\%$). The choice of a coarse grain size is ruled mainly by the

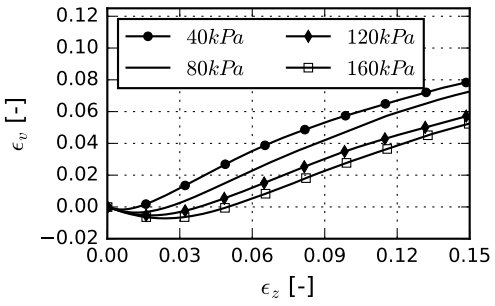
/	E_i [Pa]	ν_i [-]	ϕ_i [°]	ρ_i [kg/m^3]	β_r [-]	η_r [-]
mesh	2e10	0.30	35.0	7.45e3	/	/
soil	1e8	0.30	35.0	2.90e3	0.1	0.1
box	1e8	0.30	0.0†	/	/	/

† The bottom wall is characterised by a contact friction angle of 35°

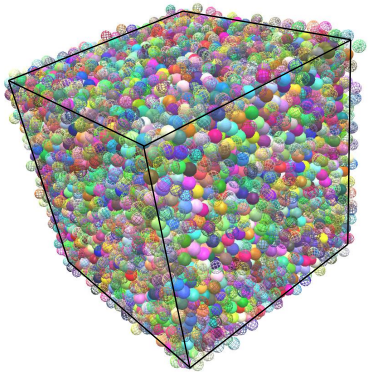
Table 6.1: Numerical contact parameters used in the "mesh-soil" problem simulation.



(a)



(b)



(c)

Figure 6.2: DEM triaxial test results of the numerical soil: (a) deviatoric curve and (b) volumetric curve. (c) Numerical triaxial specimen (the black solid line represents the boundary of the periodic cell, while the periodic clones of the particles are represented in wireframe).

need of having particles larger than the mesh opening size, and so avoiding their passage through the mesh, rather than by computational reasons. The same contact model adopted in Chapter 5 is used in the present analysis. In this case, no calibration data were available, so the numerical contact parameters have been chosen in order to fit typical values of real coarse granular materials. The macroscopic characteristics of the considered numerical soil have been derived performing 3D numerical periodic drained triaxial tests on sample of approximately 8500 particles. Before the deviatoric phase, the sample is isotropically compacted; four different values of confining pressure has been considered, namely 40kPa, 80kPa, 120kPa, 160kPa (80kPa being approximately the pressure at the middle height of the soil column that will be considered in the mesh-soil test of Sec. 6.1.3). The same porosity that characterises the soil column used in the mesh-soil test (i.e. $n = 0.41$) is reached before the deviatoric phase. For this aim, the interparticle contact friction angle is modified during the isotropic phase and the rolling resistance is temporary not considered; before the beginning of the deviatoric phase, the contact parameter are updated with the "correct" ones (existing interactions are modified accordingly). The results of the triaxial test are reported in Fig. 6.2 where q represents the deviatoric stress, ϵ_z and ϵ_v the axial and volumetric strain respectively. The numerical parameters are reported in Tab. 6.1. The obtained macroscopic parameters are: young modulus (computed at the 50% of the maximum deviatoric stress) $E_{50}^M = 19$MPa ($\pm$1MPa) , Poisson's ratio $\nu^M = 0.33$ ($\pm$0.01) and peak friction angle $\phi_S^M = 38°$ ($\pm$0.4°); the values in round brackets give the range of variation observed by varying the confining pressure.

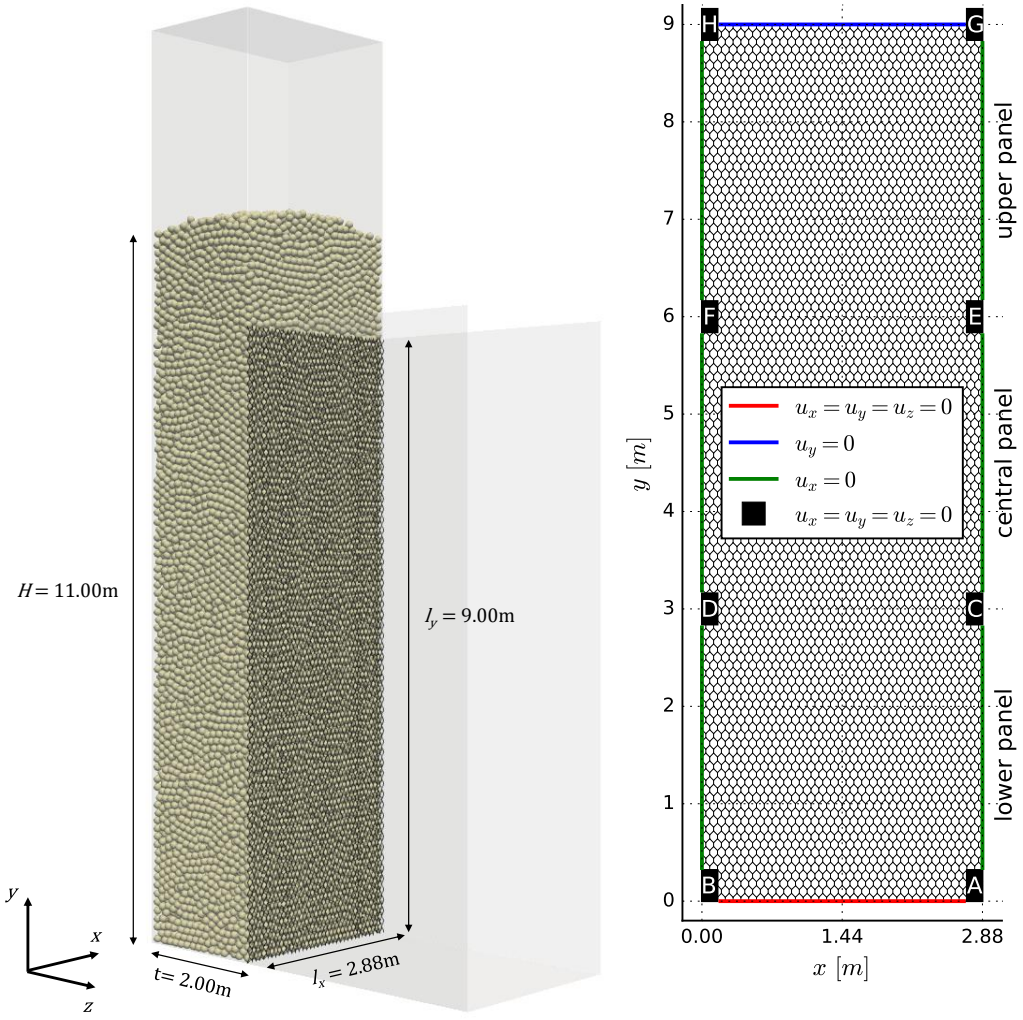
6.1.3 Mesh-soil problem numerical model

After the preliminary description of the details regarding the numerical modelling of the mesh and of the numerical soil, the test configuration adopted in the following analysis can be presented. A secured drapery system composed of three almost square mesh panels of dimensions 2.88m×3.00m each (overall system dimensions 2.88m×9m) is considered in the model. The wire mesh is numerically described by using 8250 spherical particles (gridNodes) and 12189 cylindrical elements (gridConnection). The unstable soil layer is composed of approximately 45k spherical particles, for an overall volume of 2m×2.88m×11m. The latter is contained in a box placed just behind

the mesh. All the walls that compose the box are frictionless with the only exception of the bottom wall (on the back and front of the mesh) that is characterised by a contact friction angle $\phi_w = 35°$ (same as the soil). For the sake of clarity, a 3D view of the model is shown in Fig. 6.3a.

In order to consider a realistic representation of the field conditions, idealised "in-situ" boundary conditions are imposed to the mesh system (similarly to what has been done in Chapter 4). The mesh is anchored by means of squared anchor plates having a nominal side $d_p = 0.32$m. They are represented in the numerical model, by fixing all the degrees of freedom of the nodal particles (i.e. gridNodes elements) of the mesh that are ideally intercepted by the anchor plates. The position of these anchor plates determines also the division of the mesh strip in the three panels above mentioned. In order to respect the periodicity of the problem, half of the dimension of the anchor plates is considered with respect to the x-direction along the lateral edges of the mesh strip as shown in Fig. 6.3b. For the sake of clarity, each anchor is associated with a capital letter as reported in Fig. 6.3b. This permits one to easily refer to a particular anchor and to the different sides of the mesh system; for instance, the right-bottom and left-bottom anchors are indicated with the capital letter A and B respectively, while the segment (i.e. nodes alignment) connecting them is referred as side AB. For anchors that are placed in-between two mesh panels, as for instance the anchor C, half of the anchor is associated with each panel. In this case, the considered portion of the anchor will be referred as C_b and C_t for that portion that belongs to the lower and upper panel respectively (in other words, an anchor is divided in a bottom and a top portion with respect to the common side between two neighbouring panels). Finally, specific boundary conditions are imposed at the lateral edges of the mesh strip with aiming to simulate a periodic mesh-wall drapery system in the x-direction. In particular, the mesh nodal displacement along the x-direction (u_x) is not allowed along the vertical sides, namely side AG and BH. Furthermore, the displacement along the y-direction (u_y) is not allowed for the top horizontal side, namely side HG, in order to considered that the mesh panel is fixed at the crest of the slope. Finally, the displacement of the bottom side of the mesh system, namely side AB, is fixed for all the spatial components ($u_x = u_y = u_z = 0$) to retain the soil at the toe of the slope. For the sake of clarity, the mesh dimensions and the boundary conditions are depicted in Fig. 6.3b.

The simulation is divided in three different phases:



(a) (b)

Figure 6.3: (a) 3D view of the mesh-soil problem numerical model. (b) Frontal view of the mesh panel with the indication of the boundary conditions.

- firstly, the soil volume is generated from a loose cloud of particles that is created inside a prismatic volume taller than the box considered in the next phases of the simulation. The particles are let deposit under gravity until reaching the desired height of the soil column as shown in Fig. 6.4a;
- secondly, the soil volume obtained in the previous phase is let to settled under gravity until it reaches a stable condition. The stabilisation of the soil mass is considered to be achieved when the ratio of the mean unbalanced force acting on bodies over the mean contact force is lower than 1×10^{-2}. During these two preliminary phases, the soil column is temporarily contained by a rigid retaining wall that is placed in correspondence with the mesh plane as reported in Fig. 6.4b;
- thirdly, the rigid retaining wall is removed triggering the instability of the soil column. Therefore the soil starts to interact with the mesh, exerting a pressure on it that determines the progressive activation of the mesh response (see Fig. 6.4c). The simulation is considered ended when the mesh system fails, namely it is no more able to retain the unstable soil. In the model, this condition coincides with the breakage of the wires connected to an anchor plate and determines an abrupt drop of the retaining force that the mesh system exerts on the soil (see the force-displacement curves defined hereafter).

During the last phase, the mechanical condition of each wire (i.e. actual stress and strain values) is monitored permitting the force supported by the different parts of the system to be computed, as for instance anchors and single panels. More precisely, referring for example to the central panel, the force experienced by the latter is computed by integrating the tensile force acting on each node that belongs to the panel perimeter ("reference boundary"), as exemplified in Fig. 6.5. It is therefore given by the summation of the tensile forces acting on its four edges, namely CD, CE, DF, EF, and acting on the four portion of the anchors belonging to the panel, namely C_t, D_t, E_b, F_b (the subscripts t and b indicate the top and the bottom part of the considered anchor respectively). The force is finally analysed with reference to its spatial components (i.e. F_x, F_y and F_z), as well as considering the resulting force F_{tot}; the latter is computed as the Euclidean norm of the three spatial components. It is important to specify that the forces thus defined, represent the tensile forces supported by the mesh system (or a part of it), or alternatively the forces characterising the mesh reaction to the pressure

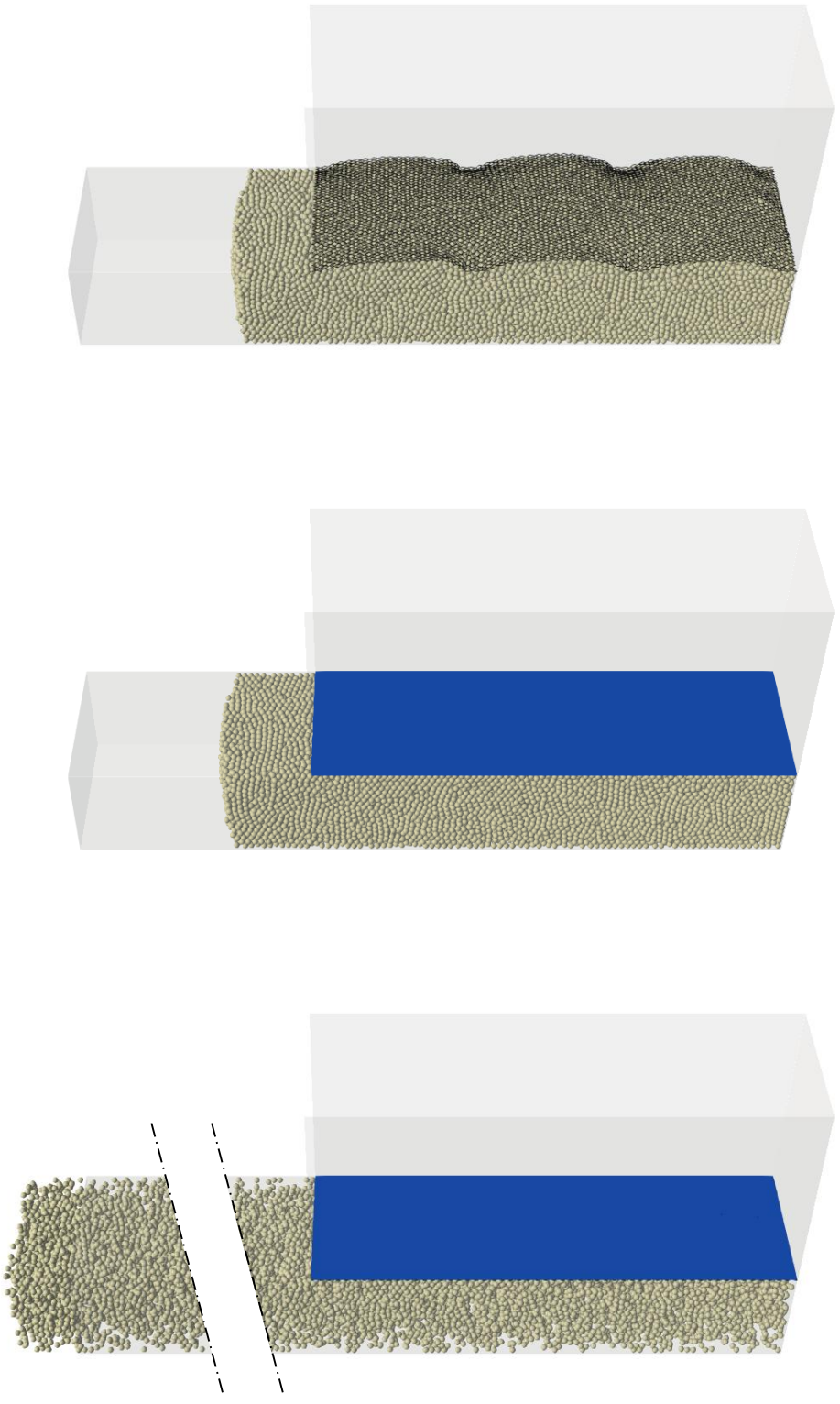
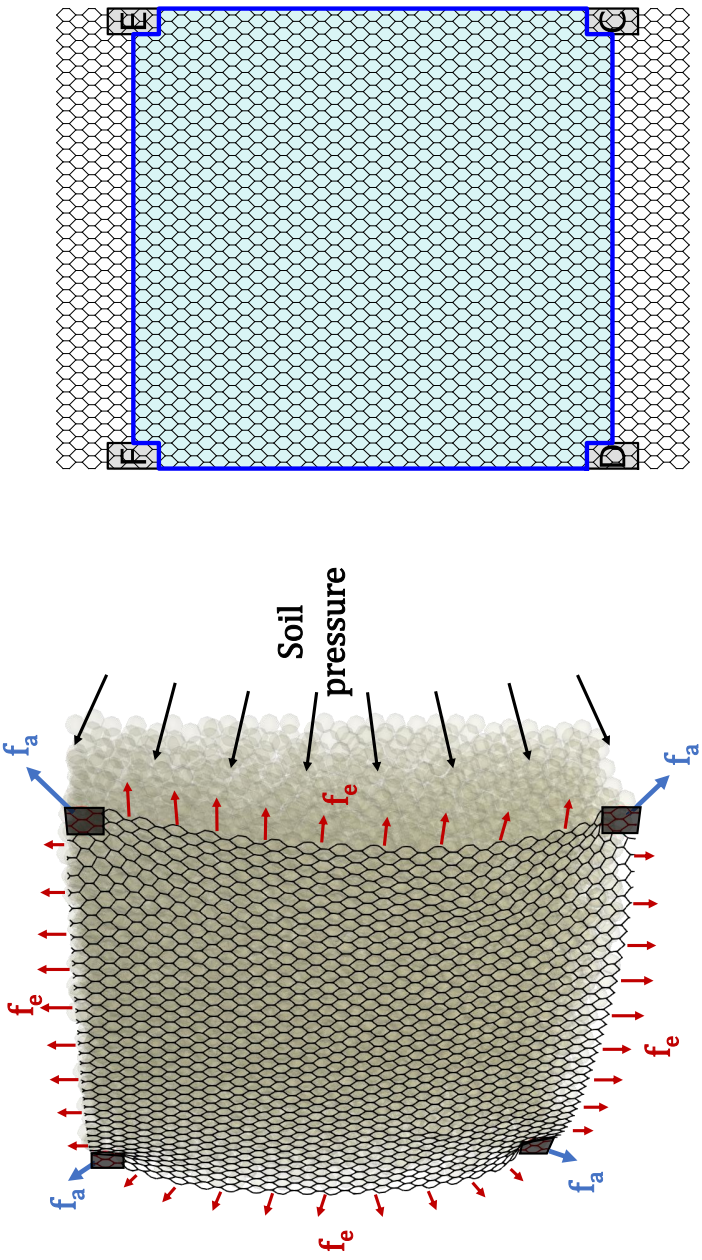


Figure 6.4: Different phases of the simulation: (a) soil volume generation phase, (b) soil volume stabilisation phase, (c) mesh-soil interaction phase.



(a) (b)

Figure 6.5: (a) 3D conceptual scheme of the forces on a generic panel: the contribution of tensile forces along the panel edges is represented by f_e (red arrows) while the one related to the anchors is represented by f_a (blue arrows). (b) Reference boundary considered for the computation of the panel reaction with reference to the central panel (analogous for the other panels).

imposed by the unstable soil layer. In this perspective, these forces permit a quantification of the stabilising action that the mesh imposes on the soil layer (for equilibrium) in order to contrast its movement. The same strategy can be also applied to measure the force acting on single parts of the mesh system, namely anchors and edges, simply changing the definition of the "reference boundary". Finally, in order to define the force-displacement relationships that characterise the evolution of mechanical response of the mesh panels, two different definitions of the panel displacement are considered, namely the displacement measured at the centre of the considered panel δ_i and the mean displacement of the panel $\bar{\delta}_i$ with respect to the z-direction (the subscript i indicates the considered panel, namely l for the lower panel, c for the central panel and u for the upper panel).

6.2 Numerical results

The results obtained from the numerical model presented in Sec. 6.1.3 are reported in the following. For the sake of clarity, the main characteristics of the latter are summarised hereafter. The system is perfectly vertical (slope angle $\alpha = 90°$), the thickness of the unstable soil layer is set equal to $t = 2.0$m and a square pattern, with a nominal spacing of 3m, is adopted for the anchors. Square anchor plates with side length $d_p = 0.32$m are considered. The soil is characterised by a macroscopic friction angle $\phi_S^M = 38°$ and the contact friction angle between the soil and the mesh elements is equal to $\phi_{ms} = 35°$.

A 3D view of the time evolution of the mesh-soil problem is reported in Fig. 6.6. In this figure the step (a) shows the initial conditions, the steps from (b) to (h) represents some of the steps that are used for the characterisation of the system mechanical response (they are "internal" steps of the third phase of the simulation as defined in Sec. 6.1.3). In particular, the step (h) corresponds to an instant prior to the failure of the mesh. Finally, the step (i) permits the complete failure at the connection between the mesh and the anchor plate to be visualised (localised at anchor F in this case), while the step (j) shows how the failure propagates inside the mesh.

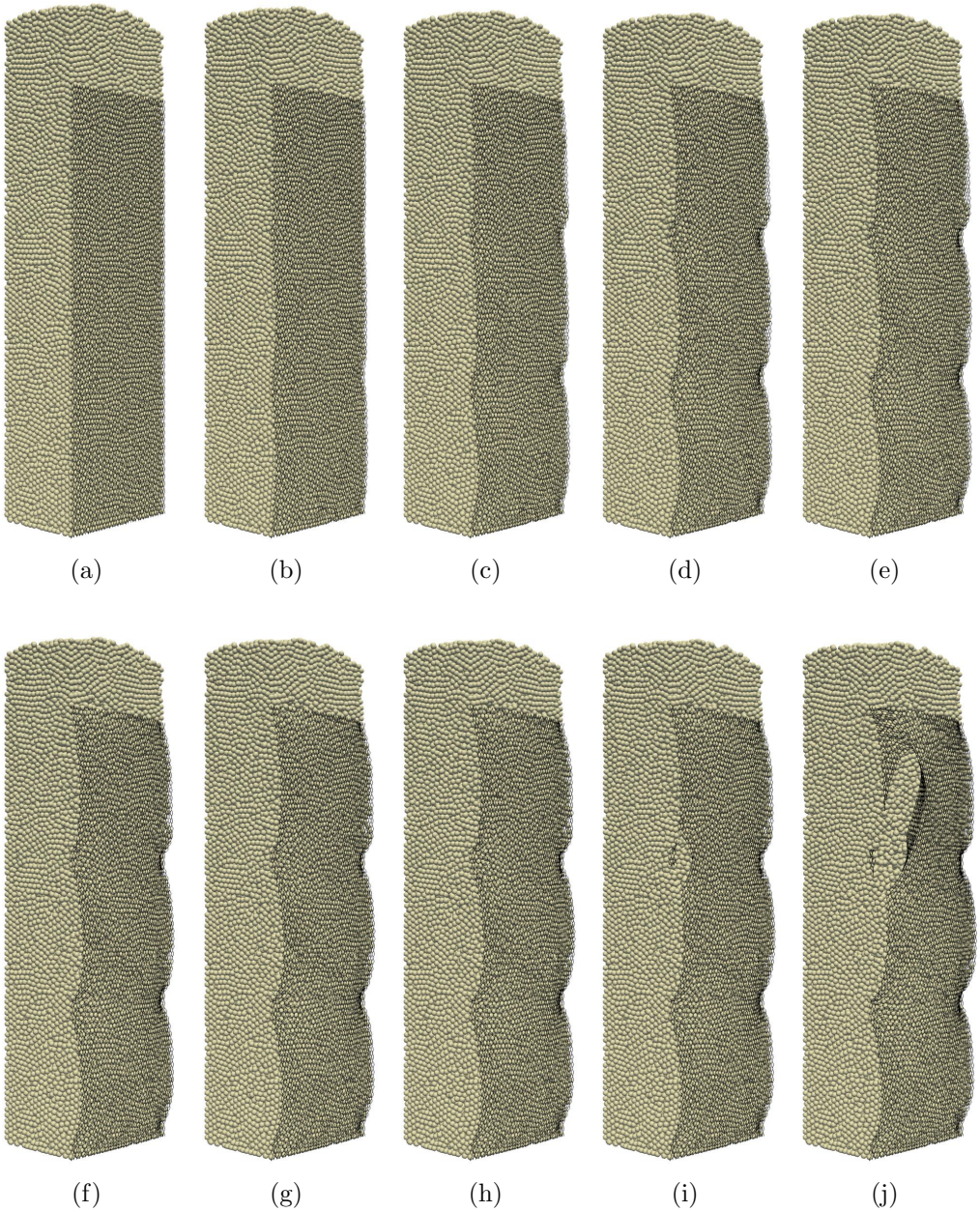


Figure 6.6: 3D view of the time evolution of the mesh-soil problem: (a) initial step, (b)-(h) steps "internal" to the phase considered for the definition of the F-δ curves (the step (h) refers to an instant prior to the mesh failure), (i) failure of the mesh-plate connection (at anchor F), (j) propagation of the failure inside the mesh.

6.2.1 Investigation of the mechanical behaviour of the system

Mechanical response of the mesh panels

The mechanical response of the three mesh panels has been computed following the strategy presented in Sec. 6.1.3. The force-displacement curves of the three mesh panels are reported in Fig. 6.7. The curves reported in Fig. 6.7a, 6.7c, 6.7e refer to the displacement measured at the centre of the considered panel (i.e. δ_i), while the ones in in Fig. 6.7b, 6.7d, 6.7f refer to the mean displacement (i.e. $\bar{\delta}_i$) of the panel. The total force F_{tot} as well as the three spatial components (F_x, F_y, F_z) are considered. The choice of referring to two different measurements of the panel displacement is related to a sake of completeness, however the information regarding the mechanical response of the mesh panels provided by the two definitions of the force-displacement relations (F-δ and F-$\bar{\delta}$) is very similar, and so in the following of the analysis only the one referring to the displacement measured at the centre of the panel δ_i will be considered. Moreover, the maximum out-of-plane displacements are observed for the wires in the central part of the mesh panels (see Sec. 6.2.3), an thus δ_i can provide a good estimation of the mesh panel deflection in serviceability condition (the F-δ relationships correlate the panel deflection to a certain level of force acting on the same panel).

From a first observation of the F-δ curves, it is possible to note that the force along the x-direction is approximately null during the whole simulation for all the three mesh panels, thus proving that the symmetry of the problem along the x-direction is respected. The other two components, namely F_y and F_z, are non-null and permit a quantification of the mesh reaction to the external load generated by the soil movements. In particular, the force F_z represents the mesh out-of-plane reaction, or in other words, the component of the stabilising action that the mesh exerts on the soil layer normally oriented with respect to the mesh panel in the undeformed condition. Instead the force F_y represents instead the mesh in-plane reaction, so the component of the stabilising action that the mesh exerts on the soil layer tangentially oriented with respect to the mesh panel in the undeformed condition. The latter can be seen as a macroscopic interface force between the mesh and the soil, and it is associated with the small volumes trapped into local "bulges" of the mesh, the interaction shear forces between soil and mesh (frictional

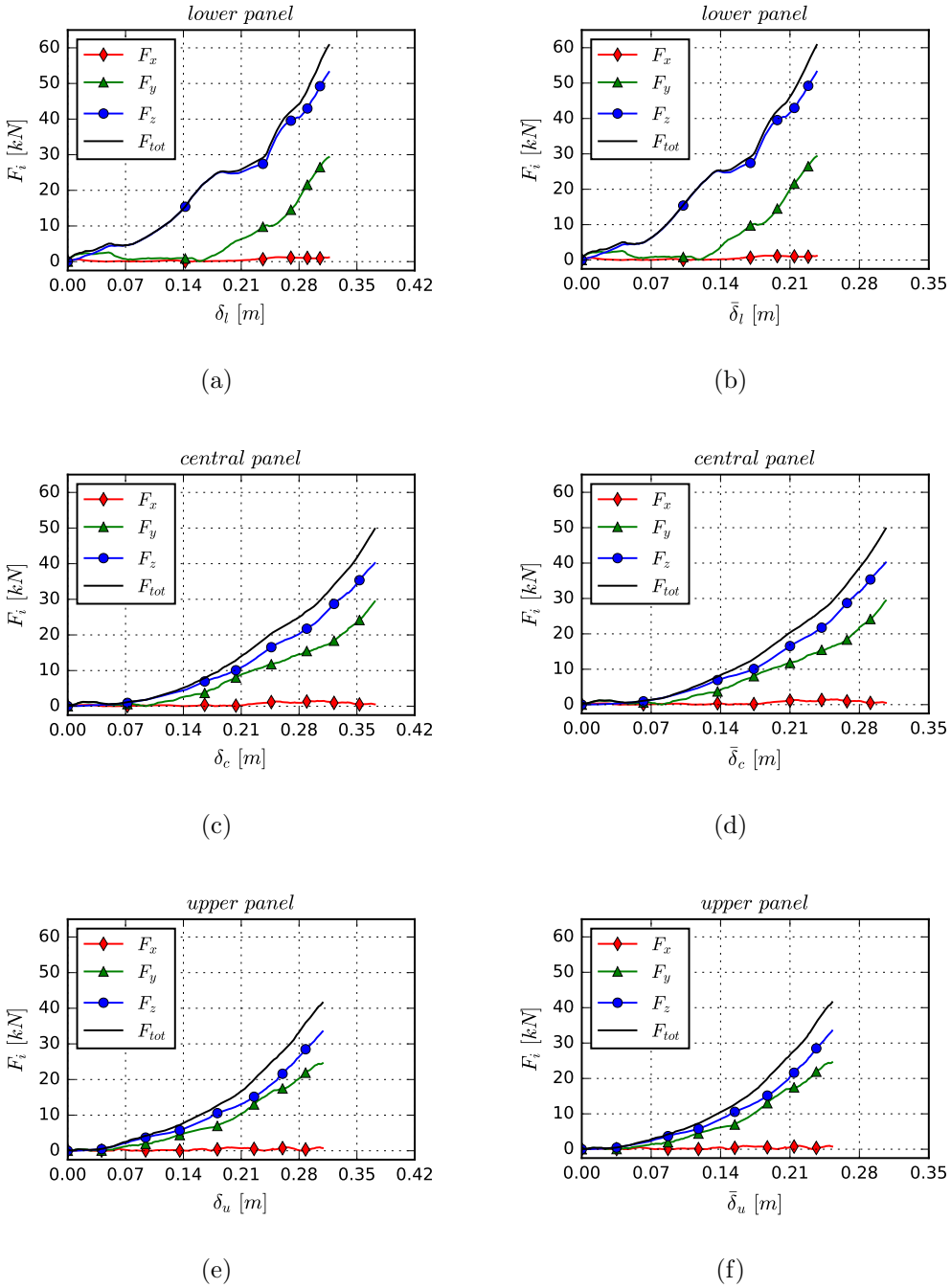
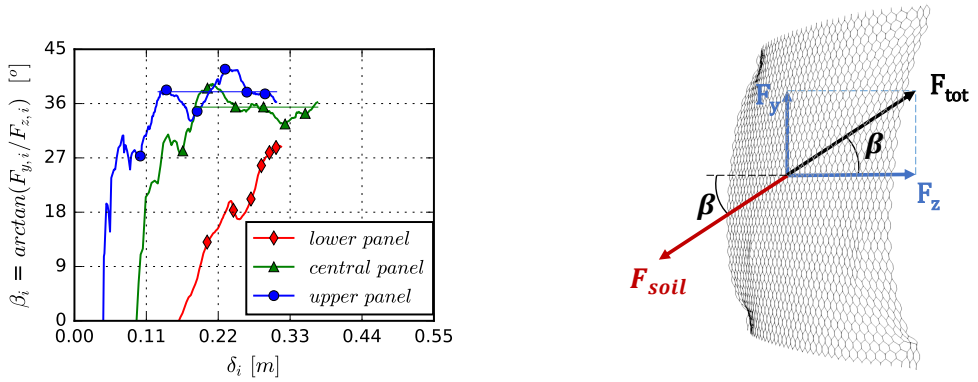


Figure 6.7: Force-displacement curves of (a,b) the lower panel, (c,d) the central panel and (e,f) the upper panel. The reported F-δ curves refer to the displacement measured at the centre of the panel δ_i (a,c,e) and to the mean panel displacement $\bar{\delta}_i$ (b,d,f) respectevely.



(a) (b)

Figure 6.8: (a) Evolution of the inclination β of the retaining forces ($F_{tot,i}$) exerted by the single panels with the panel deflection δ_i. (b) 3D graphical scheme of the considered forces for a generic mesh panel.

and interlocking effects) and the weight of the mesh (mass per unit area $\approx$1.43kg/m^2). The force-displacement curves of the three mesh panels reported in Fig. 6.7a, 6.7c, 6.7e, highlight the progressive activation of their retaining action with the system deformation. This is observable for both the macroscopic in-plane F_y and out-of-plane F_z force components. Comparing the trend of the F-δ curves of the three panels, the mechanical response of the lower one appears stiffer, and this is ascribable to the presence of the fixed side AB, which permits a prompter reaction against external forces in the z-direction. Moreover, the fixed condition imposed to side AB permits the latter to sustain a considerable amount of z-force, and this explains the higher retaining contribution provided by the lower panel with respect to the other two mesh panels. The response of the central and upper panels is instead qualitatively similar, however a lower retaining force is observed for the upper panel that may be associated to the boundary effects deriving from the finite size of the considered problem (the soil failure mechanism is characterised by a localised mechanism associated to each mesh panel as will be shown in Sec. 6.2.2). After this brief overview of the overall response of the mesh panels, it is interesting to note that F_y (macroscopic in-plane force) presents a considerable value that, in this case, is comparable, in magnitude, with the one along the z-direction (macroscopic out-of-plane force)

as observable in Fig. 6.7. This highlights that the overall stabilising force (i.e. F_{tot}) exerted by a mesh panel on the retained material is inclined, and its inclination can be estimated from the computed values of F_y and F_z. The inclination of the mesh reaction may vary during the simulation and, a priori, is a function of the main variables of the problem, as for instance, the geometric characteristic of the system (e.g. panel geometry, slope angle), the mesh mechanical properties (i.e. mesh deformability), the displacement field of the retained material and the characteristics of the mesh-soil contact. Some of these aspects will be analysed in the parametric analysis of Sec. 6.3. Referring to the configuration here adopted, the evolution of the inclination β ($\beta = arctan\,(F_y/F_z)$) of the retaining force (F_{tot}), exerted by a single mesh panel, with the panel deflection δ_i, is reported in Fig. 6.8a. For the sake of clarity, a 3D graphical scheme of the considered forces is shown in Fig. 6.8b. The data start from a certain value of the deflection ignoring the scattered values due to low force values characterising the mesh response for low deformations (i.e. at the beginning of the test). It is noticeable that the inclination β initially increases with the panel deformations, and then it stabilises to a constant value corresponding to $\beta \approx 35.5°$ and $\beta \approx 38°$ (mean value of the "plateau" of the curves as highlighted by the thin lines in Fig. 6.8a) considering the central and the upper panel respectively. Considering the lower panel, the inclination of the retaining force shows instead a monotonic incremental trend with the panel deformation and reach a value $\beta \approx 29°$ an instant prior to the mesh failure. This different trend is probably due to the fixed condition imposed to the bottom edge of the lower panel (side AB). Finally, the tensile forces supported by the different parts of the mesh system are summarised in Tab. 6.2 for the sake of completeness.

Stress and force distribution on the mesh panel

An interesting capability of the adopted approach is represented by the possibility of monitoring the stress acting on each wire element. This permits the zones of stress localisation to be highlighted, and the critical areas of the mesh panel to be identified. This also allows the force acting on each wire to be computed, thus permitting an insight on how the external load is transmitted inside the mesh. Similarly to what has been done in Chapter 4, single and double twisted wires are analysed separately in a first time. In particular, only the single wires -45° oriented with respect to the x-axis

	F_x [kN]	F_y [kN]	F_z [kN]	F_{tot} [kN]
lower panel†	1.2	29.3	53.4	60.9
central panel†	0.5	29.6	40.3	50.0
upper panel†	0.8	24.7	33.7	41.8
anchor A	2.3	2.2	3.3	-
anchor B	2.1	3.0	3.2	-
anchor C	4.1	6.4	13.2	-
anchor D	3.5	6.2	15.2	-
anchor E	3.5	5.8	17.9	-
anchor F	2.3	9.0	17.9	-
anchor G	2.6	6.9	5.2	-
anchor H	2.3	8.0	6.2	-
side AB	1.2	27.7	30.3	-
side CD	0.3	49.7	3.2	-
side EF	<0.1	61.7	2.4	-
side GH	<0.1	73.1	<0.1	-
side AC	24.0	0.5	0.4	-
side BD	24.1	0.6	0.3	-
side CE	29.2	1.1	1.4	-
side DF	30.5	1.2	1.6	-
side EG	35.7	<0.1	<0.1	-
side FH	37.3	<0.1	<0.1	-

† for the computation of the panel forces the direction of the mesh portions reaction has to be considered with its own direction (see Fig. 6.5a)

Table 6.2: Tensile forces supported by the mesh system parts an instant prior to the mesh failure.

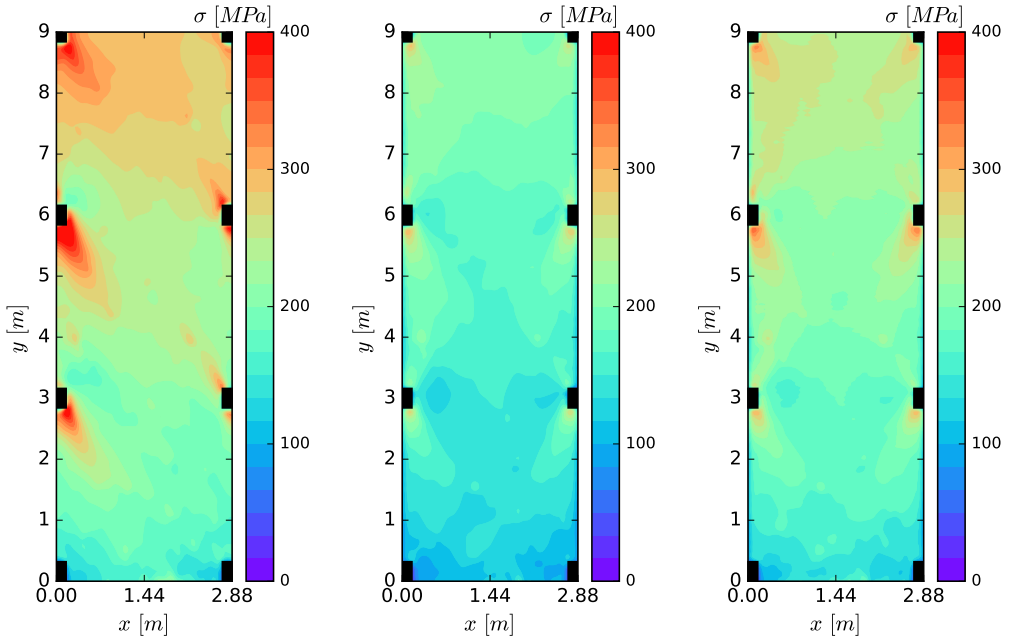


Figure 6.9: Tensile stress distribution an instant prior to the mesh failure, on (a) single wires (-45° oriented), (b) double twisted wires and (c) both wire types.

(a clockwise rotation is considered negative) are considered when referring to the single wires stress and force distributions (the distributions of the +45° oriented are symmetrical with respect to the y-axis). This distinction, based on the wire type, is necessary to correctly understand their role on the mesh mechanical response, due to their difference in terms of mechanical characteristics and ultimate strength. The tensile stress distributions are reported in Fig 6.9a and 6.9b for the single wire and the double twisted wire respectively; finally the stress distribution considering contemporary both the wire types is reported in Fig 6.9c. These distributions are computed through a linear interpolation of the tensile stress acting on the wires on a regular grid spaced of 4cm; the distributions refer to the mechanical condition of the mesh system an instant prior to its failure. Comparing the stress distributions obtained for the two wire types, it is evident that the single wires experience a higher tensile stress level than the one registered for the double twisted wires. This has also been observed with reference to a local

punching condition (see Chapter 4) and can be related to the higher cross section of the double twisted wires. The single wires stress distribution reported in Fig. 6.9a highlights the existence of a stress localisation in the area surrounding the anchor plates (only the SW -45° oriented are considered in Fig. 6.9a, the SW +45° oriented present a symmetrical distribution with respect to the y-axis). In particular, the stress concentrates on the wires converging on the lower part of the anchor plates. In correspondence to the upper anchors of the central panel, namely anchors E and F, the stress localisation is the most significant and, in fact, the failure of the mesh system starts from the anchor F as observable in Fig. 6.6 (the failure of the mesh does not start contemporary from the two anchors because of the not perfect symmetry of the soil movement behind the mesh). The stress localisation on the lower part of the mesh-plate connection is also evident from the overall stress distribution reported in Fig. 6.9c. Finally, the relatively high level of stress observed in the top part of the upper panel is due to the fact that the movement of the side GH (top side of the mesh system) along the y-direction is not allowed (this condition schematises the fixity of the secured drapery system at the crest of the slope). The load acting on that side is therefore directly supported by itself and not transmitted to neighbouring panels as instead happens for the internal horizontal sides (i.e. sides CD and EF).

The analysis of the tensile stress distribution (on the wires) has permitted the critical zones of the mesh panel to be identified. However, the two wire types being characterised by a different tensile strength (i.e. ≈3.03kN for the single and ≈5.95kN for the double twisted wires), to better understand their role on the transmission of the external force inside the mesh, it is useful to refer to the tensile force distribution. Analogously to what has been previously done, the two wire types are considered separately in the first time. The tensile force distributions are reported in Fig 6.10a and 6.10b for the single and the double twisted wires respectively; finally the force distribution considering all the mesh wires is reported in Fig 6.10c. A significant level of tensile force is observed for both wire types in the zones surrounding the anchor plates, highlighting once more the importance of these zones on the mesh system behaviour (the mechanical behaviour of these zones will be analysed in the next paragraph). Comparing the force distributions, it is possible to observe the significant role of the double twisted wires in the mesh mechanical reaction; in fact, even if they are characterised by a relatively low stress level (see Fig. 6.9b), they sustain a considerable force as observable in

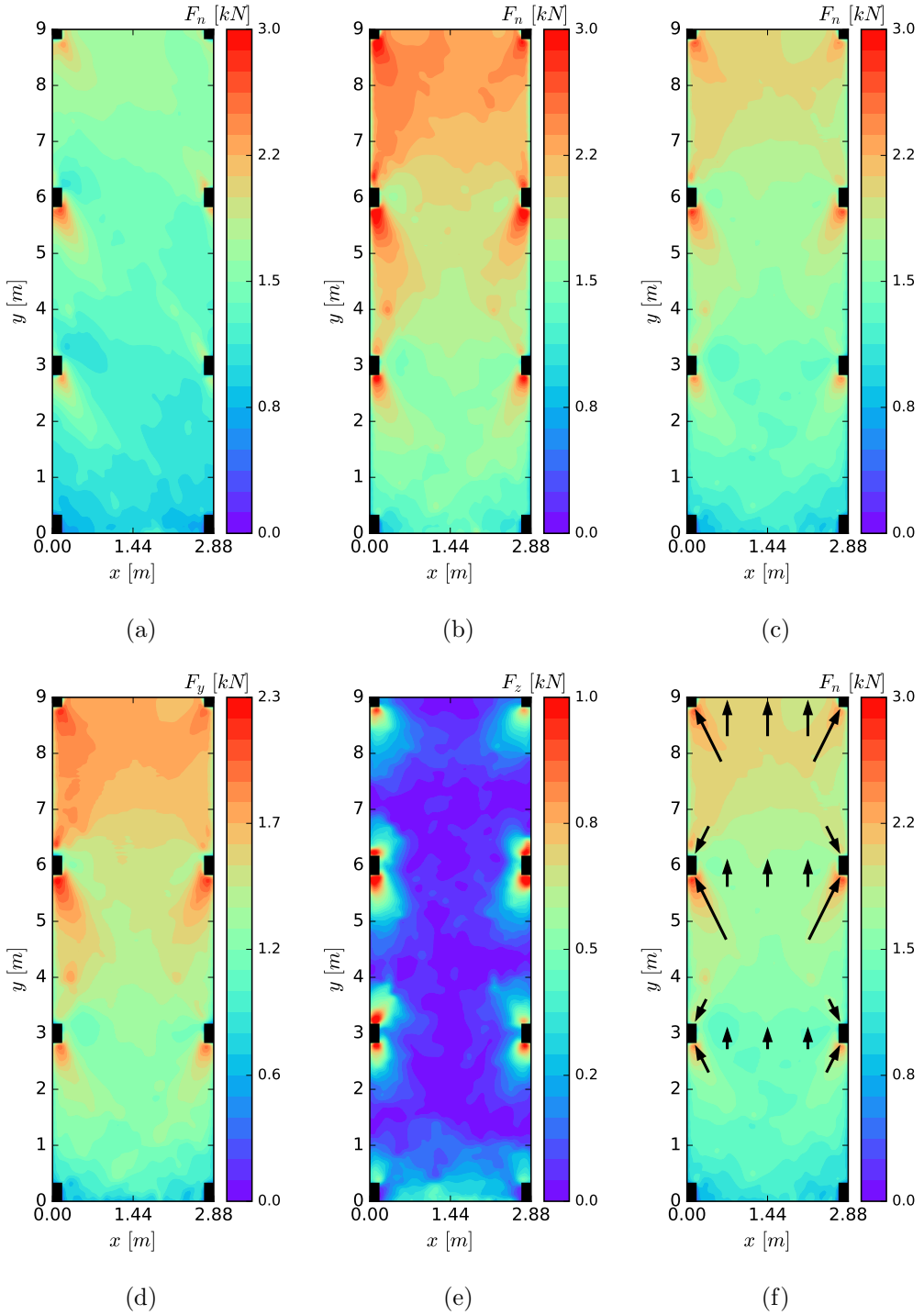


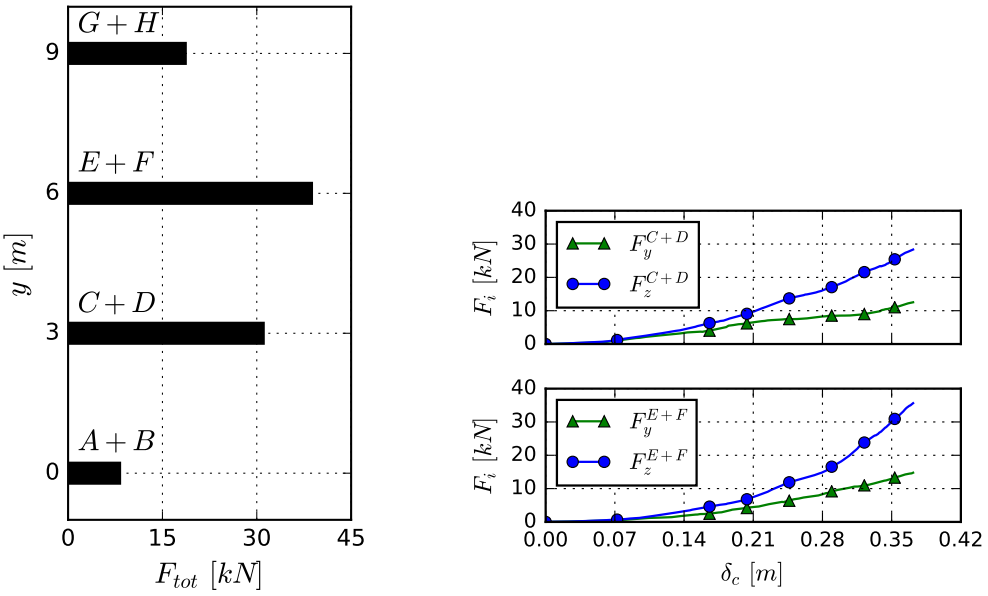
Figure 6.10: Tensile force distribution an instant prior to the mesh failure, on (a) single wires (-45° oriented), (b) double twisted wires and (c) both wire types. Distribution of the force component (d) F_y and (e) F_z on the mesh system. (f) Schematic representation of the force transmission mechanism inside the mesh.

Fig. 6.10b. Furthermore, they permit a more efficient vertical transmission of the external load inside the mesh by intercepting the load coming from two single wires (as already discussed in Chapter 4). Observing the overall force distribution on the mesh panel (see Fig. 6.10c), it can be argued that the load imposed by the unstable soil on the mesh is mainly transmitted to the anchors following inclined paths as highlighted by the arrows in Fig. 6.10f. Moreover, there is also a gradual transmission of the load along the vertical direction (i.e. same orientation of the double twisted wires), which is finally supported by the top side of the mesh (side GH). In particular, considering the force component F_y and F_z separately as reported in Fig. 6.10d and 6.10e respectively, it is notable that the out-of-plane force is mainly sustained by the wires converging to the anchors, however a significant contribution is provided by the lower mesh edge. Instead, the "macroscopic" in-plane force F_y is supported by both the anchors and the upper mesh side.

Force distribution among the anchors

The connection zone between the mesh and an anchor plate represents one of the most interesting areas of the mesh system to be investigated. As already mentioned in Chapter 4, the retaining capacity of the mesh is ensured because of the possibility to transmit the external force to a stable layer of the slope by means of the anchoring system. In real applications, the high tensile condition acting on the mesh wires in the proximity of the anchor plates frequently overcomes the mechanical resistance of the mesh-anchor connection, triggering the breakage of the wires intercepted by the anchor plate and therefore leading to the consequent failure of the mesh system [40, 76]. This failure modality is well reproduced by the model as observable in Fig. 6.6. Due to the importance of these zones, the evolution of the forces acting on the different anchor levels is analysed in this paragraph. It is worth recalling that the forces here considered are related to the solely tensile forces that the mesh transmits to the anchors (i.e. tensile forces sustained by the wires), while the force that the soil locally exerts on the backward face of the anchor plates is not considered, since the anchor bolts are supposed to completely absorb these actions (anchor plates are considered as fixed and infinitely rigid in this study).

The forces sustained by the different anchors levels, an instant before the failure of the mesh, are compared in Fig. 6.11a. In order to provide the force



(a) (b)

Figure 6.11: (a) Tensile force supported by the different anchor levels an instant before the mesh failure. (b) Force-displacement curves of the full-size anchor C+D and E+F.

acting on a full-size anchor, the forces acting on two symmetric half-anchors are added together (e.g. C+D); for the anchors placed on the upper side of the system (i.e. G+H) the force refers to a half anchor. The higher forces are supported by the anchors placed between the lower and the central panels (i.e. C and D) and the ones placed between the central and upper panels (i.e. E and F). The force-displacement relations (the displacement refers to the deflection of the central panel) associated to the full anchors C+D and E+F are shown in Fig. 6.11b, considering the y-component and the z-component of the force separately. The forces are almost equally distributed between the two symmetric half anchors, confirming that the symmetry of the problem is respected. On each full-size anchor, the x-force is negligible, while the y-force is downward oriented and the z-force is externally oriented. The F-δ curves characterising the force supported by the full-size anchors C+D and E+F have a similar trend, and show that the anchors' contribution to the system retaining capacity is increasing with the mesh deformations. The upper full-size anchor E+F supports a higher force than the full-size

	F_x [kN]	F_y [kN]	F_z [kN]
A_t†	2.3	2.2	3.3
B_t†	2.1	3.0	3.2
C_b	1.6	6.8	6.2
D_b	1.4	6.9	6.4
C_t	2.5	0.4	7.0
D_t	2.2	0.7	8.8
E_b	1.4	7.7	7.9
F_b	0.7	8.6	8.0
E_t	2.1	1.8	10.0
F_t	1.6	0.4	9.9
G_b†	2.6	6.9	5.2
H_b†	2.3	8.0	6.2

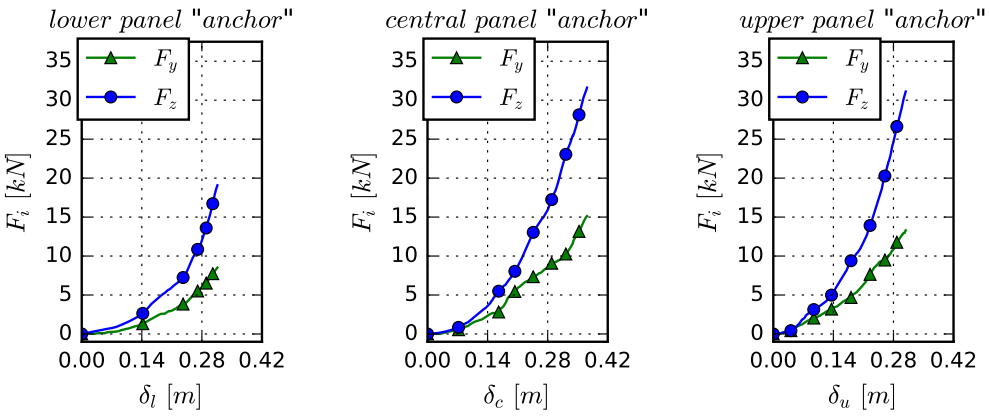
†it coincides with the entire anchor

Table 6.3: Tensile forces supported by the portions of anchors belonging to the three mesh panels (for the computation of the force supported by an entire anchor the reactions of its portions have to be considered with its own direction).

anchor C+D: $F_y^{E+F} \approx 1.16 F_y^{C+D}$ and $F_z^{E+F} \approx 1.25 F_z^{C+D}$, considering the mechanical condition an instant before the failure of the mesh.

The force contributions associated with the different portions of the anchors are reported in Tab. 6.3 for the sake of completeness. It is interesting to note that the bottom part of an anchor is, in the considered case, responsible for almost the entire force supported by the anchor along the y-direction, while the force component along the z-direction is supported by the two portions of the anchor.

In order to better understand the role of the anchors on the mechanical response of the mesh panels, the force-displacement curves associated with the amount of force supported by the anchors pertaining to the each mesh panel are reported in Fig. 6.12. For instance, considering the central panel, the force supported by the anchors is computed as the summation of the force acting on the anchors portions C_t, D_t, E_b, F_b. The resulting force is computed on the nominal area of one full anchor (0.32m×0.32m), therefore it



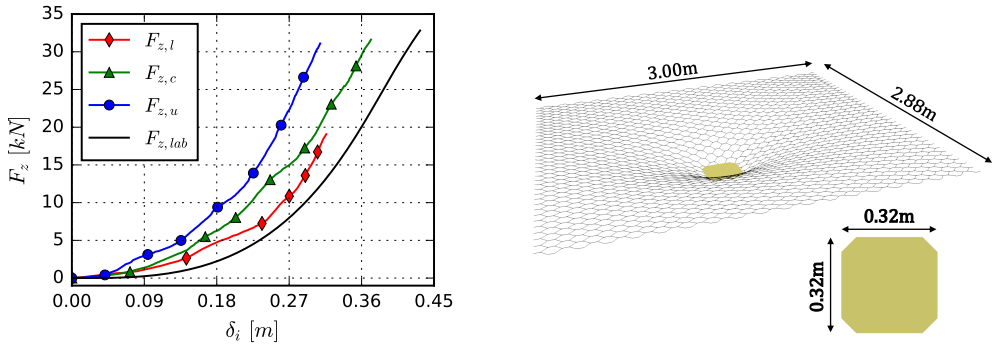
(a) (b) (c)

Figure 6.12: Force-displacement curves of the idealised anchor associated with (a) the lower panel, (b) the central panel and (c) the upper panel.

	F_y [kN]	F_z [kN]
lower panel "anchor"	8.5 (%29)	19.1 (%36)
central panel "anchor"	15.2 (%51)	31.7 (%79)
upper panel "anchor"	13.4 (%54)	31.3 (%93)

Table 6.4: Tensile forces supported by the idealised anchors associated with the three mesh panel; their contribution (in percentage) to the force supported by the related panel is reported in round brackets.

can be seen as a measure of the force supported by an ideal anchor pertaining to the central panel. In this sense, this idealised anchor will be referred as central panel "anchor" in the following (the lower and upper panel "anchors" are defined in the same manner). From the numerical results, the same qualitative trend of the F-δ curve is observable for all the three considered panel "anchors". Nevertheless, from a quantitative point of view, the anchor associated to the central panel supports the highest force level (see Fig. 6.12b), the lowest force level is instead measured considering the lower panel "anchor" (see Fig. 6.12a). The latter condition is due to presence of the fixed edge at the toe of the system, which largely contributes to the force sustained by the lower panel. Finally, a slightly lower force (considering



(a) (b)

Figure 6.13: (a) Comparison of the mechanical behaviour of the three panel "anchors" and the results of the laboratory anchor punch test. (b) 3D View of the numerical model of the anchor punch test.

both F_y and F_z) is supported by the upper panel "anchor" (see Fig. 6.12c) if compared to the central panel one. As for the overall panel force, this may be associated to the boundary effects deriving from the finite size of the considered problem. The force sustained by the panel "anchors", an instant before the failure of the mesh, are reported in Tab. 6.4.

Finally, since the panel "anchors" may be considered as idealised anchors associated with the respective mesh panel, their mechanical response in the out-of-plane direction is compared with the one obtained from a laboratory anchor punch test in Fig. 6.13a. This test is formally identical to the one reported in Chapter 3, however the mesh panel dimension, the nominal wire diameter and the anchor plate dimensions are modified in order to correctly reproduce the ones characterising the considered mesh system. The dimensions of the tested mesh panel are therefore equal to 2.88m×3.00m, while the ones of the anchor plate are 0.32m×0.32m. A 3D view of the numerical model of the anchor punch test is reported in Fig. 6.13b for the sake of clarity. It has been shown that the mesh system fails at the level of the anchor F (see Fig. 6.6), thus the mechanical condition of the idealised anchor associated with the central and the upper panels can be considered close to the failure condition (i.e. anchor F partially belongs to the central and partially to the upper panel). The force supported by these two panel "anchors" (31.7kN for the central panel "anchor" and 31.3kN for the upper

panel "anchor"), an instant prior to the failure of anchor F, is almost equal to the one that characterises the failure of the mesh panel in the anchor punch test (32.8kN). Moreover, it is notable that the stiffness that characterises the second part of the F-δ curves of the tree panel "anchors" (i.e. after the initial deformation necessary to activate the out-of-plane mesh resistance) is very similar to the one observed in the laboratory testing condition. This evidences that the anchor punch test, despite its simplicity, may provide a good estimation of the mechanical behaviour at mesh-anchor connection. In particular, it permits a quantitative estimation of the available resistance at the connection between the mesh and the anchor plates.

Stress distribution at the mesh-anchor connection

The zones of the mesh surrounding the anchor plates are generally characterised by a strong localisation of stresses as observed in Fig. 6.9. The discrete nature of the modelling approach adopted in this study permits the stress acting at the level of each wire to be analysed. Firstly, the tensile stress distribution, an instant before the mesh failure, is reported in Fig. 6.14 with reference to the wires surrounding the anchor plates. From the plots, it can be noted that most of the single wires intercepted by the edges of the anchor plates are experiencing a tensile stress closer to the maximum stress that they can support (i.e. 530MPa). Instead, a low stress condition is observed acting on the wires belonging to the anchors A and B, and this may be related to the presence of the fixed lower side (side AB) and to the low displacements that the retained material is experiencing at the toe of the system due to the constraint imposed by the bottom wall. The highest stress values are observed in the wires surrounding anchors E and F, in fact the failure of the mesh originates from the breakage of some of the wires intercepted by the anchor F. In Fig. 6.15 the stress-strain condition of the four most stressed wires, intercepted by the anchor F, is indicated on the stress-strain tensile curve characteristic of the single wire elements. Such wires are in a fully plastic phase, and in particular the wires referred as 1, 2 and 3 are very close to failure. In the simulation, the failure of the mesh is triggered by the rupture of these wires in rapid succession as shown in Fig. 6.15c. After that moment, the surrounding wires break in sequence and the failure propagates in the mesh as shown in Fig. 6.6i-6.6j.

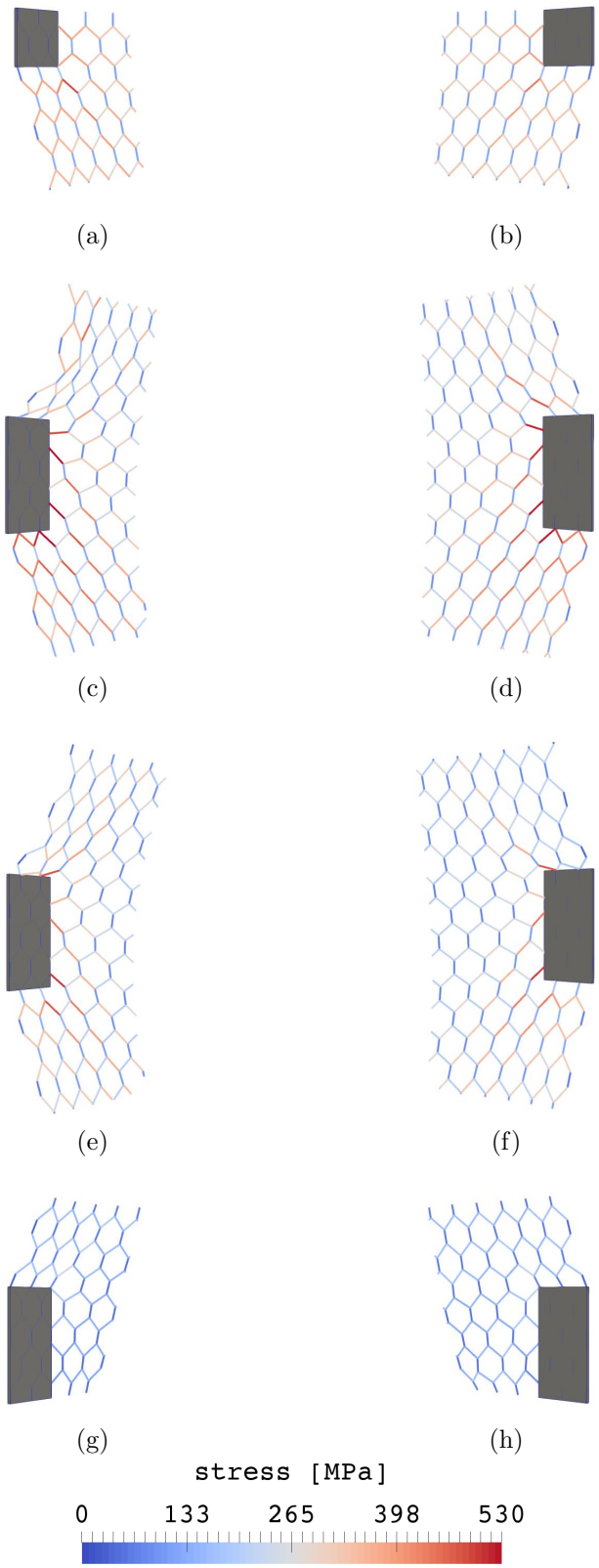
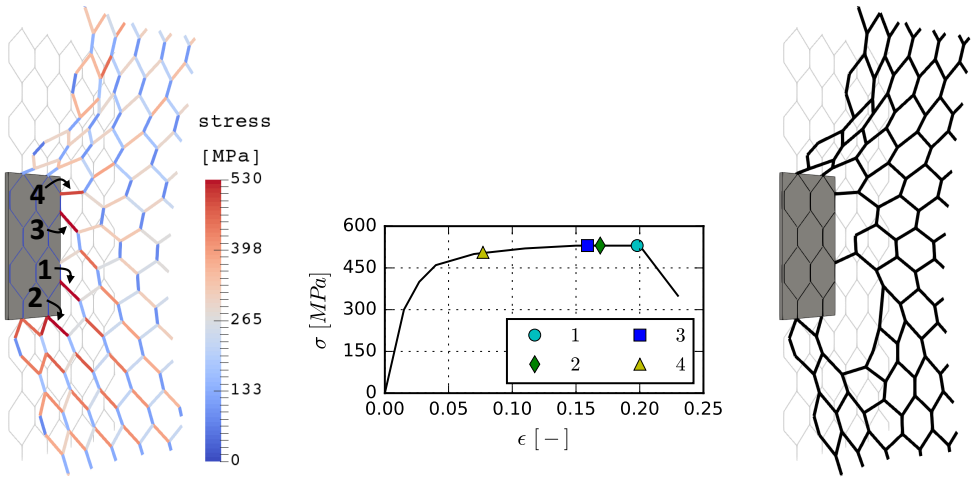


Figure 6.14: Tensile stress distribution on the wires surrounding the anchor: (a) H, (b) G, (c) F, (d) E, (e) D, (f) C, (g) B, (h) A.



(a) (b) (c)

Figure 6.15: a) Tensile stress distribution on the wires surrounding the anchor F and (b) mechanical conditions of the most critical wires an instant prior to the first breakage of a wire. (c) 3D view after the breakage of some wires.

6.2.2 Soil displacement field

In Chapter 1, when introducing the standard design methodologies, it has been pointed out that the choice of the failure mechanism occurring in the soil layer represents a fundamental assumption in order to realistically schematised the behaviour of a secured drapery system. However, the different methodologies available in the literature consider different failure mechanisms, ranging from local [22, 41] to "global" failure mechanisms [31, 61] (in the sense that the adopted failure mechanism involves the entire height of the slope). In this perspective, the definition of a precise failure mechanism appears fundamental. Recently, a large scale experimental test setup [6, 7, 18, 104] permitted the understanding of the behaviour of secured drapery system to be improved, anyway only a partial information on the failure mechanism occurring in the retained material was obtained.

In the perspective of enhancing the understanding of the failure mechanism occuring in the soil layer, the displacement of the particles in the mesh-soil numerical model has been tracked, thus permitting the computation of the displacement field of the soil volume on the back of the mesh

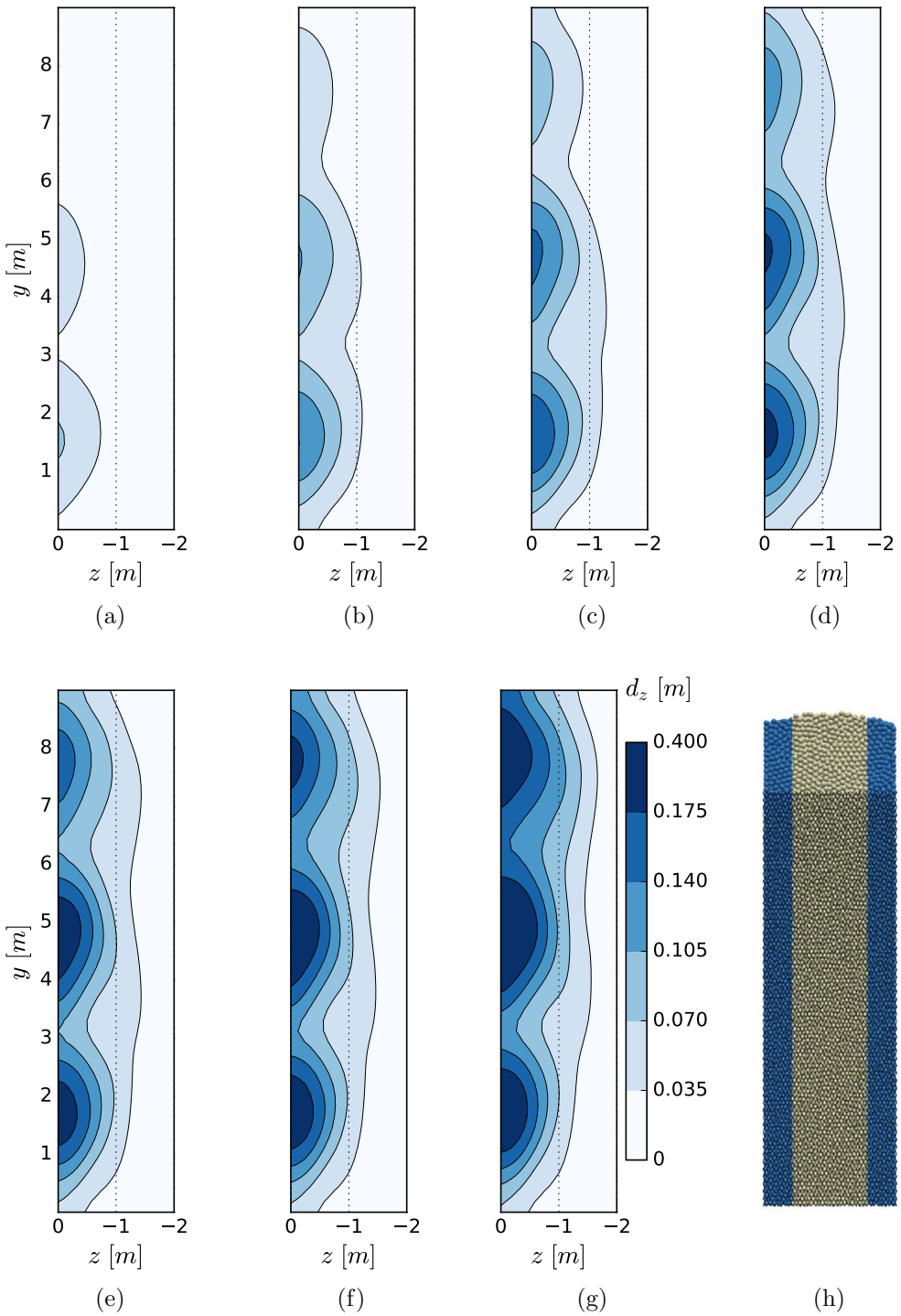


Figure 6.16: Time evolution of the z-displacement field of the unstable soil layer (the blue volumes highlight the slices of the soil domain considered in the computation of the displacement field).

system. It should be noted, that the mutual interaction between the soil and the mesh system has to be carefully consider in order to correctly reproduce the development of the failure process in the retained material. In fact, the progressive activation (with the mesh deformation) of the stabilising action that the mesh exerts on the material behind it significantly influences the soil movements, which, in turn, are responsible for the mesh deformation that activates its retaining capacity. This condition is ensured by the adopted numerical methodology. Furthermore, the discrete nature of the method permits geometrical effects such as the local interlocking of grains in the mesh, as well as soil arching in the granular layer, to be accounted for.

As the mesh retaining capacity is mainly activated by out-of-plane displacements, only the z-component of the soil particles displacement is considered for the definition of the soil displacement field. The z-displacement field is computed by linearly interpolating on a bi-dimensional regular grid (yz-plane) the z-displacement value of each particle. The value associated to each grid-cell is computed as the mean value of the z-displacement obtained by considering all the particles contained (also only partially) inside the projection of the grid-cell along the x-axis. Morevoer, in order to be consistent with the 2D schematisation used in the classical design methods, the displacement field is computed referring to the soil particles belonging to two vertical slices of width $2d_p$ in correspondence with the anchor plates as shown in Fig. 6.16 (a similar results is obtained also considering the entire soil volume). The time evolution of the z-displacement field of the soil layer is reported in Fig. 6.16. This representation permits a 2D schematisation of the soil failure mechanism to be provided, in analogy with those adopted in standard design methodologies. A 3D representation of the soil z-displacement field is instead shown in Fig. 6.17 for the sake of completeness (this latter computed considering all the soil particles). Moreover, in order to better visualise the failure surface's development in the soil layer, the incremental total displacement gradient is shown in Fig. 6.18. The numerical results show the emergence of local failure mechanisms, comprised between two anchor rows. A localised wedge-shaped failure mechanism, acting on each single mesh panel, seems therefore a proper schematisation of the unstable process. The three volumes are delimited by as many curved surfaces, where the shear strains concentrate (i.e. where the total displacement gradient is the highest). From the observation of time evolution of the soil displacement field (Fig. 6.16 and 6.17), it is possible to note a gradual

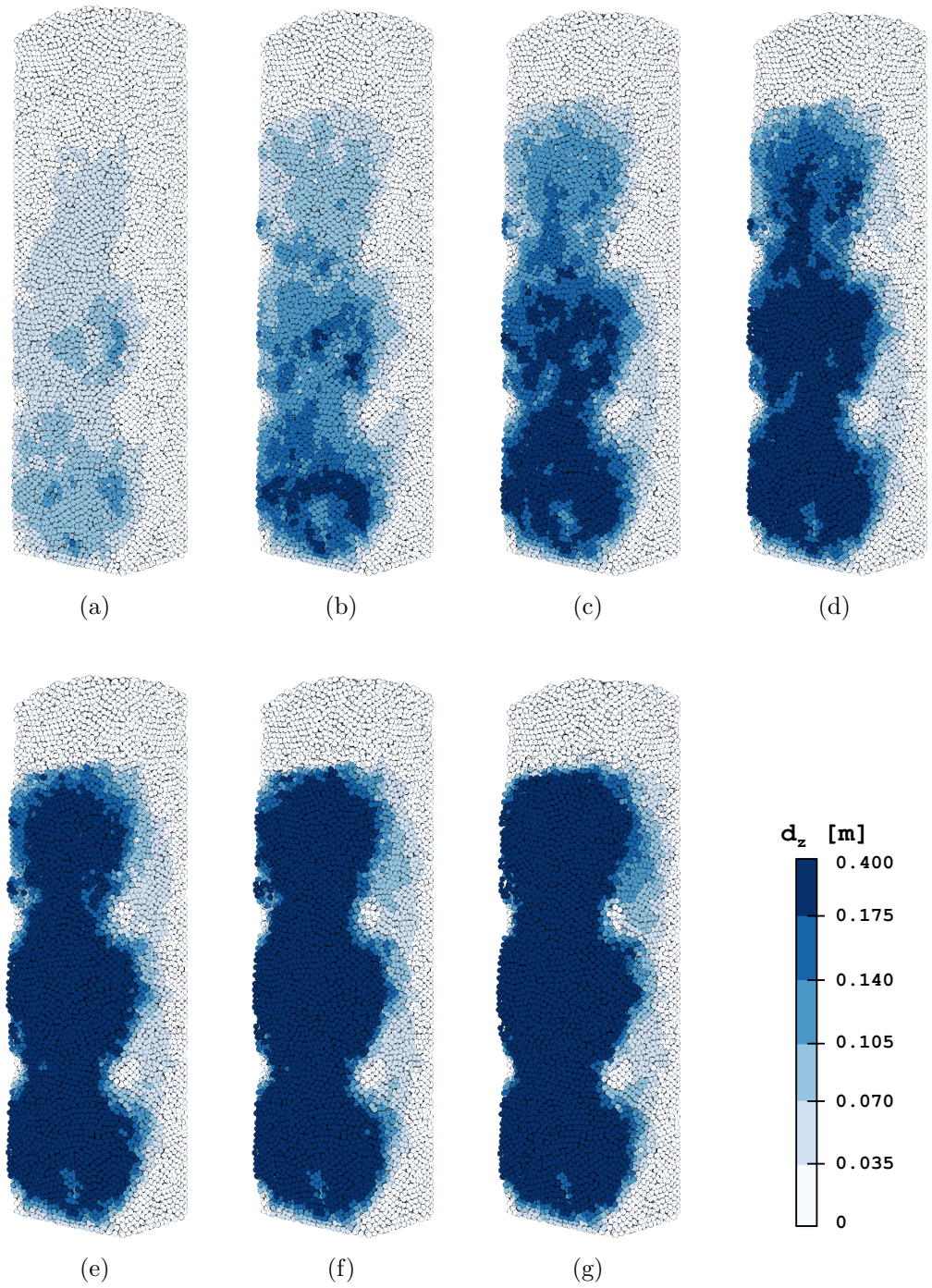


Figure 6.17: 3D view of time evolution of the z-displacement field of the unstable soil layer.

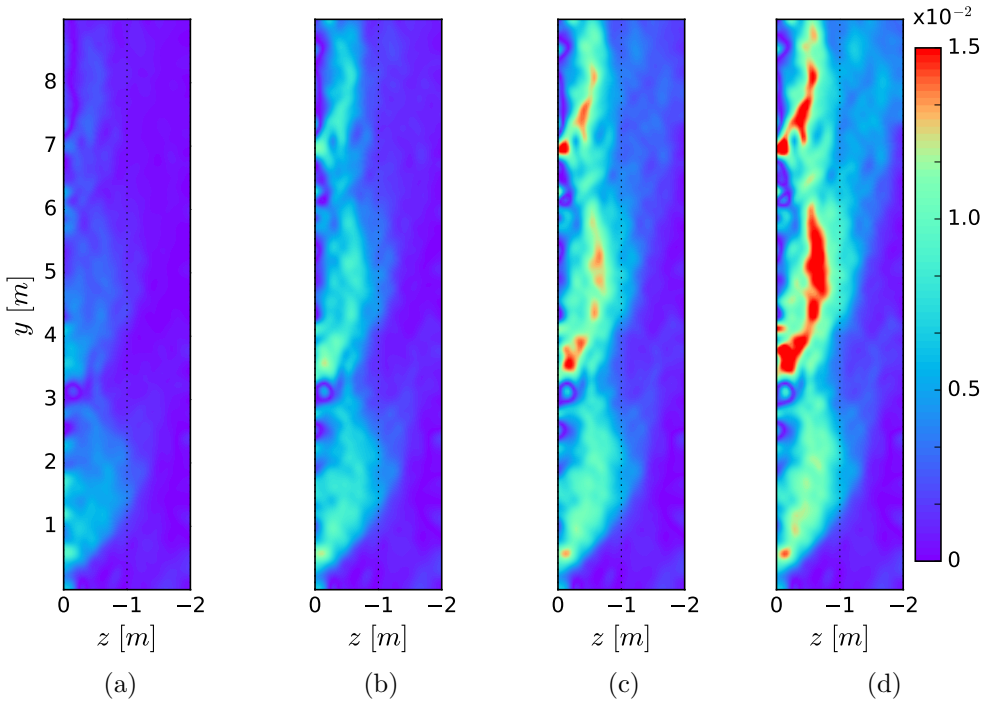


Figure 6.18: Time evolution of the incremental total displacement gradient in the soil layer.

upwards activation of the local unstable soil wedges starting from the toe of the system. Once the displacement of the lower wedge has sufficiently activated the retaining capacity of the corresponding panel, the upper wedge starts to slide and this process is progressively repeated. Furthermore, it is interesting to note that, in this case, the failure mechanisms do not interest the entire thickness of the soil layer in contrast to what is assumed in most of the standard design methodologies [30, 31, 61]. This possibility is instead considered in the methodologies proposed in [22, 59]. A detailed analysis of the influence of the unstable layer thickness will be presented in Sec. 6.3.

The volume of the sliding local wedges is quantified by considering the particles that undergo a z-displacement greater than the mean particle diameter (i.e. $d_{50} = 0.12$m). Referring to an instant before the mesh failure, the volume of the local wedges acting on each single mesh panel are $V_l = 4.4\text{m}^3$, $V_c = 6.8\text{m}^3$, $V_u = 6.5\text{m}^3$ for the lower, central and upper panel respectively.

The occurrence of the wedge-shaped local failure mechanisms is related

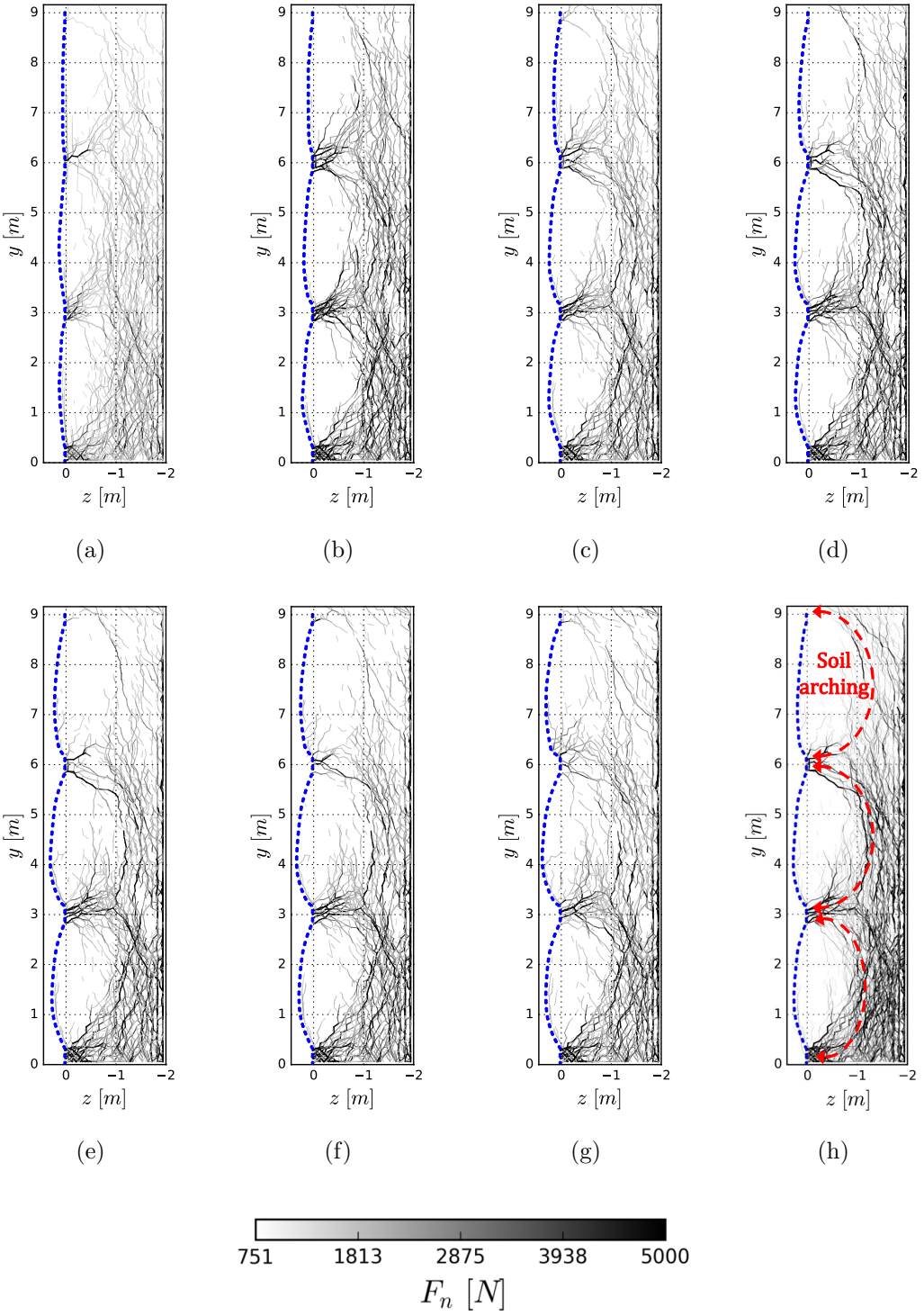


Figure 6.19: Time evolution of the contact force network (strong network) in the unstable soil layer (the considered soil volume is the same of Fig. 6.16h, while the blue dots indicate the mesh particles). The colorbar upper limit is set equal to $\max(F_n)/4$.

to the development of a stabilising arching effect between the soil and the anchor plates. The formation of particles arches is clearly visible in Fig. 6.19, where the contact force network in the granular layer is reported. Similarly to what has been done in Chapter 5 only the strong force network is considered. The formation of almost horizontally oriented (i.e. parallel to the z-axis) force chains, in the zone surrounding the anchor plates, is observed immediately after the triggering of the soil layer instability; then, moving farther from the anchor plates, the orientation of these force chains gradually varies, becoming more and more vertical (i.e. parallel to the y-axis), and thus originating "arched structures" inside the soil layer as highlighted in Fig. 6.19h. These arches of particles permit a partial self-sustaining effect inside the soil layer, thus determining the subdivision of the unstable layer into local wedge-shaped sliding volumes (the "stable" chains of particles in correspondence to the anchor plates "screen" a mesh panel from what happens above and below). The sliding wedges are well identified by the volumes characterised by a very low frequency (and magnitude) of the contact forces (i.e. the "white zones" observable in Fig. 6.19). Moreover, the existence of these "stable" arches of particles also permits the partialisation of the unstable layer to be explained, namely the occurrence of the local failure mechanisms only in a limited portion of the soil layer. Finally, it is interesting to note that the force chains located near the anchor plates (the ones that permits the development of the arching effect) are very similar to the ones observed in Chapter 5 when analysing the local behaviour of the soil volume in the zone surrounding an anchor plate (i.e. the "stabilising pressure cone" that develops into the soil due to the relative movement between the latter and the anchor plate).

6.2.3 Mesh displacement field

The mesh z-displacement field is finally analysed. Its time evolution is reported in Fig. 6.20, while in Fig. 6.21 the deformed configuration, with reference to two vertical sections of the mesh system (a central and a lateral section), is reported. The distribution of the out-of-plane displacements on the mesh system is almost symmetrical with respect to the y-axis, confirming that the periodicity of the problem along the x-direction is respected. The greatest deflection level is observed with reference to the centre of the central panel, however comparable deflection values are registered in the central part

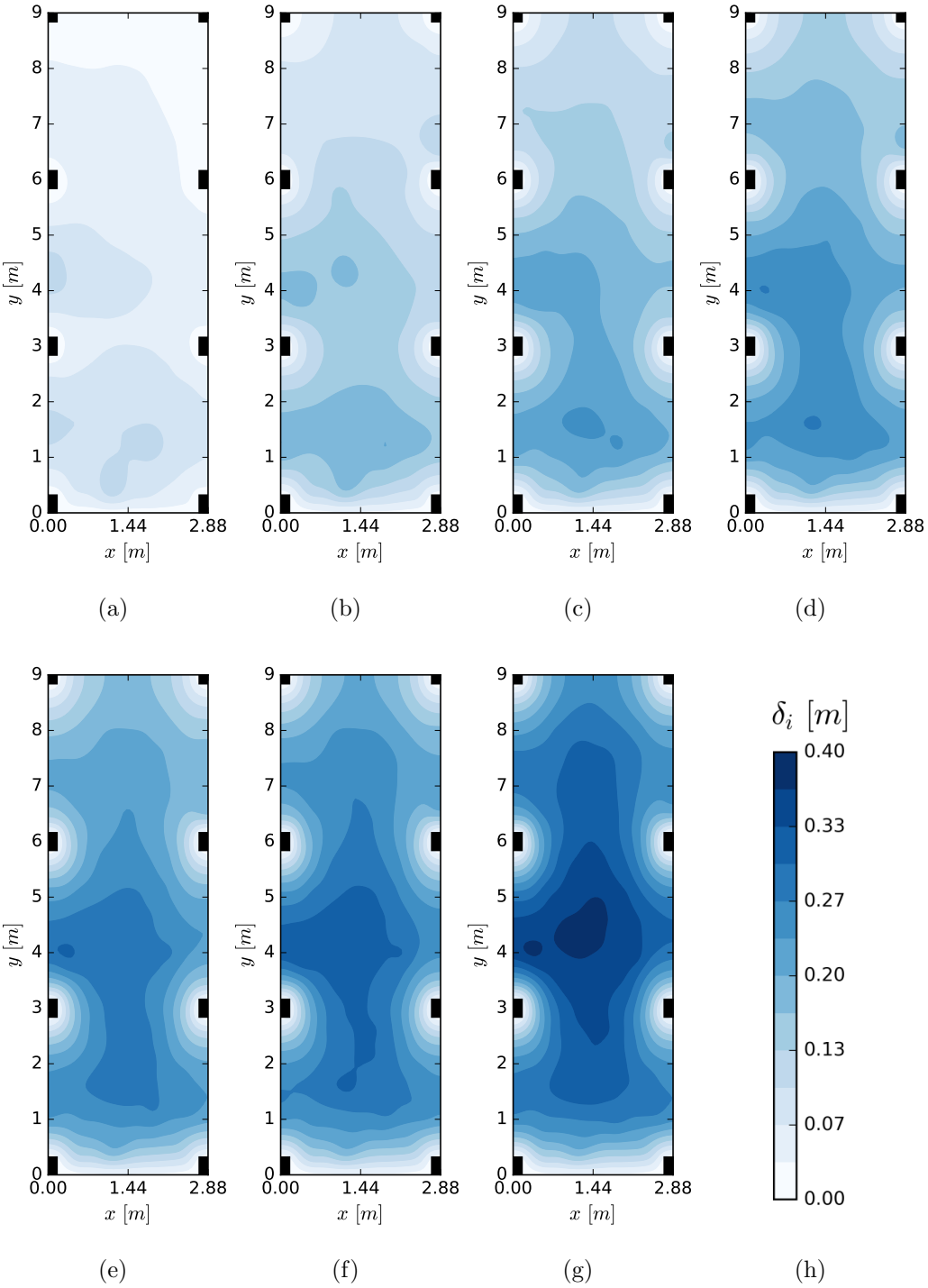


Figure 6.20: Time evolution of the z-displacement field (out-of-plane direction) of the mesh system.

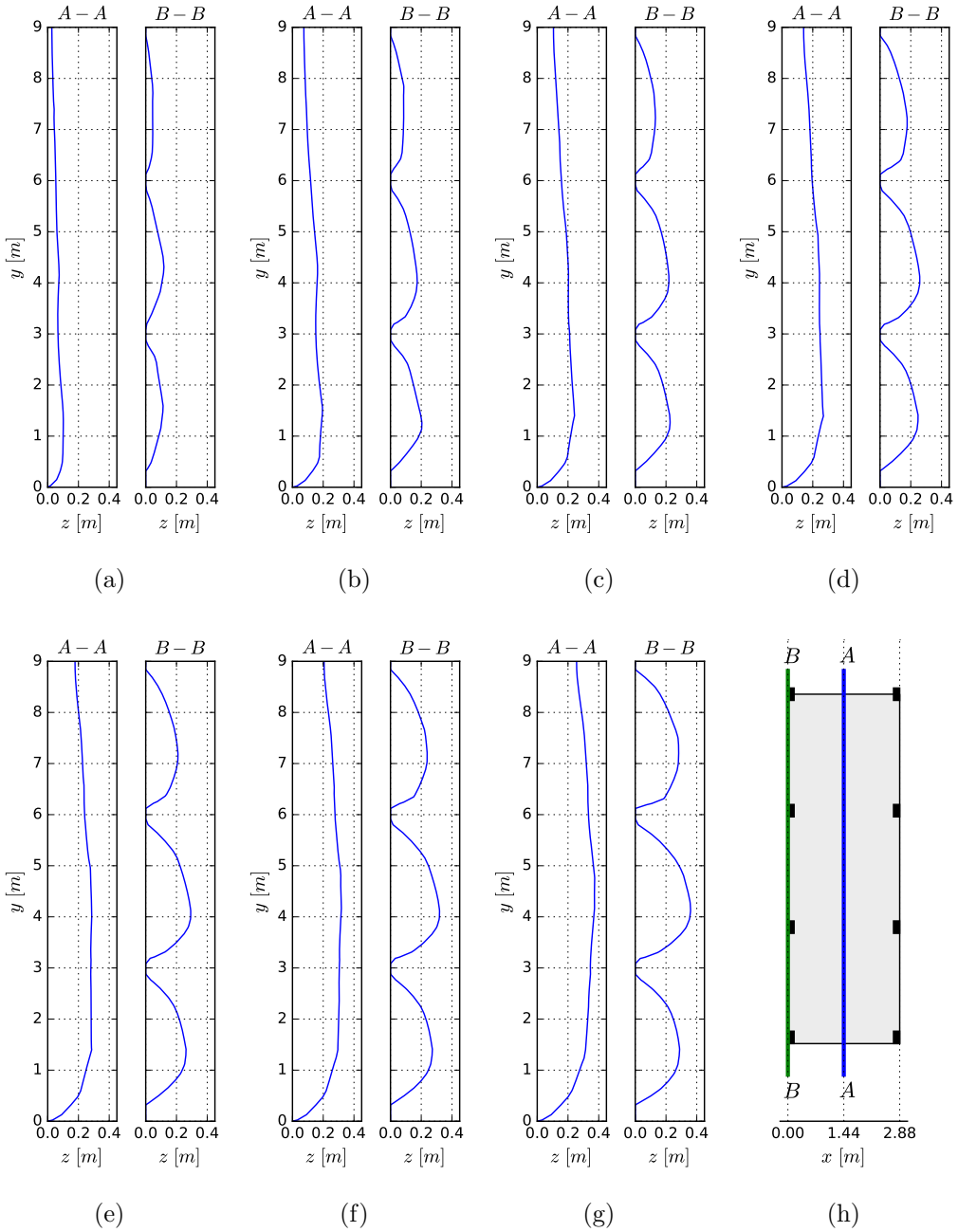


Figure 6.21: Time evolution of the mesh profile with reference to the central section A-A and a lateral section B-B of the system (a different scale is used for the two axes in order to better appreciate the out-of-plane mesh displacements).

of the other two mesh panels (see section A-A in Fig. 6.21). Similar considerations can be made referring to the lateral section B-B. Furthermore, the time evolution of the mesh displacement field permits the progressive deformation of the three mesh panels, which starts from the toe of the slope, to be highlighted. This is a direct consequence of the progressive upwards activation of the local failure mechanisms in the soil (i.e. the unstable wedges) observed in Sec. 6.2.2.

6.3 Parametric analysis

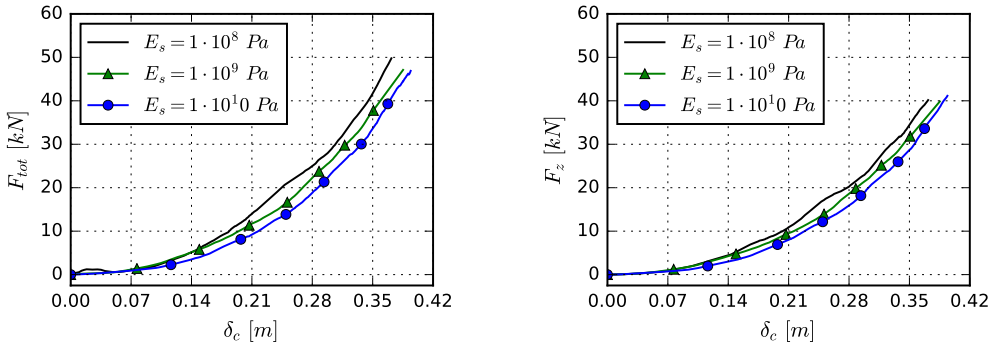
The analysis of the results obtained from the simulation of the mesh-soil problem reported in Sec. 6.2 has permitted a better comprehension of the mechanical behaviour of a secured drapery system in soil-retaining applications. The force-displacement relationship that describes the activation of the retaining action, associated with a mesh panel, has been characterised as well as the role of the connection zone between the mesh and the anchoring system. Moreover, it has been possible to identify the failure mechanism that occurs in the unstable soil layer, which can be well described as wedge-shaped local failure mechanisms, each of which comprised between two anchor rows. These results, however, have been obtained referring to a precise mesh system configuration (the reference test of Sec. 6.1.3). Thus, in this section, a parametric analysis is conducted in order to understand the role of the main variables of the problem on the mechanical response of the mesh system. In particular, the soil properties (i.e. soil stiffness, macroscopic friction angle ϕ_S^M), the mesh-soil interface mechanical properties (i.e. mesh-soil contact friction angle ϕ_{ms}), the mechanical characteristics of the mesh (i.e. the wire diameter d_w) and the geometrical characteristics of the problem (i.e. slope angle α, thickness of the column t, anchor plate dimension d_p, anchors' pattern) are considered. In light of what has been observed in Sec. 6.2, the central mesh panel is considered the most significant in order to characterise the mechanical response of a generic mesh panel composing a secured drapery mesh system. This panel is, in fact, the least affected by the boundary effects, being in-between the other two panels; moreover, its boundary conditions can be considered representative of the ones that characterise a generic mesh panel of a secured drapery system in field conditions. Thus, the following analyses will mainly focus on the behaviour of the central mesh panel. A summary of the different tests performed in the parametric study is reported

# test	E_s [Pa]	ϕ_S^M [°]†	ϕ_{ms} [°]	α [°]	t [m]	d_w [mm]	d_p [m]	anchors' pattern
1 (ref.)	$1{\cdot}10^8$	38	35	90	2.00	2.7	0.32	square
2	$\mathbf{1 \cdot 10^9}$	38	35	90	2.00	2.7	0.32	square
3	$\mathbf{1 \cdot 10^{10}}$	38	35	90	2.00	2.7	0.32	square
4	$1{\cdot}10^8$	**43**	35	90	2.00	2.7	0.32	square
5	$1{\cdot}10^8$	**33**	35	90	2.00	2.7	0.32	square
6	$1{\cdot}10^8$	**23**	35	90	2.00	2.7	0.32	square
7	$1{\cdot}10^8$	38	**25**	90	2.00	2.7	0.32	square
8	$1{\cdot}10^8$	38	**15**	90	2.00	2.7	0.32	square
9	$1{\cdot}10^8$	38	**0**	90	2.00	2.7	0.32	square
10	$1{\cdot}10^8$	38	35	**80**	2.00	2.7	0.32	square
11	$1{\cdot}10^8$	38	35	**70**	2.00	2.7	0.32	square
12	$1{\cdot}10^8$	38	35	**65**	2.00	2.7	0.32	square
13	$1{\cdot}10^8$	38	35	90	**6.00**	2.7	0.32	square
14	$1{\cdot}10^8$	38	35	90	**4.00**	2.7	0.32	square
15	$1{\cdot}10^8$	38	35	90	**1.50**	2.7	0.32	square
16	$1{\cdot}10^8$	38	35	90	**1.25**	2.7	0.32	square
17	$1{\cdot}10^8$	38	35	90	**0.75**	2.7	0.32	square
18	$1{\cdot}10^8$	38	35	90	**0.50**	2.7	0.32	square

# test	E_s [Pa]	ϕ_S^M [°]†	ϕ_{ms} [°]	α [°]	t [m]	d_w [mm]	d_p [m]	anchors' pattern
19	$1{\cdot}10^8$	38	35	90	2.00	**2.0**	0.32	square
20	$1{\cdot}10^8$	38	35	90	2.00	**3.0**	0.32	square
21	$1{\cdot}10^8$	38	35	90	2.00	**3.9**	0.32	square
22	$1{\cdot}10^8$	38	35	90	2.00	2.7	**0.16**	square
23	$1{\cdot}10^8$	38	35	90	2.00	2.7	**0.24**	square
24	$1{\cdot}10^8$	38	35	90	2.00	2.7	**0.40**	square
25	$1{\cdot}10^8$	38	35	90	2.00	2.7	**0.48**	square
26	$1{\cdot}10^8$	38	35	90	2.00	2.7	**0.56**	square
27	$1{\cdot}10^8$	38	35	90	2.00	2.7	**0.64**	square
28	$1{\cdot}10^8$	38	35	90	2.00	2.7	0.32	**diamond A**
29	$1{\cdot}10^8$	38	35	90	2.00	2.7	0.32	**diamond B**

†ϕ_S^M represents the macroscopic friction angle obtained from periodic triaxial tests

Table 6.5: Summary of the parameter sets and configurations considered in the parametric analysis. The first row corresponds to the reference test. Bold fonts are used to mark the parameter that differs from the reference test.



(a) (b)

Figure 6.22: Comparison of the central panel mechanical response in terms of (a) F_{tot}-δ and (b) F_z-δ curves obtained with a different soil stiffness.

in Tab. 6.5, where the different parameters characterising each simulation are reported (bold font is used to highlight the parameter that differs from the reference case).

6.3.1 Soil stiffness

The influence of a variation of the soil stiffness is investigated varying the soil contact elastic modulus E_s. Indeed, for a given grain size, following a dimensional analysis the soil stiffness linearly scales with the contact stiffness [20]. The numerical results, in terms of F-δ relationships of the central panel, obtained from the simulation characterised by $E_s = 1 \cdot 10^9$ Pa and $E_s = 1 \cdot 10^{10}$ Pa are compared with the one obtained from the reference case in Fig. 6.22a and 6.22b considering the total force and the z-component of the latter respectively. The soil stiffness seems to have a minor influence on the mechanical response of the mesh panel. A higher soil stiffness leads to a very slight increase of the maximum deflection and a slight decrease of the maximum supported force (this is in agreement with what observed in [14]). The weak effect that the soil stiffness has on the mesh mechanical response can be explained considering that the soil behind the mesh mostly experiences large shear deformations, which are mainly controlled by the sliding among grains (i.e. frictional effects) rather than by the soil stiffness.

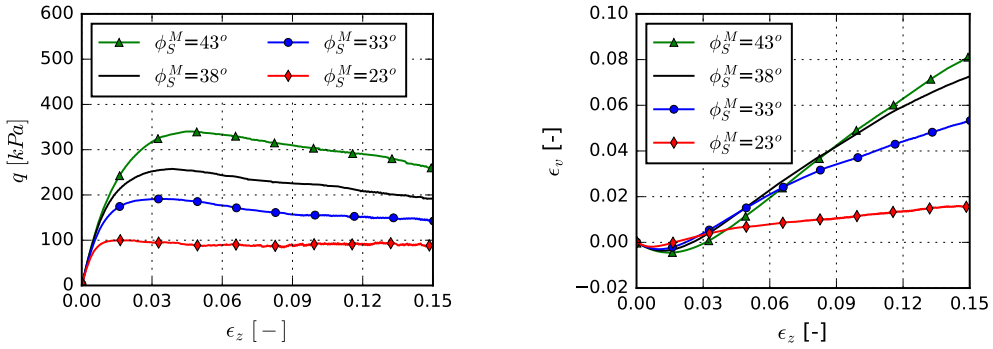
param.	*soil* 1	*soil* 2	*soil ref.*	*soil* 3
E_s [Pa]	$1 \cdot 10^8$	$1 \cdot 10^8$	$1 \cdot 10^8$	$1 \cdot 10^8$
ν_s [-]	0.30	0.30	0.30	0.30
ϕ_s [°]	35	35	35	35
β_r [-]	0.00	0.05	0.10	0.20
η_r [-]	0.00	0.05	0.10	0.20
ϕ_S^M [°]	23 ($\pm$1.0)	33 ($\pm$0.5)	38 ($\pm$0.4)	43 ($\pm$1.0)
E_{50}^M [MPa]	17 ($\pm$1.0)	18 ($\pm$1.0)	19 ($\pm$1.0)	19 ($\pm$0.5)
ν^M [-]	0.36 ($\pm$0.02)	0.34 ($\pm$0.02)	0.33 ($\pm$0.01)	0.34 ($\pm$0.01)

Table 6.6: Numerical contact parameters and macroscopic properties (the value in round brackets gives the range of variation observed by varying the confining pressure) of the soil types

6.3.2 Soil macroscopic friction angle

In order to analyse the effect of the internal shear resistance of the granular soil on the mechanical response of the mesh, three different granular soil types (other than the reference one), characterised by a different macroscopic friction angle, are considered. The macroscopic friction angle ϕ_S^M is varied considering different values of the rotational resistance parameters β_r and η_r (these parameters were defined in Chapter 5). This permits one to consider a different value of ϕ_S^M without modifying the contact friction angle of a soil particle. The macroscopic properties of these granular materials are derived from periodic drained triaxial tests on a cubic soil specimen as detailed in Sec. 6.1.2. The results of the triaxial tests related to the three soil types are reported in Fig. 6.23 (only the curves obtained for a confining pressure of 80kPa are reported), while the related contact parameters and macroscopic properties are summarised in Tab. 6.6. Even if the case $\phi_S^M = 23°$ is not common for coarse granular soils, it is interesting from a numerical perspective because it represents the limit case for which no rolling resistance is applied at the grains contact.

The force-displacement curves characterising the mechanical response of the central mesh panel, for the considered cases, are reported in Fig. 6.24a, 6.24b and 6.24c with reference to the two force components F_y and F_z and to the total force F_{tot} respectively. From the observation of the force-



(a) (b)

Figure 6.23: DEM triaxial test (isotropic compression of 80kPa) results of the numerical soil: (a) deviatoric curve and (b) volumetric curve.

displacement relationships characterising the out-of-plane mesh response (i.e. F_z-δ), it is possible to observe that, for a given deflection value of the central panel, the greater resulting force corresponds to a lower value of the soil macroscopic friction angle, which, as expected, provides the larger earth-pressure conditions on the mesh. This consideration does not apply when referring to the y-component of the force being this latter, for the same geometric configuration of the mesh-soil problem, mainly controlled by the mesh-soil contact friction angle (this will be detailed in Sec. 6.3.3).

In all the four cases, the failure condition of the mesh is reached, but the failure mechanism observed in the meh system is different. For $\phi_S^M = 23°, 33°$ the failure is caused by the rupture of some wires at the level of the anchor C, while for $\phi_S^M = 38°, 43°$ it is caused by the breakage of some wires at the level of the anchor F. Considering the maximum force supported by the central mesh panel, a reduction of the latter is observed for the lower values of ϕ_S^M, while almost the same value is observed for the cases $\phi_S^M = 38°, 43°$. This is due to a premature failure of the mesh system in the lower part of the mesh system, which is a consequence of the larger soil volumes that becomes unstable when considering a material characterised by a lower friction angle. In the cases $\phi_S^M = 23°, 33°$ the retaining action exerted by the lower panel is not sufficient to stabilise the soil volume acting at the toe of the system, and local ruptures in the bottom part of the anchor C are observed. This "premature" failure determines only a partial activation

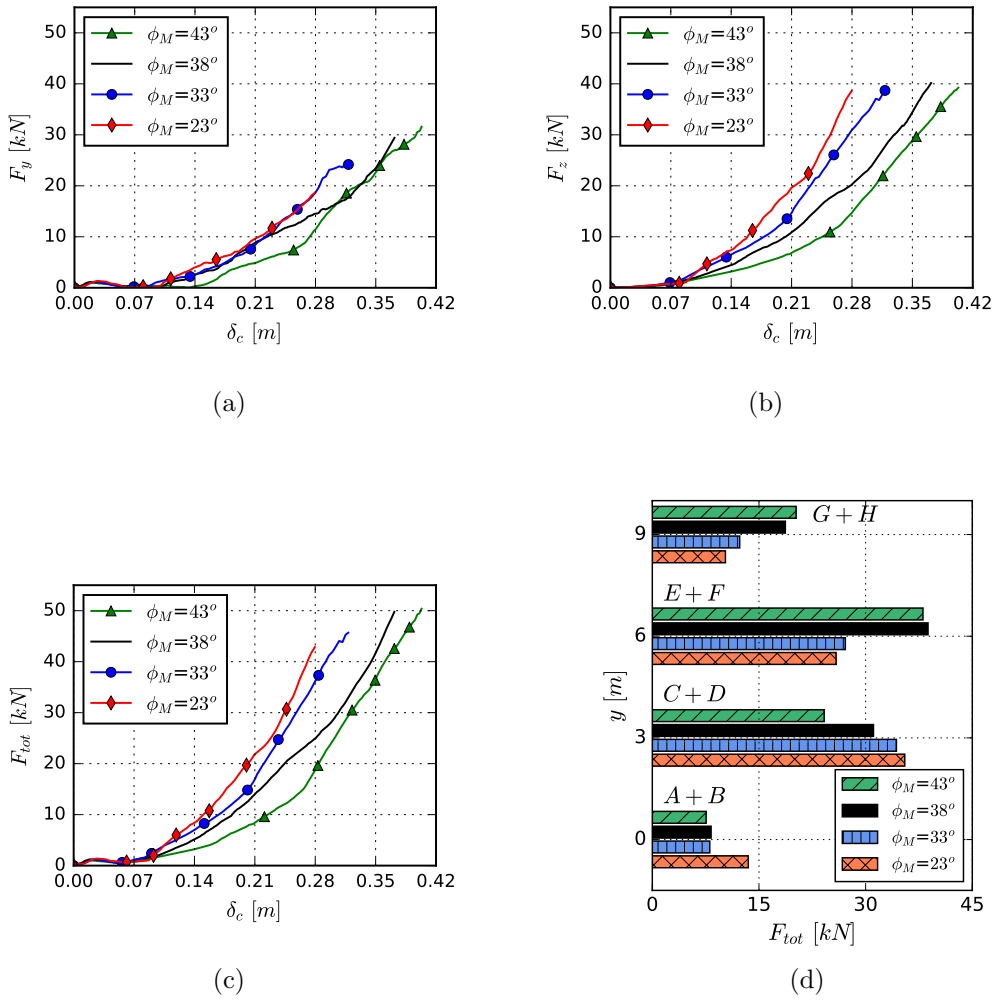


Figure 6.24: Comparison of the central panel mechanical response in terms of (a) F_y-δ, (b) F_z-δ and (c) F_{tot}-δ curves obtained varying the macroscopic friction angle ϕ_S^M of the numerical soil. (d) Tensile force supported by the different anchor levels an instant before the mesh failure.

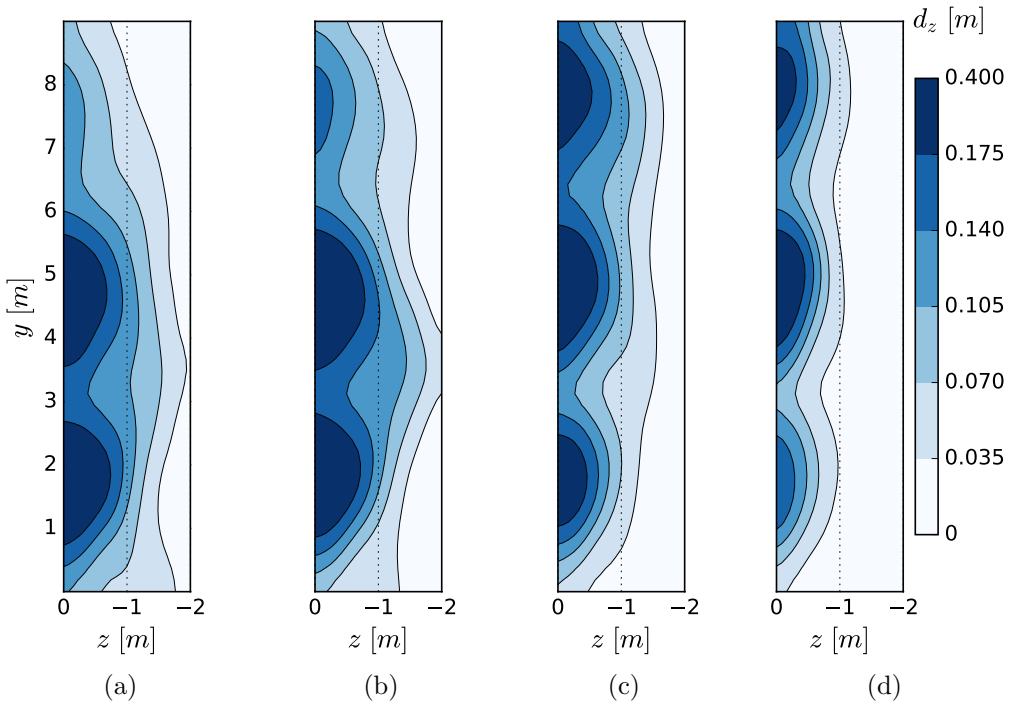


Figure 6.25: z-Displacement field of the unstable soil layer, an instant prior to the mesh failure, obtained varying the macroscopic friction angle of the numerical soil: (a) $\phi_S^M = 23°$, (b) $\phi_S^M = 33°$, (c) $\phi_S^M = 38°$ (reference case), $\phi_S^M = 43°$.

of the retaining capacity of the central panel. This effect is evident when observing the distribution of the tensile forces among the anchors, an instant before the failure of the mesh, as reported in Fig. 6.24d. The highest values of tensile forces are observed in the lower anchors (A+B and C+D) for the lower values of ϕ_S^M; conversely, the highest values are observed acting on the upper anchors (E+F and G+H) when considering the higher values of ϕ_S^M.

The difference in the system mechanical response, associated with a variation of ϕ_S^M, can be better understood observing the soil z-displacement field reported in Fig. 6.25. Considering the case $\phi_S^M = 38°, 43°$, almost homogeneous local failure mechanisms, acting at the level of each mesh panel, are observed. Instead, in the cases characterised by the lower values of ϕ_S^M, the soil movements tend to concentrate in the lower part of the system and this trend increases when decreasing the value of ϕ_S^M. This behaviour can be ex-

plained referring to the progressively upwards activation of the local failure mechanisms observed for the reference case ($\phi_S^M = 38°$) and discussed in Sec. 6.2.2. It has been observed that the activation of the local failure mechanism, associated with a mesh panel, is related to the achieving of a sufficient retaining action on the lower level ("partial stabilisation" of the lower sliding soil wedge). A soil characterised by a lower friction angle requires a higher retaining force to find a stable configuration, and for the cases characterised by the lower values of ϕ_S^M considered here, the failure conditions are reached in the lower part of the system due to limited resistance at the mesh-plate connection (in correspondence with anchor C). This "premature" failure does not permit the "complete" activation of the local failure mechanisms in the upper part of the system (see Fig. 6.25aand Fig. 6.25b), thus determining only a partial reaction of the central and upper mesh panels. Finally, it is notable that the soil movements concentrate in a shallower portion of the soil layer when the latter is characterised by a higher friction angle.

6.3.3 Soil-mesh contact friction angle

The frictional interaction at the interface between the soil and the structure plays an important role in the majority of soil-structure interaction problems (e.g. foundations, retaining walls, soil-inclusion problems). In this paragraph, the role of this interaction is analysed changing the value of the mesh-soil contact friction angle ϕ_{ms} from the reference one ($\phi_{ms} = 35°$) to a frictionless case. It should be noted that this friction angle is no longer a macroscopic friction angle (as ϕ_S^M considered in Sec. 6.3.2), but it is a pure contact friction angle; in particular, it represents the contact friction angle that characterises the tangential interaction between the mesh wires (cylindrical elements in the model) and the soil particles. In order to evaluate the effect of the frictional properties at the mesh-soil interface, a particular attention is given to the force acting along the y-direction on the central panel. This force, in fact, represents a "macroscopic" in-plane force (with reference to the mesh undeformed configuration), which can be formally associated with the tangential action generally considered in the classic limit equilibrium design methodologies to schematise the mesh-soil interface interaction. This "macroscopic" interface force can be seen as the sum of a frictional component and an interlocking component. The latter is here analysed considering the case of a frictionless contact between the

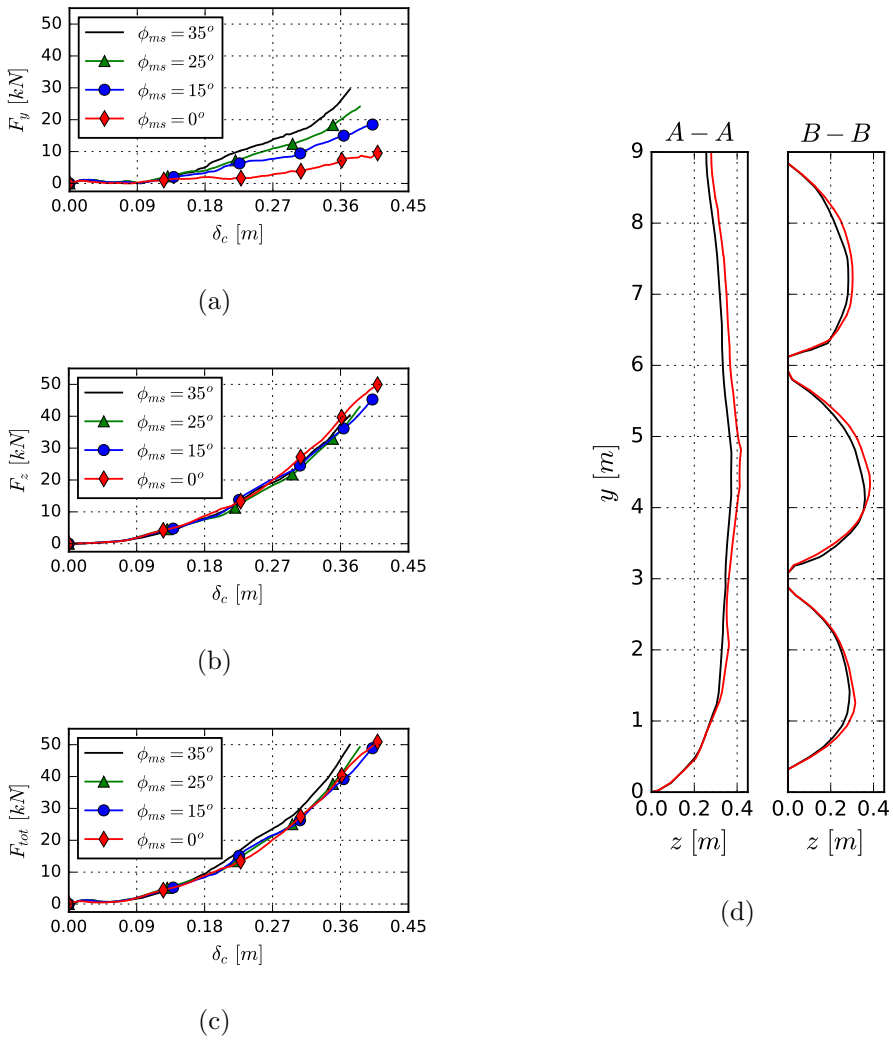
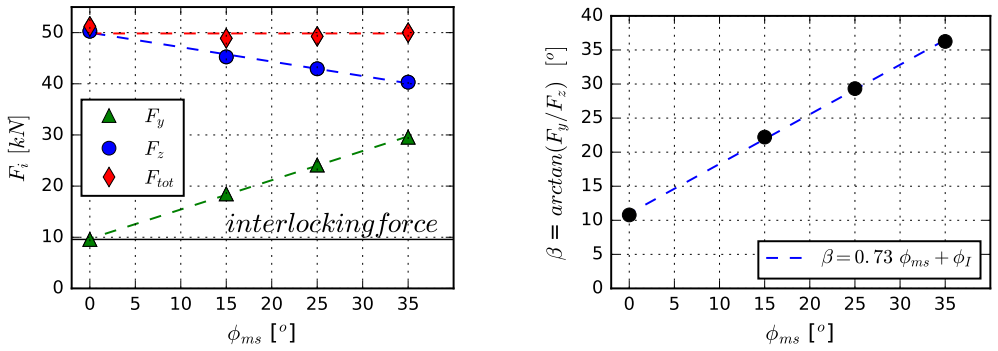


Figure 6.26: Comparison of the central panel mechanical response in terms of (a) F_y-δ, (b) F_z-δ and (c) F_{tot}-δ curves obtained varying the mesh-soil contact friction angle ϕ_{ms}. (d) Mesh profile with reference to the central section A-A and the lateral section B-B of the system for the case $\phi_{ms} = 0°$ (red line) and $\phi_{ms} = 35°$ (black line).



(a) (b)

Figure 6.27: (a) Force components F_y and F_z and total force F_{tot} values and (b) inclination angle β of the total force obtained considering different mesh-soil contact friction angle (the values refer to the mesh mechanical condition an instant prior to its failure).

mesh and the soil particles. The force-displacement relationships obtained varying the value of ϕ_{ms} are reported in Fig. 6.26.; in the same figure the deformed profile of the mesh with respect to section A-A and B-B is reported for the cases characterised by $\phi_{ms} = 35°$ and $\phi_{ms} = 0°$. Observing the trend of the macroscopic in-plane force F_y (see Fig. 6.26a) it is evident that the longitudinal force greatly increases with the interface contact friction angle (F_y ($\phi_{ms} = 35°$)=29.6kN, F_y ($\phi_{ms} = 0°$)=9.6kN), and this is due to the higher frictional forces that can be exchanged at the mesh-soil contact adopting a higher value of ϕ_{ms}. Moreover, it is interesting to observe how this variation of F_y reflects on the out-of-plane force F_z; the latter shows the opposite behaviour, namely showing a decreasing trend when increasing the ϕ_{ms} value (see Fig. 6.27a). This "complementary" behaviour is related to the constancy of the maximum total force sustainable by the panel, which is independent of the mesh-soil friction angle, as observable referring to Fig. 6.27a. The force values registered in the central mesh panel, an instant prior to its failure, are reported in Fig. 6.27a in order to better visualise role of ϕ_{ms} on the system mechanical response. A non-zero F_y ($\approx 20\%$ of F_{tot} an instant prior to the mesh failure) is registered also for the frictionless case (i.e. $\phi_{ms} = 0°$), thus showing the existence of an interlocking force. This force is related to single particles and/or small volumes that remain trapped at

the level of the central mesh panel due to its bulged deformed configuration (see Fig. 6.26) and/or in the zones surrounding the anchors. In this sense, it should be considered as a "macroscopic" interlocking force. If considering this "macroscopic" interlocking force as independent of ϕ_{ms}, the pure frictional effects can be computed as the difference between the overall value of F_y obtained in the specific case and the one resulting from the frictionless case. Finally, the influence of the mesh-soil contact friction angle, on the inclination β of the total force (as defined in Sec. 6.2.1) acting on the central mesh panel, can be observed in Fig. 6.27b. The numerical results show that β is well represented by a linear function of the mesh-soil contact friction angle as given by:

$$\beta = 0.73\phi_{ms} + \phi_I \tag{6.1}$$

where the terms ϕ_I represents a constant contribution deriving from the "macroscopic" interlocking and, for the considered cases, takes the value $\phi_I = 11°$. The inclination β being defined as the ratio of the in-plane and out-of-plane mesh panel force components (i.e. F_y and F_z respectively), it can be seen as a "macroscopic" interface friction angle. In this perspective, it can be used, in the standard limit equilibrium design methodologies, in order to relate the tangential and the normal force (with respect to the mesh plane) imposed by the mesh system on the unstable layer. Having said that, it should be noted that the "macroscopic" in-plane force is progressively mobilised as the mesh deflection increases (see Fig. 6.8a), and thus should be considered as dependent from the mesh deformability and correlated to the actual deformation level of the mesh.

6.3.4 Slope angle

Up to this point, only the mechanical properties of the numerical soil and the properties at the mesh-soil interface have been considered. In the following paragraph, the focus will be on the geometry of the soil layer, and in particular the effect of considering a different inclination of the slope is analysed. The latter is varied tilting the gravity vector as exemplified in Fig. 6.28. The resulting forces characterising the central panel mechanical response are referred to the same local reference frame, irrespective of the gravity force direction. Thus F_y represents the "macroscopic" in-plane and F_z the out-of-plane forces (with reference to the undeformed mesh panel) in all the considered cases. Different slope angles ranging from 45° to 90° are

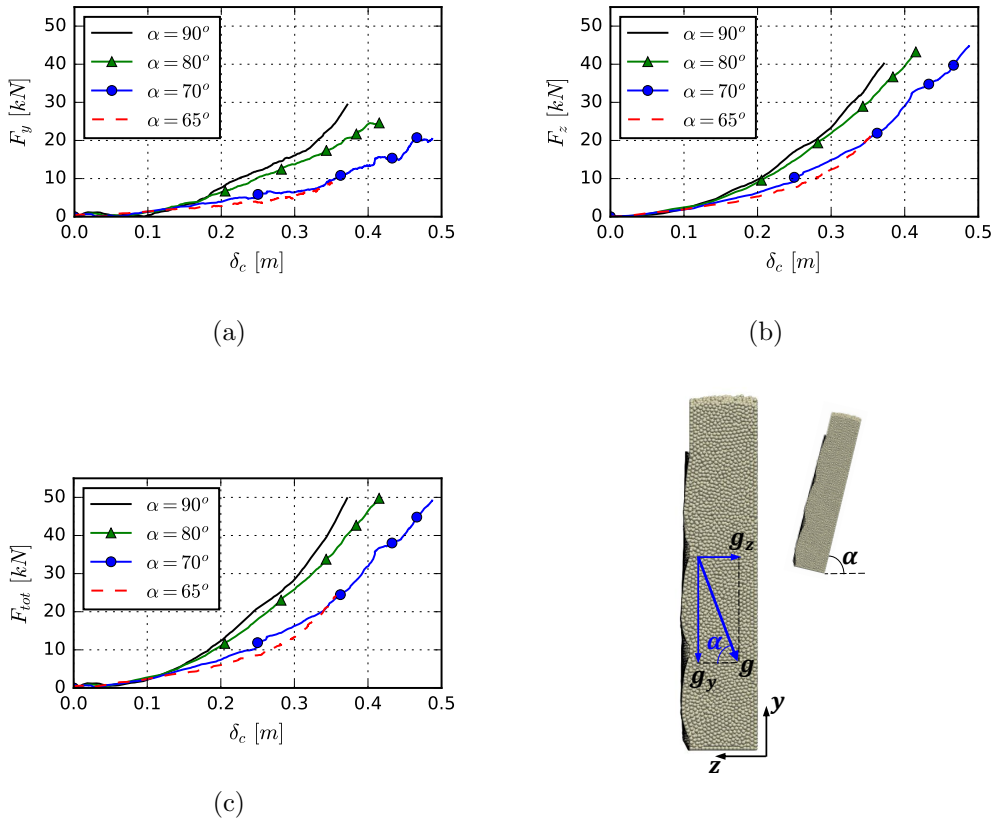
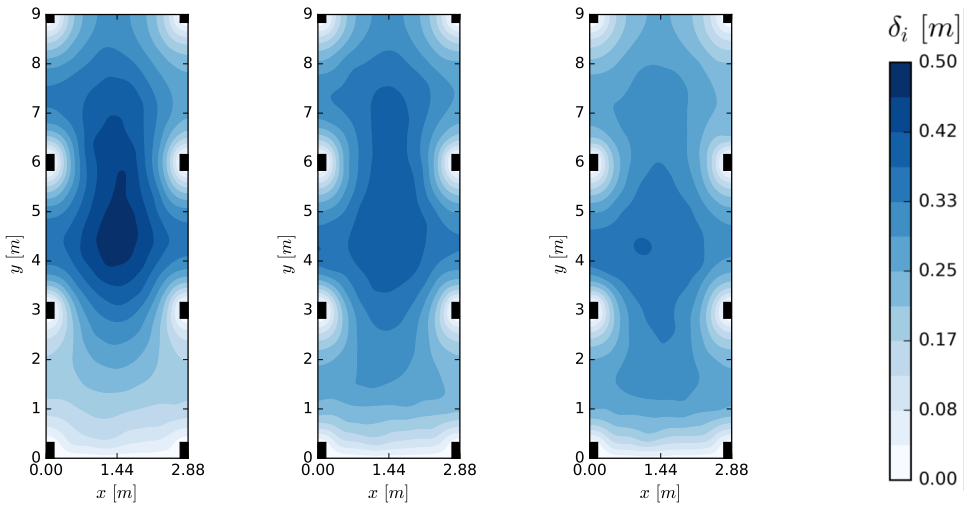


Figure 6.28: Comparison of the central panel mechanical response in terms of (a) F_y-δ, (b) F_z-δ and (c) F_{tot}-δ curves obtained varying the slope angle α.

studied. The failure of the mesh is observed for values of the slope angle $\alpha \geq 70°$. For gentler slopes, only shallow movements are observed in the granular layer and the retaining action applied by the drapery system is sufficient to lead to a stable configuration. In the following, only the limit case 65° will be analysed, while the other cases characterised by $\alpha \leq 70°$ are omitted.

The force-displacement relationships obtained for the different values of the slope angle are compared in Fig. 6.28. Considering the results obtained for $\alpha \geq 70°$, the maximum total force supported by the central panel is almost the same irrespective of the slope angle as shown in 6.28c. In all the cases, the failure starts from anchor F. For the limit case of $\alpha \geq 65°$, the mesh does not fail and, once the debris volume has reached a stable configuration, the



(a) (b) (c)

Figure 6.29: z-Displacement field (out-of-plane direction) of the mesh system, an instant prior to the mesh failure, obtained varying the slope angle: (a) $\alpha = 70°$, (b) $\alpha = 80°$, (c) $\alpha = 90°$ (reference case).

total force supported by the central panel is $F_{tot} = 24.3$kN and the deflection of the mesh panel is $\delta_c = 0.36$m.

The almost constant value of the maximum retaining force is consistent with the assumption that, when a sufficient redistribution of the load among the anchors is achieved, this is mostly a function of the mesh-anchor connection resistance. The force imposed on the mesh by the granular mass, for a given value of the panel deflection, is instead higher when a steeper slope is considered. This is in agreement with the classical geomechanics theories, which evaluate the earth pressure acting on rigid retaining structures. In fact, the soil exerts a decreasing earth pressure on the wall for a negative internal slope of the backward wall-face. For instance, according to the Coulomb's earth pressure theory, the active force decreases by 50% passing from a vertical wall to a -20° internal slope angle. A similar result is obtained: for a given deflection value, the total force obtained for $\alpha = 70°$ is from 50% to 60% lower than the one measured for the vertical case (see Fig. 6.28). Referring instead to the mechanical condition of the mesh panel an instant prior to its failure, it is interesting to note that the contribution

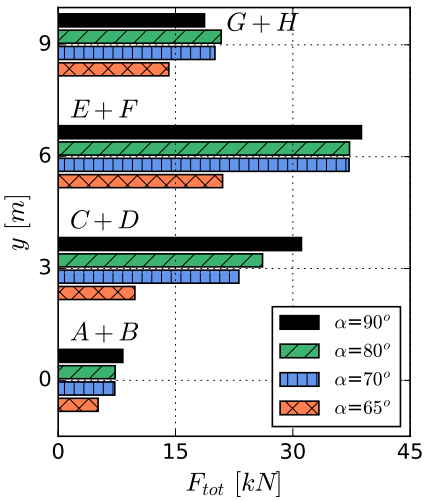


Figure 6.30: Tensile force supported by the different anchor levels an instant before the mesh failure (the failure condition is not reached for $\alpha = 65°$) for different values of the slope angle α.

of the force components (i.e. F_y and F_z) to the overall force sustained by the panel is different. This points out that the ratio between the two force components, tangentially and normally oriented with respect to the slope face, is influenced by the geometrical characteristic of the system, and is not only a function of the frictional interaction at the interface as implicitly assumed by most of the standard design methodologies [22, 31, 59]. The in-plane and out-of-plane mesh reactions are instead treated as independent in the design methodology proposed in [61]. Observing the trends of F_y reported in Fig. 6.28a, it is evident that the contribution of F_y is significantly higher in the case characterised by $\alpha = 90°$ than in the one characterise by $\alpha = 70°$. In fact, the force component, acting along the mesh in-plane direction, of the force imposed by the unstable soil volumes on the mesh panel, is higher when considering a steeper slope. Therefore, because of the constancy of the maximum force sustainable by the mesh panel, the higher value of F_y observed in steeper slopes determines a decrease of the mesh possible reaction along the z-direction (an instant prior to its failure) as observable in Fig. 6.28b. Furthermore, an higher deflection of the central mesh panel, for the same amount of supported force, is observed when reducing the slope angle α. The higher values of the in-plane force acting on the mesh panel for higher

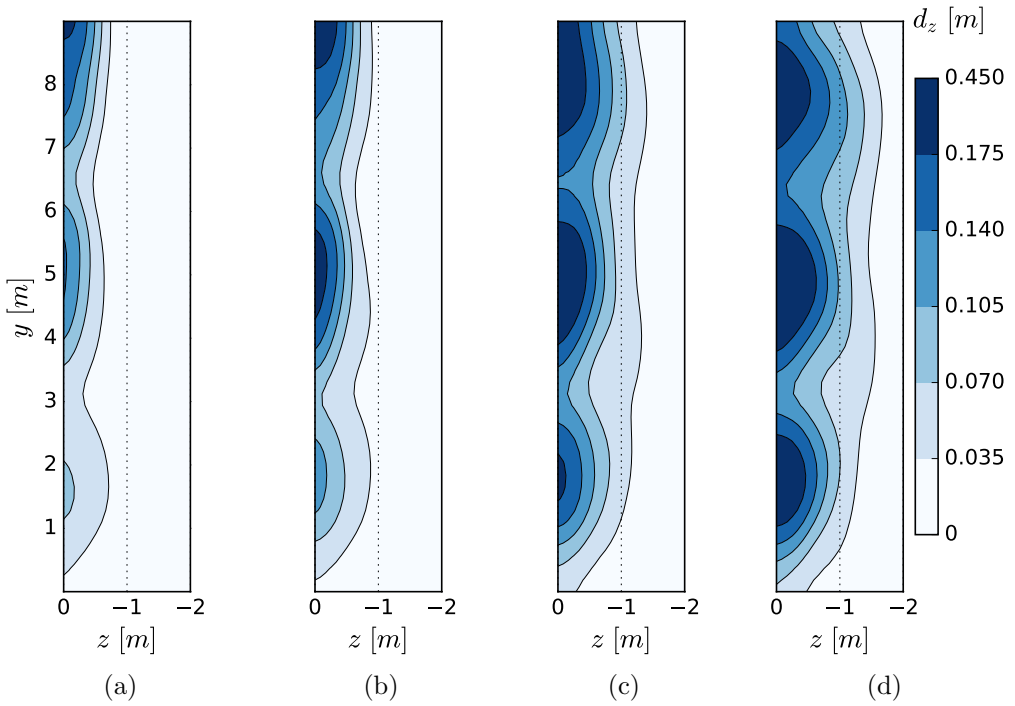
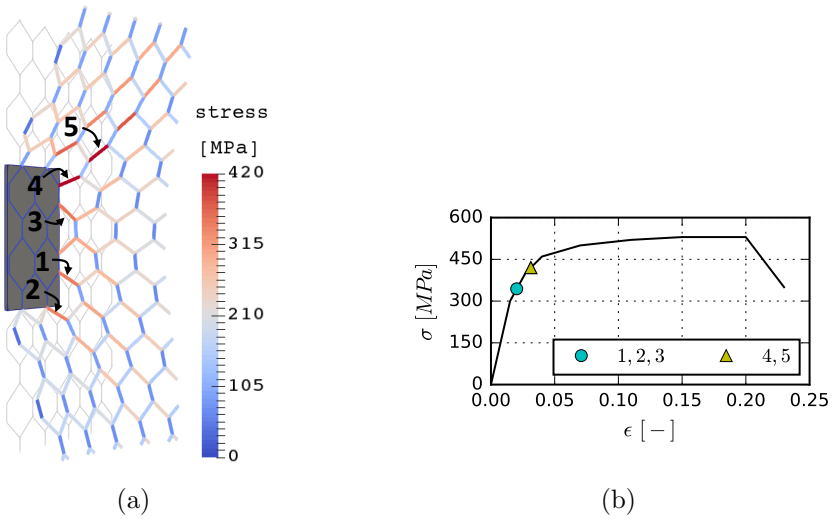


Figure 6.31: z-Displacement field of the unstable soil layer obtained varying the slope angle: (a) $\alpha = 65°$, (b)$\alpha = 70°$, (c) $\alpha = 80°$, (d) $\alpha = 90°$ (reference case). The values refer to an instant prior to the mesh failure with the only exception of the case $\alpha = 65°$ for which the system finds an equilibrium configuration before the failure of the mesh.

values of α, lead to an increment of its out-of-plane stiffness, consequently determining the observed reduction of the panel deflection. This increase of the mesh out-of-plane stiffness is confirmed observing the distribution of z-displacement field on the entire mesh system reported in Fig. 6.29.

The load transmitted by the mesh to the anchors is represented in Fig. 6.30. The force values refer to the mechanical conditions one instant before the failure of the mesh, with the only exception of the case $\alpha = 65°$ for which the debris material finds a stable configuration before the failure of the mesh. Considering the cases $\alpha \geq 70°$, a decrease of the load supported by the anchors placed on the lower part of the mesh system (i.e. A+B and C+D) is observed when considering lower slope angles, while the load acting on the anchors in the upper part of the system is approximately the same

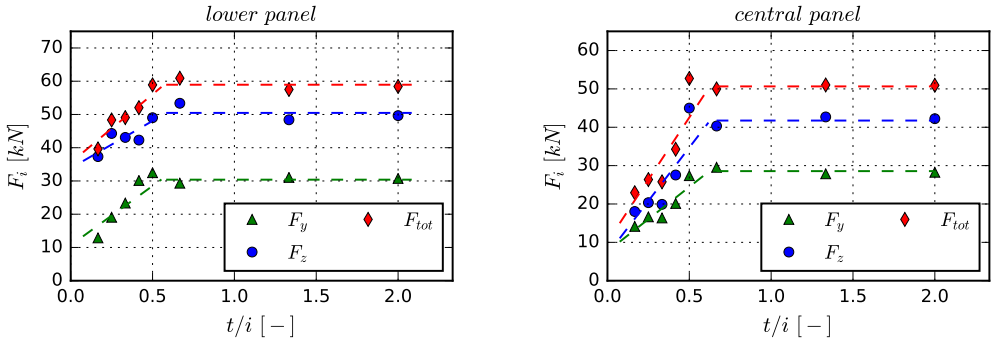


(a) (b)

Figure 6.32: (a) Tensile stress distribution on the wires surrounding the anchor F and (b) mechanical conditions of the most critical wires an instant prior to the first breakage of a wire for the case $\alpha = 65°$.

irrespective of the considered value of α. The former aspect may be related to the reduction of the soil movements observed in the lower part of the mesh system for gentler slopes as shown in Fig. 6.31. Furthermore, from the comparison of the z-displacement fields in Fig. 6.31 it can be seen that, due to a lower inclination of the slope, the mobilised debris volumes decrease (considering the central panel, the estimated unstable volume, computed as in Sec. 6.2.2, is $V_c = 3.9\text{m}^3$ for $\alpha = 70°$ and $V_c = 6.8\text{m}^3$ for $\alpha = 90°$) and they affects a more superficial portion of the debris layer. Nevertheless, the failure process occurring in the soil can still be schematised as a wedge-shaped local mechanism acting at the level of each mesh panel.

Finally, the tensile stress distribution acting on the wires surrounding the most stressed anchor (i.e. anchor F), for the case $\alpha = 65°$, is shown in Fig. 6.32a. The mechanical conditions of the five wires are reported on the stress-strain tensile curve characteristic of the single wire elements in Fig. 6.32b. The most critical mechanical condition is experienced by wire 4, which is characterised by a tensile stress $\sigma = 420\text{MPa}$ ($\sigma_{max} = 530\text{MPa}$) and by a tensile strain $\epsilon = 0.031$ ($\epsilon_{max} = 0.23$). The tensile stress distributions observed in the cases $\alpha = 70°$ and $\alpha = 80°$ are approximately the same of the one observed for the reference case and reported in Fig. 6.15a.



(a) (b)

Figure 6.33: Force components F_y and F_z and total force F_{tot} values obtained varying the soil layer thickness for: (a) the lower panel and (b) the central panel (the values refer to the mesh mechanical condition an instant prior to its failure).

6.3.5 Thickness of the unstable soil layer

The thickness of the unstable layer represents an important parameter in secured drapery applications, influencing the development of the failure mechanism in the retained material, its potential volume, and consequently the load exerted by the soil on the mesh system. In the following paragraph, the role of the soil layer thickness is analysed changing its value in the range $0.5\text{m} \leq t \leq 6\text{m}$. For the sake of generality, the numerical results are presented referring to the dimensionless ratio t/i, where i represents the vertical spacing between two anchor rows (i.e. $i = 3.00\text{m}$ in the considered case). In order to analyse the influence of t on the system mechanical response, the force components F_y and F_z, as well as the total force F_{tot}, acting on the lower and the central panels, are reported in Fig. 6.33a and 6.33b respectively. The values refer to the mesh mechanical conditions an instant before its failure. The force-displacement curves are instead omitted, these being characterised by approximately the same trend (i.e. they are superimposed), for all the considered cases, before the failure of the system (this latter occurring at different deflection level depending on the unstable layer thickness).

The numerical data highlight a non-trivial behaviour: the maximum total force sustainable by a mesh panel shows an increasing trend when increasing the soil layer thickness for $\frac{t}{i} \lesssim \frac{2}{3}$, then for higher t/i ratios the force value

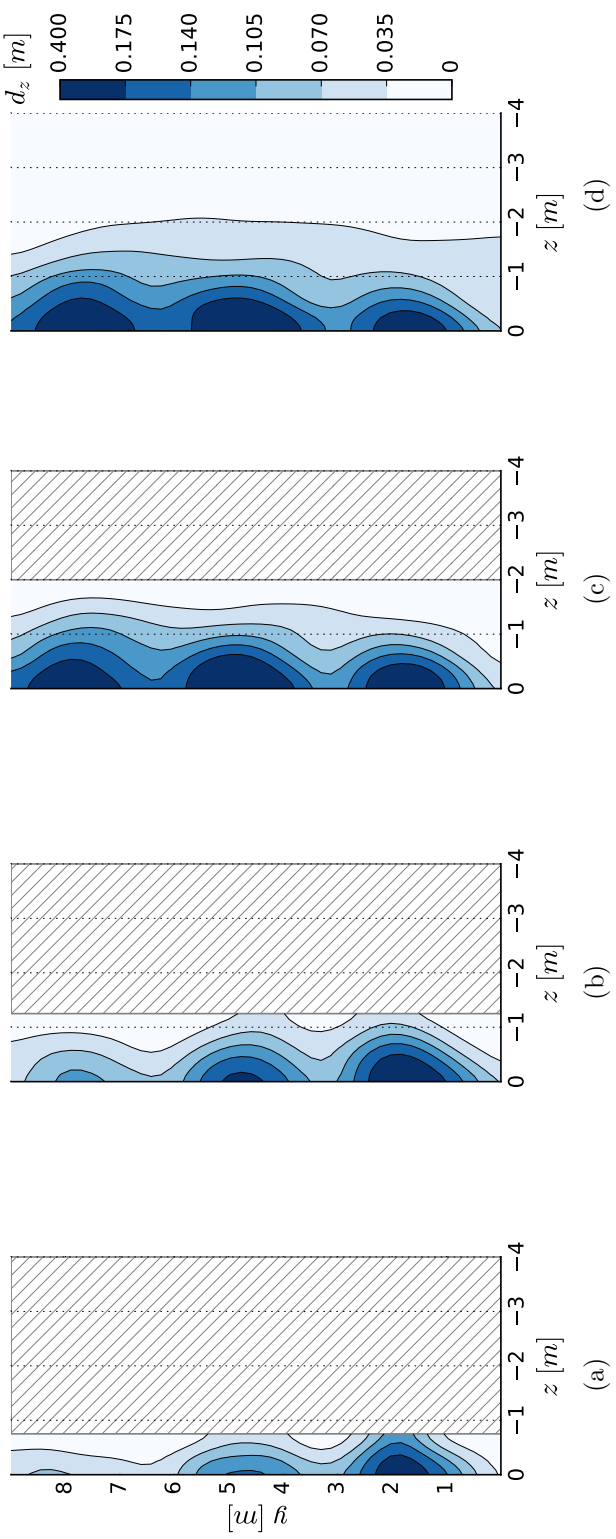


Figure 6.34: z-Displacement field of the unstable soil layer, an instant prior to the mesh failure, obtained varying the unstable layer thickness: (a) $t = 0.75$m, (b) $t = 1.25$m, (c) $t = 2.00$m (reference case), (d) $t = 4.00$m. The hatched area represents the ideal "stable part" of the slope on the back of the unstable layer.

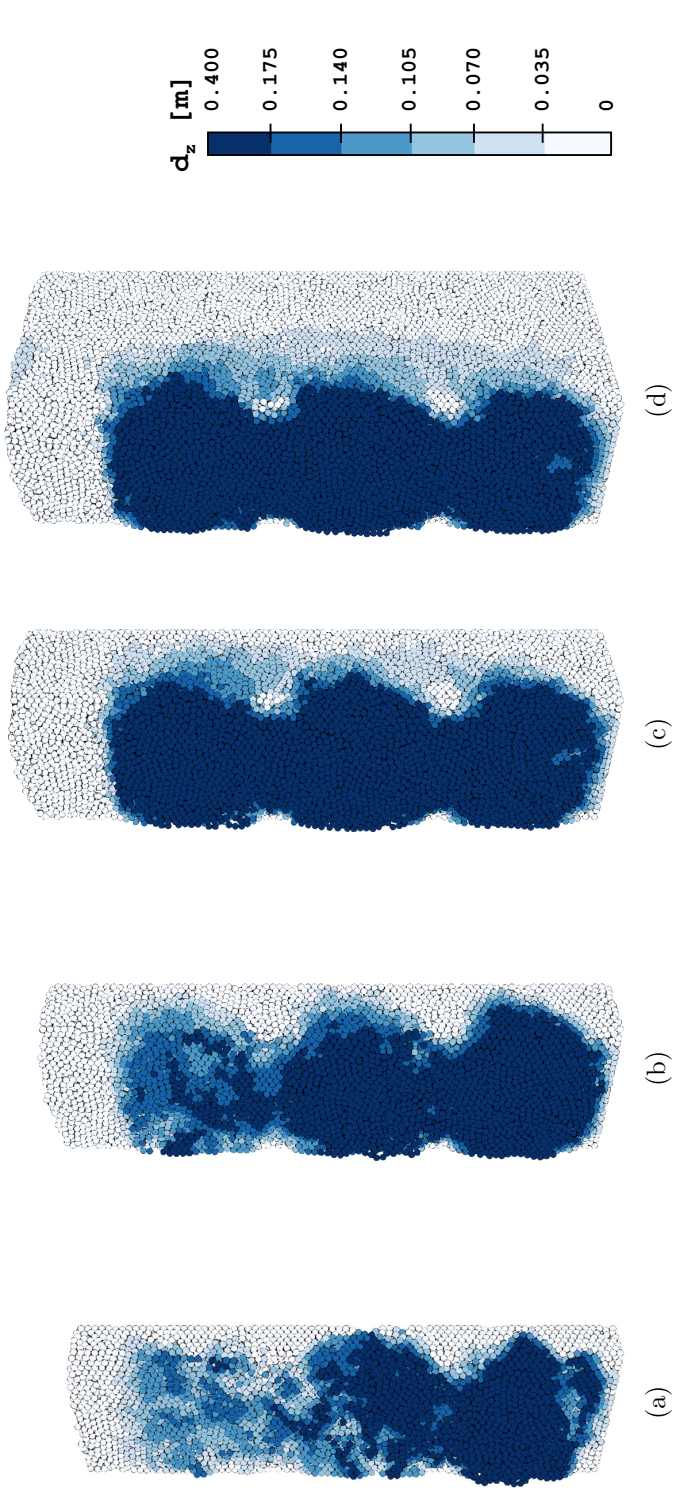


Figure 6.35: 3D view of the z-displacement field of the unstable soil layer, an instant prior to the mesh failure, obtained varying the unstable layer thickness: (a) $t = 0.75$m, (b) $t = 1.25$m, (c) $t = 2.00$m (reference case), (d) $t = 4.00$m.

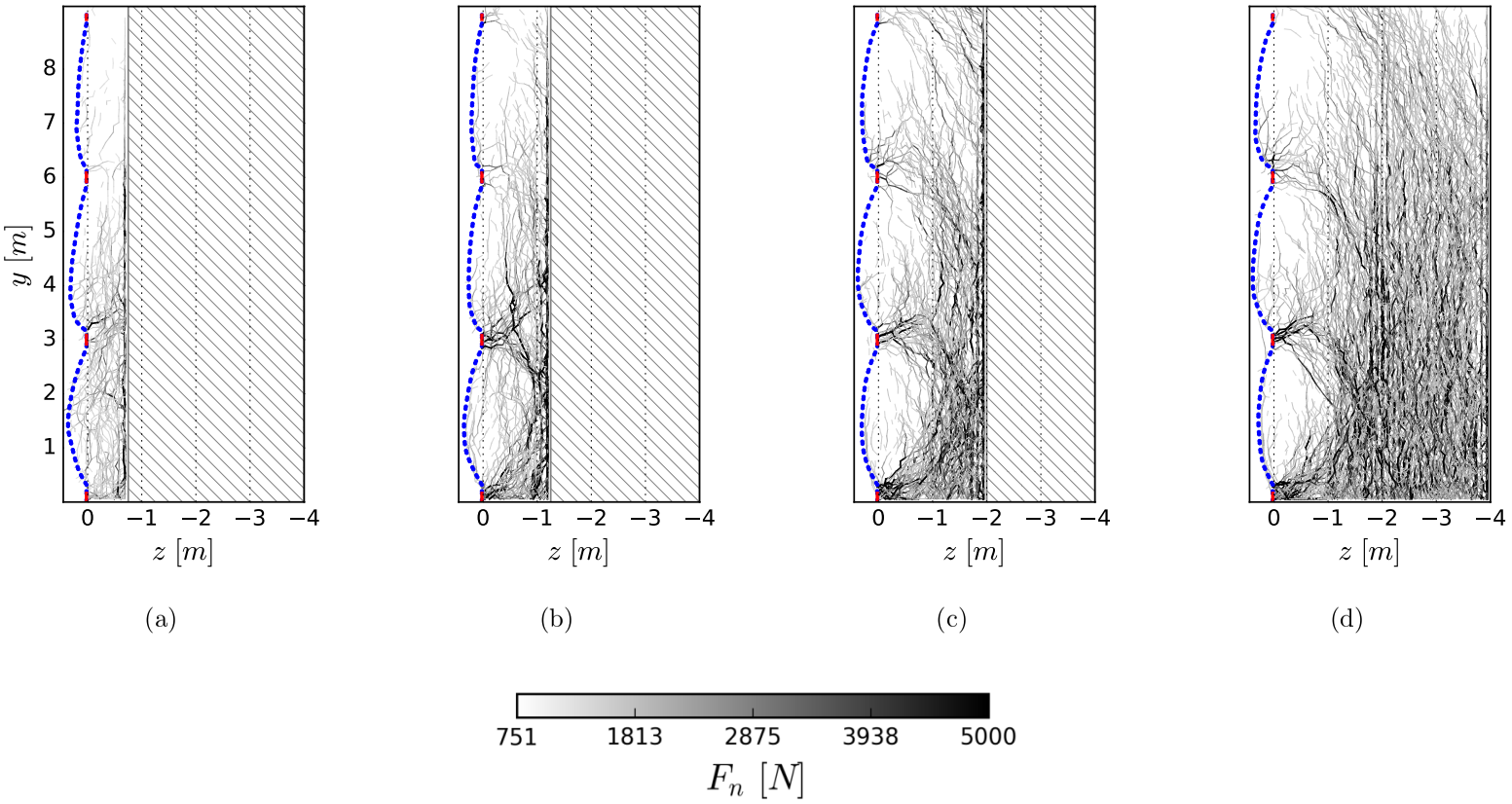


Figure 6.36: Contact force network (strong network) in the unstable soil layer, an instant prior to the mesh failure, obtained varying the unstable layer thickness: (a) $t = 0.75$m, (b) $t = 1.25$m, (c) $t = 2.00$m (reference case), (d) $t = 4.00$m.

seems to saturate to a constant value. The same trend is observed also for both the force components. This peculiar behaviour may be associated with a partial activation of the mesh panel retaining capacity, which is due to only a local interaction between the unstable volumes and the mesh panel surface. As observable considering the soil z-displacement field reported in Fig. 6.34 and in Fig. 6.35 (2D and 3D view respectively), the finite size of unstable layer can influence the development of the local failure mechanisms in the retained material. For low t/i ratios, in fact, the sliding soil wedges are limited by the thickness of the unstable layer (see Fig. 6.34a, 6.34b and Fig. 6.35a, 6.35b) and extend only for a portion of the mesh panel on which they are acting. On the other hand, the size of the unstable soil wedges is approximately the same when the ratio t/i is sufficiently large to not limit their formation (see Fig. 6.34c, 6.34d and Fig. 6.35c, 6.35d). For instance, the estimated mobilised soil volumes (as defined in Sec. 6.2.2) are 6.8m^3 for $t = 2$m and 7.0m^3 for $t = 4$m referring to the central panel, and 4.4m^3 for $t = 2$m and 4.2m^3 for $t = 4$m referring to the lower panel. For ratios $t/i > 2/3$, the unstable wedges can be considered fully developed and consequently the mesh retaining capacity is no more influenced by the thickness of the unstable layer.

In Section 6.2.2 it has been shown that the formation of the local unstable wedges derives from the onset of an arching effect inside the soil layer. Observing the contact force networks reported in Fig. 6.36, it is evident that, for very superficial instabilities ($\frac{t}{i} \lesssim \frac{2}{3}$ in the considered cases) the arching effect cannot fully develop, and thus the unstable wedges are only partially formed. As a consequence, the movements of the granular material tend to localise in the lower part of the mesh system (see Fig. 6.34); moreover, at the level of each mesh panel, the pressure exerted by the soil concentrates in the lower part of the panel, while in the upper part the granular material tends to move downwards. For low t/i ratios, the load imposed by the unstable soil volumes is not homogeneously distributed among the anchors and, in particular, a limited activation of the anchors in the upper part of the mesh system is observed as shown in Fig. 6.37. This determines a strong localisation of tensile stresses in the bottom part of the anchors placed at $y = 3$m (see Fig. 6.38), leading to a "premature" failure of the mesh due to the breakage of some wires at the connection with anchor C or anchor D. For ratios $t/i > 2/3$ instead, the arching effect can fully develop (see Fig. 6.36), and therefore the formation of the wedge-shaped unstable volumes is not

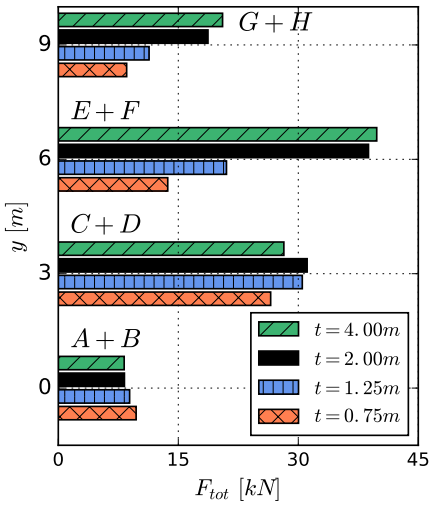


Figure 6.37: Tensile force supported by the different anchor levels an instant before the mesh failure for different values of the soil layer thickness t.

limited by the layer thickness (see Fig. 6.34). This permits a homogeneous distribution of the external load among the anchors (see Fig. 6.37) and thus a better exploitation of the retaining capacity of the mesh system. Having said that, it should be noted that in real applications the thickness of the unstable layer is generally limited to $t \leq 3$m. This limit is imposed mainly by two reasons. Firstly, the technical limitations related to the maximum depth that can be reached in the drilling operations for the anchor bolts installation (generally limited to 3m, these being carried out manually by climbing operators). Secondly, in order to contain the number of the bolts necessary to ensure the system stability; in fact, for unstable layers thicker than 3m, the required number of bolts will significantly increases and the system becomes more similar to a soil-nailing intervention rather than a secured drapery system [40]. The range of t/i in which the latter may influence the retaining capacity of the mesh system is the one typical of real applications, thus this geometric parameter has to be accurately considered in the design phase of a secured drapery in order to optimise its performances.

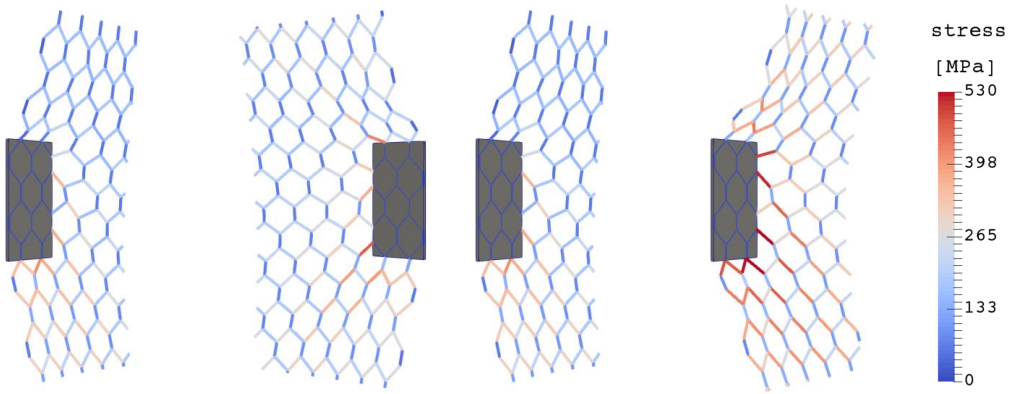


Figure 6.38: Tensile stress distribution on the wires surrounding the anchor C: (a) $t = 0.75$m, (b) $t = 4.00$m, and surrounding the anchor F: (c) $t = 0.75$m, (d) $t = 4.00$m.

6.3.6 Mesh mechanical properties

The mechanical properties of the mesh are varied by considering a different nominal diameter d_w of the mesh wires. This permits the resistance of the mesh, as well as its out-of-plane stiffness to be modified, without a significant modification of the mesh internal mechanical behaviour and the mesh geometry. In particular, three different diameters, namely d_w =2.0mm, 3.0mm, 3.9mm, as well as the reference one (i.e. $d_w = 2.7$mm) are considered. The different force-displacement relationships are compared in Fig. 6.39a, 6.39b, 6.39c, while the maximum force values registered during the simulations are compared in Fig. 6.39d, with reference to the force components F_y and F_z and to the total force F_{tot}. It should be noted that, for the case characterised by $d_w = 3.9$mm, the mesh system is able to retain the granular layer, and thus the failure condition of the mesh is not reached. In order to emphasise this difference with respect to the other cases, this latter test is represented with dashed lines in Fig. 6.39a, 6.39b, 6.39c and with empty markers Fig 6.39d respectively. Observing the F-δ curves, it is evident that the adoption of a larger wire diameter determines an increase of the out-of-plane stiffness of the mesh panel response, as well as an increment of the maximum force sustainable by the mesh panel (and consequently of its retaining capacity). The values of the total force (and of its components) supported by the cen-

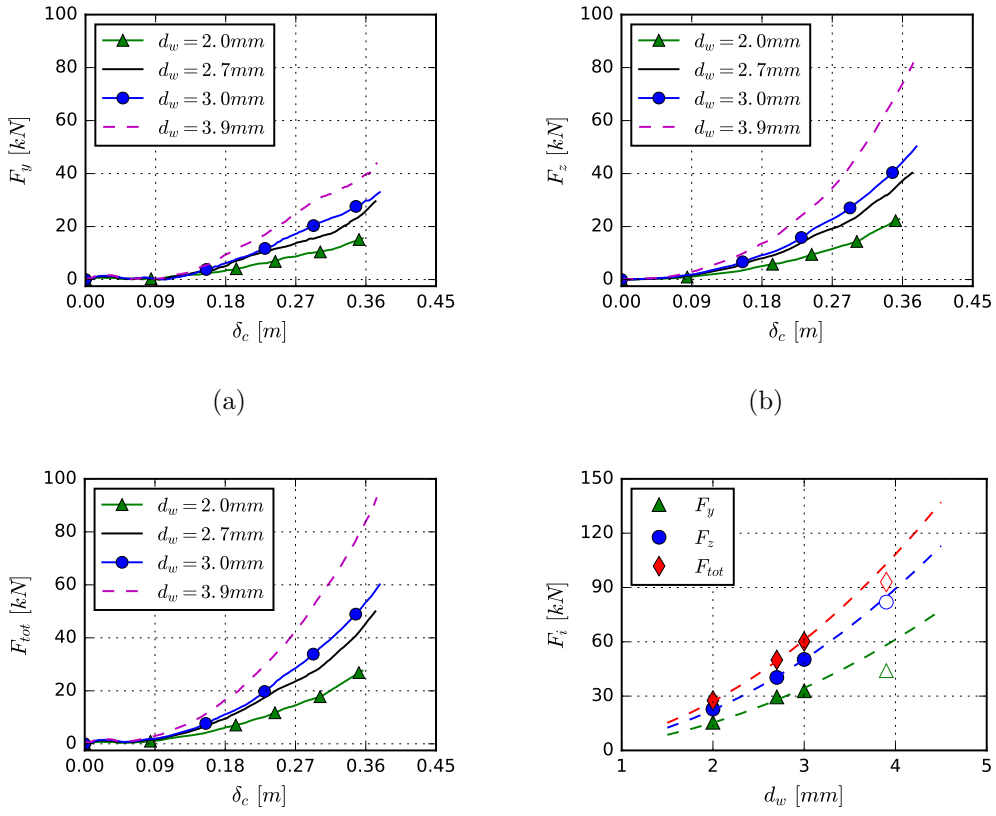


Figure 6.39: Comparison of the central panel mechanical response in terms of (a) F_y-δ, (b) F_z-δ and (c) F_{tot}-δ curves obtained varying the wire diameter d_w. (d) Maximum values of the force components and total force registered on the central panel (the values refer to the mesh mechanical condition an instant prior to its failure with the only exception of the case $d_w = 3.9$mm for which the failure is not reached).

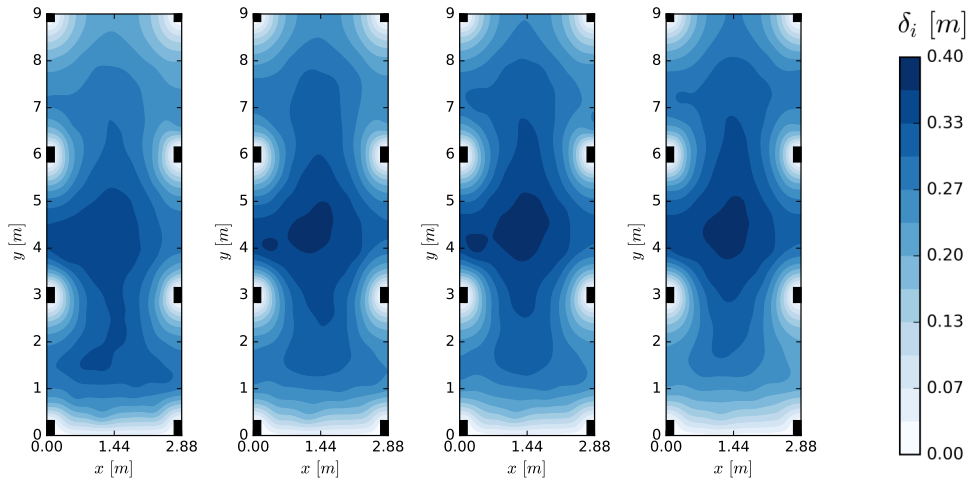


Figure 6.40: z-Displacement field (out-of-plane direction) of the mesh system, an instant prior to the mesh failure, obtained varying the wire diameter: (a) $d_w = 2.0$mm, (b) $d_w = 2.7$mm (reference case), (c) $d_w = 3.0$mm, (d) $d_w = 3.9$mm (no mesh failure).

tral panel, an instant prior to the mesh failure, seem to be well fitted by a quadratic function of the wire diameter (i.e. $F_i^{max} \propto d_w^2$); the values obtained for the case $d_w = 3.9$mm lie under the fit lines because the mesh failure is not reached. In order to understand this result, it is useful to recall that the system resistance is mainly controlled by the available resistance at the mesh-plate connection. This is, if considering the same plate dimension, a function of the resistance of the wires intercepted by the anchor plate which scales with the wires cross-section (the same stress-strain relationships are used independently of the d_w value adopted in the simulations), thus explaining the quadratic growth of the maximum force sustainable by a mesh panel with the wire diameter d_w.

Finally, the mesh and the soil z-displacement fields, obtained from the considered cases, are reported in Fig. 6.40 and Fig. 6.41 respectively. They refer to an instant prior to the mesh failure with the only exception of the one obtained considering $d_w = 3.9$mm for which the mesh was able to stabilise the soil layer behind it. A small reduction of the volume of the sliding wedge associated with the lower panel and a very slight growth of the one associ-

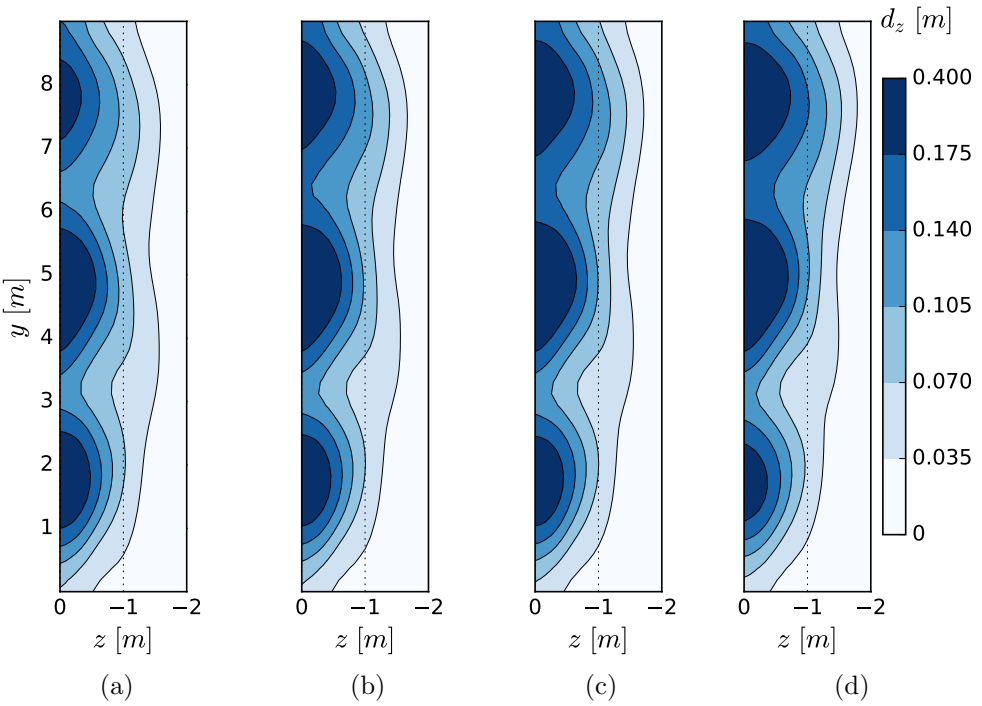
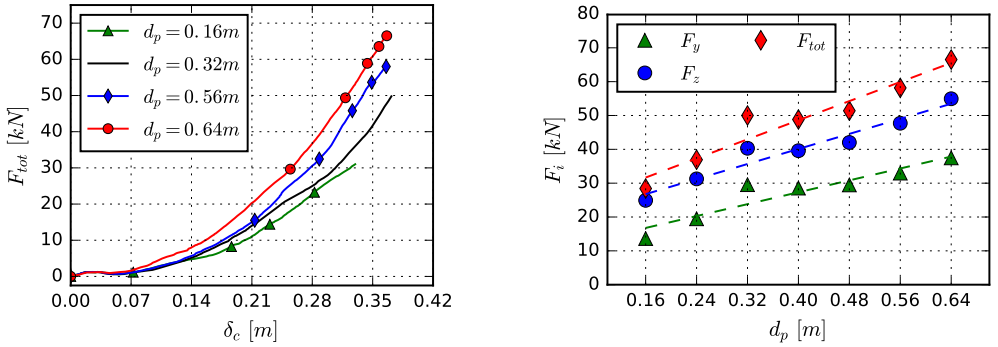


Figure 6.41: z-Displacement field of the unstable soil layer, an instant prior to the mesh failure obtained varying the wire diameter: (a) $d_w = 2.0$mm, (b) $d_w = 2.7$mm (reference case), (c) $d_w = 3.0$mm, (d) $d_w = 3.9$mm (no mesh failure).

ated to the upper panels are observed when increasing the wire diameter. This behaviour may be related to the higher retaining force that the mesh can exert increasing the value of d_w for the same amount of the panel deflection. This permits a "prompter" (in terms of panel deflection) stabilisation of the soil wedge acting on the lower panel, and consequently to a "quicker" activation of the upper wedges, thus leading to a "complete" activation of the unstable mechanisms associated to the upper panels. Despite the small differences above mentioned, the displacement field obtained adopting a different wire diameter results approximately the same for the four considered cases. Nevertheless, it should be kept in mind that, the failure mechanism occurring in the soil being influenced by the mutual interaction between the mesh and the soil, the mechanical characteristics of the mesh may influence the development of the soil failure mechanism.



(a) (b)

Figure 6.42: (a) Comparison of the central panel mechanical response in terms of F_{tot}-δ curves obtained varying the anchor plate dimension d_p. (b) Force components F_y and F_z and total force F_{tot} acting on the central panel an instant prior to its failure.

6.3.7 Anchor plate dimension

The dimension of the anchor plate d_p is modified in order to quantify the variation that this entails of the system resistance. As already observed, the maximum sustainable force by a mesh panel is mainly controlled by the available resistance at the mesh-plate connection that, if the same mesh is adopted, can be considered as a function of the anchor plate dimension. Moreover, when increasing the dimension of the anchor plate, the stabilising action deriving from the arching effect observed in Sec. 6.2.2 may become more significant, and thus influencing the failure mechanism occurring in the soil material behind the mesh system.

The mechanical response in terms of total force sustained by the central mesh panel is reported in Fig. 6.42a for four of the considered dimensions of the anchor plate, namely d_p =0.16m, 0.32m, 0.56m, 0.64m. The comparison of these curves highlights an increment of the out-of-plane stiffness of the mesh panel when increasing the dimension d_p of the anchor plate. Concerning the maximum sustainable force, this shows an approximately linear increasing trend with the dimension d_p as shown in Fig. 6.42b (same for its components). This effect is in agreement with what has been observed when considering a local punching condition in Chapter 4. The gentle step trend of the data in Fig. 6.42b may be ascribed to the discrete nature of the

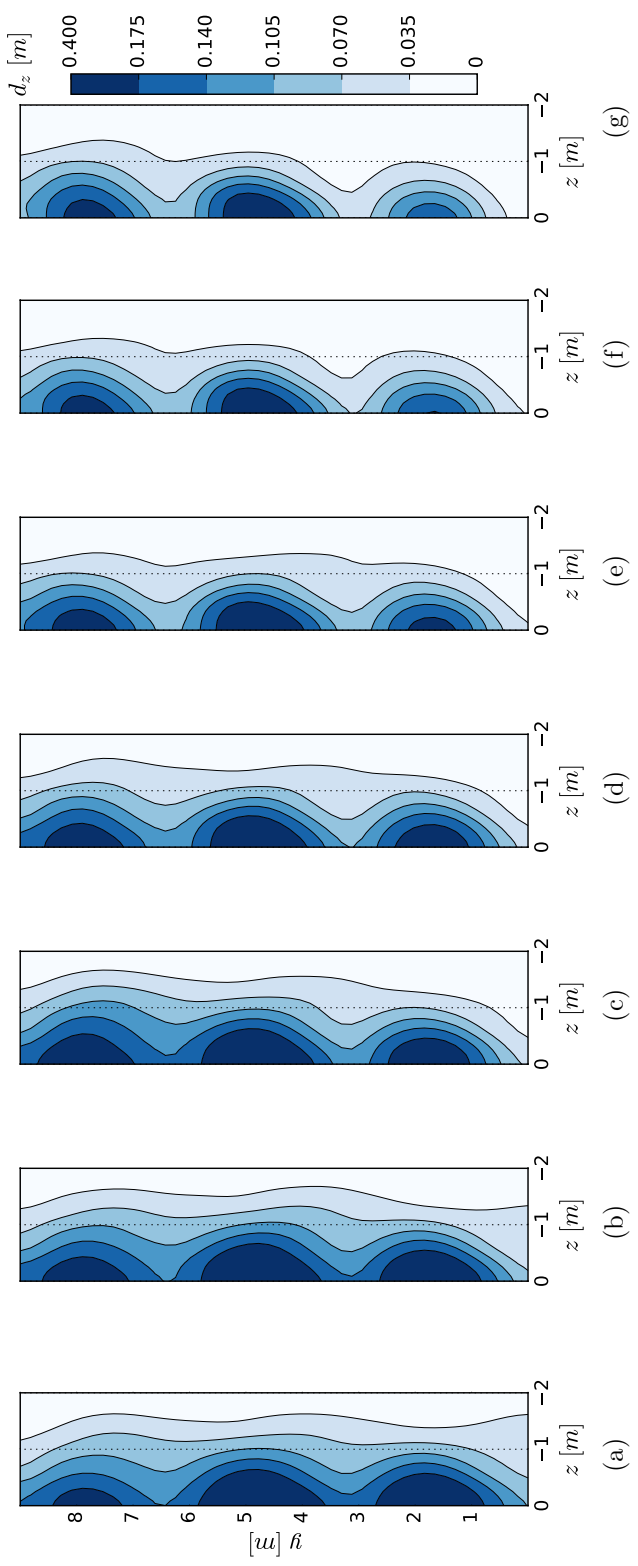


Figure 6.43: z-Displacement field of the unstable soil layer, an instant prior to the mesh failure, obtained varying the anchor plate dimension: (a) $d_p = 0.16$m, (b) $d_p = 0.24$m, (c) $d_p = 0.32$m (reference case), (d) $d_p = 0.40$m, (e) $d_p = 0.48$m, (f) $d_p = 0.56$m, (g) $d_p = 0.64$m.

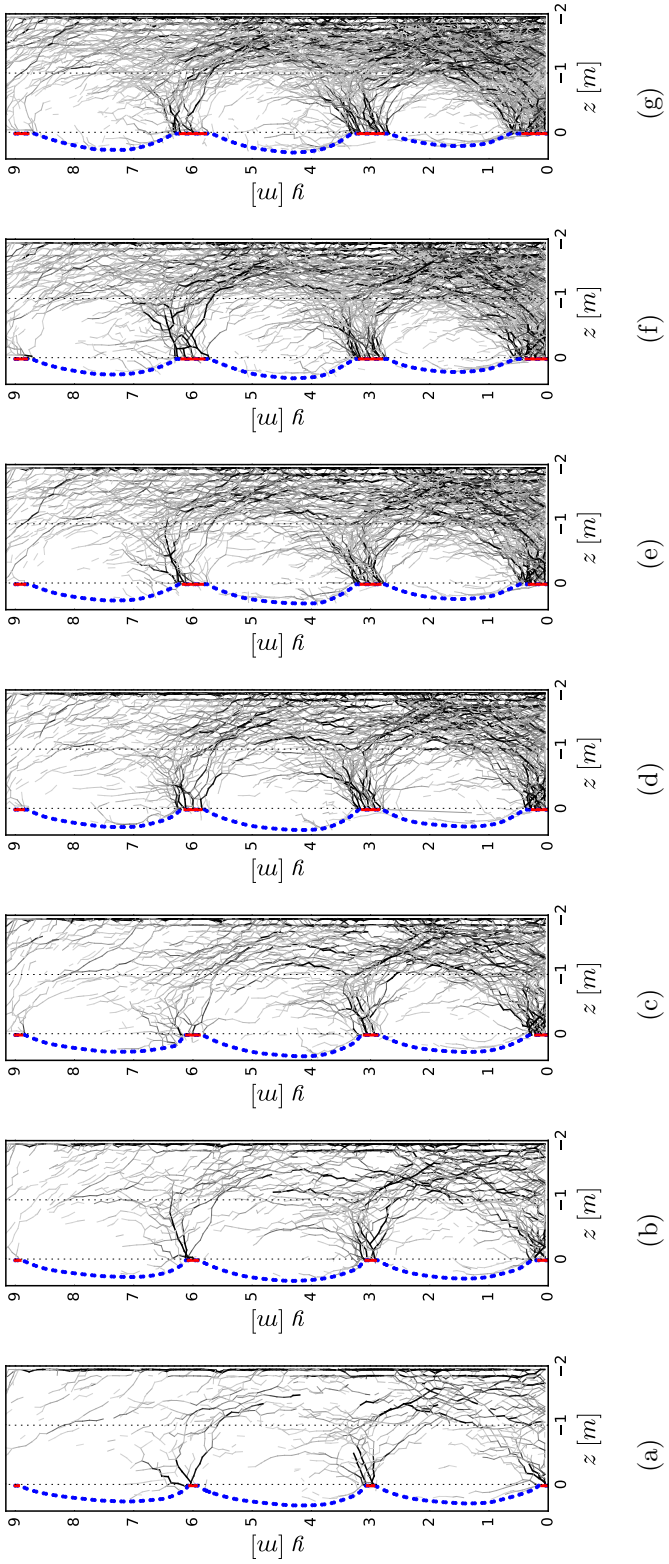


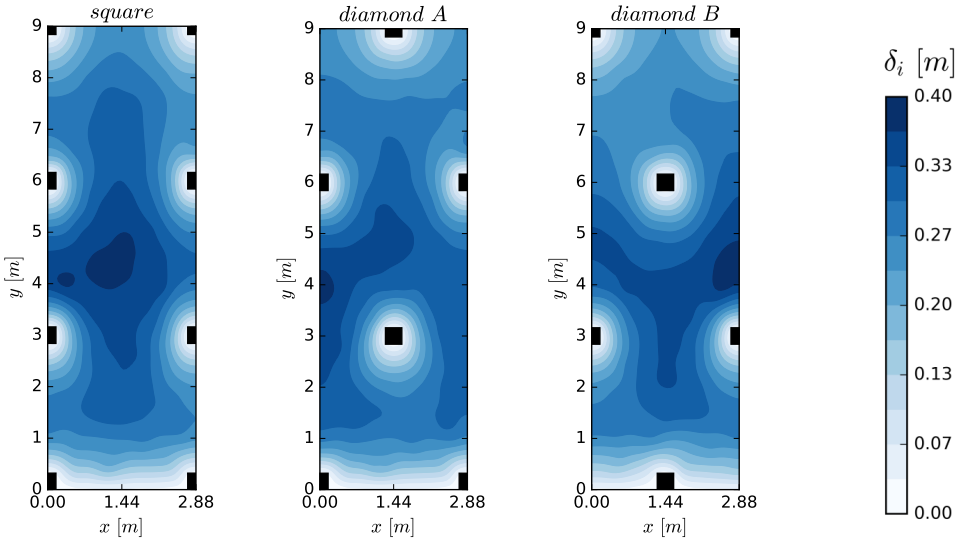
Figure 6.44: Contact force network (strong network) in the unstable soil layer, an instant prior to the mesh failure, obtained varying the anchor plate dimension: (a) $d_p = 0.16$m, (b) $d_p = 0.24$m, (c) $d_p = 0.32$m (reference case), (d) $d_p = 0.40$m, (e) $d_p = 0.48$m, (f) $d_p = 0.56$m, (g) $d_p = 0.64$m (the mesh section is represented by blue dots, while the anchor plates are highlighted by red continuous lines). The colorbar upper limit is set equal to $\max(F_n)/4$.

mesh model, and in particular to the not perfect proportionality between the plate dimension and the number (and typology) of wires that the former can embrace in the model.

The soil z-displacement fields obtained adopting a different dimension of the anchor plates are reported in Fig. 6.43. Moreover, for a better understanding of the influence of d_p on the soil movements, the related force contact (strong) networks are reported in Fig. 6.44. Both the force networks and the displacement fields computed considering the soil particles belonging to two vertical slices of width $2d_p$ in correspondence with the anchor plates (same as Fig. 6.16h, but considering the variation of d_p). Observing the contour plots of Fig. 6.43, it is possible to note a reduction of the depth of the soil layer interested by the failure process when increasing the anchor plate dimension. This is related to a stronger stabilising action that derives from the arching effect. In fact, increasing the anchor plate dimension, stronger "particles arches" are formed; moreover, due to the reduction of the distance between the borders of the anchor plates increasing d_p, the arches' span reduces and permits the formation of stable "particle arches" in a shallower portion of the unstable layer (using an analogy with structural arches, the arches' rise reduces). This permits a stabilisation of a greater portion of the unstable layer, leading to more superficial failure mechanisms. This condition can be observed in Fig. 6.44: increasing d_p the zone interested by a high frequency of strong contact forces (zones characterised by a high number of black thick lines) on the back layer of the soil volume increases as well, showing the "stabilisation" of a greater soil volume. Consequently, the zones characterised by a lower frequency (and amplitude) of the contact forces ("white zones" in Fig. 6.44) are smaller for higher value of d_p, highlighting the variation of the volume of the unstable local wedges. The volume of the unstable local wedge (estimated as in Sec. 6.2.2) acting on the central panel mesh, an instant before the failure of the latter, is equal to: $V_c = 7.1\text{m}^3$ for $d_p = 0.16\text{m}$, $V_c = 6.8\text{m}^3$ for $d_p = 0.32\text{m}$, $V_c = 5.6\text{m}^3$ for $d_p = 0.48\text{m}$, $V_c = 5.0\text{m}^3$ for $d_p = 0.64\text{m}$.

6.3.8 Anchors' pattern

In this paragraph, the influence of the geometrical pattern adopted for the anchors is analysed. In addition to the square pattern previously considered, a diamond arrangement represents the other common choice in practice. In



(a) (b) (c)

Figure 6.45: z-Displacement field (out-of-plane direction) of the mesh system, an instant prior to the mesh failure, obtained varying the anchor pattern: (a) *square*, (b) *diamond A*, (c) *diamond B*.

the model the mesh strip has a horizontal extension of a single mesh panel, therefore two configurations are possible in the case of a diamond pattern, namely the "*diamond A*" configuration and the "*diamond B*" as reported in Fig. 6.45. In the former, the considered mesh strip is characterised by the presence of the two lateral anchor plates at the base of the system, while in the latter a central anchor plate is placed at the toe of the system.

A comparison between the obtained mesh z-displacement fields, an instant prior to the mesh failure, is depicted in Fig 6.45. Referring to the diamond pattern, the maximum displacements are observed in correspondence to the mesh sections vertically aligned with the anchor rows. Moreover, two principal zones of material accumulation are observed, one in the lower part of the central panel and the other in the upper part of the lower panel. It is worth noting that this distribution of the mesh panel z-displacements is qualitatively in agreement with the one observed in the large scale test of [6, 104] (nevertheless, some differences in the system geometry and regarding the considered mesh type exist between the experimental test and the numerical model considered).

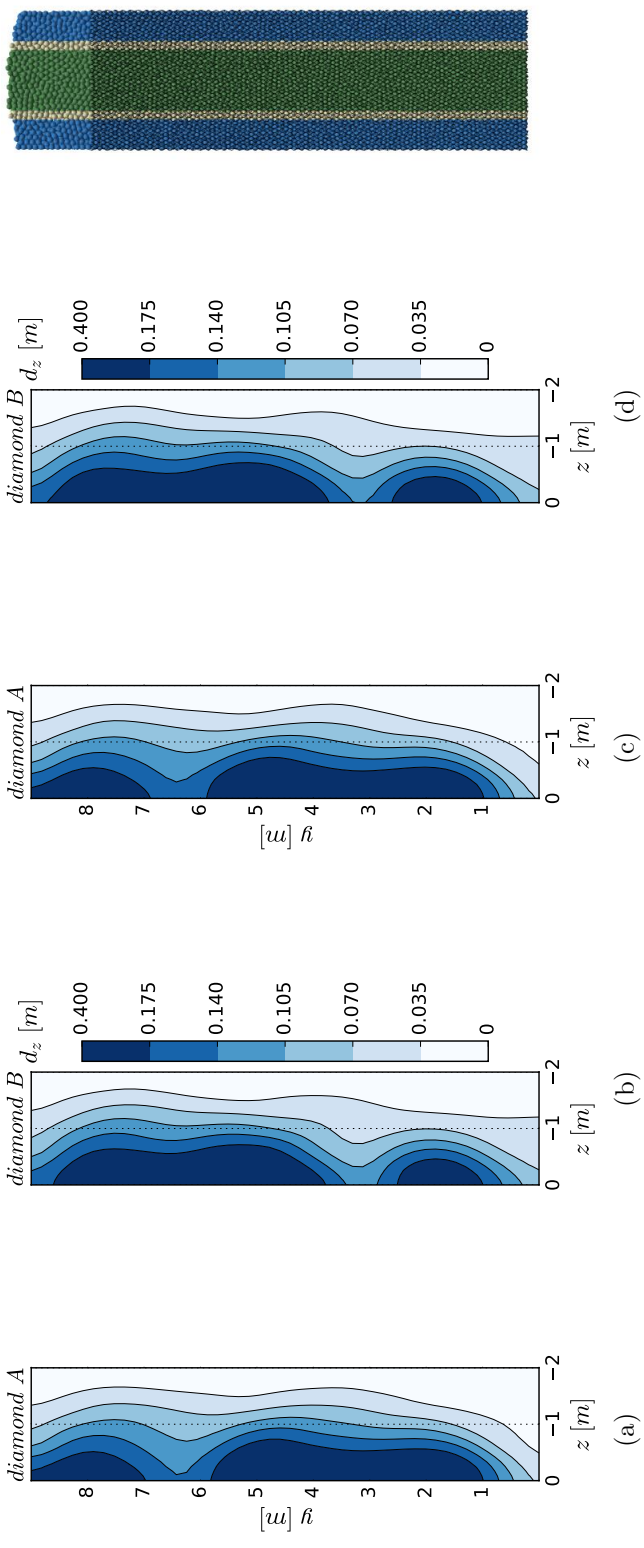
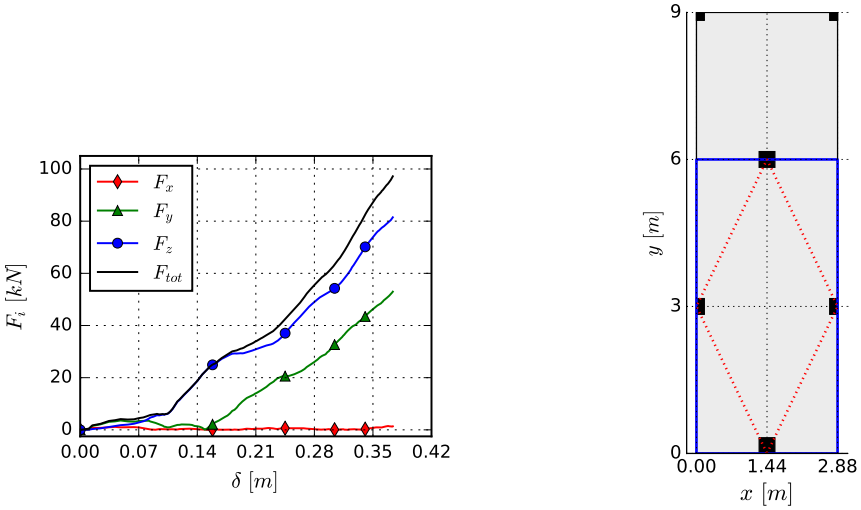


Figure 6.46: z-Displacement field of the unstable soil layer (an instant prior to the mesh failure) adopting the two configurations of the diamond anchor pattern obtained considering: (a, b) the lateral slices (blue volumes) and (c, d) the central slice (green volume).

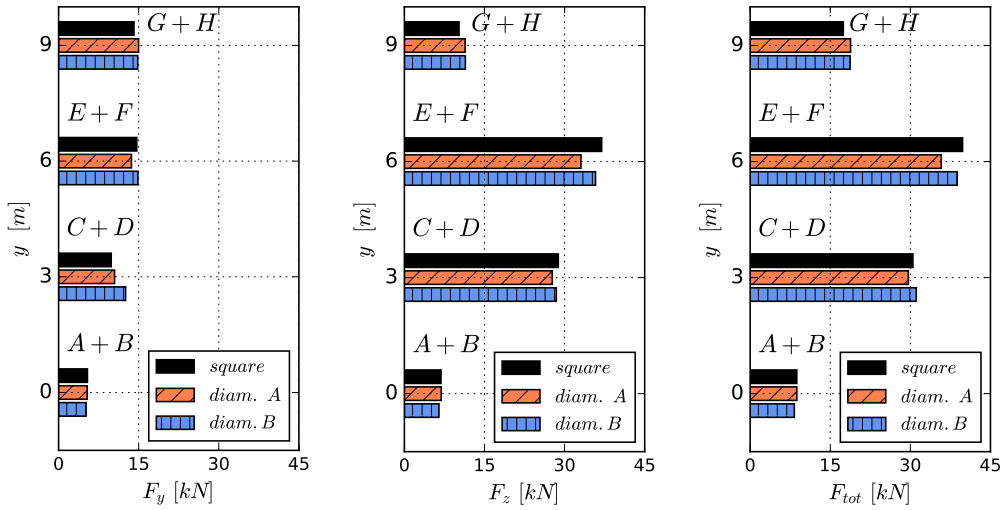


(a) (b)

Figure 6.47: (a) Force-displacement curves of the "reference panel" considered for the configuration "diamond B" of the anchor pattern. (b) The blue line represents the "reference boundary" considered for the force computation, while the red dotted line represents the boundary of the "ideal periodic panel".

The z-displacement field of the soil layer, an instant prior to the mesh failure, is reported in Fig. 6.46. In this case, due to the geometrical arrangement of the diamond pattern, two different reference volumes are used for computing the displacement field. The first is defined by two slices of width $2d_p$ starting at the lateral mesh edges (i.e. $x \leq$0.64m or $x \geq$2.24m), the other one is defined by a slice of width $4d_p$ centred in the middle section of the mesh system (i.e. 0.80 m$\leq x \leq$ 2.08m). This permits one to visualise the shape of the failure mechanism in correspondence to the anchors alignments, in analogy to what assumed in the classic design methodologies. For the sake of clarity, the particles belonging to the reference volumes are highlighted in Fig. 6.46 in blue for the former and in green for the latter reference volume respectively.

Similarly, to what has been observed adopting a square anchor pattern, a localised failure mechanism comprised between two anchor rows is observed also considering a diamond pattern. Nevertheless, in this latter case, the dimension of the sliding soil wedge is greater, the distance between two ver-



(a) (b) (c)

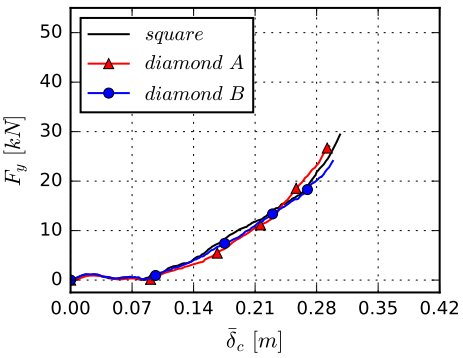
Figure 6.48: Force components (a) F_y, (b) F_z and (c) total force F_{tot} acting on the different anchor levels for the three geometric arrangements of the anchors. The plots refer to the system condition an instant prior to its failure.

tically aligned anchor plates being larger (3m for the square pattern and 6m for the diamond one). Moreover, the peculiar geometric arrangement of the anchors determines the occurrence of 3D effects in the soil and entails a variation of the unstable wedges vertical extension in-between two consecutive anchor alignments (compare Fig. 6.46a, 6.46c and/or 6.46b, 6.46d). The reduction of the wedge dimension in the upper part of the system, observable in Fig. 6.46a and Fig. 6.46b, is instead due to the finite size of the model. In light of the obtained results, the 2D schematisation of the unstable process as several localised wedge-shaped failure mechanisms, acting in-between two anchor rows, proposed in Sec. 6.2.2, can be extended also to the case of a system characterised by a diamond arrangement of the anchors. However, when adopting a diamond pattern, a greater vertical extension of the local unstable wedges has to be considered because of the increase of the vertical spacing between two anchor rows.

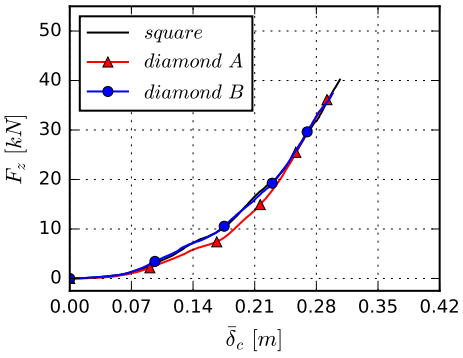
In this case, a direct comparison of the mechanical response of a mesh panel is not straightforward because of the geometric difference that exist between the square and the diamond pattern. Moreover, the different exten-

sion of the sliding soil volumes (compare Fig. 6.16 and Fig. 6.46) suggests a different definition of the reference panel. In this perspective, for the case "*diamond B*", the force-displacement (the displacement is measured at the centre of the reference panel) relationships characterising the response of the mesh reference panel is computed on a "reference boundary" that considers the portion of the mesh strip characterised by $y \leq 6.0$m (highlighted by the blue line in Fig. 6.47). It should be noted that this latter does not precisely follows the boundary of an "ideal periodic panel" (because of the difficulty to define a precise edge between two "periodic panels" due to the discrete nature of the mesh model), nevertheless it can provide an estimation of the mechanical response of a mesh panel (associated to a local unstable wedge) when using a diamond pattern for the anchors. The trends of the F-δ curves reported in Fig. 6.47 show an approximately linear activation of the mesh retaining force with the mesh deflection. It is worth mentioning that, in this case, the panel force is computed considering two full anchors and this explains the approximately double value, if compared to the one characterising the reference panel of the square pattern configuration, of the force at failure.

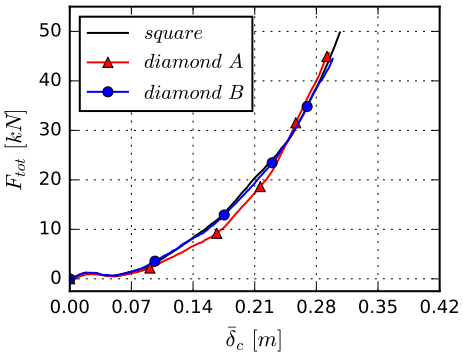
In order to compare the mechanical performance of the mesh obtained using a diamond and a square anchors' pattern, the force supported by the different anchor levels, an instant prior to the failure of the mesh, is reported in Fig. 6.48. The results denote that the force supported by the anchors is approximately the same for all the three considered cases. Therefore, the mechanical performance of the mesh at the connection with the anchor plates seems independent of the arrangement adopted for the anchors and only a function of the vertical position. Finally, the mechanical response of the central portion of the mesh panel (i.e. $3.0\text{m} \leq y \leq 6.0\text{m}$), obtained for the two configurations of the diamond pattern, is compared with the one obtained for the square pattern in Fig. 6.49. Even if when referring to the diamond pattern the force-displacement curve in Fig. 6.49 cannot be directly associated with a mesh panel, it permits the force that the central portion of the mesh is imposing on the unstable soil volume to be evaluated; this allows a first comparison between the two anchor arrangements (for all the configuration the nominal area of one anchor plate is considered in the forces computation). In this case, the mean displacement $\bar{\delta}_c$ measured on the considered mesh portion is used for the definition of the force-displacement relationships. Observing the F-$\bar{\delta}$ curves, it is notable that the reaction of



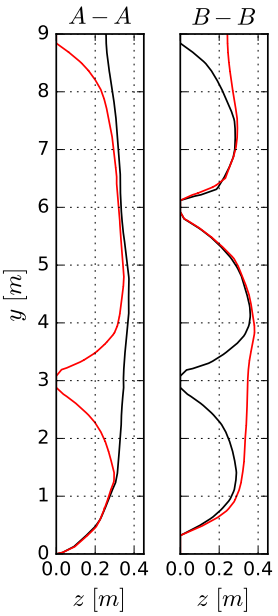
(a)



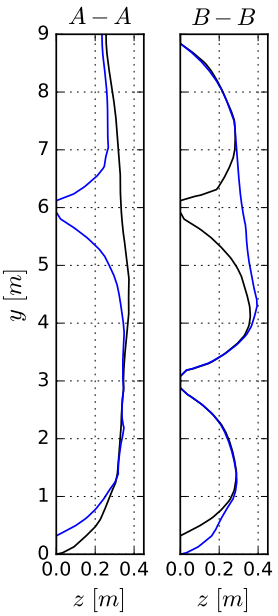
(b)



(c)



(d)



(e)

Figure 6.49: Comparison of the central panel mechanical response in terms of (a) F_y-$\bar{\delta}$, (b) F_z-$\bar{\delta}$ and (c) F_{tot}-$\bar{\delta}$ curves obtained varying the anchor pattern. Mesh profile with reference to the sections A-A and B-B for the configuration (d) "*diamond A*" and (e) "*diamond B*".

the central portion of the mesh system is approximately the same irrespective of the adopted anchors' arrangement. When comparing the maximum force sustained by the considered portion of the mesh system, a very slight difference is observable between the two anchors' patterns. In particular, the square pattern configuration shows a force that is less than 10% higher than the one registered for the diamond case (the mechanical behaviour of the configurations "*diamond A*" and "*diamond B*" is almost identical). The deformed configuration of the mesh (an instant prior to the mesh failure), referring to section A-A and section B-B (as defined in Sec. 6.2.3), is compared with the one obtained for the square pattern case in Fig. 6.49d and Fig. 6.49e for the configuration "*diamond A*" and "*diamond B*" respectively.

From the obtained results, despite the differences in the soil failure mechanism extension and in the mesh displacement field, the mechanical performance of the mesh is very similar, thus denoting that there is not an "a priori" optimal choice for the anchors' pattern. The choice of the latter may therefore be linked to other evaluations about the geometrical and mechanical characteristics of the slope. For instance, it can be argued that for slopes of high vertical extension the adoption of a diamond pattern permits the length of the free-fall corridors, between the mesh and the slope face, to be limited as pointed out by Ferraiolo and Giacchetti [40]. This allows the debris accumulation at the toe of the system to be contained, which instead may be significant when using a square pattern. On the other hand, a diamond arrangement for the anchors may lead to the formation of "suspended" local debris volumes that may significantly increase the cost of the maintenance operations related to the removal of the debris accumulation. Moreover, considering a generic mesh typology, its preferential internal force transmission mechanism (linked to the geometrical arrangement of the wires and their mechanical properties) should be carefully accounted in order to adopt an anchors' pattern (and eventually also the spacing) that permits the mechanical performance of the mesh to be optimised.

6.4 Conclusive remarks

In this chapter, the mechanical behaviour of a secured drapery system when considering interventions aimed to retain soil or highly fractured rock layers was investigated considering an idealised "in-situ" condition. The adopted numerical model ("mesh-soil" problem described in Sec. 6.1.3) represents a

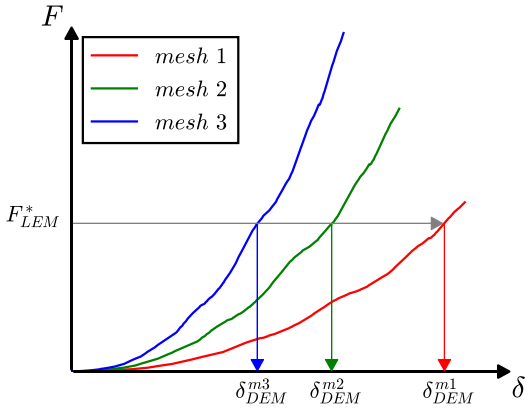


Figure 6.50: Conceptual scheme of the "coupling" between the standard limit equilibrium calculation and the discrete elements characteristic curves.

realistic schematisation of the field conditions, and thus it permits a detailed study of the mechanical behaviour of the mesh system. In particular, it was possible to identify the zones of localisation of stresses on the mesh (i.e. zones surrounding the anchor plates) and to highlight the force transmission mechanism inside the mesh. The force is mainly transmitted, inside each mesh panel, following inclined paths that connect the panel central section to the anchors, and it is partially vertically transmitted from a panel to the upper one, and it is finally supported by the top side of the mesh system. A fundamental result is represented by the definition of the force-displacement relations (i.e. F-δ curves) that permit one to characterise the activation of the mechanical response of the system with its deflection, thus providing a precise description of its mechanical behaviour. In this sense, the F-δ curves can be seen as "characteristic curves" of the system. Particular attention was given to the characteristic curve associated with the central panel, considering this latter a well representation of a generic panel belonging to a secured drapery system. The characteristic curves can be used for the definition of a more realistic design methodology (if compared with the standard ones reported in Chapter 1) in which the progressive activation of the mesh retaining action with its deflection can be duly accounted (displacement-based approach [46, 47]). Furthermore, the characteristic curves can also be "coupled" with the standard design methodologies (see Chapter 1), thus permitting the force computed from a limit equilibrium analysis to be as-

sociated with an estimation of the expected deflection in serviceability conditions (hybrid approach). For the sake of clarity, a conceptual example of this procedure is reported in Fig. 6.50 where three generic mesh types are considered: initially the retaining force F^*_{LEM} necessary to stabilise the failure mechanism in the soil is computed from a limit equilibrium calculation, then one can "enter" in the characteristics curves (determined from discrete element simulations) obtaining the expected deflection δ^m_{DEM} of the mesh.

Finally, the numerical analysis has permitted the failure mechanism occurring in the retained material to be identified, which can be considered as the one characteristic of the problem. The observed unstable process is characterised by several localised wedge-shaped volumes, each of which acting at the level of a single mesh panel. In this perspective, the adoption of a localised failure mechanism (as for instance the ones adopted in [22, 41]) seems a proper schematisation of the unstable process when applying a limit equilibrium analysis. This result permits uncertainty related to the choice of the failure mechanism to be overcome, which probably represents the main difference between the design methodologies proposed in the literature.

The main results obtained from the parametric analysis are summarised in the following:

- the frictional interaction at the interface between the mesh and the soil controls the inclination of the retaining force that a mesh panel can exert on the unstable material behind it. Nevertheless, the existence of a "macroscopic" interlocking force was pointed out considering a frictionless contact between the mesh elements and the soil particles. This interlocking is due to the soil volumes that may remain trapped in the zones surrounding the anchor plates and/or in the "bulged" zones of the mesh. A simple relation, accounting for both frictional and interlocking effects, which permits one to estimate the inclination of the retaining force, was provided. This can be used in the standard limit equilibrium design methodologies for the definition of the "macroscopic" in-plane mesh retaining force (i.e. the force tangentially oriented with respect to the slope face at the mesh-soil interface).
- the inclination of the slope face influences the depth of the soil layer interested by the failure mechanism. In particular, the observed local sliding wedges are shallower when considering a gentler slope. Nevertheless, greater out-of-plane displacements of the mesh are observed for gentler slopes.

- the thickness t of the unstable layer was found to be a significant parameter to be considered in the design of a secured drapery system. This can influence the mesh performances, and more precisely, it may lead to a reduction of the mesh maximum retaining capacity when its value is not duly considered for the selection of the anchor spacing i. In fact, in cases in which the ratio t/i is less than 2/3, a linear reduction of the maximum force supportable by the mesh is observed. This behaviour is a consequence of the partial activation of the mesh panels, which is due to the reduction of the interaction surface between a single mesh panel and the associated unstable soil wedge (the thickness t limits the development of the wedge-shaped local failure mechanisms).
- the nominal wire diameter controls (for the same mesh typology and anchor plate dimension) the mechanical response of the mesh, and in particular, it influences its out-of-plane stiffness and the maximum force supportable by the mesh panel. The numerical data have shown that the gain in terms of mesh resistance can be estimated considering that the maximum retaining force scales as a square function of the wire diameter.
- the anchor plate dimension controls (for the same mesh typology) the available resistance at the connection between the mesh and the anchoring system, and consequently it mainly controls the resistance of a mesh panel (and thus also of the mesh system). The numerical data have shown that the mesh panel resistance linearly scales with the anchor plate dimension.
- the adoption of larger anchor plates determines an increment of the stabilising arching effect inside the soil layer, which reflects in a reduction of the extension of the unstable local volumes and in a decrease of the depth of the soil layer interested by the soil movements.
- local wedge-shaped failure mechanisms were observed also adopting a diamond arrangement for the anchors. However, in this latter case a greater vertical extension of the local wedges should be considered being the vertical spacing between two anchor rows greater than the one characterising the square pattern.

Conlcusions and Perspectives

Conclusions

The use of secured drapery wire mesh systems represents a solution, which is worldwide adopted in order to contrast shallow unstable phenomena along soil and rock slopes and to avoid the detachment and the consequent free-fall of rock blocks. Despite the large utilisation of these systems, the knowledge of their mechanical behaviour is still limited and it is mainly related to the results of standard laboratory tests [99]. On one hand, these tests may permit comparison of the performance of different mesh types, if a common test configuration is adopted, and allow one to provide performance metrics to describe the mechanical response of a wire mesh under a specific loading condition. On the other hand, the boundary conditions imposed to the mesh panel in the laboratory test configurations (i.e. fixed outer boundary) strongly differ from the ones typical of field applications. Moreover, the loading condition may be not very representative of the one encountered in the field (e.g. earth-pressure due to debris accumulation). Therefore, the mechanical response obtained from standard laboratory tests should not be directly adopted for characterising the behaviour of the mesh in field applications. The implementation of large-scale experimental tests in field condition represents a difficult task from both a technical and a financial perspective; only two tests were found in the technical literature [6, 8]. Furthermore, the information that can be eventually derived from these tests hardly permits a precise characterisation of the mesh mechanical behaviour. This thesis work was aimed to fill the gap between the standard laboratory characterisation and the in-field mechanical behaviour of secured drapery systems. In light of the above mentioned difficulty to realise experimental tests representative of the field conditions, it was chosen to address the problem from a numerical perspective. The Discrete Element Method, which has been efficiently used

to study dynamic impacts on flexible mesh structures, was here extended to the study of wire meshes in secured drapery applications.

The adopted DEM approach was proved to be a very efficient tool permitting the large deformations typical of secured drapery systems to be accounted for, and the failure of mesh elements to be handled. It was therefore possible to characterise the entire mechanical response of the mesh (i.e. from small deformations to failure conditions) and to observe the propagation of the failure inside the mesh system. The DE schematisation of a wire mesh adopted in this work, which only requires the knowledge of the tensile behaviour of the wire elements, was able to well reproduce the mesh mechanical response obtained from different experimental conditions ranging from simple tensile conditions to more complex configurations in which the mesh interacts with large external elements (punch test) and/or a granular soil layer (punch against soil test). The effectiveness of the adopted approach in reproducing the experimental response of a wire mesh can be of great interest from an industrial perspective permitting one to predict the effect of a variation of mechanical properties of the wires (e.g. material, diameter), of the mesh cell geometry (i.e. wire arrangement) and of the insertion of specific reinforcement elements (e.g. high-resistance steel ropes). This will permit one to have access to fundamental information, for the optimisation of the mesh mechanical behaviour, without the necessity to perform several experimental tests, thus representing a cost saving solution.

Different modelling approaches can be used for the numerical description of a wire mesh in a discrete element framework: a cell based (CB), a node-wire based (NWB), a cylinder-wire based (CWB). The CB approach permits a minimal discretisation of the mesh, in terms of elements, thus improving the computational efficiency of the model. A possible drawback is that the CB approach requires a precise calibration of the contact wire model (a single interaction represents one or several elementary cells of the mesh); furthermore, the CB approach does not permit a proper representation of the mesh geometry and therefore it is not recommended when geometrical aspects are relevant (e.g. mesh fabric, presence of superimposed structural elements, soil-inclusion problems). The NWB approach permits a proper schematisation of the mesh geometrical fabric and thus the effect of the latter to be considered without an ad hoc calibration of the contact wire model. A possi-

ble drawback is related to the fact that the physical shape of the mesh is not discretised (a mesh wire is represented by interconnected spherical particles). The NWB approach is therefore not recommended when analysing problems in which geometrical effects at the wire scale are relevant (i.e. soil-inclusion problems, retaining problems). Conversely, it is well suited when the focus is on the macroscopic behaviour of the mesh and when the mesh is interacting with sufficiently large external bodies. The CWB approach permits a proper schematisation of both the geometrical fabric and the physical shape of the mesh. It is therefore recommended when dealing with problems in which also effects at the wire scale are relevant. Furthermore, the CWB approach allows one to simulate the presence of structural elements superimposed on the mesh (e.g. reinforcement cables), as well as the relative motion between structural elements and connecting devices (e.g. sliding rings). The main drawback of the CWB approach is related to the increment of the computational time required by this approach with respect to the CB and the NWB approaches.

Three different numerical models were developed in order to analyse local and global behaviours that are considered characteristic of secured drapery systems. The 8x10 hexagonal double twisted mesh (produced by Officine Maccaferri SpA) was used as the reference mesh in this thesis work. The main results are listed in the following.

The analysis of the effect associated with the application of an intial load at the level of the connection between the anchor plate and the mesh had shown that the force-displacement behaviour of the system is characterised by two main phases. In the first phase, characterised by a low settlement of the anchor plate, the load applied to the latter is directly transmitted to the soil underneath, leading to the formation of a stabilising pressure cone in the soil volume surrounding the anchor plate. In the second phase, the mesh mechanical response is progressively activated leading to the application of a retaining action on the soil layer and to the onset of the mesh-soil interaction. Referring to the latter phase, it was shown that, for avoiding a significant loss in the applied initial load, the mesh type (or better its mechanical performance) should by selected in order to permit the activation of its mechanical response before the development of a failure mechanism in the soil layer.

The analysis of the punching behaviour of an anchored mesh panel had shown that, due to the boundary conditions adopted in the standard laboratory characterisation, the latter is not representative of the mechanical response of a mesh panel in field conditions. Considering an anchored mesh panel two different failure mechanisms were observed: a "block-punching" mechanism and an "anchor-punching" mechanism. The former is a condition likely when the mesh panel is loaded by a very sharp rock block; this determines a premature failure of the mesh before exploiting the entire retaining capacity of the mesh system. When the failure of the mesh is instead characterised by an "anchor-punching" mechanism, its retaining capacity is mainly controlled by the available resistance at the connection between the mesh and the anchor plate. The internal force transmission mechanism of the mesh significantly influences its mechanical response and is mainly controlled by the geometrical orientation and mechanical properties of the mesh elements, as well as by the boundary conditions. It was shown that the anchor spacing can be used in a performance perspective during the design phase, allowing one to control the deflection level necessary to activate a certain amount of the retaining force. In this perspective, specific curves (i.e. f_m-i curves) providing the rate of retaining capacity, associated to an admissible deflection level, as a function of the anchor spacing were derived. Moreover, it was shown that the aspect ratio of the mesh panel is an important parameter. In particular, the adoption of a mesh panel, which is more elongated along the direction of the double twisted wires, determines an enhancement of the mechanical performance. Finally, it was observed that the relative position between the unstable block and the anchor plates influences the mesh performance. In order to optimise the performance of a secured drapery system, it is therefore advisable, when possible, to consider this aspect during the design and the installation phases of the system.

The mechanical behaviour of a secured drapery system in soil retaining applications was studied defining a large-scale model. The adoption of a particle-based approach had permitted the mutual interaction between the mesh and the unstable material behind it to be accounted for. This aspect is fundamental for a correct description of the mechanical behaviour of the mesh as well as of the evolution of the failure process in the retained material. It was possible to identify the failure mechanism occurring in the

unstable soil layer on the back of the mesh system. This is characterised by local wedge-shaped local failure mechanisms, each of which is acting at the level of a single mesh panel. Such a failure mechanism is considered as typical of this kind of applications and can be used as the reference one when applying a limit equilibrium calculation for the design of a secured drapery system. The division in local wedges derives from the onset of a stabilising arching effect in the soil layer, which is caused by the interaction between the soil particles and the anchor plates. It was shown that, if the thickness of the unstable soil layer is sufficiently large to allow the complete formation of the arching effect, only a shallow portion of the soil layer is interested by the failure process. This entails the complete formation of the local sliding wedges permitting a full activation of the mesh panel retaining capacity. On the other hand, if the unstable layer is too superficial, the arching effect cannot fully develop and the sliding wedges are only partially formed. This leads to a localisation of the soil movements, in particular at the toe of the mesh system. In this case, the retaining capacity of the mesh panels is only partially exploited and a premature failure of the mesh system is observed. The threshold between these two conditions was observed for a thickness of the unstable layer approximatively equal to 2/3 of the anchor spacing. The mechanical response associated with a single mesh panel (a local failure mechanism is related to a single panel) was characterised providing specific force-displacement relationships (characteristic curves). These permit one to describe the progressive activation of the mesh retaining capacity with its deformation, pointing out the fact that secured drapery systems have to be considered as passive structures. The obtained force-displacement relations can be used in a coupled way with the standard LE design methodologies, thus permitting an estimation of the expected displacement of the system in serviceability conditions (hybrid approach). Alternatively, the characteristic curves can be used for the definition of a more proper design method, which permits the mobilised retaining action of the system, associated to a given displacement field into the retained material, the to be accounted for (displacement-based approach).

It was found that the retaining capacity of a mesh panel (and thus also of the mesh system) is mainly controlled by the available resistance at the connection between the mesh and the anchor plate. For the considered mesh (hexagonal double twisted mesh), a linear relation between this resistance

and the anchor plate dimension was found. An analogous behaviour was observed also considering a secured drapery system under a punching loading condition showing that the mesh-plate connection resistance may be a good indicator of the ultimate strength of an anchored mesh panel.

A summary of the numerical analyses performed in this thesis work is reported in Annex A.

Future perspectives

This thesis work has permitted information for the enhancement of the comprehension of the mechanical behaviour of secured drapery systems to be provided. However, it represents only a first step for an exhaustive understanding of these systems and it is characterised by some limitations. These are critically discussed in the following and possible improvements, as well as future perspectives are reported.

The 8x10 hexagonal double twisted wire mesh was used as the reference mesh in this work. Nevertheless, the extension of the adopted approach to other mesh typologies is very straightforward. A systematic study of the types of meshes commonly adopted in practice will permit a large dataset of characteristic curves to be created, thus allowing comparison of the mechanical behaviour of the different mesh typologies. This can be of great help to practitioners in the choice of the optimal mesh to adopt for a specific intervention.

The mesh model was validated against several laboratory test conditions, nevertheless the possibility to compare the numerical predictions against tests more representative of the field conditions can increase the reliability of the model. In this perspective, the development of a experimental punch setup in which an anchored mesh panel is tested appears an interesting and doable possibility. The realisation of large-scale field tests, even if it may entail a high cost, can be extremely useful for a further improvement of the numerical model.

The adoption of the Cylinder Wire Based approach (CWB) permits one to consider the presence of external elements superimposed on the mesh (an

example of this possibility was recently presented in [85]). In real applications, the installation of high resistance external ropes (also after the system installation) represents a common practice. A detailed study of the load transmission between the ropes and the mesh, as well as of the influence of their spatial distribution (e.g. horizontally oriented, diagonally oriented) on the system mechanical performances, can therefore provide helpful information in order to optimise such interventions. Moreover, the adopted approach permits the effect of the presence of external ropes on the movement of the retained material to be analysed.

The mechanical behaviour of a secured drapery system in rock slope applications was limited to the study of a single element acting of an anchored mesh panel. Although this analysis had permitted some key aspects to be highlighted, the field conditions can be more complex. The mesh system may be contemporary loaded by different blocks at different locations and/or the instability of local blocks can be triggered by the deformations experienced by the mesh. Moreover, the unstable blocks may slide along the slope face and interact between them and/or with some parts of the mesh system (e.g. anchor plates). These aspects can be studied by directly describing the rock mass in the discrete element model starting from the distribution and mechanical properties of the discontinuities that characterise rock mass (different strategies can be used for this purpose [86, 91]).

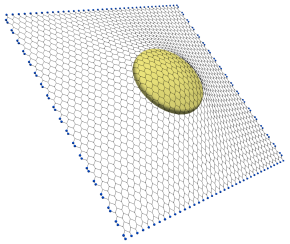
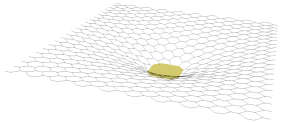
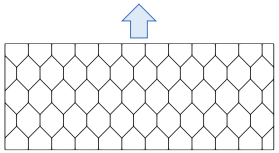
This research had pointed out the importance of the resistance of the connection between the mesh and the anchor plate on the overall resistance of a secured drapery system. A detailed study of the mesh anchoring system connection may lead to the definition of an optimal connection system, which may permit the performance of the considered mesh to be largely improved.

From the results of a set of numerical simulations, it will be possible to obtain data for the definition of simple tools, as for instance design charts (or analytical relationships), which can guide practitioners in the first phases of the design of a secured drapery system.

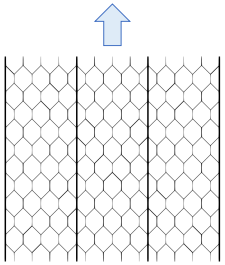
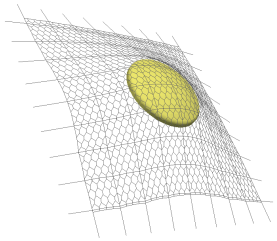
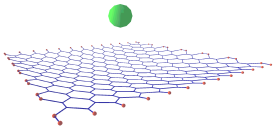
The design methodologies adopted to the present day for secured drapery applications do not consider the progressive activation of the mesh retaining capacity; moreover, they arbitrarily define the failure mechanism occurring

in the unstable layer (the latter differs in the various design methodologies). This may lead to a not adequate design of these structures, as also pointed out in [13, 85]. This thesis work was a first step of a wider research project whose aim is the definition of a more realistic design approach of secured drapery systems; the information obtained from the present work will be used for the development of a new design methodology based on a displacement based approach [46, 47].

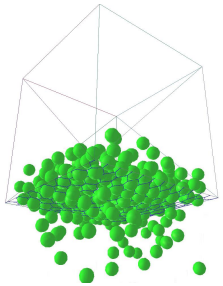
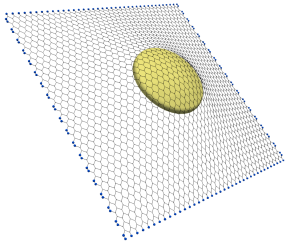
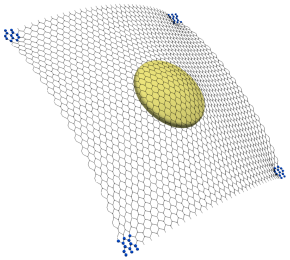
Annex A

View of the model	Description	Analyses	App.	Ref.
	Standard UNI punch test: the mechanical response of a planar mesh panel to an out-of-plane loading condition is investigated. The outer boundary of the mesh panel is fixed; the load is imposed by the movement of a dome-shaped punching element.	model validation, test setup dimension, modelling approaches comparison	NWB, CWB	Chapter 3 Sec. 3.3.1, 3.4.4
	Anchor punch test: the mechanical response of a planar mesh panel to an out-of-plane loading condition is investigated. The outer boundary of the mesh panel is fixed; the load is imposed by the movement of a square anchor plate.	model validation, nominal wire diameter	NWB	Chapter 3 Sec. 3.3.1
	Standard UNI tensile test: the mechanical response of a planar mesh panel to an in-plane loading condition is investigated. The load is imposed by moving one side of the mesh panel while the opposite one is kept fixed.	modelling approaches comparison	NWB, CWB	Chapter 3 Sec. 3.4.1

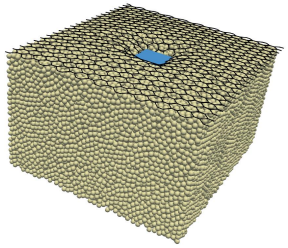
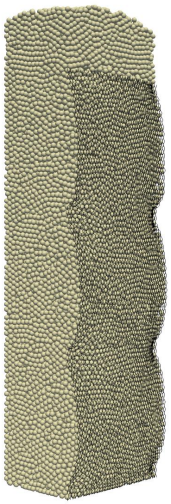
Summary of the numerical simulations performed in the thesis work.

View of the model	Description	Analyses	App.	Ref.
	Tensile test on mesh prototypes: the mechanical response of a planar mesh panel to an in-plane loading condition is investigated. The load is imposed by moving one side of the mesh panel while the opposite one is kept fixed.	model validation, mesh types comparison, effect of tensile direction	NWB	Chapter 3 Sec. 3.3.3
	Punch test on mesh prototypes: the mechanical response of a planar mesh panel to an out-of-plane loading condition is investigated. The outer boundary of the mesh panel is fixed; the load is imposed by the movement of a dome-shaped punching element.	model validation, mesh types comparison, effect of boundary conditions	NWB	Chapter 3 Sec. 3.3.4, Chapter 4 Sec. 4.3
	Drop test: the dynamics of a dropping sphere and its interaction with a mesh panel are investigated. The outer boundary of the mesh panel is fixed; the impact energy is kept fixed while the sphere dimension is varied.	modelling approaches comparison	NWB, CWB	Chapter 3 Sec. 3.4.2

Summary of the numerical simulations performed in the thesis work.

View of the model	Description	Analyses	App.	Ref.
	Retaining test: a granular volume is poured on a mesh panel and the retaining efficiency of the latter is investigated. The outer boundary of the mesh panel is fixed; the size of the particles is varied.	modelling approaches comparison	NWB, CWB	Chapter 3 Sec. 3.4.3
	Standard UNI punch test: the mechanical response of a planar mesh panel to an out-of-plane loading condition is investigated. The outer boundary of the mesh panel is fixed; the load is imposed by the movement of a dome-shaped punching element.	punching element dimension, punching element position, panel dimension, panel aspect ratio	NWB	Chapter 4 Sec. 4.1.3
	"In-situ" punch test: the mechanical response of a planar mesh panel to an out-of-plane loading condition is investigated. The mesh panel is anchored at its corners and periodic boundary conditions are imposed to the panel's sides; the load is imposed by the movement of a dome-shaped punching element.	punching element dimension, punching element position, anchor plate dimension, panel dimension, anchor spacing, panel aspect ratio	NWB	Chapter 4 Sec. 4.2.2

Summary of the numerical simulations performed in the thesis work.

View of the model	Description	Analyses	App.	Ref.
	Punch test against soil: the mechanical response of a planar mesh panel lied on a granular soil layer to an out-of-plane loading condition is investigated. The load is imposed by the movement of a square anchor plate.	boundary conditions, mesh mechanical properties, soil macroscopic friction angle, anchor plate dimension	NWB	Chapter 5 Sec. 5.2 Sec. 5.4
	Mesh-soil problem: the mechanical response of a large-scale secure drapery system loaded by a granular soil column is investigated. The mesh system is divided in three mesh panel that are locally anchored, moreover periodic boundary conditions are imposed to the panel's sides.	soil stiffness, soil macroscopic friction angle, mesh-soil interface friction angle, slope angle, thickness of the soil layer, mesh mechanical properties, anchor plate dimension, anchors' pattern	CWB	Chapter 6 Sec. 6.3

Summary of the numerical simulations performed in the thesis work.

Bibliography

[1] A. Albaba, "Discrete element modeling of the impact of granular debris flows on rigid and flexible structures," Ph.D. thesis, Université Grenoble Alpes, 2015.

[2] A. Albaba, S. Lambert, F. Kneib, B. Chareyre, and F. Nicot, "DEM Modeling of a Flexible Barrier Impacted by a Dry Granular Flow," *Rock Mechanics and Rock Engineering*, vol. 50, no. 11, pp. 3029–3048, 2017.

[3] B. Andreotti, Y. Forterre, and O. Pouliquen, *Granular Media: Between Fluid and Solid*. Cambridge University Press, 2013.

[4] ASTM A975, "Standard Specification for Double-Twisted Hexagonal Mesh Gabions and Revet Mattresses," 2016.

[5] T. C. Badger and J. D. Duffy, "Rockfall : characterization and control," A. Turner and R. Schuster, Eds. Washington DC: Transportation Research Board, 2012, pp. 554–576.

[6] P. Baraniak, K. Schwarz-Platzer, M. Stolz, T. Shevlin, and A. Roduner, "Large scale field tests for slope stabilizations made with flexible facings," in *GEOHAZARDS 6*, Kingston, Ontario, Canada, 2014.

[7] P. Baraniak, M. Stolz, B. Schoevaerts, and C. Wendeler, "New results of high-tensile steel meshes tested in first large scale field test application," in *Proceedings of the first Southern African Geotechnical Conference*, Jacobsz, Ed. Taylor & Francis Group, 2016, pp. 361–366.

[8] P. Bertolo, C. Oggeri, and D. Peila, "Full-scale testing of draped nets for rock fall protection," *Canadian Geotechnical Journal*, vol. 46, no. 3, pp. 306–317, 2009.

[9] D. Bertrand, F. Nicot, P. Gotteland, and S. Lambert, "Modelling a geocomposite cell using discrete analysis," *Computers and Geotechnics*, vol. 32, no. 8, pp. 564–577, 2005.

[10] D. Bertrand, F. Nicot, P. Gotteland, and S. Lambert, "Discrete element method (DEM) numerical modeling of double-twisted hexagonal mesh," *Canadian Geotechnical Journal*, vol. 45, no. 8, pp. 1104–1117, 2008.

[11] D. Bertrand, A. Trad, A. Limam, and C. Silvani, "Full-Scale Dynamic Analysis of an Innovative Rockfall Fence Under Impact Using the Discrete Element Method : from the Local Scale to the Structure Scale," *Rock Mechanics and Rock Engineering*, vol. 45, pp. 885–900, 2012.

[12] E. Blanco-Fernandez, D. Castro-Fresno, J. J. Del Coz Díaz, and J. Díaz, "Field measurements of anchored flexible systems for slope stabilisation: Evidence of passive behaviour," *Engineering Geology*, vol. 153, pp. 95–104, 2013.

[13] E. Blanco-Fernandez, D. Castro-Fresno, J. Del Coz Díaz, and L. Lopez-Quijada, "Flexible systems anchored to the ground for slope stabilisation: Critical review of existing design methods," *Engineering Geology*, vol. 122, no. 3, pp. 129 – 145, 2011.

[14] E. Blanco-Fernandez, D. Castro-Fresno, J. J. Del Coz Díaz, A. Navarro-Manso, and M. Alonso-Martinez, "Flexible membranes anchored to the ground for slope stabilisation: Numerical modelling of soil slopes using SPH," *Computers and Geotechnics*, vol. 78, pp. 1 – 10, 2016.

[15] A. Bonati and V. Galimberti, "La valutazione sperimentale di sistemi di difesa attiva dalla caduta massi," in *Proceedings of: Bonifica dei versanti rocciosi per la protezione del territorio*, Trento, 2004, pp. 11–15.

[16] F. Bourrier, F. Kneib, B. Chareyre, and T. Fourcaud, "Discrete modeling of granular soils reinforcement by plant roots," *Ecological Engineering*, vol. 61, pp. 646 – 657, 2013.

[17] F. Bourrier, S. Lambert, and J. Baroth, "A Reliability-Based Approach for the Design of Rockfall Protection Fences," *Rock Mechanics and Rock Engineering*, vol. 48, pp. 247–259, 2015.

[18] R. Bucher, C. Wendeler, and P. Baraniak, "New results of large-scale testing of high-tensile steel meshes and soil nails for slope stabilisation and validation of modelling software," in *Proceedings of the First Asia Pacific Slope Stability in Mining Conference, Australian Centre for Geomechanics*, Perth, 2016, pp. 709–720.

[19] M. Cała, D. Flum, A. R. R. Rüegger, and S. Wartmann, *TECCO® Slope Stabilization System and RUVOLUM® Dimensioning Method*, 2012.

[20] F. Calvetti, "Discrete modelling of granular materials and geotechnical problems," *European Journal of Environmental and Civil Engineering*, vol. 12, no. 7-8, pp. 951–965, 2008.

[21] F. Calvetti, C. di Prisco, and R. Nova, "Experimental and numerical analysis of soil-pipe interaction," *Journal of Geotechnical and Geoenvironmental Engineering*, vol. 130, no. 12, pp. 1292–1299, 2004.

[22] D. Castro-Fresno, "Estudio y análisis de las membranas flexibles como elemento de soporte para la estabilización de taludes y laderas de suelos y/o materiales sueltos," Ph.D. thesis, Universidad de Cantabria, Santander, 2000.

[23] A. Cazzani, L. Mongioví, and T. Frenez, "Dynamic finite element analysis of interceptive devices for falling rocks," *International Journal of Rock Mechanics and Mining Sciences*, vol. 39, no. 3, pp. 303 – 321, 2002.

[24] H. Cheng, H. Yamamoto, and K. Thoeni, "Numerical study on stress states and fabric anisotropies in soilbags using the dem," *Computers and Geotechnics*, vol. 76, pp. 170 – 183, 2016.

[25] M. O. Ciantia, M. Arroyo, J. Butlanska, and A. Gens, "Dem modelling of cone penetration tests in a double-porosity crushable granular material," *Computers and Geotechnics*, vol. 73, pp. 109 – 127, 2016.

[26] J. B. Coulibaly, "Modélisation numérique discrète du comportement mécanique sous impact des structures d'écrans de filets pare-pierres," Ph.D. thesis, Université Grenoble Alpes, 2017.

[27] J. B. Coulibaly, M.-A. Chanut, S. Lambert, and F. Nicot, "Nonlinear Discrete Mechanical Model of Steel Rings," *Journal of Engineering Mechanics*, vol. 143, no. 9, 2017.

[28] P. A. Cundall, "A Computer Model for Simulating Progressive Large Scale Movements in Blocky Rock Systems," in *Proceedings of the Symposium of the International Society for Rock Mechanics (ISRM)*, vol. 2, 1971.

[29] P. A. Cundall and O. D. L. Strack, "A discrete numerical model for granular assemblies," *Géotechnique*, vol. 29, no. 1, pp. 47–65, mar 1979.

[30] A. Da Costa, "Inestabilidades por degradación superficial de taludes en suelos. Corrección mediante sistemas de refuerzo anclados," Ph.D. thesis, Universidad de Cantabria, Santander, 2004.

[31] A. Da Costa and C. Sagaseta, "Analysis of shallow instabilities in soil slopes reinforced with nailed steel wire meshes," *Engineering Geology*, vol. 113, pp. 53–61, 2010.

[32] C. G. di Prisco, F. Besseghini, and F. Pisanò, "Modelling of the mechanical interaction between anchored wire meshes and granular soils," *Geomechanics and Geoengineering*, vol. 5, no. 3, pp. 137–152, 2010.

[33] J. Duffy and W. Hoon, "Field tests and evaluation of cuesta grade chain link fence, gawk screen, fence and jersey barrier," California Department of Transportation, San Luis Obispo, CA (USA), Tech. Rep., 1996.

[34] J. Duffy and W. Hoon, "Field tests and evaluation of hi-tech low energy chain link rockfall fence," California Department of Transportation, San Luis Obispo, CA (USA), Tech. Rep., 1996.

[35] A. Effeindzourou, B. Chareyre, K. Thoeni, A. Giacomini, and F. Kneib, "Modelling of deformable structures in the general framework of the discrete element method," *Geotextiles and Geomembranes*, vol. 44, no. 2, pp. 143–156, 2016.

[36] A. Effeindzourou, K. Thoeni, A. Giacomini, and C. Wendeler, "Efficient discrete modelling of composite structures for rockfall protection," *Computers and Geotechnics*, vol. 87, pp. 99–114, 2017.

[37] EN 10223-3, "Steel wire and wire products for fencing and netting - Part 3: Hexagonal steel wire mesh products for civil engineering purposes," 2014.

[38] J. Escallón, V. Boetticher, C. Wendeler, E. Chatzi, and P. Bartelt, "Mechanics of chain-link wire nets with loose connections," *Engineering Structures*, vol. 101, pp. 68 – 87, 2015.

[39] J. Escallón, C. Wendeler, E. Chatzi, and P. Bartelt, "Parameter identification of rockfall protection barrier components through an inverse formulation," *Engineering Structures*, vol. 77, pp. 1 – 16, 2014.

[40] F. Ferraiolo and G. Giacchetti, "Rivestimenti corticali: alcune considerazioni sull'applicazione delle reti di protezione in parete rocciosa," in *Atti del convegno Bonifica dei versanto rocciosi per la protezione del territorio*, Trento, 2004, pp. 147–176.

[41] D. Flum, T. Frenez, and G. U. Guasti, "L'impiego di sistemi di consolidamento flessibili in reti di acciaio ad alta resistenza nell'ingegneria geotecnica in ambiti di adeguamento e protezione delle infrastrutture." in *Congresso AGI XXII Convegno Nazionale di Geotecnica*, Torino, 2004.

[42] F. Gabrieli, A. Pol, N. Mazzon, and M. L. Deana, "Discrete element simulations of punch tests for the mechanical characterization of cortical meshes," in *Rock Mechanics for Natural Resources and Infrastructure Development*, S. A. da Fontoura, R. Jose Rocca, and J. P. Mendoza, Eds. London: CRC Press, 2020, pp. 3401–3407.

[43] F. Gabrieli, A. Pol, and K. Thoeni, "Comparison of two DEM strategies for modelling cortical meshes," in *Proceedings of Particle-based Methods - Fundamentals and Applications, Particles 2017*, 2017, pp. 489–496.

[44] F. Gabrieli, A. Pol, K. Thoeni, and N. Mazzon, "Particle-based modelling of cortical meshes for soil retaining applications," in *Numerical*

Methods in Geotechnical Engineering IX. London: CRC Press, 2018, pp. 391–397.

[45] F. Gabrieli, S. Cola, and F. Calvetti, "Use of an up-scaled dem model for analysing the behaviour of a shallow foundation on a model slope," *Geomechanics and Geoengineering*, vol. 4, no. 2, pp. 109–122, 2009.

[46] A. Galli and C. di Prisco, "Displacement-based design procedure for slope-stabilizing piles," *Canadian Geotechnical Journal*, vol. 50, no. 1, pp. 41–53, 2013.

[47] A. Galli, R. Maiorano, C. Di Prisco, and S. Aversa, "Design of slope-stabilizing piles: From ultimate limit state approaches to displacement based methods," *Rivista Italiana di Geotecnica*, vol. 51, no. 3, pp. 77–93, 2017.

[48] C. Gentilini, L. Govoni, S. de Miranda, G. Gottardi, and F. Ubertini, "Three-dimensional numerical modelling of falling rock protection barriers," *Computers and Geotechnics*, vol. 44, pp. 58 – 72, 2012.

[49] Geobrugg AG, *Software manual: SPIDER Single block protection.*, 2017.

[50] W. Gerber, H. Grassl, A. Böll, and W. Ammann, "Flexible rockfall barriers - development, standardisation and type-testing in switzerland," in *International Conference on Landslides - Causes, Impacts and Countermeasures*, Davos, 2001, pp. 515–524.

[51] G. Giacchetti and A. Grimod, "Rockfall mitigation using simple drapery system: Design approach," in *Engineering Geology for Society and Territory - Volume 2*, G. Lollino, D. Giordan, G. B. Crosta, J. Corominas, R. Azzam, J. Wasowski, and N. Sciarra, Eds. Cham: Springer International Publishing, 2015, pp. 1881–1884.

[52] A. Giacomini, K. Thoeni, C. Lambert, S. Booth, and S. Sloan, "Experimental study on rockfall drapery systems for open pit highwalls," *International Journal of Rock Mechanics and Mining Sciences*, vol. 56, pp. 171 – 181, 2012.

[53] G. Gottardi and L. Govoni, "Full-scale modelling of falling rock protection barriers," *Rock Mechanics and Rock Engineering*, vol. 43, pp. 261–274, 2010.

[54] L. Govoni, S. de Miranda, C. Gentilini, G. Gottardi, and F. Ubertini, "Modelling of falling rock protection barriers," *International Journal of Physical Modelling in Geotechnics*, vol. 11, no. 4, pp. 126–137, 2011.

[55] H. Grassl, A. Volkwein, E. Anderheggen, and W. J. Ammann, "Steelnet rockfall protection - experimental and numerical simulation," in *WIT Transactions on The Built Environment*, Lisbon, 2002.

[56] I. Gratchev, D. Kim, and M. Chung, "Study of the interface friction between mesh and rock surface in drapery systems for rock fall hazard control," *Engineering Geology*, vol. 199, pp. 12–18, 2015.

[57] A. Grimod and G. Giacchetti, "Design approach for secured drapery systems," in *Landslide Science for a Safer Geoenvironment*, K. Sassa, P. Canuti, and Y. Yin, Eds. Cham, 2003, pp. 99–105.

[58] A. Grimod and G. Giacchetti, "Design approach for rockfall protections with simple drapery systems," in *Landslide Science for a Safer Geoenvironment*, K. Sassa, P. Canuti, and Y. Yin, Eds. Cham: Springer International Publishing, 2014, pp. 77–82.

[59] G. U. Guasti, "Dimensionamento degli interventi di consolidamento di frane superficiali per mezzo di reti in acciaio ad alta resistenza Tecco®," in *Giornate di Studio 2003, Dimensionamento delle strutture, stabilità e materiali per interventi minori su versante*, Torino, 2003.

[60] G. Hearn, R. K. . Barrett, and H. . H. Henson, "Development of effective rockfall barriers," *Journal of transportation engineering*, vol. 121, no. 6, pp. 507–516, 1995.

[61] IberoTalud and Universidad de Cantabria, *DRET®. Programa de dimensionamiento de redes para estabilización de taludes. Manual de ayuda*, 2005.

[62] Itasca Consulting Group, *PFC2D 2.00 Particle Flow Code in Two Dimensions*. Itasca Consulting Group, Inc., 1998.

[63] M. Jean, "The non-smooth contact dynamics method," *Comput. Methods Appl. Mech. Eng*, no. 177, pp. 235–257, 1999.

[64] M. Jean and J. J. Moreau, "Unilaterality and dry friction in the dynamics of rigid body collections," in *Proceedings of Contact Mechanics International Symposium*, A. Curnier, Ed. Lausanne: Presses Polytechniques et Universitaires Romandes,, 1992, pp. 31–48.

[65] K. L. Johnson, K. Kendall, and A. D. Roberts, "Surface energy and the contact of elastic solids," *Proc. R. Soc. Lond*, no. 324, pp. 301–313, 1971.

[66] X. Li and J. Zhao, "A Unified CFD-DEM Approach for Modeling of Debris Flow Impacts on Flexible Barriers," *International Journal for Numerical and Analytical Methods in Geomechanics*, vol. 42, pp. 1643–1670, 2018.

[67] C. Liu and L. Chen, "Application and study of passive flexible protective net in slope protection," *Highway*, vol. 6, pp. 44–50, 2015.

[68] Maccaferri, *MACRO1 Theory and Background*, 2019.

[69] Maccaferri Innovation Center, "Internal report 1 - Punch test without soil," Tech. Rep., 2011.

[70] Maccaferri Innovation Center, "Internal report 2 - Punch test without soil," Tech. Rep., 2011.

[71] Maccaferri Innovation Center, "Internal report 3 - Punch test against soil," Tech. Rep., 2011.

[72] Maccaferri Innovation Center, "Internal report 5 - Mechanical characterization of mesh prototypes: punch tests," Tech. Rep., 2017.

[73] Maccaferri Innovation Center, "Internal report 6 - Mechanical characterization of mesh prototypes: tensile tests," Tech. Rep., 2017.

[74] G. R. McDowell, O. Harireche, H. Konietzky, S. F. Brown, and N. H. Thom, "Discrete element modelling of geogrid-reinforced aggregates," *Proceedings of the Institution of Civil Engineers - Geotechnical Engineering*, vol. 159, no. 1, pp. 35–48, 2006.

[75] R. Mindlin and H. Deresiewicz, "Elastic Spheres in Contact under Varying Oblique Force," *J. Appl. Mech*, no. 20, pp. 327–344, 1953.

[76] B. Muhunthan, S. Shu, N. Sasiharan, and O. A. Hattamleh, "Analysis and design of wire mesh/cable net slope protection," Washington State Transportation Commission Department of Transportation, Tech. Rep., 2005.

[77] H. Muraishi, M. Samizo, and T. Sugiyama, "Development of a flexible low-energy rockfall protection fence," *Quartely Report of Railway Technical Research Institute*, vol. 43, pp. 161–166, 2005.

[78] F. Nicot, B. Cambou, and G. Mazzoleni, "Design of rockfall restraining nets from a discrete element modelling," *Rock Mechanics and Rock Engineering*, vol. 34, no. 2, pp. 99–118, 2001.

[79] F. Nicot, B. Cambou, and G. Mazzoleni, "From a constitutive modelling of metallic rings to the design of rockfall restraining nets," *International Journal for Numerical and Analytical Methods in Geomechanics*, vol. 25, no. 1, pp. 49–70, 2001.

[80] Officine Maccaferri SpA, "Internal report 4 - Mechanical characterization of DT mesh: punch tests," Tech. Rep., 2012.

[81] C. O'Sullivan and J. Bray, "Selecting a suitable time step for discrete element simulations that use the central difference time integration scheme," *Engineering Computations*, vol. 21, pp. 278–303, 2004.

[82] D. Peila, S. Pelizza, and F. Sassudelli, "Evaluation of behavior of rockfall restraining nets by full scale tests," *Rock Mechanics and Rock Engineering*, vol. 31, pp. 1–24, 1998.

[83] A. Phear, C. Dew, B. Ozsoy, N. Wharmby, J. Judge, and A. Barley, *Soil nailing - best practice guidance*. CIRIA, 2005.

[84] A. Pol, F. Gabrieli, and L. Brezzi, "Discrete element analysis of the punching behaviour of a secured drapery system: from laboratory characterization to idealized in-situ conditions," *Acta Geotechnica*, (accepted).

[85] A. Pol, F. Gabrieli, and N. Mazzon, "Enhancement of Design Methodologies of Anchored Mesh Systems Using the Discrete Element Method," in *Geotechnical Research for Land Protection and Development*, F. Calvetti, F. Cotecchia, A. Galli, and C. Jommi, Eds. Lecco, Italy: Springer International Publishing, 2020, pp. 500–508.

[86] D. O. Potyondy and P. A. Cundall, "A bonded-particle model for rock," *International Journal of Rock Mechanics and Mining Sciences*, vol. 41, no. 8, pp. 1329 – 1364, 2004.

[87] F. Radjai, S. Roux, and J. J. Moreau, "Contact forces in a granular packing," *Chaos: An Interdisciplinary Journal of Nonlinear Science*, vol. 9, no. 3, pp. 544–550, 1999.

[88] F. Radjai and R. Vincent, "Contact dynamics as a nonsmooth discrete element method," *Mechanics of Materials,*, no. 41, pp. 715–728, 2009.

[89] A. M. Ritchie, "Evaluation of rockfall and its control," *HighwayResearch Record 17*, pp. 13–28, 1963.

[90] B. Salm, "Snow forces," *Journal of Glaciology*, vol. 19, no. 81, pp. 67 – 100, 1977.

[91] L. Scholtès and F.-V. Donzé, "Modelling progressive failure in fractured rock masses using a 3d discrete element method," *International Journal of Rock Mechanics and Mining Sciences*, vol. 52, pp. 18 – 30, 2012.

[92] S. Shu, B. Muhunthan, and T. C. Badger, "Snow loads on wire mesh and cable net rockfall slope protection systems," *Engineering Geology*, vol. 81, no. 1, pp. 15 – 31, 2005.

[93] V. Šmilauer, E. Catalano, B. Chareyre, S. Dorofeenko, J. Duriez, A. Gladky, J. Kozicki, C. Modenese, L. Scholtès, L. Sibille, J. Stránský, and K. Thoeni, "Yade documentation," in *Release 2015-03-09.gita2be717*, 2015.

[94] A. S. J. Suiker and N. A. Fleck, "Frictional Collapse of Granular Assemblies," *Journal of Applied Mechanics*, vol. 71, no. 3, p. 350, 2004.

[95] K. Terzaghi and R. Peck, *Soil Mechanics in Engineering Practice*. John Wiley, 1967.

[96] K. Thoeni, A. Giacomini, C. Lambert, S. W. Sloan, and J. P. Carter, "A 3D discrete element modelling approach for rockfall analysis with drapery systems," *International Journal of Rock Mechanics and Mining Sciences*, vol. 68, pp. 107–119, 2014.

[97] K. Thoeni, C. Lambert, A. Giacomini, and S. W. Sloan, "Discrete modelling of a rockfall protective system," in *Particle-based methods II: Fundamentals and applications. II International conference on particle-based methods*, E. Oñate and D. Owen, Eds., no. October 2014, 2011, pp. 24–32.

[98] K. Thoeni, C. Lambert, A. Giacomini, and S. W. Sloan, "Discrete modelling of hexagonal wire meshes with a stochastically distorted contact model," *Computers and Geotechnics*, vol. 49, no. June 2014, pp. 158–169, 2013.

[99] UNI 11437, "Rockfall protective measures - tests on meshes for slopes coverage," 2012.

[100] A. Vesic, "Bearing capacity of shallow foundations," in *Foundation Engineering Handbook*. Van Nostrand Reinhold Company, Inc., 1975, ch. 3.

[101] P. Villard and B. Chareyre, "Design methods for geosynthetic anchor trenches on the basis of true scale experiments and discrete element modelling," *Canadian Geotechnical Journal*, vol. 41, no. 6, pp. 1193–1205, 2004.

[102] A. Volkwein, "Numerical simulation of flexible rockfall protection systems," in *Computing in Civil Engineering (2005)*, Lisbon, 2005, pp. 1–11.

[103] A. Volkwein, K. Schellenberg, V. Labiouse, F. Agliardi, F. Berger, F. Bourrier, W. G. Luuk Dorren, and M. Jaboyedoff, "Rockfall characterisation and structural protection - a review," *Natural Hazards and Earth System Sciences*, vol. 11, pp. 2617–2651, 2011.

[104] C. Wendeler, R. Luis, and S. I. Choi, "High-tensile steel meshes used in slope stabilization systems, tested in first large scale field test application," in *Proceedings of the 19th International Conference on Soil Mechanics and Geotechnical Engineering*, Seoul, 2017, pp. 2219–2222.

[105] C. Xu, D. D. Tannant, and W. Zheng, "Discrete element analysis of the influence of bolt pattern and spacing on the force-displacement response of bolted steel mesh," *International Journal for Numerical and Analytical Methods in Geomechanics*, pp. 1–20, 2019.

[106] C. Xu, D. D. Tannant, W. Zheng, and K. Liu, "Discrete element method and support vector machine applied to the analysis of steel mesh pinned by rockbolts," *International Journal of Rock Mechanics and Mining Sciences*, vol. 125, 2020.

[107] J. Yang, S. Duan, Q. Li, and C. Liu, "A review of flexible protection in rockfall protection," *Natural Hazards*, vol. 99, pp. 71 – 89, 2019.